4 1949

THE PHYSICAL REVIEW

Series Number 3

FEBRUARY 1, 1949

for the

PHYSICAL SOCIETY

of

AMERICA

New York, N. Y.

A journal of exp

Published by the American Institute of P
for the
AMERICAN PHYSICAL SOCIE

Officers

President

J. R. Oppenheimer
Institute for Advanced Study
Princeton, New Jersey

Vice-President

F. W. Loomis
University of Illinois
Urbana, Illinois

Secretary

K. K. Darrow
Bell Telephone Laboratories
Office:
Columbia University
New York 27, New York

Treasurer

G. B. Pegram
Columbia University
New York 27, New York

Local Secretary
for the Pacific Coast

J. Kaplan
University of California at L
Angeles
Los Angeles, California

Managing Editor

John T. Tate
University of Minnesota
Minneapolis, Minnesota

The Physical Review
Entered as second-class matter M
Acceptance for mailing at special r

THE PHYSICAL REVIEW

A journal of exp *published by E. L. Nichols in 1*

BOARD OF EDITORS

Associate Editors

H. A. Bethe
S. A. Goudsmit
W. H. Zachariasen

Manuscripts for publication should be submitted to John T. Tate, University of Minnesota, Minneapolis, Minnesota.

All correspondence concerning papers in the process of publication should be addressed to the Publication Manager, American Institute of Physics, 57 East 55th Street, New York 22, New York.

Subscription Price

United States and Canada .....
Foreign .....

Back Numbers

Second Series. Vol. 1, 1913–Vol. 74, 1948
each.
Volumes each, prior to July, 1929;
each, July, 1929–December, 1941;
each, January, 1942–December, 1948.
Volumes each.

Orders and inquiries for back numbers should be addressed to the Business Manager, Lancaster, Pennsylvania, or to the American Institute of Physics, 57 East 55th Street, New York 22, New York.

Change of address for members of the American Physical Society should be addressed to the Treasurer; in the case of other subscribers, to the Business Manager, American Institute of Physics.

Editorial Associate: Physics Department, Cornell University.

Published monthly by the American Institute of Physics, 57 East 55th Street, Lancaster, Pennsylvania
Entered as second-class matter at the Post Office at Lancaster, Pennsylvania, under the Act of March
Acceptance for mailing at special rate of postage provided for in paragraph (d) section 538, P. L. & R., authorized

THE
PHYSICAL REVIEW

A journal of experimental and theoretical physics established by E. L. Nichols in 1893

SECOND SERIES, VOL. 75, No. 3 FEBRUARY 1, 1949

Experiments on *N–P* Scattering with 90- and 40-Mev Neutrons*

J. HADLEY, E. KELLY, C. LEITH, E. SEGRÈ, C. WIEGAND, AND H. YORK
Radiation Laboratory, Department of Physics, University of California, Berkeley, California

(Received October 25, 1948)

In this paper we describe some measurements of the neutron-proton scattering cross section at neutron energies of approximately 40 and 90 Mev. Both the total scattering cross section and the differential cross section as a function of the angle of scattering were measured.

I. INTRODUCTION

ONE of the important experiments that became feasible as soon as the 184-inch cyclotron started to operate was an investigation of the *n-p* scattering at a neutron energy around 90 Mev. As is well known, *n-p* scattering at high energy may yield interesting clues to the nuclear forces and data on it constitute important experimental material against which any future theory must be checked. The investigation acquires particular important if the De Broglie wave-length of the neutron in the center of gravity system (c.g. system) is comparable with the range of nuclear forces. The De Broglie wavelength is given by

$$\lambda\!\!\!^{-}=\hbar/p=9.0\times10^{-13}/E^{\frac{1}{2}}\text{ cm}.$$

(E in Mev in laboratory system; p = reduced mass × relative *n-p* velocity) and in the region of $E=100$ Mev has a value favorable for investigating *n-p* scattering. Neutrons of this energy are produced when the deuterons of the cyclotron are stripped in collision with nuclei of the target. A beam of neutrons of small, angular aperture and of fairly narrow energy distribution results.[1,2] This energy distribution has a maximum at about 90 Mev ($\lambda\!\!\!^{-}=0.95\times10^{-13}$ cm).

In the investigation to be described we have studied (*a*) the angular dependence of the scattering cross section, (*b*) the total cross section[3] at neutron energies of 90 Mev and 40 Mev. The angular measurements were extended over scattering angles in the c.g. system from 36 to 180 degrees.

To avoid unnecessary repetitions we shall now define the angles used in this paper (see Fig. 1). We shall call the angle of scattering of the neutron in the c.g. system θ; the angle of scattering of the neutron in the laboratory system Θ; the angle between the direction of motion of the incoming neutron and the recoil *proton* in the c.g. system and in the laboratory system, φ and Φ, respectively.

Between these angles we have the following relations:

$$\text{tg}\Theta=(1-\beta^2)^{\frac{1}{2}}\,\text{tg}(\theta/2), \tag{1}$$

$$\text{tg}\Phi=(1-\beta^2)^{\frac{1}{2}}\,\text{cotg}(\theta/2), \tag{2}$$

$$\frac{d}{d}\frac{\cos\Phi}{\cos\theta}=\frac{1}{4}\frac{1}{1-\beta^2}\frac{(1-\beta^2\cos^2\Phi)^2}{\cos\Phi}, \tag{3}$$

$$E_n=Mc^2(2\beta^2/1-\beta^2), \tag{4}$$

$$E_p=2\beta^2Mc^2/(1-\beta^2+\text{tg}^2\Theta), \tag{5}$$

where E_n and E_p are the kinetic energies of neutron and

* A short preliminary report of this work has been given in Phys. Rev. 73, 1114 (1948).

[1] A. C. Helmholz, E. M. McMillan, and D. Sewell, Phys. Rev. 72, 1003 (1947).

[2] R. Serber, Phys. Rev. 72, 1008 (1947).

[3] See also Cook, McMillan, Peterson, and Sewell, Phys. Rev. 72, 1264 (1947).

proton in the laboratory system, M is the rest mass of proton or neutron (considered equal), and β is the ratio of the velocity of the neutron in the c.g. system to the velocity of light. In our experiments ($E_n = 88$ Mev)β is equal to 0.2124 and the relativity effects start to be visible.

The principle of our experiment is to measure the number of protons scattered from a hydrogenous target into a fixed solid angle $d\Omega = d\psi d\cos\Phi$ at angle Φ; this number is proportional to the differential cross section $\sigma(\Phi)$ and from this we find the differential cross section $\sigma(\theta) = \sigma(\Phi)(d\cos\Phi/d\cos\theta)$ in the c.g. system. The direct measurement of $\sigma(\Phi)$ is not on an *absolute* scale, but we can normalize it and pass to an absolute scale by requiring that

$$\int \sigma(\Phi) d\Omega = \text{total scattering cross section} = \sigma_t. \quad (6)$$

This last quantity is obtained by measuring the attenuation of the neutron beam in passing through suitable absorbers. In practice, polyethylene or paraffin was used and the effect of carbon was measured (using graphite) and subtracted.

The main results of the investigation are contained in Tables II, III, and IV, and in Fig. 10.

II. ANGULAR DISTRIBUTION EXPERIMENTS

A. General Description

For angles Φ between 0° and 60° we have used apparatus A and B, the general arrangement of which is shown in Fig. 2. For angles $\Phi > 55°$ we have used a different apparatus to be described later. The neutron beam coming from the cyclotron was produced by stripping 180-Mev deuterons on beryllium. It was monitored either by protons scattered from an auxiliary polyethylene target or by a bismuth fission chamber.[4]

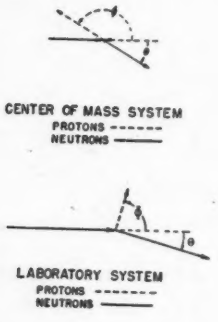

FIG. 1. Definitions of angles referred to in the text.

The scattered protons were detected by a telescope of three proportional counters pointing at the scatterer. The counter telescope was made insensitive to protons generated by primary neutrons of energy less than 66 Mev, by interposing between the last two counters an aluminum absorber (absorber A of Fig. 2) of a thickness such that it would stop all protons of an energy $< 66\cos^2\Phi$ Mev.

We measured the relative number of protons scattered by a polyethylene target per impinging neutron by registering the ratio R_1 between coincidence counts obtained in the telescope and the counts of the monitor. Subsequently the polyethylene target was replaced by a graphite target having the same stopping power for protons as the polyethylene target, and the ratio R_2 similar to R_1 was measured. Finally without any target we obtained the ratio R_3.

The effect, H, resulting from the hydrogen is obtained by

$$\begin{aligned} H &= (R_1 - R_3) - 0.713(R_2 - R_3) \\ &= R_1 - 0.713R_2 - 0.287R_3, \end{aligned} \quad (7)$$

where the coefficient 0.713 is the ratio between the number of atoms per cm² of carbon in the polyethylene target and the graphite target having the same stopping power for protons. H/t (t is the effective thickness of the target) is proportional to the cross section for n-p scattering. The statistical standard deviation of H, δH, is given by

$$[(\delta R_1)^2 + (0.713\delta R_2)^2 + (0.287\delta R_3)^2]^{\frac{1}{2}} = \delta H, \quad (8)$$

where δR_1 is the standard deviation of R_1, etc.

To fit the data obtained in different runs we proceeded as follows: Runs Nos. 1, 2, 12 (see Table II) have eight values of Φ in common. For these values the geometrical mean of the H/t values was calculated and a curve drawn. The other runs have one or more points in common with runs 1, 2, 12. These points were used to normalize the run in such a way that for the values of Φ common to the run in question and to the curve obtained from runs 1, 2, 12, the value of H/t would be the same, or, in case of more points in common, make a best fit. In doing

[4] C. Wiegand, Rev. Sci. Inst. 19, 790 (1948).

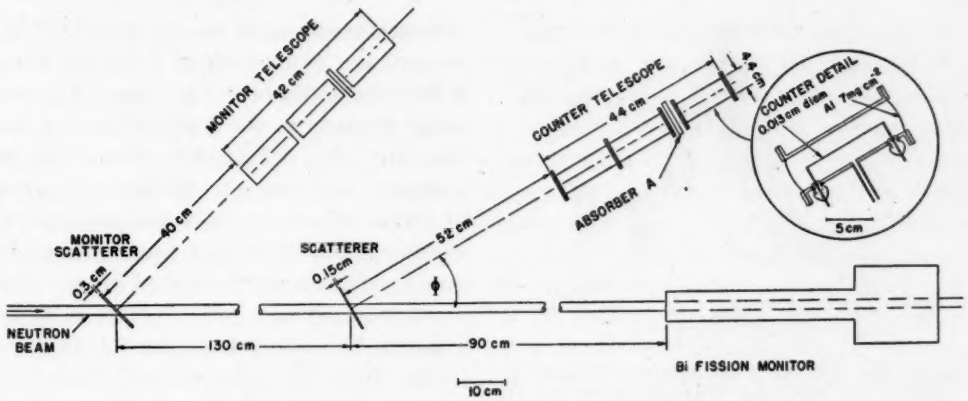

FIG. 2. General arrangement of apparatus A and B.

this we added to the statistical error of the measurement of H/t a fitting error equal to $(H/t)\times\delta\rho$, where $\delta\rho$ is the error in the normalization factor ρ. This can be estimated from the variation of ρ for various values of Φ or from the statistical errors of the single measurements. The statistical error of the single measurements and $(H/t)\delta\rho$ add by the usual rule:

$$\{[\delta(H/t)]^2+[(H/t)\delta\rho)^2]\}^{\frac{1}{2}}. \qquad (9)$$

Having thus obtained H/t as a function of Φ, we have at once on a relative scale the n-p scattering cross section as a function of Φ. To show the results obtained we report in Table II the values of H/t obtained in all runs and treated as described above to bring them all to the same scale. The errors listed are the standard deviations calculated from statistics on the single measurements. No account has been taken of the effect of $\delta\rho$.

We now give details of the instruments and of the single phases of the experiment.

B. Neutron Beam

The neutron beam was produced by stripping 180-Mev deuterons on a 1.27-cm thickness of beryllium. Its average energy is about 90 Mev. The beam was collimated by a hole in the 10-foot thick concrete walls of the cyclotron shield and emerged through an aperture of a diameter that has been varied in the different experiments from 7.5 cm to 1 cm. This aperture consisted of holes in two 50-cm long copper plugs, one at each side of the concrete shield. The beam was accurately centered either by obtaining a photographic image on an x-ray film in front of which we had put some paraffin or by looking with a cathetometer at the beryllium probe in the cyclotron.

The energy distribution of the neutrons to be expected in the primary beam is given by Serber's theory.[6] It is desirable, however, to have a direct experimental confirmation of the distribution because although the excellent agreement with the angular distribution of neutrons as measured[1] is good proof of the soundness of the picture, we want to know also if there are many neutrons of lower energy arising from other effects. We have, for this reason, taken a curve of coincidence counting rate as a function of the thickness of the absorber A, keeping Φ constant at 15°. From this curve it is possible to calculate by differentiation the energy distribution of the protons passing through absorber A, and by taking into account the dependence of the np scattering cross section on energy and angle it is possible to reconstruct the energy distribution of the neutrons in the primary beam.

The same distribution has also been investigated by lowering the voltage in the counter behind absorber A in the telescope in such a way that it was sensitive only to protons near the end of their range. The results of both experiments are shown in Fig. 3 together with Serber's theoretical curve. Agreement with Serber's diagram is good for the high energy region, but we have some indications of an appreciable number of neutrons of lower energy. This subject has not been further investigated because all our detectors were operated in such a way as to be

[6] R. Serber, Phys. Rev. 72, 1008 (1947).

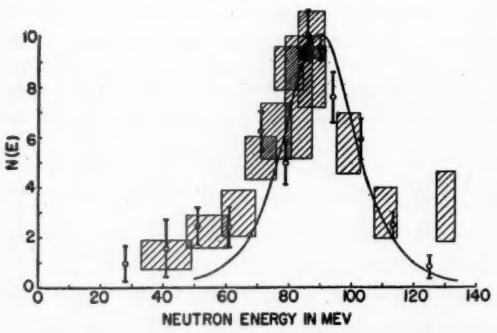

FIG. 3. Energy distribution of the primary neutrons in the beam obtained by stripping 190-Mev deuterons on 1.27-cm thick beryllium. The solid curve is from Serber's theory. The shaded rectangles are the results obtained by desensitizing the counter behind absorber A and varying the thickness of absorber A. The vertical lines are the results obtained by variation of absorber A and differentiation of the curve of absorber thickness *versus* number of coincidences.

insensitive to protons generated by primary neutrons of energy lower than 66 Mev. The cloud-chamber group[6] has obtained very good histograms of the energy of the neutrons in the primary beam showing agreement with Serber's theory.

At 45 Mev we do not have direct data on the energy distribution of the neutrons in the primary beam and we have assumed that Serber's theory gives the correct distribution.

C. Detecting Telescope

The scattered protons were detected with a telescope of three proportional counters pointing at the scatterer. The counters were brass cylinders 5 cm in diameter, about 13 cm long, with a 5-mil wire on the axis, filled at atmospheric pressure with a mixture of argon and carbon dioxide in the ratio 25 to 1 by volume. The front windows were 45 mg cm^{-2} copper or 7 mg cm^{-2} aluminum.

As we have already said, the telescope was made insensitive to protons generated by primary neutrons having an energy smaller than 66 Mev by interposing between the last two counters an aluminum absorber (absorber A of Fig. 2) of a thickness such that it would stop all protons of an energy smaller than 66 Mev $\cos^2\Phi$. More precisely, the absorber A placed in the coincidence telescope was chosen so that the minimum energy a neutron must have in order to give a detectable scattered proton was 66 Mev, if the proton was generated in an infinitesimal layer at half the depth of the scatterer. The energy loss of the protons in the scatterer makes this condition only approximate for other layers of a thick scatterer, and since the thickness of the scatterer in terms of energy loss becomes greater as Φ increases, the error increases with Φ. However, even in the case of the widest angles measured, a neutron must have (66+7) Mev in order to give a detectable proton from the side of the scatterer farther from the detector, and (66−7) Mev if it originates from the side nearer to the detector. The neutron energy distribution as measured by us, when multiplied by $\sigma(E)\simeq(A/E)$, shows that the correction necessitated by the effect of the thickness of the scatterer is negligible (±2 percent) because the number of protons originating at the far side of the scatterer and lost by absorption is almost exactly compensated by the excess of low energy protons originating at the near side of the scatterer.

At the neutron energies used in this experiment, the absorbers A are so thick (several grams/cm^2) that some protons which would otherwise pass through are removed either by Rutherford scattering or nuclear absorption. For apparatus A, where the absorber was placed immediately in front of the last counter, Rutherford scattering was negligible, and only the nuclear absorption produced any effect.

In apparatus C (see Section F and Fig. 7) it was necessary to place the absorber in front of all three counters. In the experimental arrangement, about one-half of the protons scattered by more than 3° would not be counted by the coincidence counter telescope. The fraction of protons lost due to this scattering is proportional to $N\sigma_\alpha$, where N is the number of atoms per cm^2 in the absorber, of atomic number Z, and σ_α is the cross section of the absorber for Rutherford scattering through an angle greater than α. σ_α is proportional to $Z/\alpha^2E_p^2$ and since at each angle Φ, N is varied approximately proportionately to E_p^2, the fraction of protons lost is nearly independent of Φ. To check this point and to find out what fraction was lost, we counted the number of protons going through various absorbers with the same stopping power but with differing Z. For this purpose C, Al, Cu, and Pb

[6] K. Bruckner, W. Hartsough, E. Hayward, and W. Powell; to be submitted to Phys. Rev.

were used. By plotting counting rate *versus* NZ^2/E_p^2, and extrapolating to $Z=0$, we found that at $\Phi=10°$, 45°, and 65° the fraction lost was about constant and equal to 4 percent for carbon, which was the absorber actually used with apparatus *C*. At the largest angle used, there was no carbon absorber in front of the counters, the principal part of the absorber being the gas in the counters themselves. Any Rutherford scattering which occurred would have taken place in the counters, and essentially no protons would have been lost due to this effect. Therefore, a correction of −4 percent has been applied to the value of $\sigma(\Phi)$ at 71.6° in order to be consistent with the rest of the data.

An estimate of nuclear scattering and absorption, originating from nuclear interaction, by the absorber *A* shows that it will not exceed about 4 percent in the worst conditions. Moreover, the difference between the magnitude of these effects at various angles is about half the absolute value. For this reason this effect has been neglected.

The amplifiers were conventional ones with times of rise varying from 0.2 microsecond in some of the sets to 0.5 microsecond in others. The scaling circuits were also quite conventional and allowed the recording of individual counts in each of the counter tubes. The coincidence circuits were of two types: In one model delay lines were used to obtain the gate-open times; in the other model multivibrators were used to form the gates. Gate times varied from about 0.5 to 12 microseconds and will be discussed in Section E.

D. Geometry and Scatterer

The approximate angular resolution of our apparatus was given by the diameter d of the counter furthest from the scatterer divided by its distance D from the scatterer, i.e., 2/50 radians. Since the scatterer itself was extended, the resolution was perhaps 3°. If one wishes to take into account the error in $\sigma(\Phi)$ introduced by the imperfect resolution, it is easily shown that the finite resolving power introduces a negligible correction unless the curve has very sharp irregularities. Only near $\Phi=0°$ may this correction be of any significance; at that point we estimate that it will raise the true cross section above the observed one by at least 10^{-27} cm² (7 percent) for the 90-Mev case and not appreciably affect it in the 40-Mev case.

The scattering targets were always very thin to neutrons; their thickness was determined by consideration of the energy lost in the scattering target by scattered protons. The target was always kept perpendicular to the direction of the telescope. The neutrons thus traversed an effective target thickness t equal to $s/\cos\Phi$, where s is the true target thickness. At constant beam, the number of neutrons crossing the target per unit time multiplied by the effective target thickness was independent of Φ if the beam always filled the whole scatterer, because on varying Φ the change of effective area was exactly compensated by the change of effective thickness. On the other hand, if the beam was smaller than the target area, the number of neutrons crossing the target per unit time multiplied by the effective target thickness was proportional to $s/\cos\Phi$. Both modes of operation were used. The detecting telescope could always see the whole scattering target.

E. Tests on the Apparatus and Typical Performance

It was necessary to ascertain that we counted all the protons of energy larger than 66 Mev $\cos^2\Phi$ coming from the target and nothing else. For this purpose we first studied the counter response *versus* voltage. With the telescope set at 10°, in order to be dealing with protons of practically maximum energy and hence minimum specific ionization, the coincidence counting rate *versus* the collection voltage of the counters was measured. Plateaus extending over about 300 volts were quite readily obtainable as shown in

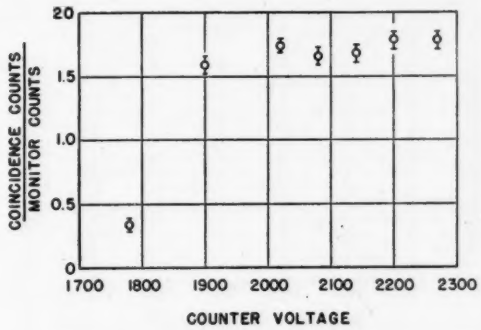

FIG. 4. Typical voltage plateau of counters.

TABLE I. Typical data.

Counter voltage	Angle Φ deg.	R^*	Time sec.	Counts in each tube No. 1	No. 2	No. 3	Coinc. counts	Monitor counts	Coinc. mon.	Absorber mg cm^{-2} Al	Scatterer mg cm^{-2}
2200 volts	10	2	200	40200	43000	42400	995	1559	0.638±0.03	3857	CH_2 150
2080	10	2	200	27800	28600	28800	1007	1523	0.662±0.03	3857	CH_2 150
1960	10	2	200	14400	12800	13100	685	1118	0.613±0.03	3857	CH_2 150
2120	10	2	600	46400	46600	47600	1560	2309	0.676±0.02	3857	CH_2 150
2120	10	2	200	15600	17300	16600	232	768	0.302±0.02	3857	C 182
2120	10	2	200	14600	13800	15900	114	795	0.143±0.01$_4$	3857	blank
2120	45	2	600	45200	42600	41600	499	2106	0.237±0.01	900	CH_2 150
2120	45	2	200	17900	16900	16100	126	1017	0.124±0.01	900	C 182
2120	45	2	110	10500	9720	9720	20	636	0.031±0.01	900	blank

Notes.—R^* is the reading of a "radiation" meter near the yoke of the cyclotron magnet. It is just a check on the operation of the cyclotron and not suitable as a beam monitor.
The first three readings were taken to check the counter voltage *vs.* coincidence/monitor plateau.
The results of the above two runs give: $H_{10°}=0.420\pm0.03$, $H_{45°}=0.139\pm0.01_4$.

Fig. 4. When the counters were adjusted to detect protons of 100-Mev energy, we found that the counters were also sensitive to the recoil electrons produced when a source of radium was brought near the counter. This was to be expected on the basis of the ionization produced by high energy protons and the ionization made by electrons. The sensitivity to these electrons provided a means of rough preliminary adjustment of the counters. Although the voltage plateau would indicate that all of the protons were being counted, more certainty can be obtained from the following experiment: With the counters in operation at a fixed angle, e.g., 10°, the triple coincidence counting ratio R_1 was obtained. Then the middle counter was disconnected (this procedure leaves the geometry unchanged) and a double coincidence count was obtained with the first and third counters in coincidence. If the number of protons recorded from the scatterer is the same as with the triple coincidence set-up, we feel justified in assuming that the efficiency is practically 100 percent,

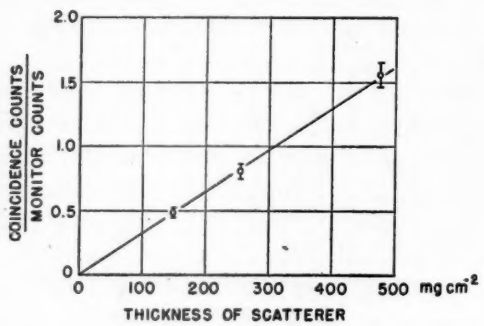

FIG. 5. Coincidence counts *versus* thickness of scatterer.

because if it were not, the use of only two counters would increase the number of coincidences obtained. A similar experiment was also done using four counters in coincidence and only the suppression of the counter farthest from the target, which obviously changes the geometry, had any effect on R_1. The reason for using triple coincidence rather than double coincidence is that a better radio of R_1 to R_3 is obtained, and that accidental coincidences are practically zero.

Another test is to determine the accidental coincidences. This was done by again setting the telescope at 10°, and obtaining the triple coincidence ratio R_1. Then the middle counter was removed physically from the telescope and placed just adjacent to its regular position. In this position the coincidence counts were reduced by a factor of about 1000, showing that the accidental coincidences were negligible. This is what one should expect if the apparatus were working properly. It is easy to overload the counters because of the fact that the neutrons are emitted by the cyclotron in short bursts. The last test described shows conclusively that this is not the case because spurious coincidences, which are unaffected if we put the counters out of line with the target, were not present. This point was further confirmed by showing that H/t was independent of the target thickness t and of the beam intensity in the region of operation, as shown in Fig. 5.

Experiments on the counting of protons with various gate times of the coincidence circuits showed that approximately the same counting efficiency was obtained with gate widths from

TABLE II. 90-Mev $\sigma(\Phi)$ in 10^{-27} cm² per steradian. All runs have been fitted to the average of runs 1, 2, and 12.

Run number	1	2	3	4	5	6	7	8	9	10	11	12		
Symbol in Fig.	○	●	△	×	□	▽	▭	▲	▯	▽	□	○		
Date	2-4-48	2-9-48	2-19-48	3-18-48	5-21-48	6-17-48	7-29-48	3-23-48	4-10-48	4-21-48	5-10-48	6-2-48		
Apparatus	*A*	*A*	*A*	*A*	*A*	*A*	*A*	*C*	*C*	*C*	*C*	*B*		
Φ(degrees)													θ(degrees)	$\frac{d\cos\Phi}{d\cos\theta}$
0						68.6±4.9	61.3±3.6						180.0	0.239
2				56.4±5.6									175.9	0.239
3				55.5±4.0	53.6±1.2								173.9	0.239
5	49.6±3.8	50.8±5.6		58.2±4.0	50.9±1.6								169.8	0.240
7												46.4±1.8	165.7	0.241
10	42.8±3.1	50.0±4.2		41.8±1.6	43.5±1.2	47.6±1.2	45.0±2.0						44.9±1.1	159.5	0.243
15	36.7±2.1	38.3±2.7											35.2±1.1	149.3	0.249
20	32.2±2.2	29.5±2.9				29.5±1.5							31.2±1.0	139.1	0.256
25	22.5±1.3	25.4±2.5											25.2±0.9	129.0	0.268
30	22.1±1.5	20.7±2.2											21.5±0.7	118.8	0.282
35	17.5±1.1	17.0±2.0	17.7±1.0										18.0±0.9	108.8	0.301
40	14.8±1.1	13.0±1.9											13.8±0.6	98.7	0.324
45	12.9±1.4	12.4±1.2	12.0±0.6	11.8±0.9	12.5±1.0			12.2±1.1	11.2±1.1	10.7±0.7	12.2±1.1	12.0±0.4	88.7	0.354
50	10.5±0.9	8.4±1.3											78.7	0.393
55	9.0±0.8	8.1±0.6	8.6±0.7						9.0±1.2	9.7±0.9			68.8	0.443
59		6.3±1.1											60.8	0.497
60								9.0±1.1		10.0±0.9	11.1±0.9		58.9	0.511
65									8.3±0.9	10.5±0.7			49.0	0.610
71.6								9.3±0.9	8.7±1.0	10.5±0.8	8.3±0.9		36.0	0.824

about 2 to 10 microseconds. Appropriate settings for the gate times amounted to 2 to 3 microseconds, as shown in Fig. 6.

An actual run started by a check of the gain of the amplifying systems effected by placing a radium source in a standard position with respect to the counter tubes and observing with an oscillograph the maximum height of the pulses produced by recoil electrons from the walls of the counters. This was done with a collection voltage on the counter tubes which was found to be on the plateau of the coincidence counting rate *versus* voltage curve of the previous run. The observed pulses were synchronized one on top of the other so that the pulse shape was shown. Pulses from the three proportional counter tubes were checked to make sure that the rise and decay times, respectively, were approximately equal in the three counters. These were rather qualitative checks but were capable of showing immediately any large changes in the characteristics of the counting system. A standard size pulse was applied in turn to the inputs of each of the scaling circuits to check that the minimum pulse height to trip the discriminators had not changed. The coincidence circuit gate length was checked on a calibrated sweep.

The measurements for different Φ in a single run were alternated so as to minimize possible trends in systematic errors, e.g., the following order was used in a run: $\Phi=10°$, 45°, 30°, 20°, 50°, 15°, 40°, 25°, 35°, 5°, 55° (February 4, 1948). (See Table I.)

We report in Table I the original data of the beginning of a typical run. They were taken with the following set-up:

Diameter of neutron beam exit hole was 2.22 cm.
Distance from exit hole to scatterer was approximately 350 cm.
Distance from scatterer to first counter was 85 cm.
Distance from scatterer to monitor was 140 cm.
Triple coincidence was used.
The scatterers measured 11 by 11 cm and were made of polyethylene and graphite.
The thickness of the scatterers and absorbers is indicated in Table I.

A word must be added on the measurements in the direction of the primary beam ($\Phi=0°$): The value of the cross section at $\Phi=0°$ was obtained with apparatus *A* using the same procedure as that used in measuring at $\Phi\neq0°$ but with some added precautions due to the fact that the primary neutron beam passed directly through the counters. The beam was stopped

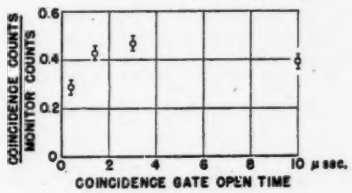

FIG. 6. Influence of the length of the gate open time on the coincidence counting rate.

down to an aperture 1.25 cm in diameter at the concrete shield and the intensity was reduced to about 3 percent of the usual operating intensity. The loss in intensity was partially compensated by using a thicker scattering target. The results obtained at 0° are given in Table II.

F. The Apparatus for $\Phi > 60°$

The apparatus schematically drawn in Fig. 2 was used for angles between 0 and 60°. At larger angles the thickness of the scatterer itself, the air, windows, etc., make this type of apparatus inadequate. A new apparatus shown in Figs. 7

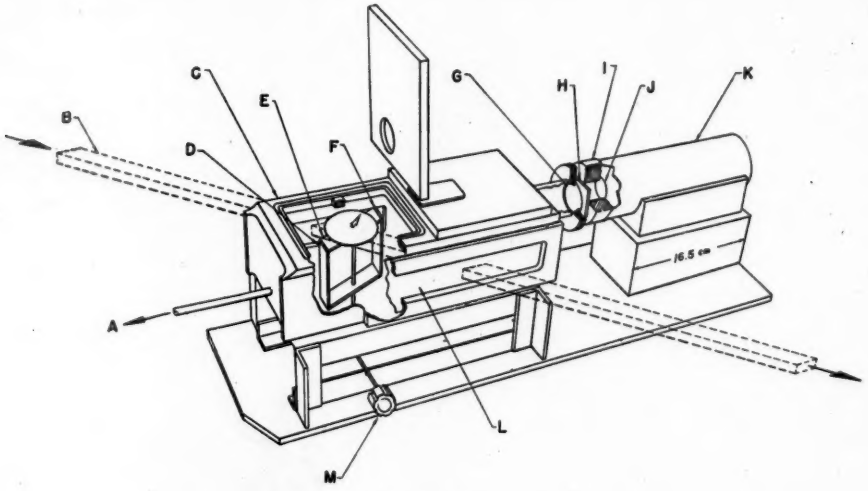

FIG. 7. Drawing of apparatus *C*.

A—to pump
B—neutron beam
C—vacuum scattering chamber
D—carbon scatterer
E—scatterer support
F—polyethylene scatterer
G—aluminum window
H—carbon absorber
I—diaphragm
J—mica window
K—counter telescope (four counters)
L—0.002-in. steel window
M—scatterer locator

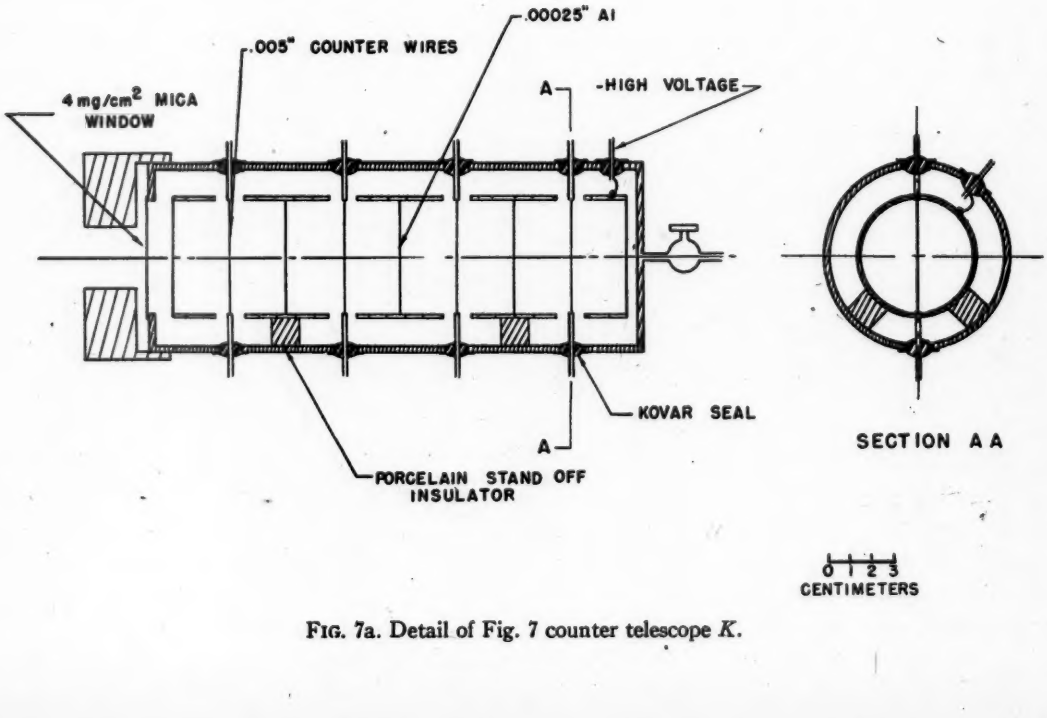

FIG. 7a. Detail of Fig. 7 counter telescope *K*.

TABLE III. 40-Mev $\sigma(\Phi)$ in 10^{-27} cm² per steradian. All runs have been fitted to the average of runs 2, 3, and 5.

Run number	1	2	3	4	5	6	7	8		
Symbol in Fig. 10	▼	○	●	□	○	△	×	▭		
Date	4-20-48	4-29-48	6-23-48	8-5-48	8-5-48	4-30-48	6-26-48	8-4-48		
Apparatus	*A*	*A*	*A*	*A*	*A*	*C*	*C*	*C*		
Φ (deg.)									θ (deg.)	$\frac{d\cos\Phi}{d\cos\theta}$
0				76.1±2.8					180	0.250
5			68.1±2.2						170	0.251
10	63.2±3.0	65.2±2.2	66.5±1.7	69.8±1.6	66.7±2.2				160	0.254
15		53.2±5.4	62.1±1.7		59.3±2.2				150	0.258
20		54.7±4.5	57.8±2.1	52.2±1.1	54.6±1.9				140	0.258
25		52.2±4.7	55.0±1.6		49.2±1.9				130	0.276
30	44.2±1.1	45.3±2.1	43.9±1.5		42.5±1.9				120	0.289
35		39.4±2.9	40.8±1.6		39.8±1.9	35.4±2.3	39.4±1.6	38.9±1.6	110	0.306
40		35.4±2.2	36.2±1.3		43.5±1.9				100	0.327
45	34.6±2.6	35.9±2.2	30.2±0.9		36.2±1.9	36.5±1.9	32.5±1.2	33.0±1.6	90	0.354
50						22.7±4.5		29.9±1.5	80	0.389
55						28.5±1.8		25.2±1.2	70	0.435
59						27.0±1.9	24.8±1.0	19.6±1.6	62	0.485

and 7a was built and was used to measure the scattering cross section for $35° \leq \Phi \leq 71.6°$. At larger angles all the difficulties introduced by matter in the path of the scattered beam and by the thickness of the scatterer become critical, and the rapidly increasing difficulty of the experiment made it impractical to exceed the angle of 71.6° with our present apparatus.

The apparatus shown in Fig. 7 relieved some of the difficulties mentioned above by providing for the evacuation of a space surrounding the scatterer and extending almost to the counter tube. Two benefits were obtained from this. First, the direct replacement of a 33-cm air column (equivalent to about 50 mg cm^{-2} Al) by an 11-mg cm^{-2} Al window and, second, the removal of the air from the beam path, which greatly decreased the background radiation. This fact in turn made it possible to use thinner scatterers (25-mg cm^{-2} CH_2), thus decreasing absorption within the scatterer.

The apparatus was made in the form of an aluminum alloy box, with 38-mg cm^{-2} rectangular stainless steel windows on opposite sides to allow passage of the beam. The arrangement provided for minimum production of protons by interaction of the beam with the box walls. On a third side was fixed an 11-mg/cm² aluminum window, through which the protons scattered by the target pass to reach the counting tubes. The carbon and polyethylene scatterers inside of the box were mounted on a rack which could be rotated from the outside to place either scatterer at a point within the beam and perpendicular to the axis of the counting tubes, or to place both out of the beam. A scale calibrated in degrees was attached to the rack, and a transparent window placed in the top of the box, so that the scatterers could be accurately placed for a run. The telescope of counting tubes was fixed permanently to the vacuum box, and adjustment to various scattering angles was made by rotating the entire apparatus on a pivot directly under the point occupied by the scatterer when in place for a run. The beam windows were made long enough to allow for this shifting of beam position with respect to the box. A removable cover was placed over the scatterers to provide access to them. Since there was no need to attain a very high degree of vacuum, no special precautions were necessary in making the box vacuum tight. It was evacuated by a small mechanical pump which ran continuously during the course of an experiment.

In order to decrease the amount of material in the path of the scattered protons all four tubes of the counting telescope were built into one envelope with resultant elimination of the windows between the individual units, as indicated in Fig. 7a. With this arrangement, of course, it was impossible to place absorbers between the last two tubes of the counting telescope. Consequently they had to be put in front of the whole telescope and the effect of Rutherford scattering by the absorber was somewhat more serious than in the other apparatus. This effect has been discussed under "*C*."

G. Lower Energy Experiments

By reducing the radius at which the beryllium probe is hit by the deuteron beam it is possible to obtain, by the stripping process, neutrons of lower energy. Unfortunately the width of the energy distribution in the forward direction does not decrease as much as the most probable energy, so that poorer energy resolution is obtained. This is born out in Fig. 8, where the theoretical neutron energy distribution is plotted for $E_D=98$ Mev and a target of 1-cm beryllium. Be this as it may, we have repeated the experiments with the same apparatus at a lower energy. The results are reported in Table III and in Fig. 10.

H. Summary of All the Experimental Results

Tables II and III contain a summary of all the experimental results of this investigation thus far obtained on the angular dependence of np cross section.

It must be added that several authors have found that for energies lower than 15 Mev $\sigma(\vartheta)$ is independent of ϑ.

III. TOTAL CROSS-SECTION EXPERIMENTS

In order to place the measured cross sections on an absolute scale it is necessary to determine the total scattering cross section. This can be accomplished by an attenuation measurement of the neutron beam using good geometry. Actually in the experiments we measured

$$\int N(E)D(E)dE \qquad (10)$$

and

$$\int N(E)D(E)\exp[-s\sigma_t(E)]dE, \qquad (11)$$

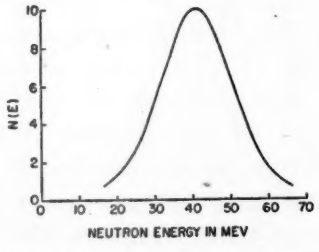

FIG. 8. Theoretical neutron energy distribution for stripping of 98-Mev deuteron on 1-cm thick beryllium. The neutrons are in the forward direction.

where $N(E)dE$ is the number of neutrons between energies E and $E+dE$ impinging on the absorber, $D(E)$ is the probability that one of these neutrons is counted by the special detector used, $\sigma_t(E)$ is the total cross section of the attenuator nuclei, and s is the number of nuclei per cm² of the attenuator. If the neutrons employed were monochromatic, $N(E)$ a delta-function, or if $D(E)$ were a delta-function, the ratio of (11) to (10) would immediately give $\sigma_t(E)$. Unfortunately, this is not the case and there is appreciable uncertainty in the interpretation of the attenuation measurements.

The experiments were performed using as attenuator a column of hydrocarbon (pentane, polyethylene, etc.) and also a column of graphite containing approximately the same amount of carbon as that in the hydrocarbon. The attenuation produced by each absorber under good geometry conditions was measured and from it the hydrogen cross section was deduced.

Typical geometrical conditions as shown by Fig. 9 were: diameter of neutron beam, 1.9 cm; length of absorber, 58 cm; cross section, 5×5 cm; distance between closest end of absorber and detector, 50 cm; diameter of detector, 4.4 cm.

Estimates of multiple scattering effects show them to be negligible.

In Table IV we report the main results thus far obtained.

We can estimate an effective average energy for the neutrons used and calculate $E_{\text{eff}}\sigma_t(E_{\text{eff}})$; we may expect the last quantity to be nearly constant. This is roughly the case if we assume a primary neutron distribution similar to that predicted by Serber plus a low energy tail of an amplitude of about 20 percent of the maximum extending down to 20 Mev, reasonable functions $D(E)$, and $\sigma_t(E)$ inversely proportional to E_n. The E_{eff} of Table IV have been calculated under these hypotheses.

In conclusion we can assume $\sigma_t=6.85/E$ (E in Mev, σ_t in 10^{-24} cm²) with about 10 percent uncertainty. This value does not match too well with the approximate values of $\sigma_t=9.8/E$ reported by Sleator[7] on the basis of measurements in the 20- to 24-Mev energy interval; there is,

[7] W. Sleator, Jr., Phys. Rev. **72**, 207 (1947). See also for further bibliography.

however, no reason why $E\sigma_t(E)$ should be constant over such large energy intervals.

IV. CONCLUSION

In Tables II and III we give $\sigma(\Phi)$. In order to find the corresponding $\sigma(\theta)$ we have to multiply $\sigma(\Phi)$ by $d\cos\Omega/d\cos\theta$ and put this value at the angle θ corresponding to the Φ considered. Table II also gives θ and $d\cos\Phi/d\cos\theta$ as a function of Φ for 88 Mev. For 40 Mev, we have used the non-relativistic formulae

$$-\theta=\pi-2\Phi;\quad \frac{d\cos\Phi}{d\cos\theta}=\frac{1}{4\cos\Phi}.$$

The normalization of the curves is done as explained before by requiring that

$$\int\sigma(\theta)d\omega=\sigma_t=\begin{matrix}0.076\times10^{-24}\text{ cm}^2\text{ for 90 Mev}\\0.170\times10^{-24}\text{ cm}^2\text{ for 40 Mev.}\end{matrix}$$

Since $\sigma(\theta)$ is known only in a limited range, we have arbitrarily extrapolated $\sigma(\theta)$ in the unknown region in a way very close to curve *I* of Fig. 11. The contribution of this part of the curve to the total cross section is 15 percent of the total for the 90-Mev curve. The extrapolated part of the curve is also consistent with data obtained in the cloud-chamber investigation of *n-p* scattering by Bruckner *et. al.*[6] We have assumed the 40-Mev curve to be symmetrical around 90°.

The values of $\sigma(\theta)$ obtained in *all* runs are reproduced in Fig. 10. The stars are, in our judgment, the best average of the measurements we have at the present date; in drawing them we have weighted the experimental runs. For clarity it has been impossible to give the statistical errors which can be easily read out of Tables II and III. The spread of the points gives a fair over-all impression of the accuracy of the measurements.

Messrs. R. Christian and E. Hart of the theoretical group of the Radiation Laboratory have calculated the *n-p* cross sections under various assumptions.[8] One of the simplest used,

TABLE IV. Results of total cross-section measurements. ρl gives the thickness of absorber with which the measurements were taken. In runs 1, 2, 4, and 5 about 85 percent of the detected protons came from hydrogen recoils, the rest from carbon and background. In run 6 only protons coming from hydrogen recoils were taken into account. The approximate total cross section of carbon at 90 Mev is 0.53×10^{-24} cm² and at 40 Mev 0.93×10^{-24} cm².

Run no.	Absorber	g cm⁻²	Method of neutron detection	E_{eff} Mev	σ_t 10^{-24} cm²	$E\sigma_t$
1	Polyethylene	35.3	Protons from CH_2	40	0.177±0.010	7.08
2	Polyethylene	35.3	Protons from CH_2	40	0.154±0.015	6.16
3	Paraffin[a]		$C^{13}(n,2n)C^{11}$	78	0.083±0.004	6.47
4	Pentane	67.2	Protons from CH_2	88	0.075±0.010	6.60
5	Polyethylene	53.4	Protons from CH_2	88	0.086±0.010	7.56
6	Polyethylene	53.4	H recoils from CH_2	88	0.066±0.018	5.80
7	Pentane[b]	67.2	Fission of Bi	95	0.074±0.002	7.03
8	Polyethylene	53.4	Fission of Bi	95	0.062±0.007	5.89

[a] Cook, McMillan, Peterson, and Sewell, Phys. Rev. **72**, 1264 (1947).
[b] J. DeJuren, N. Knable, and B. J. Moyer, private communication.

which agrees fairly well with the experimental results, is the following.

The *n-p* scattering depends on a potential

$$V(r)=g^2(e/r)^{-Kr}(1+P/2),$$

where the constant g^2 has two values, one for scattering with parallel and the other with antiparallel spins. These values correspond to $g^2/hc=0.405$ and 0.280, respectively, and are chosen so as to fit the scattering cross section for epithermal neutrons and the binding energy of the deuteron. The constant $1/K$ is $1.2\cdot10^{-13}$ cm. If we interpret $1/K$ as the "Compton wavelength" of a particle, this particle has the mass of 326 electronic masses which is not very different from the π-meson mass; moreover, this is the value of the range of the nuclear forces used by Breit in interpreting *p-p* scattering, and it also fits the coherent scattering observed in neutron scattering by ortho and parahydrogen. *P* is an

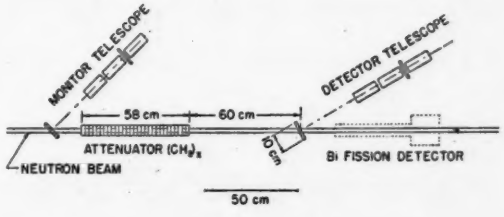

FIG. 9. Typical arrangement for measurement of the total scattering cross section.

[8] A review of the subject is given in L. Rosenfeld, *Nuclear Forces* (Interscience Publishers, Inc., New York, 1948). Other calculations on *n-p* high energy scattering: M. Camac and H. A. Bethe, Phys. Rev. **73**, 191 (1948); J. Ashkin and Ta-You Wu, Phys. Rev. **73**, 973 (1948).

operator that exchanges the spatial coordinates of neutron and proton.

The above potential gives an angular distribution as shown in Fig. 11, curve *I*, and a total cross section at 90 Mev of 0.090×10^{-24} cm². The agreement is fairly good and the simplicity of the hypotheses make this result attractive, although the theoretical total cross section is appreciably larger than the experimental one.

On the other hand, tensor forces must be

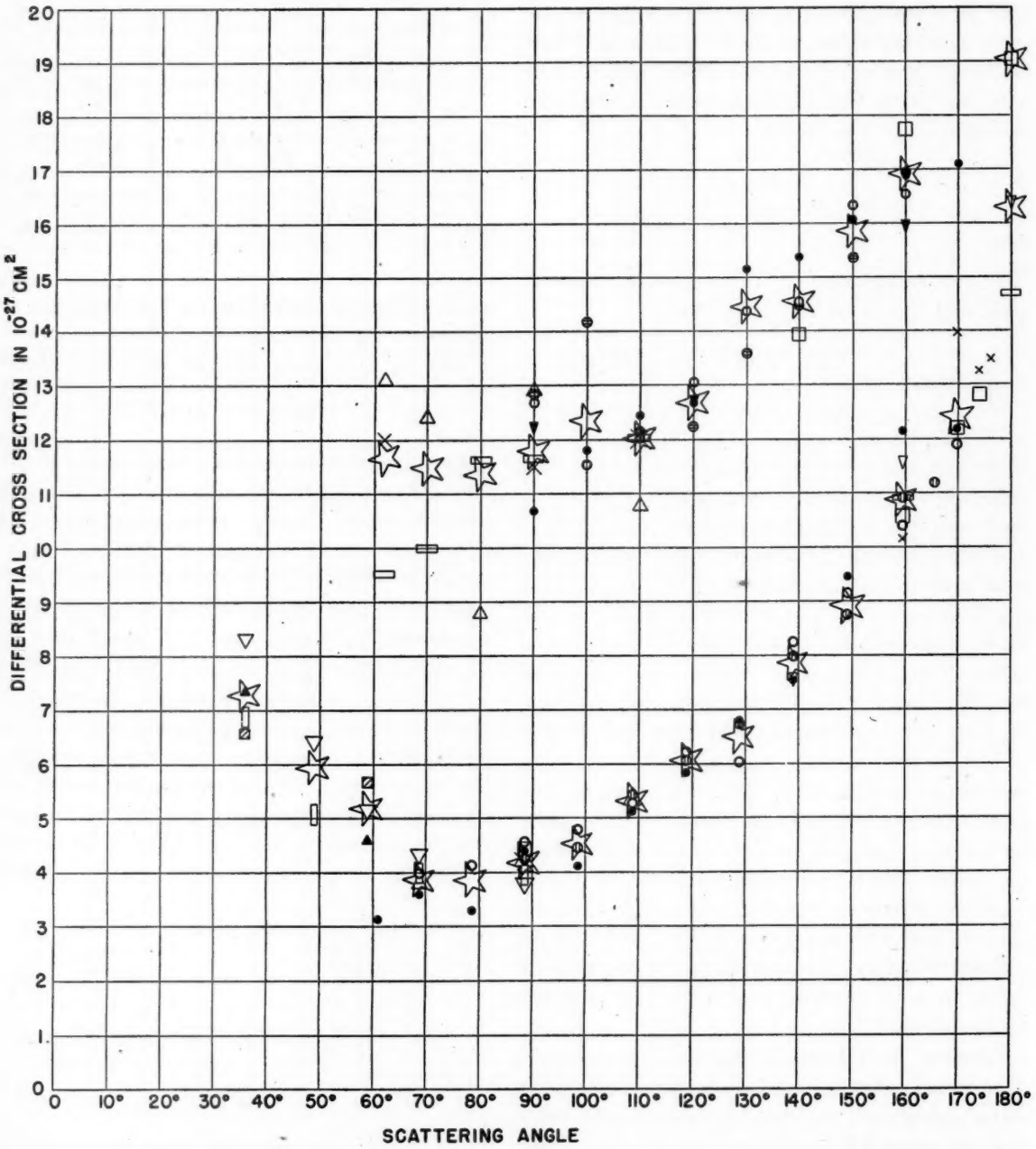

FIG. 10. Differential neutron proton cross section in the center of gravity system in 10^{-27} cm²/steradians. All measurements are included (see key to symbols in Tables II and III). The stars are the final best available average corrected as described in the text. The upper curve represents the data taken with 40-Mev neutrons; the lower curve with 90-Mev neutrons.

present to account for the electric quadrupole moment of the deuteron and they can be introduced by changing the potential to

$$V'(r)=g^2\left\{\frac{e^{-Kr}}{r}+\gamma\left(\frac{3(\sigma_1\cdot r)(\sigma_2\cdot r)}{r^2}-\sigma_1\cdot\sigma_2\right)\frac{e^{-K'r}}{r}\right\}\frac{1+P}{2},$$

where σ_1, σ_2 are the spin operators, γ is a constant fixing the amount of tensor force and K' is the range of the tensor forces. Choosing $\gamma=0.16$ and $K'=0.3K$ it is possible to account for the electric quadrupole moment of the deuteron. However, the total cross section becomes even larger: 0.093×10^{-24} cm², and the angular distribution hardly agrees with the experimental one.

It must be remembered that relativistic effects have been neglected and they may be of the order of 20 percent.

More detailed theoretical studies to bring out the separate influences of the single factors involved in the *n-p* cross section are in progress.

The authors wish to thank Professor E. O. Lawrence for his interest in this work, and the cyclotron operating crew for their valuable assistance in making the runs.

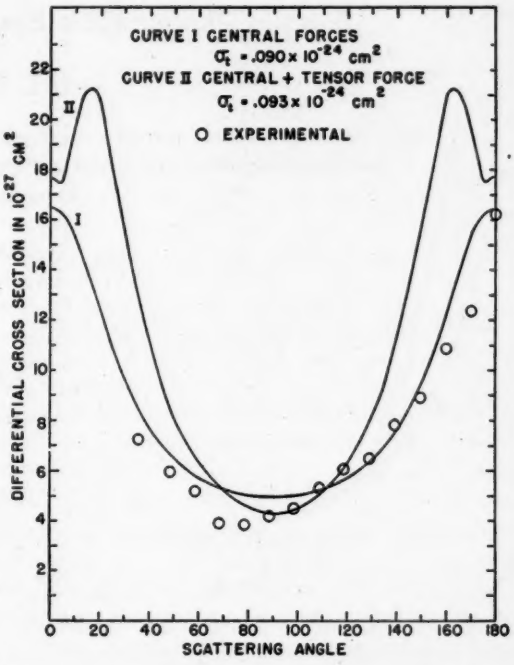
CURVE I CENTRAL FORCES
$\sigma_t = .090\times10^{-24}$ cm²
CURVE II CENTRAL + TENSOR FORCE
$\sigma_t = .093\times10^{-24}$ cm²
EXPERIMENTAL
II
I
DIFFERENTIAL CROSS SECTION IN 10^{-27} CM²
SCATTERING ANGLE
0 20 40 60 80 100 120 140 160 180
2 4 6 8 10 12 14 16 18 20 22

FIG. 11. Theoretical *n-p* scattering curves drawn according to the hypotheses discussed in the "Conclusions" section. Curve I central forces $\sigma=0.09\times10^{-24}$ cm²; curve II tensor forces $\sigma_t=0.093\times10^{-24}$ cm². Circles are the experimental points.

This paper is based on work performed under the auspices of the Atomic Energy Commission.

Stars in Photographic Emulsions Initiated by Deuterons.

Part I. Experimental[1]

EUGENE GARDNER AND VINCENT PETERSON
Radiation Laboratory, Department of Physics, University of California, Berkeley, California
(Received March 2, 1948)

Photographic plates have been bombarded with deuterons in the 184-inch Berkeley cyclotron, and a group of 1200 stars in the emulsion has been studied. The group included 300 stars at each of the following energies: 35 Mev, 90 Mev, 130 Mev, and 190 Mev. At each of these energies the average number of prongs per star was close to 3.0. About three times as many prongs were observed in the forward direction of the beam as in the backward direction. The study was made with desensitized plates, which do not show tracks of high energy protons. The results are to be interpreted as including all alpha particles and heavier nuclear fragments but only the lower energy protons.

I. INTRODUCTION

DEUTERONS accelerated by the 184-inch Berkeley cyclotron[2] are found to produce stars in photographic plates which are similar to stars produced by cosmic rays. For individual stars initiated by deuterons from the cyclotron we have not been able to tell with any assurance what type of nucleus is being disintegrated. Moreover, we do not know how many neutrons are given off or in which directions, so it is not possible to make a momentum or an energy balance. Thus it appeared that a detailed study of individual stars would not yield results which could be interpreted very easily. It was pointed out by Professor Robert Serber and Mr. Wendell Horning that experimental observations of large numbers of stars would yield statistical results which could be compared with theoretical predictions. The present paper reports the results of an experimental study of the number of prongs (i.e., the number of tracks making up the star) and the direction of the prongs with respect to the direction of the beam. The accompanying paper of Horning and Baumhoff gives a comparison of these experimental results with theoretical predictions.

II. EXPERIMENTAL PROCEDURE

The plates used in this study were bombarded before the deflector of the 184-inch cyclotron was in operation, and the only method of exposure to deuterons was with the circulating beam. Now that the deflector is in operation,[3] the circulating beam will probably be superseded by the deflected beam for bombarding photographic plates. The method of exposing plates to the circulating beam is shown in Fig. 1. The plate is wrapped in black paper and is mounted on the probe in a position such that the plane of the emulsion is approximately tangent to the deuteron trajectories. The deuterons strike the edge of the emulsion as shown in Fig. 2. A bombardment with deuterons of any energy up to the maximum available from the cyclotron can be obtained by placing the plates at the appropriate radius. It is assumed that stars which are found near the edge where the beam first strikes the plate were initiated by deuterons of the energy of the circulating beam at the radius at which the plate was exposed. The exposure required is small, and one of the problems is to make the circulating beam small enough. The cyclotron normally operates with a pulsed arc ion source, but we found that even one pulse gives too many deuterons. The plates used in the present study were exposed without an arc pulse; the arc filament was left on, and the r.f. was turned on for about half a second. The number of deuterons accelerated was controlled by varying the dee voltage.

The photographic plates used were Ilford

[1] Reported at meetings of the American Physical Society, July 11–12, 1947, and January 2–3, 1948.
[2] Brobeck, Lawrence, MacKensie, McMillan, Serber, Sewell, Simpson, and Thornton, Phys. Rev. **71**, 449 (1947).
[3] W. M. Powell, L. R. Henrich, Q. A. Kerns, D. C. Sewell, and R. L. Thornton, Rev. Sci. Inst. **19**, 506 (1948).

Nuclear Research plates,[4,5] type C.1, with an emulsion thickness of 50 microns. The chemical composition, as given by Ilford Limited, is shown in Table I. The C.1 plates are desensitized so that lightly ionizing particles do not make recognizable tracks. In this study the complete tracks of the initiating deuterons could just be seen at the lowest energy (35 Mev) but not at higher energies. Desensitization is an advantage because it permits a heavier exposure than would be possible with plates which show the tracks of the initiating particles. With the C.1 plates we were able to use deuteron intensities high enough to obtain useful plates with star densities as high as 10 stars per mm². In star studies using plates which render the tracks of the initiating particles visible, it is necessary to reduce this number by a factor of perhaps a hundred. Desensitization is also a disadvantage, however, since lightly ionizing particles from the stars will not show recognizable tracks. It is hard to give a definite value for the proton energy below which a proton track will always be visible. The possibility of seeing a track depends on the background of developed grains in the plate and on the length of track which lies in the emulsion. Proton tracks of length corresponding to an energy of 10 Mev are heavy enough so that it seems unlikely that we would miss tracks of this energy or lower. The length of a 10-Mev proton track, as given by Lattes, Fowler, and Cuer,[6] is 560 microns. From the fact that deuterons can just be seen at 35 Mev but not at higher energies, we conclude that we could not see proton tracks of energy higher than about 17 Mev. In the region between 10 and 17 Mev we might see some prongs and not see others, depending on the background of developed grains and the length of track which lies in the emulsion. The results of this study of star prongs should be interpreted as including all alpha particles and heavier nuclear fragments but only the lower energy protons.

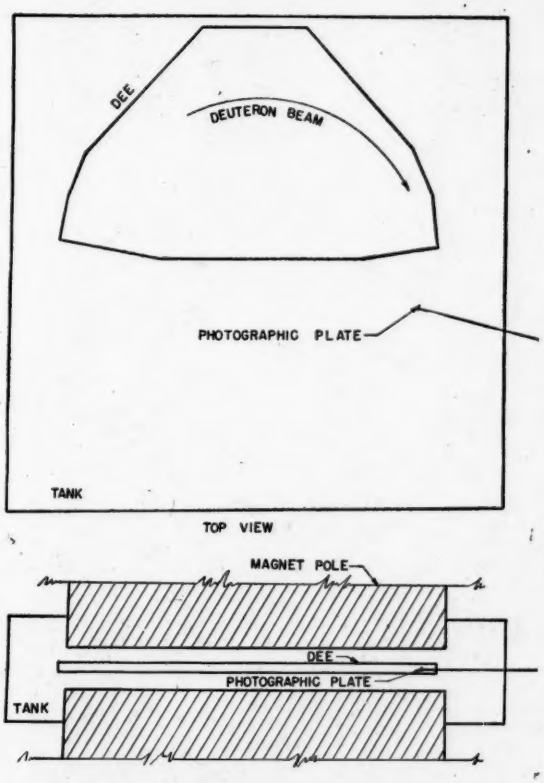

FIG. 1. Location of photographic plate for exposure to circulating beam.

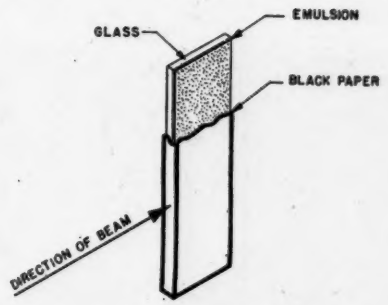

FIG. 2. Direction of deuteron beam with respect to photographic emulsion.

A group of stars initiated by deuterons of energy 190 Mev is shown in Fig. 3. Stars with various numbers of prongs are shown, but there has been no attempt to make the relative number of each type of star correspond to the statistical data. The number of long prongs shown is larger than would be expected in random sampling.

III. EXPERIMENTAL RESULTS

The study included about 300 stars at each of four deuteron bombarding energies: 35 Mev, 90 Mev, 130 Mev, and 190 Mev. Several plates

[4] Powell, Occhialini, Livesey, and Chilton, J. Sci. Inst. 23, 102 (1946).
[5] C. F. Powell and G. P. S. Occhialini, *Nuclear Physics in Photographs* (Clarendon Press, Oxford, 1947).
[6] C. M. G. Lattes, P. H. Fowler, and P. Cuer, Proc. Phys. Soc. 59, 883 (1947).

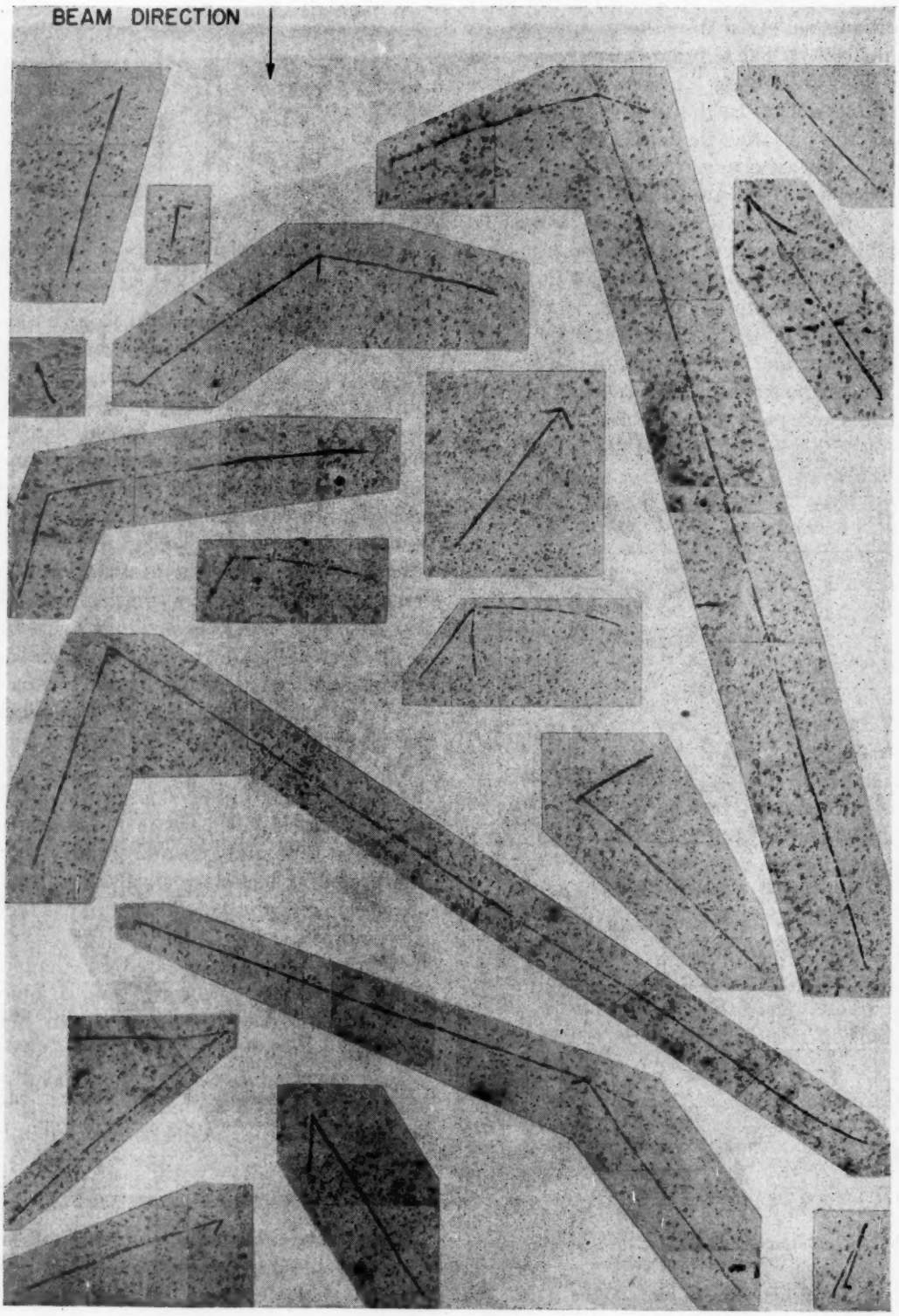

FIG. 3. Group of stars initiated

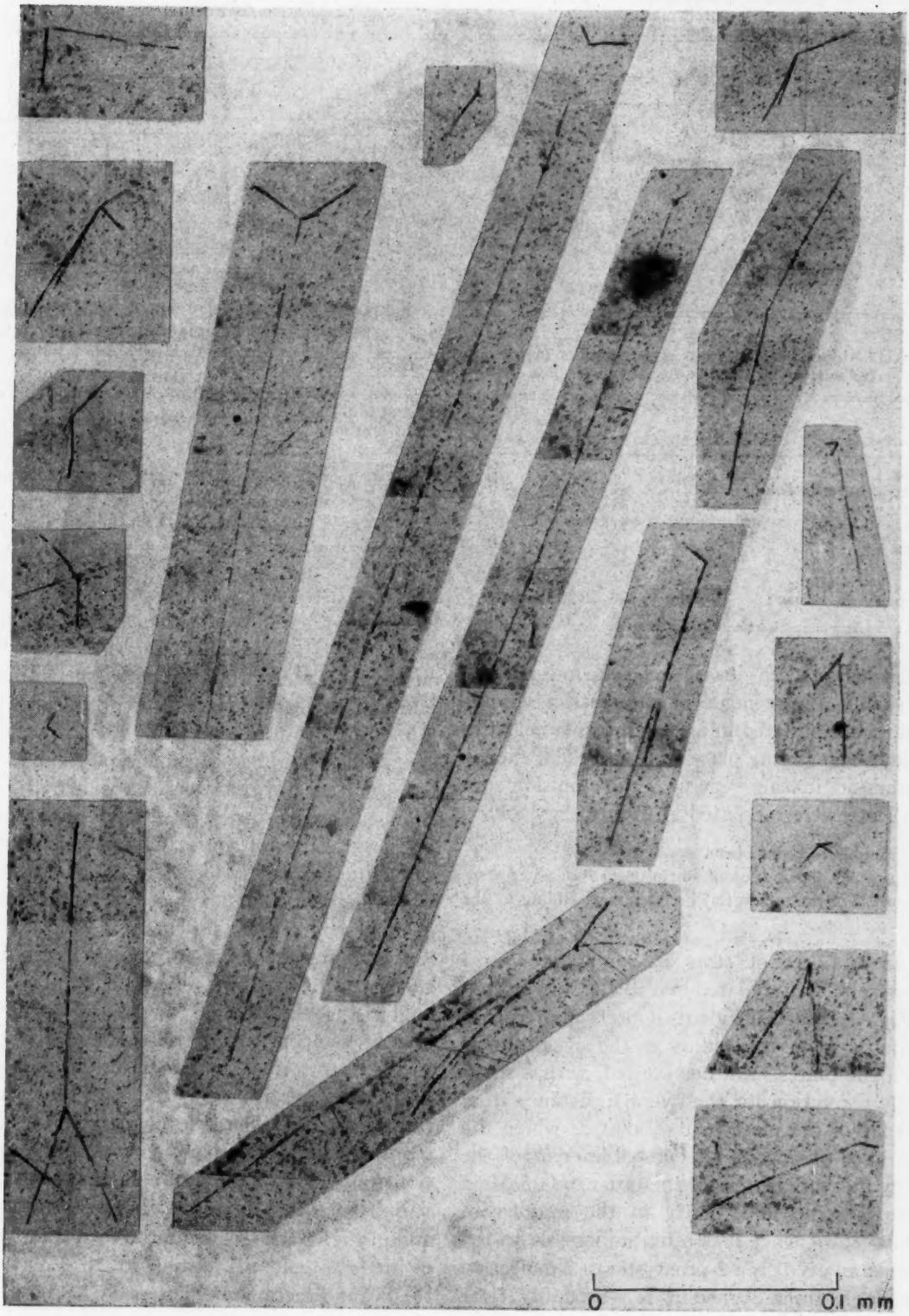

by deuterons of energy 190 Mev.

TABLE I. Chemical composition of Ilford nuclear research plates.

Element	Weight (grams per cc of emulsion)
Ag	1.85
Br	1.34
I	0.052
C	0.272
H	0.056
O	0.266
N	0.067
S	0.010
Ca, P, Cr, Si, Na	Traces

TABLE II. Number of stars of a given number of prongs for various incident deuteron energies.

Type of star	Number of stars 35 Mev	90 Mev	130 Mev	190 Mev
2-Prong ("probable")	60	63	41	59
2-Prong ("questionable")	27	44	60	40
3-Prong	155	153	121	122
4-Prong	56	52	68	71
5-Prong	2	9	8	10
6-Prong	0	1	3	0
All types	300	322	301	302

at each energy were viewed under the microscope, and sketches were made of the stars observed. All stars encountered in a scanning area near the incident edge of the plate were included, except for stars originating very near the emulsion surface. Data were tabulated at each energy for:

(a) number of prongs per star,
(b) angular distribution of star prongs, and
(c) average prong length of star prongs ending in the emulsion.

The numbers of stars having 2 prongs, 3 prongs, etc. are tabulated in Table II and plotted in Fig. 4. Each incident deuteron energy is computed from the radius in the cyclotron at which the plates were bombarded, with a small energy correction for the average distance from the edge of the plate to the point at which the stars were observed. The probable error of the energy measurement is of the order of ± 5 Mev. There is some uncertainty in the number of 2-prong stars, since it is often impossible to tell whether an event is a 2-prong star or a deflection in a single track. When it is reasonably clear from the grain densities of the tracks, or from other considerations, that the event is a 2-prong

TABLE III. Angular distribution of star prongs for various incident deuteron energies.

Angular range	Angle from beam direction to center of sector	Number of star prongs 35 Mev	90 Mev	130 Mev	190 Mev
$-30°$ to $+30°$	0°	326	335	295	267
$+30°$ to $+90°$ and $-30°$ to $-90°$	60°	385	366	339	388
$+90°$ to $+150°$ and $-90°$ to $-150°$	120°	128	166	184	187
$+150°$ to $-150°$	180°	42	55	58	66
	Total	881	922	876	908

TABLE IV. Average observed projected track lengths of star prongs ending in the emulsion.

	35 Mev	90 Mev	130 Mev	190 Mev
Percent of prongs ending in the emulsion	75	65	56	62
Average observed prong length for star prongs ending in the emulsion (microns)	20	32	35	42

star, it is listed as "probable." If it is impossible to tell whether it is a star or a deflection, it is listed as "questionable." In some cases it is clear that the event is a deflection of a single track, and these cases do not appear in the tabulation at all. From Table II it is seen that the average number of prongs per star is close to 3.0 for each of the energies studied.

When the stars are formed in the emulsion the star prongs can, of course, take any direction in three-dimensional space. The emulsion shrinks when the plates are developed, and the stars are compressed toward a plane. As the stars are viewed under the microscope, one sees essentially the projection of the stars on a plane. The analysis of the angular distribution which we give does not refer to the three-dimensional stars as they are formed in the emulsion, but to the projections on a plane as they are seen through the microscope. The field of view of the microscope was divided into 60° sectors, and a tabulation was made of the numbers of prongs in the various sectors. The results are given in Table III and in Fig. 5. The sector in the forward direction of the beam extends from $-30°$ to $+30°$, where the beam direction is taken as 0°. In cases where there are two sectors whose centers make the same angle with the beam direction, the total

number of prongs observed in both sectors is tabulated in Table III; but the value plotted in Fig. 5 is the average for one sector. There are about three times as many prongs in the three forward sectors as in the three backward sectors.

No systematic attempt was made to identify the prong particles. However, some of the prongs had a change in grain spacing such that they were tentatively identified by inspection as proton tracks. In order to give an order of magnitude for the lengths of the star prongs for the various energies of the initiating deuterons, we have listed in Table IV the percent of prongs ending in the emulsion and the observed average prong lengths for tracks which ended in the emulsion. This does not give a true measure of the average prong length for two reasons: (1) the longer prongs have a greater probability of leaving the emulsion, and (2) the length as seen through the microscope is the prong length projected on a plane. Both of these factors tend to make the values given in Table IV too small. The energy associated with a proton track or an alpha particle track of given length can be found from the range-energy relationships given by Lattes, Fowler, and Cuer.[6] For example, the energy of a track of length 40 microns is given as 2 Mev if the particle is a proton, or about four times this energy if it is an alpha particle.

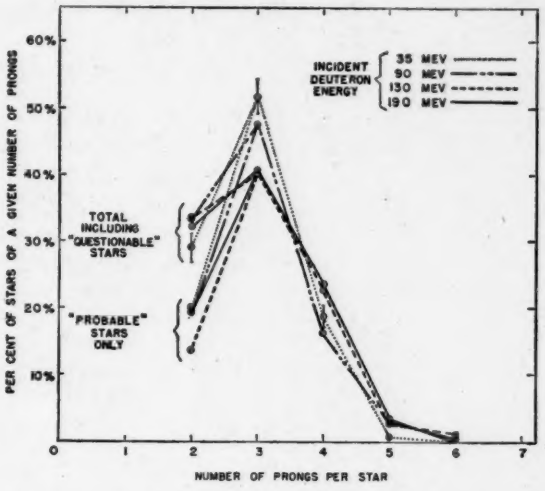

FIG. 4. Number of stars with 2, 3, and more prongs for various incident deuteron energies.

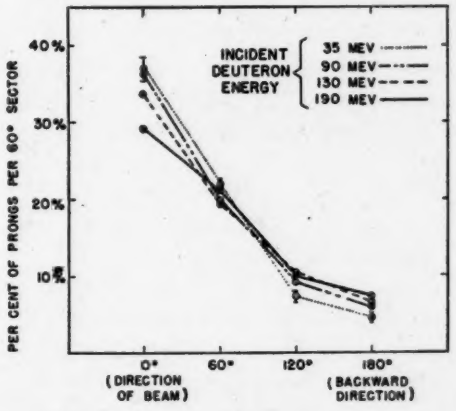

FIG. 5. Number of prongs in various 60° sectors.

IV. ACKNOWLEDGMENTS

The authors wish to express their appreciation to Professor Ernest O. Lawrence for his continued interest in this study. We are indebted to Professor R. L. Thornton and Professor E. M. McMillan for helpful discussions. We also wish to thank Mr. A. J. Oliver for the preparation of Fig. 3, Mr. Duane Sewell and the cyclotron crew for bombarding the plates, and Mr. C. Waller of Ilford Limited for information regarding Ilford Nuclear Research Plates.

This paper is based on work performed under Contract No. W-7405-eng-48, with the Atomic Energy Commission, in connection with the Radiation Laboratory, University of California, Berkeley, California.

Stars in Photographic Emulsions Initiated by Deuterons.

Part II. Theoretical

W. HORNING AND L. BAUMHOFF
Radiation Laboratory, Department of Physics, University of California, Berkeley, California

(Received September 27, 1948)

The theory of high energy nuclear stars depends on a theory of nuclear transparency and on a theory of nuclear evaporation. The transparency can be computed on the basis of a model proposed by R. Serber as soon as the interactions between the nucleons and the incident particle are known. The evaporation can be computed on the basis of the statistical model of the nucleus as soon as the nuclear entropy and binding energies of the evaporated particles are known. With approximate values for the above interactions, entropies, and binding energies, a probability distribution has been computed for the number of prongs per star. The results are in qualitative agreement with the observations on photographic emulsions described in Part I.

I. INTRODUCTION

IT is of interest to see how far current ideas on nuclear mechanics lead toward an interpretation of nuclear stars. If the kinetic energy of the incident heavy particle is of the order of 100 Mev, then resonance phenomena and leakage through the nuclear potential barrier should be small effects. In such a case, particles may be ejected from the struck nucleus by at least two processes—direct recoil and evaporation. If a struck nucleon receives so much energy from the incident particle that it leaves the nucleus in a time short compared to a nuclear period ($\sim 10^{-21}$ sec.), then we have a recoil prong or recoil star. If, on the other hand, the energy of the incident particle is evenly distributed throughout the nucleus by many collisions of the nucleons among one another, and if particles are ejected only after many nuclear periods, then we have an evaporation star. Cosmic-ray stars appear to be of both these types.[1]

The formation of an evaporation star depends on nuclear evaporation proper, and also on nuclear transparency, which concerns the probability that an incident particle pass through a nucleus with the loss of only some fraction of its energy. Each of these parts of the theory depends on an elementary probability: transparency on the probability $Y(E, \epsilon)$ per cm path distance per Mev of energy loss that an incident particle with kinetic energy E collides with a nucleon, losing kinetic energy ϵ; evaporation on the probability $W(X, \xi)$ per second per Mev energy loss that a nucleus with excitation energy X evaporate some particle or other, losing excitation ξ.

II. THE ELEMENTARY PROBABILITIES

Unless E_0, the incident energy, is large compared to the average energy loss per collision of the incident particle ($\sim$25 Mev), the incident particle will almost certainly be unable to penetrate through the nucleus, and there will be almost zero transparency. But if E_0 is many times this critical value, things may be more complex. To get an idea of what happens, assume the stopping power of the nucleus to be like that of a Fermi gas of protons and neutrons, so that when a particle strikes it the resulting action may be analyzed into a series of $n-n$, $n-p$, and $p-p$ collisions.[2]

We represent the interaction between the incident proton or neutron and an average particle of the nucleus by $g^2 e^{-r/a}/r$. A value $a^{-1}=1.19\cdot 10^{13}$ cm^{-1} is used.[3] A value of g^2 is used corresponding to an average total cross section of 0.058 barn; since total cross sections for $n-n$ and $n-p$ scattering have been measured with the results 0.034 and 0.083 barn at 90 Mev incident energy.[4] This yields $g^2/\hbar c=0.26$. The use of the above average of the $p-n$ and $n-n$ cross sections is a

[1] W. Heisenberg, *Cosmic Radiation* (Dover Publications, New York), p. 131.

[2] For the physical model here involved see R. Serber, Phys. Rev. 72, 115 (1947).

[3] L. E. Hoisington, S. S. Share, and G. Breit, Phys. Rev. 56, 884 (1939).

[4] Cook, McMillan, Peterson, and Sewell, Phys. Rev. 72, 1264 (1947).

reasonable approximation whether the $p-n$ interaction is of the ordinary or exchange type. It is a better approximation for an interaction of exchange type.

The Born approximation with the above interaction gives for the differential scattering cross section

$$\sigma(E_0, \rho)d\rho = \pi m b^4 g^4 \rho d\rho / E_0(1+b^2\rho^2)^2 \quad (1)$$

where ρ is the momentum transfer, and E_0 is the energy of the incident particle in the reference system in which the struck particle is at rest, and $b=a/\hbar$. This result should be modified when applied to collisions within the nucleus, since then the struck particle is not at rest, and the exclusion principle limits possible momentum transfers. This modified cross section $\tau(E, \epsilon)$, is obtained by averaging (1) over a portion of the Fermi momentum sphere, whose radius we call p_0. That is

$$\tau(E, \epsilon)d\epsilon = d\epsilon \int \sigma(\mathbf{P}, \mathbf{p}, \epsilon)d\mathbf{p} \Big/ \frac{4}{3}\pi p_0^3. \quad (2)$$

Here p and p' are the original and final momenta of the struck nucleon, P and P' the corresponding momenta of the incident particle, E and ϵ the incident energy and energy transfer, all in the laboratory system. It is convenient to introduce $\mathbf{q}$, the momentum of the incident particle, after collision of the two particles, in their center of mass system. By definition

$$\mathbf{q} = -\rho + \tfrac{1}{2}(\mathbf{P}-\mathbf{p}). \quad (3)$$

Conservation of energy and momentum require that

$$q^2 = \tfrac{1}{4}(\mathbf{P}-\mathbf{p})^2; \quad (4)$$

and the condition that the energy transfer be ϵ is

$$[\mathbf{q}+\tfrac{1}{2}(\mathbf{P}+\mathbf{p})]^2 = P'^2 = P^2 - 2m\epsilon. \quad (5)$$

To get the cross section $\sigma(\mathbf{P}, \mathbf{p}, \epsilon)d\epsilon$ for energy loss in range $d\epsilon$, for given $\mathbf{P}$ and $\mathbf{p}$, requires an integration around the azimuth φ', whose axis is the line of centers of the two spheres (4) and (5) in $\mathbf{q}$ space. The direction of this axis is that of $\mathbf{p}+\mathbf{P}$. From (4) and (5)

$$\rho^2 = \tfrac{1}{2}(\mathbf{P}-\mathbf{p})^2[1-\cos(\mathbf{q}, \mathbf{P}-\mathbf{p})].$$

We write

$$\theta' = \sphericalangle(\mathbf{q}, \mathbf{P}+\mathbf{p}), \quad \theta''(\mathbf{P}-\mathbf{p}, \mathbf{P}+\mathbf{p})$$
$$\cos(\mathbf{q}, \mathbf{P}-\mathbf{p}) = \cos\theta' \cos\theta'' + \sin\theta' \sin\theta'' \cos\varphi'.$$

In contrast to the more familiar case in which $p=0$, ρ here involves the azimuth. Expanding (5) according to the law of cosines gives

$$\cos\theta' = \frac{P^2-p^2-4m\epsilon}{|\mathbf{P}-\mathbf{p}||\mathbf{P}+\mathbf{p}|}, \quad \sin\theta' d\theta' = \frac{4md\epsilon}{|\mathbf{P}-\mathbf{p}||\mathbf{P}+\mathbf{p}|}.$$

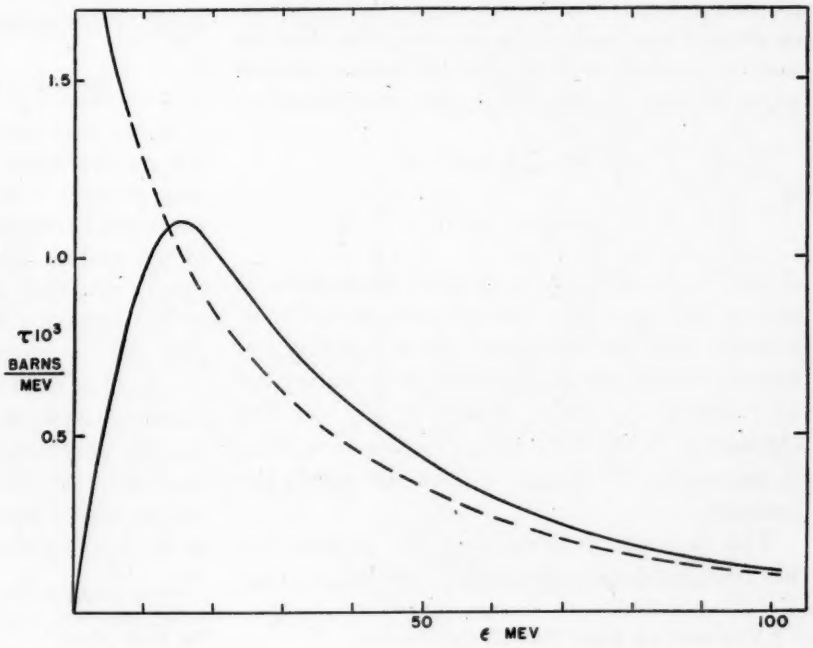

FIG. 1. Differential cross section τ for energy transfer in a collision between an incident particle of energy 100 Mev and a nucleon.

Dotted curve: struck particle free and at rest.
Solid curve: struck particle within a nucleus.

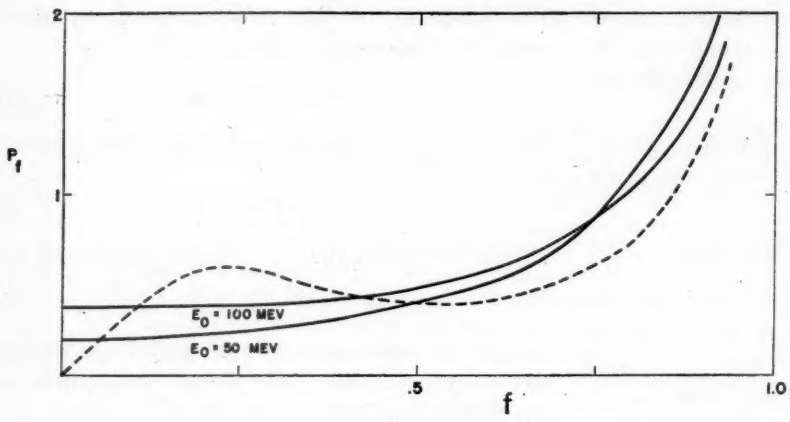

FIG. 2. $P(f)df$ is the probability that an incident nucleon with energy E_0 just after entering a nucleus of the heavy component, will have lost a fraction f of its energy in range df, just before completing its path through the nucleus.

Applying the law of cosines to the identity $2\mathbf{p}=(\mathbf{P}+\mathbf{p})-(\mathbf{P}-\mathbf{p})$ gives

$$\cos\theta''=\frac{P^2-p^2}{|\mathbf{P}-\mathbf{p}|\,|\mathbf{P}+\mathbf{p}|}.$$

Substituting in (1) and performing the elementary azimuthal integration yields

$$\sigma(\mathbf{P},\mathbf{p},\epsilon)=2\pi m^3b^4g^4(A+BC)\times(A+2BC+B^2[4m\epsilon]^2)^{-\frac{1}{2}}$$
$$A=(\mathbf{P}-\mathbf{p})^2(\mathbf{P}+\mathbf{p})^2,\quad B=\tfrac{1}{2}b^2(\mathbf{P}-\mathbf{p})^2$$
$$C=A+(p^2-P^2+4m\epsilon)(P^2-p^2). \tag{6}$$

We now substitute from (6) in (2), after expanding σ as a power series in p/P, less than one in the experiments here of interest. The integration of (2) is to be done over the spherical shell $p<p_0$, $p'>p_0$. This last inequality may be written

$$p'^2-p^2=2m\epsilon>p_0^2-p^2$$

or

$$p>(p_0^2-2m\epsilon)^{\frac{1}{2}}.$$

If $2m\epsilon>p_0^2$, then the region of integration is instead $p<p_0$, $p>0$. The angular integrals of terms in odd powers of p/P are 0. Keeping the first three non-vanishing terms in the expansion of τ yields the result shown in Fig. 1. The elementary probability $Y(E,\epsilon)$ is simply τ times d, the numerical density of nucleons within the nucleus.

The elementary probability for evaporation has been treated by Weisskopf.[5] His Eq. (3) may be put

$$W(X,\xi)d\xi=\gamma(\xi-V-E_b)\times\exp(S_B(X-\xi)-S_A(X))d\xi,$$
$$\gamma=\sigma_0 jm/\pi^2\hbar^3, \tag{7}$$

where S_A and S_B are the entropies of the nucleus before and after the evaporation of a particle with binding energy E_b, kinetic energy $\xi-E_b$, potential barrier V, mass m, and statistical weight j; and where σ_0 is the geometrical cross section of the nucleus. On the basis of an approximate nuclear model we may write

$$S(X)\simeq\left(\frac{A}{2.2}\right)^{\frac{1}{2}}X^{\frac{1}{2}},\quad X \text{ in Mev},$$

where A is the mass number.

III. NUCLEAR TRANSPARENCY*

In the experiments of Part I, the elements of the photographic emulsion fall principally into two groups: a heavy component composed of silver and bromine, with an average mass number of 95, and a light component composed principally of carbon and oxygen. Since the hydrogen of the emulsion has too simple a structure to give rise to starts of the kinds observed, it is counted in neither component. By use of the chemical analysis listed in Part I, and values for the geometrical cross sections of the nuclei involved, we deduce that the relative probabilities that a fast incident particle hit a nucleus of the heavy component, of carbon, or of oxygen

[5] V. Weisskopf, Phys. Rev. 52, 296 (1937).

* The problem of nuclear transparency has been treated, using a different method, by M. L. Goldberger, Phys. Rev. 74, 1269 (1948).

are 0.76, 0.13 and 0.11. A calculation will be made for the stars from the heavy component, which are predominately evaporation stars. Some remarks will then be made about stars from the lighter elements.

As an approximation, let us ignore the scattering of the incident particle, but take account of its energy loss by the quantity $\tau(E, \epsilon)$ which expresses the probability per cm path distance per Mev energy loss, that the incident particle, with energy E, lose energy ϵ. Let $P(x, E)$ be the probability, after the incident particle has penetrated a distance x into the nucleus that it possess a kinetic energy less than E. If, at $x=x_1$, the energy E of the incident particle were known to be E_1, then the increment of P would satisfy

$$[\Delta P(x, E)]_{x=x_1} = \Delta x \int_{E_1-E}^{E_1} \tau(E_1, \epsilon) d\epsilon.$$

Since, however, the quantity E follows a probability distribution, we have in general

$$\frac{\partial P(x, E)}{\partial x} = \int_E^{E_0} \frac{\partial P(x, E')}{\partial E'} dE' \int_{E'-E}^{E'} \tau(E', \epsilon) d\epsilon. \quad (8)$$

This equation has been solved numerically, with τ as given in Fig. 1, and $E_0 = 100$ Mev. The result is shown by the dotted curve in Fig. 2. To make possible an analytic solution we replace τ by τ', where

$$\tau' \equiv \frac{Ae^{-b\epsilon}}{1-e^{-bE}}, \quad \int_{E'-E}^{E'} \tau(E', \epsilon) d\epsilon = By'/y$$

$$B \equiv A/b, \quad y = y(E) = e^{-bE}/(1-e^{-bE}), \quad y' = y(E').$$

The two functions τ and τ' are equivalent in a semi-quantitative way except for $\epsilon < 10$ Mev, if we put $b = 0.021$ (Mev)$^{-1}$ and $B = 3.6 \cdot 10^{12}$ cm^{-1}. In view of the uncertainties in the Fermi model of the nucleus, we may regard τ' as a reasonable representation of the scattering cross section.

The advantage of the function τ' is that it yields a kernel for the integral equation which is a function of E only times a function of E' only. The Laplace transform of (8) is

$$-P(0, y) + \lambda \bar{P} = \int_y^{y_0} \frac{\partial \bar{P}}{\partial y'} dy' B \frac{y'}{y}$$

$$\bar{P} = \int_0^\infty e^{-\lambda x} P dx. \quad (9)$$

The boundary condition at $x=0$ is $P(0, y) = st(y_0 - y)$, where $st(x)$ is a step function defined by $st(x) = 0, 1$ according as $x < 0$ or $x > 0$. Here $y_0 = y(E_0)$ where E_0 is the energy of the incident particle within the nucleus and at the start of its nuclear traverse. Multiplying (9) by y and differentiating to y yields

$$(\lambda + B) y (\partial \bar{P}/\partial y) + \lambda \bar{P} = st(y_0 - y) - y\delta(y_0 - y). \quad (10)$$

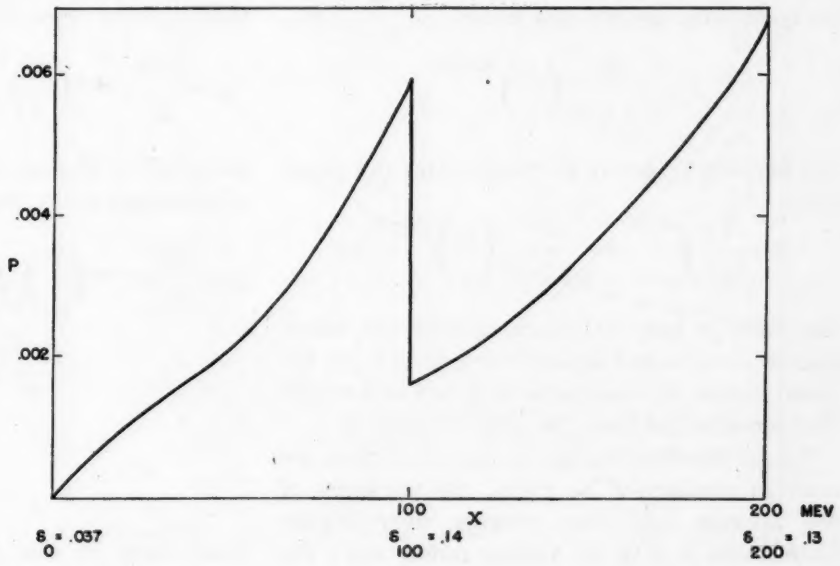

FIG. 3. $P(X)dX$ is probability of a nuclear excitation X, in range dX, when a nucleus of the heavy component is hit by a deuteron of energy 200 Mev.

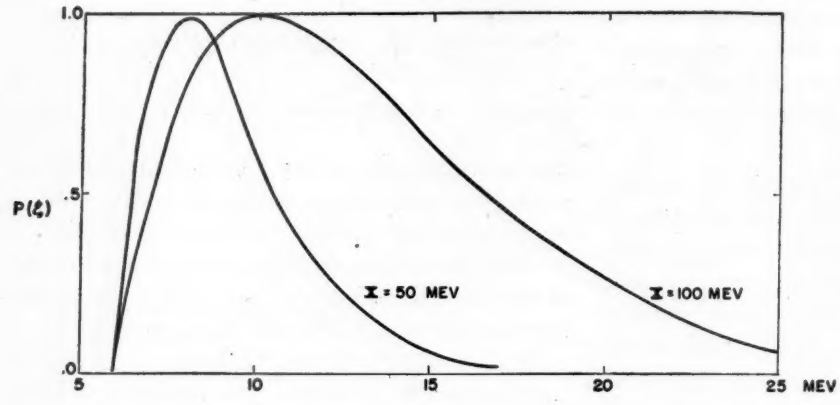

FIG. 4. $P(X, \xi)d\xi$ is proportional to the probability that a proton, evaporated from a heavy component nucleus of excitation X, reduces this excitation by an amount ξ in range $d\xi$.

A solution of the homogeneous equation corresponding to (10) is

$$P_1 = y^{(-\lambda/\lambda+B)}.$$

A solution of the inhomogeneous equation is

$$P_2 = \frac{1}{\lambda}, \quad y < y_0;$$

$$P_2 = \left(\frac{1}{\lambda} - \frac{1}{\lambda+B}\right)\left(\frac{y_0}{y}\right)^{(\lambda/\lambda+B)}, \quad y < y_0.$$

The general solution is $\bar{P} = P_2 + CP_1$. In (9) put $y = y_{0+}$ and substitute for $\bar{P}$. The result is

$$\lambda\left[\frac{1}{\lambda} - \frac{1}{\lambda+B} + C\left(\frac{1}{y_{0+}}\right)^{(\lambda/\lambda+B)}\right] = \frac{B}{\lambda+B}$$

from which $C=0$. The solution satisfying boundary conditions, for $y > y_0$ is thus

$$\bar{P} = \frac{B}{\lambda(\lambda+B)}\left(\frac{y_0}{y}\right)^{(\lambda/\lambda+B)}.$$

The inversion theorem for the Laplace transform yields

$$P = \frac{1}{2\pi i}\int_{\gamma-i\infty}^{\gamma+i\infty} e^{\lambda x}\frac{B}{\lambda(\lambda+B)}\left(\frac{y_0}{y}\right)^{(\lambda/\lambda+B)} d\lambda.$$

The contour may be deformed into two infinitesimal circuits, one around the pole at $\lambda=0$, the other around the essential singularity at $\lambda=-B$. The contribution from the pole is simply 1.

To get information on nuclear excitation, we need to evaluate P at $x=x_0$, the thickness of the nucleus, and then average over impact parameters. If R is the nuclear radius and r the impact parameter, then

$$x_0 = 2(R^2-r^2)^{\frac{1}{2}}, \quad 4rdr = -x_0 dx_0.$$

The desired average is then

$$P(E, R) = \frac{1}{\pi R^2}\frac{1}{4i}\oint\left(\frac{2R}{\lambda}e^{2R\lambda} - \frac{e^{2R\lambda}}{\lambda^2} + \frac{1}{\lambda^2}\right) \times \frac{B}{\lambda(\lambda+B)}\left(\frac{y_0}{y}\right)^{(\lambda/\lambda+B)} d\lambda$$

$$\equiv (p_1+p_2+p_3)/\pi R^2.$$

To evaluate the integral p_1, put $\lambda = -B+t$. Then

$$p_1 = \frac{2RB}{4i}e^{-2RB}\frac{y_0}{y}\oint\frac{\exp(2Rt - Bt^{-1}\log(y_0/y))dt}{t(t-B)^2}.$$

Put $t = (a/2R)^{\frac{1}{2}}\tau$ and $a = B\log(y/y_0)$, greater than 0 in the range of y of interest, and get

$$p_1 = \frac{2RB}{4i}e^{-2RB}\left(\frac{y_0}{y}\right)\oint\frac{\exp((2aR)^{\frac{1}{2}}(\tau+\tau^{-1}))d\tau}{\tau[(a/2R)^{\frac{1}{2}}\tau - B]^2}.$$

If $(a/2R)^{\frac{1}{2}} < B$, then expand the denominator in a binominal series, obtaining

$$p_1 = \frac{2RB}{4i}e^{-2RB}\left(\frac{y_0}{y}\right)\oint\frac{\exp((2aR)^{\frac{1}{2}}(\tau+\tau^{-1}))d\tau}{B^2} \times\left[\frac{1}{\tau} + 2\left\{\frac{1}{B}\left(\frac{a}{2R}\right)^{\frac{1}{2}}\right\} + \frac{2\cdot 3}{1\cdot 2}\left\{\frac{1}{B}\left(\frac{a}{2R}\right)^{\frac{1}{2}}\right\}^2\frac{1}{\tau} + \cdots\right].$$

Each term in this series involves a modified

Bessel function, according to the standard formula

$$I_n(z)=\frac{1}{2\pi i}\oint\frac{\exp\left(\frac{z}{2}(\tau+\tau^{-1})\right)d\tau}{\tau^{n+1}}.$$

The series, which converges with moderate rapidity if $(a/2R)^{\frac{1}{2}}<B$ may now be used to get the numerical value of p_1. If $(a/2R)^{\frac{1}{2}}>B$, the similar series obtained by using the alternate binominal expansion of the denominator is used. The evaluation of p_2 is similar to that of p_1. Evaluating p_3 involves only elementary functions.

Let $\mathcal{P}(f)df$ be the probability that the incident particle lose a fraction f of its incident energy E_0 in range df, during a nuclear traverse. Then

$$\mathcal{P}(f)=E_0\frac{\partial}{\partial E_0}P(E_0-E, R).$$

In Fig. 2, $\mathcal{P}(f)$ is plotted for mass number 95, and for incident energies of 100 and 50 Mev. When the kinetic energy of the incident particle becomes about $E_F=22$ Mev, the depth of the Fermi potential well, it can then no longer emerge from the nucleus. Thus the continuous curve $\mathcal{P}(f)$ should be corrected by making it 0 from $f=(E_0-E_F)/E_0$ to $f=1$; and by adding to it a δ-function at $f=1$, with a coefficient equal to the area under $\mathcal{P}(f)$ between $f=(E_0-E_F)/E_0$ and $f=1$.

To get the corresponding result for deuteron bombardment, we introduce $\bar{r}=1.7\cdot10^{-13}$ cm, the average of the projected distance between the two deuteron particles on a plane perpendicular to the incident beam. This value is easily computed with an approximate deuteron wave function of form e^{-ar}/r. If we assume the two deuteron particles always have this average projected spacing, then when one of these particles hits the nucleus, the other must do so also, unless the first hits the nucleus within a projected distance $\bar{r}$ of the edge. On the average, when one of the particles hits the nucleus with impact parameter such that the second has a non-zero chance of not hitting, the first will hit at distance $\bar{r}/2$ from the edge; then the chance of the second not hitting will be $\sim\frac{1}{3}$, if $\bar{r}<R$, R the nuclear radius. The probability of one particle hitting the nucleus and the other not hitting is thus

$$\frac{2}{3}\frac{R^2-(R-\bar{r})^2}{R^2}$$

which for a nucleus of the heavy component is 0.30. Let $P_1(E_0, \epsilon)$ be the distribution function for energy transfer ϵ when only one particle of the deuteron hits the nucleus, E_0 being the incident energy of such a particle. If $P_2(E_0, \epsilon)$ is the corresponding function when both particles of the deuteron hit, then

$$P_2(E_0, \epsilon)=\int_0^{\epsilon}P_1(E_0, \epsilon_1)P_1(E_0, \epsilon-\epsilon_1)d\epsilon_1.$$

And then the corresponding distribution, given simply that a deuteron collides with the nucleus, will be $P_d=0.3P_1+0.7P_2$. A plot of P_d is given

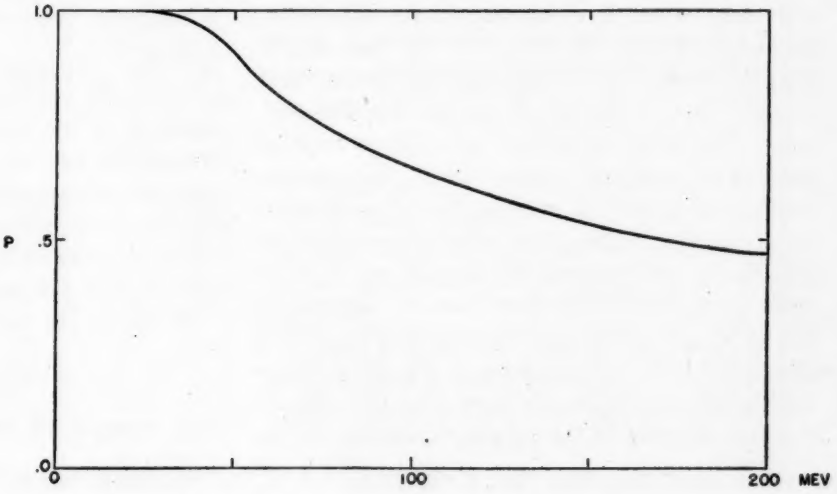

FIG. 5. $P_p(X)$ is probability that an ion evaporated from a nucleus of the heavy component be a proton, when the nucleus is at excitation X.

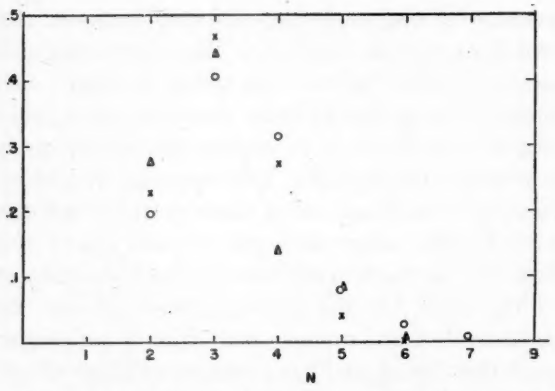

FIG. 6. The ordinate is the probability that a nuclear star contain N prongs formed by the paths of charged particles. The crosses give the prong distribution in the photographic emulsion as observed in the experiments of Part I. The triangles give the distribution observed in cloud chamber filled with air and alcohol vapor, with a neutron beam of 95 Mev. The circles give the theoretical distribution for stars from the heavy component of the emulsion produced by a deuteron beam of 200 Mev.

in Fig. 3. The rather striking discontinuity in this curve arises from the strongly discontinuous mass distribution within the deuteron.

IV. NUCLEAR EVAPORATION

To apply formula (7) to the heavy component of the photographic emulsion ($A=95$), binding energies for the neutron proton, alpha particle and deuteron are needed. According to the Weizsäcker formula,[6] they are

$$E_n=8.0, \quad E_p=8.0, \quad E_\alpha=4.0, \quad E_d=13.3 \text{ Mev}.$$

The Coulomb barrier for the proton and deuteron is taken to be $V=6.2$, for the alpha particle $2V$. The least change in the excitation energy X of a nucleus when it evaporates a particle is, in the approximation for large X, the sum of the binding energy and Coulomb energy for that particle, or the "threshold energy" for the particle. This threshold energy for a given type of evaporated particle varies when the parent nucleus, as a result of evaporation, travels down the Heisenberg valley. It is reasonable to suppose that the excited nucleus will usually not wander more than about three steps from the bottom of the valley, in which case these variations in the thresholds will be a secondary, though perhaps not entirely negligible effect, at least for a heavy nucleus. In what follows, these variations will be neglected. The formula (7) yields a finite probability for the evaporation of particles even heavier than the alpha particle. But even for 200 Mev excitation of the heavy component, these probabilities are small and will be neglected.

Gardner and Peterson[7] have observed stars with two, three, and more visible prongs, each prong consisting of the track of an evaporated ion; they have measured the relative frequencies of these types of stars. To compute these frequencies, we introduce a function $P(\nu, X)$, the probability that the excited nucleus will have emitted ν or more prongs when, as a result of evaporation, its excitation has fallen to a value X from an original value $X_0>X$. Let $q(X)$ be the probability per unit drop in excitation that the nucleus emit an ion. Then P will satisfy the equation

$$\frac{\partial P(\nu+1, X)}{\partial X}=[P(\nu+1, X)-P(\nu, X)]q(X).$$

Or, putting

$$Q=\int_0^X q(X)dX$$

$$\frac{\partial P(\nu+1, Q)}{\partial Q}=P(\nu+1, Q)-P(\nu, Q). \quad (11)$$

The use of a continuous function $q(X)$, to describe evaporation is justified only if the excitation is many times the threshold energy for evaporation of a particle. This condition is quite well satisfied when the excitation is of the order of 200 Mev. We write

$$(1/q(X))=\xi_i+(p_n/p_i)\xi_n \quad (12)$$

where ξ_i is the average drop in excitation per evaporated ion, at excitation X, ξ_n the average drop per evaporated neutron; p_n and p_i are the relative probabilities for neutron and ion evaporation at excitation X. The quantities on the right of (12) are easily calculated from (7).

To solve (11), we note that $P(0, Q)=1$. Hence

$$e^{-Q}P(1, Q)=e^{-Q}+C_1.$$

The constant of integration C_1 is fixed by re-

[6] H. A. Bethe, Rev. Mod. Phys. 8, 165 (1936).

[7] E. Gardner and V. Peterson, Phys. Rev. 75, 364 (1949).

quiring that $P(1, X)=0$ when $X=X_1\equiv X_0-T_p$ where T_p is the least of the ion thresholds, and X_0 the original excitation. That is $C_1=-e^{-Q_1}$, $Q_1\equiv Q(X_1)$. Similarly

$$e^{-Q}P(2, Q)=e^{-Q}-C_1Q+C_2,$$

$$C_2=-e^{-Q_2}+C_1Q_2,$$

$$Q_2=Q(X_0-2T_p)$$

$$e^{-Q}P(3, Q)=e^{-Q}+C_1\frac{Q^2}{2}-C_2Q+C_3,$$

$$C_3=-e^{-Q_3}-C_1\frac{Q_3^2}{2}+C_2Q_3,$$

$$Q_3=Q(X_0-3T_p).$$

. . . .

The probability of evaporating just ν prongs is

$$p_\nu=P(\nu, Q_T)-P(\nu+1, Q_T), \quad Q_T=Q(T_p). \quad (13)$$

The mean prong number $\bar{\nu}=\Sigma\nu p_\nu$ turns out to be 4.0 at $X=200$ Mev.

A more accurate method of finding $\bar{\nu}$ involves the use of the function $P(t, X)$, which is the probability at time t, after the nucleus is struck, that it have excitation X or less. Let

$$W(X, \xi)=W_n+W_p+W_\alpha+W_d$$

be the sum of the function (7) for the four types of evaporated particles. Then

$$\frac{\partial P(t, X)}{\partial t}=\int_X^{X_0}\frac{\partial P(t, X')}{\partial X'}dX'\int_{X'-X}^{X'}W(X', \xi)d\xi.$$

The complicated form of the kernel makes difficult an analytic solution. Differentiating this equation yields

$$\frac{\partial p(t, X)}{\partial t}=-p(t, X)\int_0^X W(X, \xi)d\xi$$

$$+\int_X^{X_0}p(t, X')dX'W(X', X'-X),$$

$$p(t, X)=\frac{\partial}{\partial X}P(t, X). \quad (14)$$

Multiply (14) by $e^{-\lambda t}$ and integrate between $t=0$ and $t=\infty$. Write

$$\bar{p}(\lambda, X)=\int_0^\infty p(t, X)e^{-\lambda t}dt,$$

$$-p(0, X)+\lambda\bar{p}(\lambda, X)=\int_0^\infty\frac{\partial p(t, X)}{\partial t}e^{-\lambda t}dt.$$

Then to solve the resulting equation numerically break the interval from 0 to X_0 into a number of equal parts $(0, X_n)$, $(X_n, X_{n-1})\cdots(X_1, X_0)$; and take $\bar{p}(\lambda, X)$ as an unknown constant in each such sub-interval except (X_1, X_0), in which take $\bar{p}(\lambda, X)=1$. Then the integral equation breaks up into n algebraic equations which are easy to solve successively, since only those values of the kernel $W(X', X'-X)$ enter into the equation for which $X'>X$. The principal labor is in tabulating the function $W(X', X'-X)$. The method yields $\bar{p}(\lambda, X)$ as a histogram in X.

If $N(t)$ is the expected number of ions evaporated between the instant the nucleus is hit and time t

$$\frac{dN(t)}{dt}=\int_0^{X_0}p(t, X')dX'\int_0^{X'}W_i(X', \xi)d\xi$$

where $W_i(X_1\xi)=W_p+W_\alpha+W_d$. Then

$$\lambda\bar{N}(\lambda)=\int_0^{X_0}\bar{p}(\lambda, X')dX'\int_0^{X'}W_i(X', \xi)d\xi$$

which yields $\lambda\bar{N}(\lambda)$ as the result of a quadrature. But

$$\bar{\nu}=\lim_{\lambda\to 0}\lambda\bar{N}(\lambda).$$

When $X_0=200$ Mev and the interval $(0, X_0)$ is broken into 30 parts, the numerical method just described yields

$$\bar{\nu}=4.4.$$

The distribution (13) thus yielded a mean prong number about 10 percent too small. The distribution will hence be improved by multiplying by a scale factor and renormalizing so as to get a mean 4.4.

To get a result to compare with experiment, the distribution (13) must now be evaluated for $X_0=150$, 100 and 50 Mev as well as 200 Mev. The results for various X_0's are then weighted according to the graph of Fig. 3.

We may crudely represent the insensitivity of the emulsion to high energy protons by assuming that it detects all protons with energies below 15 Mev, but none with energies above this value. To subtract from the computed prong number distribution the effect of unobserved protons, the energy distribution of the evaporated protons is needed, shown for a special case in Fig. 4. For this is needed also the proportion of all evaporated ions which are protons, shown in Fig. 5. After a correction for this emulsion insensitivity to protons, the calculated prong number distribution for the heavy component, at 190 Mev bombarding energy, becomes as shown by the circles in Fig. 6.

It is doubtful whether a simple statistical theory can be applied to the evaporation of ions from a highly excited nucleus as light as carbon or oxygen. Fortunately, information on this process has been obtained by cloud-chamber measurements.[8] Of 499 stars produced by the 90 Mev neutron beam in a chamber filled with water vapor and alcohol, the numbers with 2, 3, ··· prongs were as follows:

2 prongs	267 stars
3 prongs	159 stars
4 prongs	46 stars
5 prongs	25 stars
6 prongs	2 stars

Of 106 two pronged stars, observed in detail in the chamber, 66 percent were observed to possess at least one prong with an energy in excess of 15 Mev. Multiplying the entry 267 by $\frac{1}{3}$ yields a corrected prong distribution for the cloud chamber stars as shown by the circles in Fig. 6.

As the deuteron bombarding energy varies from 35 to 190 Mev, the prong distribution in the photographic emulsion remains the same, within the limit of experimental error. The mean of the theoretical distribution, for the heavy component, varies from about 1.1 at 35 Mev bombarding energy to 3.3 at 190 Mev. Since at 35 Mev a struck nucleus of the heavy component is almost sure to evaporate neutrons only; the cross section for production of a visible star from a nucleus of the heavy component varies from about $0.1\sigma_0$ at 35 Mev to over $0.9\sigma_0$ at 190 Mev, where σ_0 is the geometrical cross section. Due to the ease with which carbon and oxygen nuclei may break up into alpha-particles, the cross section for visible star production from these lighter nuclei may be expected, in contrast, to change very slowly with bombarding energy.

The stars observed by Gardner and Peterson must then arise almost entirely from the lighter component of the emulsion at the lower bombarding energies, and predominantly from the heavy component at the higher energies. If we make the plausible assumption that the prong number distribution for the light component is almost unchanging throughout the range of bombarding energies used, then the observed and calculated distributions are in good qualitative agreement.

V. ANGULAR DISTRIBUTION

The angular distribution of star prongs observed in Part I is predominantly in the forward direction. We may assume that particles evaporated from a nucleus emerge with an angular distribution spherically symmetric with respect to the nucleus. But the nucleus itself may be moving. In the case of the heavy component, the mean recoil velocity of the center of the excited nucleus, just after it is struck, will be small compared to the mean velocity of the evaporated ions. But in the case of the light component, it will be of the same order or exceed the mean velocity of the ions evaporated from it. The observed asymmetry is of the order to be expected on the assumption that it is due primarily to this recoil of the lighter nuclei.

VI. ACKNOWLEDGMENTS

We wish to thank Professor Robert Serber for suggesting and guiding this problem.

This paper is based on work done under the auspices of the United States Atomic Energy Commission in connection with the Radiation Laboratory, University of California, Berkeley, California.

[8] Cloud-Chamber Group, Radiation Laboratory, University of California private communication.

Stars in Photographic Emulsions Initiated by Alpha-Particles

EUGENE GARDNER
Radiation Laboratory, Department of Physics, University of California, Berkeley, California
(Received September 27, 1948)

A study has been made of stars in photographic emulsions initiated by alpha-particles from the 184-inch Berkeley cyclotron. These stars are similar to stars initiated by deuterons, which were described in an earlier paper. Eastman NTA plates were used. Plates from the emulsion number used will record alpha-particles of energy about 200 Mev and lower and protons of about 10 Mev and lower. The contribution of the high energy protons may be missing from the results given. The average number of prongs observed is close to 3. The ratio of the number of prongs in the three sectors in the forward direction of the beam to the number in the three backward sectors is about 6. The cross section for the formation of stars has been estimated by counting sections of alpha-particle tracks and the stars associated with these tracks. For alpha-particles of energy 130 Mev we obtain a value of the cross section, averaged over all of the atoms in the emulsion, of 3×10^{-25} cm^2 with an estimated uncertainty of 30 percent.

I. INTRODUCTION

A STUDY has been made of stars in photographic emulsions initiated by alpha-particles from the 184-inch Berkeley cyclotron.[1] The method of bombarding photographic plates in the cyclotron has been described in a paper on stars initiated by deuterons.[2] The stars initiated by alpha-particles are similar to those initiated by deuterons; however, in the case of the alpha-particle stars we were able to see the tracks of the initiating particles and, hence, to get an estimate of the cross section for the formation of stars.

The photographic plates used were Eastman NTA plates of emulsion thickness 35 microns. All were from the same batch, Emulsion No. 340,387, received February, 1947. This is the emulsion number used in a study[3] of alpha-particle and deuteron tracks, in which it was found that alpha-particles of 200 Mev and lower and protons of 10 Mev and lower can be followed easily. Tracks of higher energy protons may be missed. We are not able to tell from the experimental data how many proton tracks are missed for this reason. It is hoped that the data of the following sections will give useful qualitative information about the alpha-particle stars even though the contribution of the protons above 10 Mev is all, or in part, missing. Plates are now available which are much more sensitive than the plates used in this study. With the new plates it would be possible to see proton tracks at all energies which one would be likely to encounter in stars initiated by alpha-particles from the 184-inch cyclotron. Also it would be possible to extend the study to 380 Mev, the full energy output from the cyclotron. We hope at some time in the future to do a study of alpha-particle stars using the new Eastman NTB plates or one of the new Ilford types.

TABLE I. Composition of Eastman NTA emulsion.

Element	Percent composition	Weight (grams/cc)	Atoms/cc $\times10^{-22}$
Ag	47.1	1.700	0.0950
I	1.49	0.054	0.0026
Br	33.90	1.220	0.0920
O	4.80	0.173	0.0651
N	3.06	0.112	0.0482
C	8.47	0.305	0.1530
H	1.17	0.042	0.2509
Total		3.606	0.7067

II. NUMBERS AND DIRECTIONS OF STAR PRONGS

A group of stars initiated by alpha-particles of energy about 100 Mev is shown in Fig. 1. Stars

TABLE II. Average cross section for formation of stars by alpha-particles.

Energy (Mev)	No. of stars	Total path length (cm)	Mean path length (cm/star)	Average cross section (cm^2) $\times10^{24}$
50	12	2060	170	0.08
95	102	6870	67	0.21
130	138	6690	48	0.29
170	115	7650	67	0.21
210	99	9500	96	0.15

[1] W. M. Brobeck *et al.*, Phys. Rev. **71**, 449 (1947).
[2] E. Gardner and V. Peterson, Phys. Rev. **74**, 364 (1948).
[3] R. L. Brock and E. Gardner, Rev. Sci. Inst. **19**, 299 (1948).

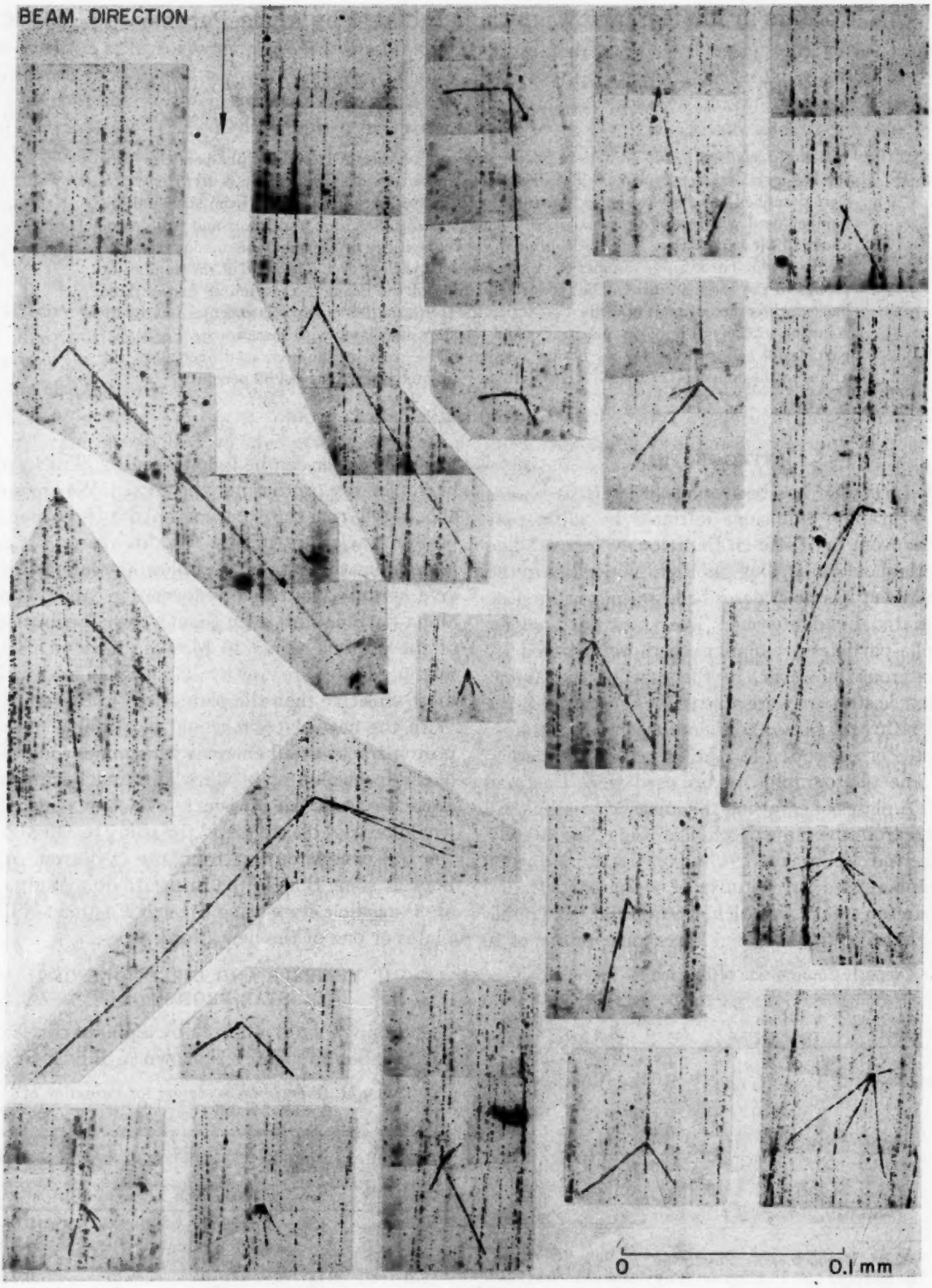

FIG. 1. Group of stars initiated by alpha-particles of energy about 100 Mev. (Photomicrographs made with 3-mm apochromatic objective lens.)

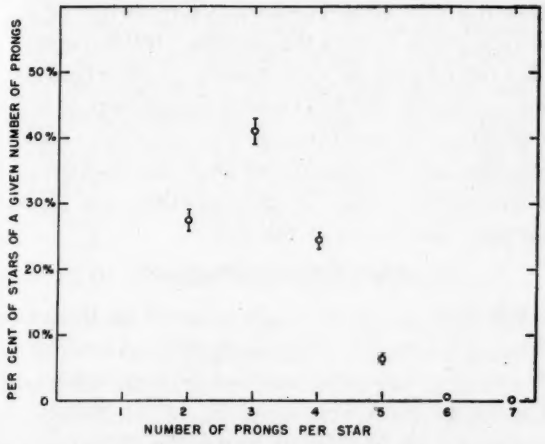

FIG. 2. Frequency distribution of stars of various numbers of prongs. Graph gives percent of stars of a given number of prongs as a function of the number of prongs. Stars from all energies (about 50 to 200 Mev) have been lumped together. Errors shown are statistical probable errors.

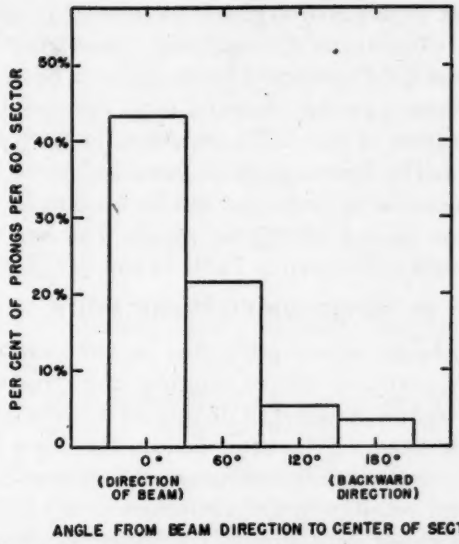

FIG. 3. Angular distribution of prongs. Histogram gives percent of prongs per 60° sector as a function of angular position of sector. Stars from all energies (about 50 to 200 Mev) have been lumped together.

initiated by alpha-particles at other energies were also observed; the full study included about 450 stars at energies from about 50 to 200 Mev. The numbers of prongs per star and the directions of the prongs with respect to the beam direction were remarkably similar for all energies studied, no differences being observed which were significantly larger than the statistical probable errors. In presenting the data here, stars from all energies have been lumped together. The frequency distribution of stars of various numbers of prongs is shown in Fig. 2. It is similar to the corresponding curve for stars initiated by deuterons.[2] The direction of the prongs with respect to the beam direction is shown in Fig. 3. The directions do not refer to the directions in three dimensions as the stars are originally formed in the emulsion, but to the projected directions as seen through the microscope. The field of view of the microscope was divided into 60° sectors, and a tabulation was made of the number of prongs in the various sectors. The ratio of the number of prongs in the three sectors in the forward direction of the beam to the number in the three backward sectors is about 6. This is to be compared with a ratio of 3 found for stars initiated by deuterons.[2]

III. CROSS SECTION FOR FORMATION OF STARS

In the photomicrographs shown in Fig. 1 the tracks of the direct alpha-particle beam can be seen as straight sections which are approximately parallel. Occasionally one of the tracks terminates in a star. By counting sections of tracks and the stars originating on these tracks, it is possible to get an estimate of the mean path length for formation of stars. The number of sections of tracks was found by counting tracks in sample areas. The number of sections actually counted was about 10 times the number of stars. The length of track was found by multiplying the number of sections of track by the diameter of the field of view of the microscope.

Since we have not been able to tell which elements in the emulsion were responsible for the stars observed, we are not able to find the cross sections associated with the different elements.

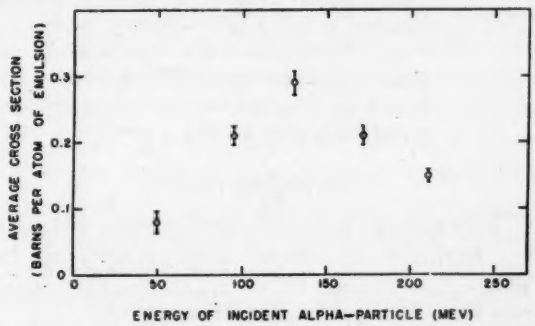

FIG. 4. Average cross section for formation of stars by alpha-particles as a function of the energy of the initiating alpha-particle.

All that we are able to give is an average over-all of the elements in the emulsion, calculated by using the total number of atoms per cc. The number of atoms per cc, as found from the chemical composition of the NTA emulsion, is shown in Table I. The figures given in Table I apply to the dry emulsion, no correction having been made for moisture picked up by the plates. The average cross section is shown in Table II and in Fig. 4.

IV. DEUTERON CONTAMINATION

One factor which prevented us from making a more accurate determination of the cross section was the presence of deuterons in the alpha-particle beam. Even after helium has been run into the ion source continuously for several days it is still possible to find deuterons in the beam. The number of deuteron tracks in the photographic plates varied from a few percent of the number of alpha-particle tracks to approximately as many as the number of alpha-particle tracks. Although deuteron tracks are not ordinarily seen at the energies at which we were working, they seemed to contribute enough developed grains so that there was some uncertainty in the count of the alpha-particle tracks. Different observers counting the same tracks have reported alpha-particle track counts which differ by 30 percent. This introduces an uncertainty in the cross sections given in Table II and Fig. 4. There is little confusion between stars initiated by alpha-particles and stars initiated by deuterons since it is ordinarily easy to tell whether an alpha-particle track ends at the star.

V. ACKNOWLEDGMENTS

We wish to express appreciation to Professor Ernest O. Lawrence for his continued interest in this study. The program was greatly helped by discussions with Professors R. L. Thornton, R. Serber, E. M. McMillan, and L. W. Alvarez. We wish to thank Mr. D. J. O'Connell for making the alpha-particle track and star count, Mr. A. J. Oliver for the preparation of Fig. 1, Mr. Duane Sewell and the cyclotron crew for bombarding the plates, and the Eastman Kodak Company for information regarding Eastman NTA plates. This paper is based on work performed under contract No. W-7405-eng-48 with the Atomic Energy Commission in connection with the Radiation Laboratory, University of California, Berkeley, California.

PHYSICAL REVIEW VOLUME 75, NUMBER 3 FEBRUARY 1, 1949

Positive Mesons Produced by the 184-Inch Berkeley Cyclotron

JOHN BURFENING,* EUGENE GARDNER, AND C. M. G. LATTES**
Radiation Laboratory, Department of Physics, University of California, Berkeley, California
(Received October 11, 1948)

Positive mesons produced by 380-Mev alpha-particles in the 184-inch Berkeley cyclotron have been detected by means of photographic plates. The experimental arrangement is similar to that used for detecting negative mesons except that the plates are placed in a position to receive positive instead of negative particles from the target. Heavy positive mesons are observed to decay into secondary mesons in the manner described by Lattes, Occhialini, and Powell. Relative numbers of positive and negative mesons coming from a target are found by placing plates symmetrically on opposite sides of the target. Preliminary results indicate that for a $\frac{1}{16}$-inch carbon target there are about one-fourth as many heavy positive mesons as heavy negative ones for meson energies of 2–3 Mev in the laboratory system.

I. INTRODUCTION

THE mesons first observed[1] at the 184-inch Berkeley cyclotron[2] were known to be negatively charged, since the photographic plates used for detecting them were placed in a position to receive negative but not positive particles from the target. We have now detected positive mesons by placing plates in a position to receive positively charged particles from the target. As with the exposures to negative mesons, the target

* Lieutenant Colonel, U. S. Army. Present address: Sandia Base, Albuquerque, New Mexico.
** On leave of absence from University of São Paulo, Brazil.
[1] E. Gardner and C. M. G. Lattes, Science **107**, 270 (1948).
[2] Brobeck, Lawrence, MacKensie, McMillan, Serber, Sewell, Simpson, and Thornton, Phys. Rev. **71**, 449 (1947).

was bombarded with the circulating beam of 380-Mev alpha-particles. Most of our work has been done with a carbon target $\frac{1}{16}$-inch thick. The photographic plates which we have found to be most suitable for detecting positive mesons are Ilford C 2 and C 3, and Eastman NTB, each of emulsion thickness about 100 microns.

II. DESCRIPTION OF APPARATUS

Two methods of making exposures to positive mesons have produced plates suitable for study. The first method makes use of positive mesons which follow trajectories like the one illustrated in Fig. 1. Plates are placed below the circulating beam, as shown in Fig. 2. Mesons are received which leave the target moving at a small angle downward from the beam direction. Plates to receive negative mesons of about the same energy and angular range may be placed on the opposite side of the target, as shown in Fig. 2. Shielding is provided on the side from which the beam comes in order to prevent scattered beam particles from reaching the plates. For mesons which strike the plate at right angles to the edge, the energy range is about 2-5 Mev in the laboratory system. For meson trajectories at other angles the energy at a given point on the plate is larger, so that the energy range of the mesons counted on the plates is not very well defined.

In a second method of detecting positive mesons, the photographic plates are placed in a position to receive mesons which leave the target in a direction opposite to the beam direction. The arrangement is shown in Fig. 3. Plates exposed in this way have tracks of negative mesons along one edge, and tracks of positive mesons along the opposite edge. In this method, as in the preceding one, the energy range of the mesons received by the plates is not well defined.

In addition to the meson tracks found on the plates there is a "background" of tracks caused by protons and alpha-particles. Some of the background tracks are attributed to stars and recoils produced by neutrons, and some to low energy protons and alpha-particles from the target. Neither of the methods for making exposures to positive mesons gives as high a ratio of meson tracks to background tracks as that obtained in exposures to negative mesons.[1]

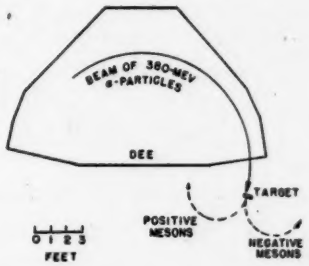

FIG. 1. Plan view of cyclotron showing direction in which positive and negative mesons are deflected by the magnetic field.

III. DESCRIPTION OF THE POSITIVE MESON TRACKS

The appearance of the positive meson tracks under the microscope is similar to that of negative meson tracks.[1] They have a characteristic grain density change along the track and a characteristic wandering associated with small-angle scattering. For mesons which come from the target a measurement of the mass can be obtained by measuring the bending in the magnetic field of the cyclotron and the range in the emulsion. The radius of curvature of the trajectory is calculated from the position on the plate at which the track is found and the angle which the track makes with the edge of the plate. The mass determination has not yet been made with any precision; however, preliminary measurements indicate that there are two groups of mesons having masses of about 300- and 200-electron masses, respectively. It is presumed that they are the same as the π- and μ-mesons described by Lattes, Occhialini, and Powell.[3] The total number of light and heavy mesons observed so far is about 200.

Neither the heavy nor the light positive mesons initiate stars. Most of the heavy positive mesons disintegrate to give observable secondary mesons, as shown in Figs. 4–6. Figure 4 is taken from an Eastman NTB plate, Fig. 5 from an Ilford C 2, and Fig. 6 from an Ilford C 3. In each case the heavy positive meson enters from the bottom left. At the point at which the heavy positive meson stops a secondary meson is initiated, moving toward the right. It is thought that all, or almost all, of the heavy positive mesons give secondaries; but in some cases the secondaries

[3] C. M. G. Lattes, G. P. S. Occhialini, and C. F. Powell, Nature **160**, 453, 486 (1947).

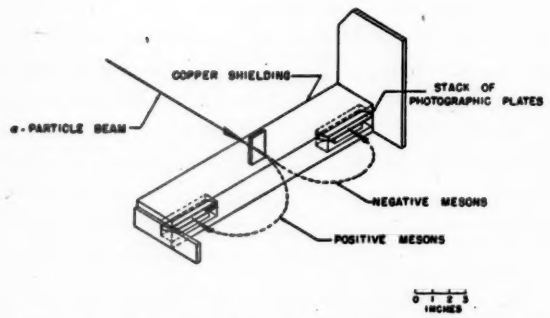

FIG. 2. Apparatus used for placing photographic plates below the circulating beam for exposure to both positive and negative mesons.

move up or down at a steep angle through the emulsion, and the tracks are not seen. The fraction of the heavy mesons which are observed to give secondaries depends on the thickness and sensitivity of the emulsion and on the background of other tracks in the vicinity. Of the emulsions which we have used, the Ilford type C 3 seems to be best for showing secondaries.

For all of the secondary mesons which stop in the emulsion the range is about 600 microns, corresponding to an energy of about 4 Mev. Table I gives the ranges of five secondary mesons which stopped in the emulsion (Ilford plates).

In addition to the light meson tracks which start at the ends of heavy positive meson tracks, other tracks are found which have a grain density change characteristic of light mesons. It is assumed that they are positively charged and that they come from heavy mesons which disintegrate at positions other than in the emulsion. There are two groups: (a) Tracks with random orientation, found in all regions of the plate where heavy positive meson tracks are found. These mesons

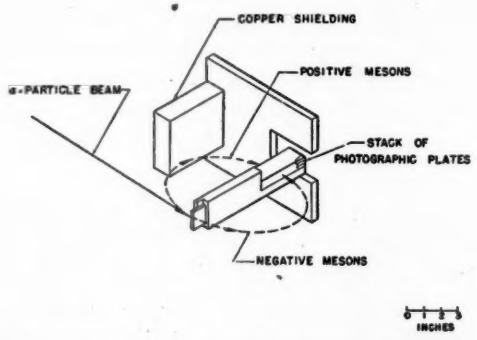

FIG. 3. Apparatus used for placing photographic plates in a position to receive positive mesons which leave the target in a direction opposite to the beam direction.

are presumed to arise from local disintegration of heavy positive mesons in the glass above or below the emulsion. For the disintegrations which are observed in the emulsion, the secondary mesons come off in random directions, so that some remain in the emulsion and some pass out of the emulsion into the glass. Similarly, it is to be expected that disintegrations above or below the emulsion would produce some secondaries which would enter the emulsion from the glass. (b) Tracks which start from the edge of the plate. These probably come from the target, or from some region not too far distant. The evidence for this is that if the masses are calculated by means of bending in the magnetic field and range in the emulsion on the assumption that the mesons come from the target, values are obtained which give an average of about 200-electron masses. The spread in mass values is rather large, suggesting that perhaps not all of the light meson trajectories originate at the target. If the energies of these mesons are calculated from their ranges, assuming a mass of 200-electron masses, almost all of the values found are less than 4 Mev. This suggests that most of them probably come from the decay of heavy mesons at rest, since 4 Mev is about the kinetic energy which a light meson receives from the disintegration of a heavy one.

The light mesons from the target may come from the decay of heavy ones which did not have enough energy to escape from the target. Another possibility is that a heavy meson goes through a 360° trajectory, as illustrated in Fig. 7, and then returns to the target, where it disintegrates into a light meson. It is probable that more light mesons arise from heavy mesons which decay without leaving the target than from those which return, because many of the 360° trajectories spiral up or down enough to miss the target.

Some of the light mesons may not come directly from the target but may come from heavy mesons which disintegrate in flight. Another possibility for a light meson trajectory which does not start at the target is illustrated in Fig. 8. Here a heavy meson from the target comes to rest in the copper of the plate holder in a position such that the secondary meson can reach the photographic plate.

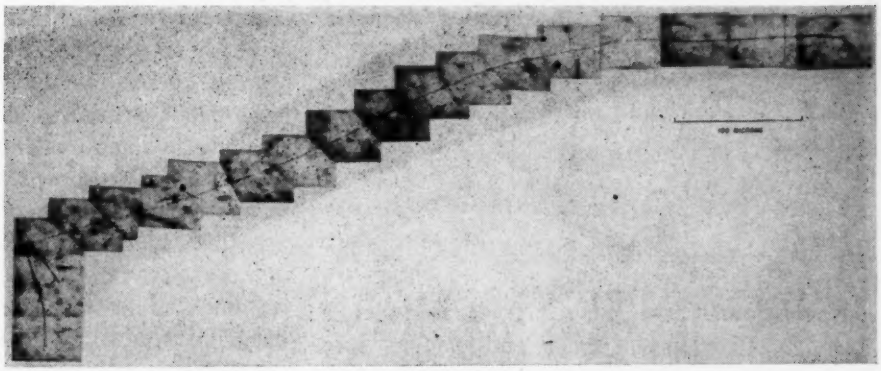

FIG. 4. Disintegration of a heavy positive meson to give a secondary. Photomicrograph made from Eastman NTB plate.

A rather hasty survey indicates that the numbers of light mesons found in various positions on the plate are about what would be expected from the decay of the heavy ones as suggested above. The relative numbers of light and heavy mesons may be illustrated by one group of mesons found in 100-micron Ilford C 3 plates. Of the 34 mesons in the group, 20 entered from the edge of the emulsion and 14 entered from the glass above or below the emulsion. For the 20 mesons which entered from the edge of the emulsion a measurement of bending in the magnetic field and range in emulsion showed that 16 had masses measured as greater than 260-electron masses. The remaining 4 had masses measured between 150- and 230-electron masses. All of the 16 heavy mesons gave observable secondaries. It is assumed that the 14 which entered the emulsion from the glass were light mesons which came from decay of heavy mesons in the glass above or below the emulsion.

Since the magnetic field of the cyclotron separates the positive mesons from the negative ones, we can be reasonably sure that disintegrations of the type shown in Figs. 4–6 are due to positive mesons. No disintegrations of this type have been found in a study[4] of negative mesons produced by the cyclotron. This study has included about two thousand heavy negative meson tracks. Light meson tracks have been found, but

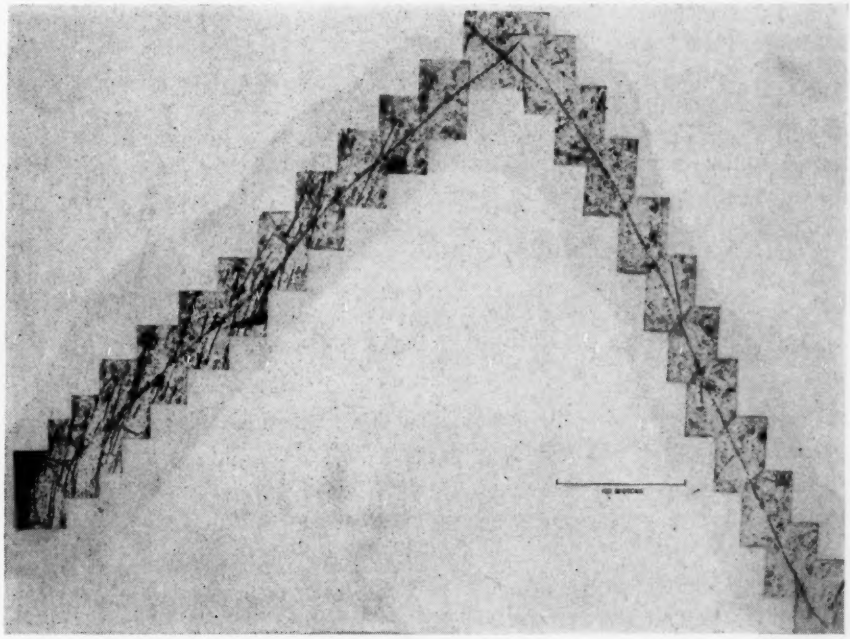

FIG. 5. Disintegration of a heavy positive meson to give a secondary. Photomicrograph made from Ilford C 2 plate. The heavy tracks on the left-hand side of the photomicrograph are due to protons from the target. They are often the most troublesome part of the background.

[4] Frank Adelman and Stanley Jones, private communication.

TABLE I. Ranges of secondary mesons which stopped in the emulsion (Ilford plates).

Track No.	Range in microns
1	625
2	630
3	612
4	604
5	560

none of them started at the point at which a heavy negative meson track ended. This substantiates the assumption of Lattes, Occhialini, and Powell[3] that positive mesons are responsible for the events in which a heavy meson comes to rest in the emulsion and then disintegrates to give a secondary meson.

IV. RELATIVE NUMBERS OF POSITIVE AND NEGATIVE MESONS

By means of symmetrically placed plates, as shown in Fig. 2, we plan to measure the relative numbers of positive and negative mesons produced in targets of various materials. So far only carbon has been studied, and the study has included only a limited range of meson energies. The target was the usual $\frac{1}{16}$-inch carbon. The energy range studied is not very well defined, but is of the order of 2–3 Mev in the laboratory system. In this energy range 40 positive mesons have been counted as compared with 136 negative ones in an equivalent area. Of the 40 positive mesons, 26 are known to be heavy since they form observable secondaries. Some of the secondaries may have been missed, so that the number of heavy mesons may be larger than 26. It is estimated that more than 90 percent of the 136 negative mesons are heavy.

Operation with the arrangement illustrated in Fig. 3 has shown that there are some heavy positive mesons which leave the target in a direction opposite to beam direction. In order to illustrate the relative numbers of positive mesons in the backward beam direction and negative mesons in the forward direction, the numbers will be given for one run made with a $\frac{1}{16}$-inch carbon target. For this run, mesons were counted along the full 3-inch edge of the plate, so that the energy range is of the order of 2–5 Mev in the laboratory system. 144 negative mesons were counted along one edge of the plate and 16 positives along the opposite edge. The numbers given include both light and heavy mesons.

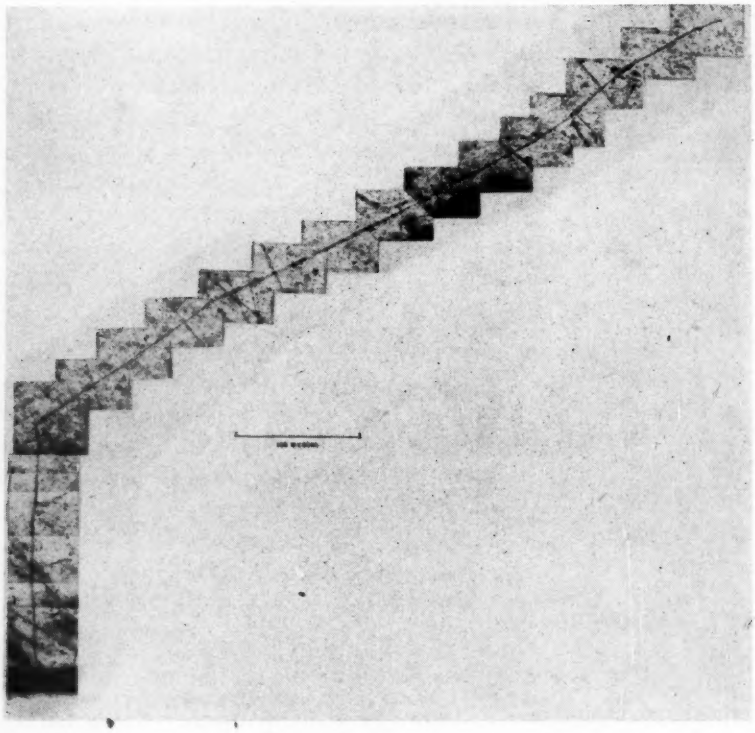

FIG. 6. Disintegration of a heavy positive meson to give a secondary. Photomicrograph made from Ilford C 3 plate.

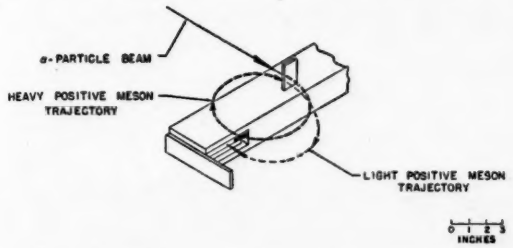

FIG. 7. Diagram showing a possible method of production of light mesons in the target. Heavy meson goes through 360° trajectory and returns to the target, where it disintegrates to give a light meson.

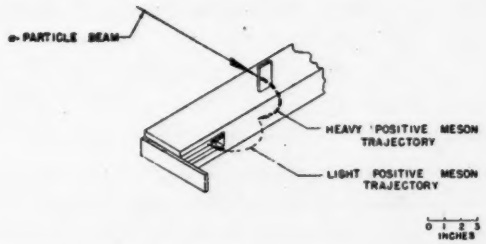

FIG. 8. Diagram showing how a light meson trajectory could start at a point not at the target. Heavy meson from the target comes to rest in the copper of the plate holder in a position such that the secondary meson can reach the photographic plate.

V. CONCLUSIONS

Positive mesons of mass about 300-electron masses are produced when a beam of 380-Mev alpha-particles strikes a carbon target. At points in the emulsion at which these heavy positive mesons come to rest, tracks of secondary mesons of mass about 200-electron masses are ordinarily observed. The fraction of the heavy positive meson tracks for which secondaries are observed depends on the sensitivity and thickness of the emulsion; however, it is thought that all, or almost all, of the heavy positive mesons decay to give secondaries. All of the secondaries have a range which corresponds to a kinetic energy of about 4 Mev. Light meson tracks are observed which do not start at the ends of heavy meson tracks; these are attributed to light mesons which come from the decay of heavy positive mesons at positions other than in the emulsion. It is thought that all of the light positive mesons observed come from the decay of heavy positive mesons.

Preliminary results indicate that for a $\frac{1}{16}$-inch carbon target there are about one-fourth as many heavy positive mesons as heavy negative ones for meson energies of 2–3 Mev in the laboratory system. This is not inconsistent with the ratio expected on the bases of Coulomb interaction. A calculation by Serber[5] gives the ratio of heavy positive to heavy negative mesons in this energy range as about 1 to 3.5.

VI. ACKNOWLEDGMENTS

The authors wish to express their appreciation to Professor Ernest O. Lawrence, whose interest and encouragement have made this work possible. The program has been greatly aided by discussion with Professors R. L. Thornton, E. M. McMillan, R. Serber, L. W. Alvarez, and E. Segrè. We are indebted to Dr. Walter H. Barkas of the Office of Naval Research in San Francisco for microscope observations and suggestions. We wish to thank Mr. A. J. Oliver for the preparation of Figs. 4–6, and Mr. James Vale and the cyclotron crew for making the bombardments. This paper is based on work performed under Contract No. W-7405-eng-48 with the Atomic Energy Commission, in connection with the Radiation Laboratory, University of California, Berkeley, California.

[5] R. Serber, private communication.

PHYSICAL REVIEW VOLUME 75, NUMBER 3 FEBRUARY 1, 1949

On the Self-Energy of a Bound Electron*

NORMAN M. KROLL** AND WILLIS E. LAMB, JR.
Columbia University, New York, New York

(Received October 7, 1948)

The electromagnetic shift of the energy levels of a bound electron has been calculated on the basis of the usual formulation of relativistic quantum electrodynamics and positron theory. The theory gives a finite result of 1052 megacycles per second for the shift $2^2S_{\frac{1}{2}}-2^2P_{\frac{1}{2}}$ in hydrogen, in close agreement with the non-relativistic calculation by Bethe.

I. INTRODUCTION

BETHE[1] has recently discussed the anomalous fine structure[2] in hydrogen on the basis of non-relativistic quantum electrodynamics. His result for the $2^2S_{\frac{1}{2}}-2^2P_{\frac{1}{2}}$ displacement was

$$\Delta W = W(2^2S_{\frac{1}{2}}) - W(2^2P_{\frac{1}{2}}) = (\alpha^3 Ry/3\pi)\log(K/\bar{\epsilon}), \quad (1)$$

where $\alpha = e^2/\hbar c \sim 1/137$ the fine structure constant, Ry the Rydberg energy $\alpha^2mc^2/2$, and $\bar{\epsilon}$ an average excitation energy of the atom, calculated to be $17.8Ry$. As Bethe's calculation diverged logarithmically, it was necessary for him to introduce a cut-off energy K for the light quanta which could be emitted and reabsorbed by the atom. On the basis of speculations as to the improved convergence of a relativistic calculation which included positron theoretic effects, Bethe took K equal to mc^2. This led to a value of $\Delta W/h = 1040$ megacycles per second, which was in very good agreement with the then available observation[3] of 1000 Mc/sec.

The purpose of this paper is to show that a relativistic calculation of ΔW does, in fact, give a convergent answer, and to present the results and some details of a calculation based on the 1927–1934 formulation of quantum electrodynamics due to Dirac, Heisenberg, Pauli, and Weisskopf. It will appear from this that the formal relativistic invariance of the present theory is to some degree illusory in that all self-energies diverge logarithmically, so that the difference of two energies such as $W(2^2S_{\frac{1}{2}})$ and $W(2^2P_{\frac{1}{2}})$, although finite, is not necessarily unique. The method we have used has a certain simplicity in its motivation, however, and the results are surprisingly plausible in their mathematical appearance. In any case, the calculations may serve as an illustration of the extent to which physical results may be derived from a divergent field theory.

The calculation is incomplete in several well defined respects. It is only made to order α in the coupling between the electron and the electromagnetic field, and to fourth order in the ratio of the velocity of the atomic electron to the velocity of light. It is expected that these deficiencies will be made up elsewhere. We will make no effort to improve on the low frequency part of the calculation as done by Bethe, for this is essentially a non-relativistic problem.

II. DERIVATION OF EQUATIONS FOR SELF-ENERGY

We start from the Hamiltonian for a system of N electrons moving in an external static electric potential energy field V and interacting with the radiation field. After elimination of the longitudinal and scalar photons in the usual way, we obtain the Hamiltonian

$$H = H_{\text{rad}} + H_{\text{mat}} + H_{\text{int}}, \quad (2)$$

$$H_{\text{rad}} = \int d\mathbf{k} \sum_{\lambda=1}^{2} N_{\mathbf{k}\lambda}\hbar c|\mathbf{k}|, \quad (3)$$

* Work supported by the Signal Corps.

** Now National Research Fellow at The Institute for Advanced Study.

[1] H. A. Bethe, Phys. Rev. **72**, 339 (1947). It may be of some interest to observe that if the non-relativistic theory is taken seriously to such an extent that retardation and the recoil energy in the energy denominators are retained, the dynamic self-energy diverges only *logarithmically*, and the $S-P_{\frac{1}{2}}$ level shift *converges*, and, in fact, with K determined to be $K=2mc^2$. The resulting shift of 1134 Mc is in disagreement with the observations.

[2] W. E. Lamb, Jr. and R. C. Retherford, Phys. Rev. **72**, 241 (1947).

[3] A later tentative value reported at the April 1948 Washington Physical Society meeting was 1065±20 Mc/sec.

$$H_{\text{mat}}=\sum_{i=1}^{N}[c\boldsymbol{\alpha}_i\cdot\mathbf{p}_i+\beta_i mc^2+V(\mathbf{r}_i)], \quad (4)$$

$$H_{\text{int}}=-\sum_{i=1}^{N}e\boldsymbol{\alpha}_i\cdot\mathbf{A}(\mathbf{r}_i)+\tfrac{1}{2}\sum_{i=1}^{N}\sum_{j=1}^{N}e^2/r_{ij}. \quad (5)$$

Here e is the (negative) charge on the electron; α, β are the Dirac matrices in the form

$$\alpha=\begin{pmatrix}0 & \sigma\\ \sigma & 0\end{pmatrix},\quad \beta=\begin{pmatrix}I & 0\\ 0 & -I\end{pmatrix}, \quad (6)$$

where σ are the usual two-component Pauli matrices. The vector potential of the radiation field is expanded in plane waves normalized in the continuous spectrum as

$$\mathbf{A}(\mathbf{r})=-(i/2\pi)\int d\mathbf{k}\sum_{\lambda=1}^{2}(\hbar c/k)^{\frac{1}{2}}\mathbf{b}_{\mathbf{k}\lambda}\mathbf{e}_{\mathbf{k}\lambda}\times\exp(i\mathbf{k}\cdot\mathbf{r})+\text{conj.}, \quad (7)$$

where $\mathbf{b}_{\mathbf{k}\lambda}^{+}$, $\mathbf{b}_{\mathbf{k}\lambda}$ are the creation and destruction operators for a light quantum of wave vector $\mathbf{k}$ and polarization type $\lambda=1, 2$.

In position theory, because of the indefiniteness of the number of electrons, it is convenient to use second quantization for the electrons as well as for the light quanta. Then

$$H_{\text{mat}}\rightarrow\int d\mathbf{x}\psi^{+}(\mathbf{x})\{c\boldsymbol{\alpha}\cdot\mathbf{p}+\beta mc^2+V(\mathbf{x})\}\psi(\mathbf{x}), \quad (8)$$

$$H_{\text{int}}\rightarrow-\int d\mathbf{x}\psi^{+}(\mathbf{x})e\boldsymbol{\alpha}\cdot\mathbf{A}(\mathbf{x})\psi(\mathbf{x})+\int\int d\mathbf{x}d\mathbf{x}'\psi^{+}(\mathbf{x})\psi(\mathbf{x})(e^2/|\mathbf{x}-\mathbf{x}'|)\times\psi^{+}(\mathbf{x}')\psi(\mathbf{x}')=\mathbf{H}_1+\mathbf{H}_C, \quad (9)$$

where $\psi^{+}(\mathbf{x})$ and $\psi(\mathbf{x})$ are, respectively, creation and destruction operators for an electron. We will expand $\psi(\mathbf{x})$ in terms of the eigenfunctions $u_n(\mathbf{x})$ of the potential field V

$$\psi(\mathbf{x})=\sum_{n}\mathbf{a}_n u_n(\mathbf{x}), \quad (10)$$

where the coefficients $\mathbf{a}_n$ are operators corresponding to the destruction of an electron in state n, etc.

We are concerned with the self-energy of a "single" electron bound in some stationary state $u_a(\mathbf{r})$ in the potential field V. In positron theory, this is taken to mean "self-energy of one electron in state a plus the vacuum electrons" minus "self-energy of the vacuum electrons alone." The highly divergent interaction of the extra electron with the infinite charge density of the vacuum electrons must still be removed. This is done by the process of symmetrization[4,5] in which the calculation is also made using the equally justified picture that all the electrons in existence are positively charged, so that the observance of a negatively charged electron in state a corresponds to a vacancy in the sea of negative energy states otherwise filled with positively charged particles. Then the results of the two methods of calculation are averaged. Since in the first picture there is one particle present in addition to the vacuum particles, and in the second picture one particle fewer, the self-term $i=j$ in the electrostatic energy cancels out as does the direct Coulomb interaction between the bound electron and the vacuum electrons, insofar as the latter are not polarized by an external electric field. The result is an avoidance of all singularities worse than logarithmic, and these may be plausibly discarded by renormalization of charge[6] and mass.

The self-energy to order α consists of the first-order Coulomb self-energy W_C and the second-order electrodynamic self-energy W_D. The former will split naturally into a direct or vacuum polarization term W_P and a static exchange term W_S. The static and dynamic terms W_S and W_D were first calculated by Weisskopf[5] in 1934 for the case of a free electron.

To calculate W_C we need the expectation values of the operator

$$H_C=\frac{1}{2}\int\int d\mathbf{x}d\mathbf{x}'\psi^{+}(\mathbf{x})\psi(\mathbf{x})\times(e^2/|\mathbf{x}-\mathbf{x}'|)\psi^{+}(\mathbf{x}')\psi(\mathbf{x}') \quad (11)$$

$$=\sum_{\alpha}\sum_{\beta}\sum_{\gamma}\sum_{\delta}A_{\alpha\beta\gamma\delta}\mathbf{a}_\alpha^{+}\mathbf{a}_\beta\mathbf{a}_\gamma^{+}\mathbf{a}_\delta,$$

where

$$A_{\alpha\beta\gamma\delta}=\frac{1}{2}\int\int d\mathbf{x}d\mathbf{x}'u_\alpha^{*}(\mathbf{x})u_\beta(\mathbf{x})\times(e^2/|\mathbf{x}-\mathbf{x}'|)u_\gamma^{*}(\mathbf{x}')u_\delta(\mathbf{x}'), \quad (12)$$

[4] W. Heisenberg, Zeits. f. Physik 90, 209 (1934).
[5] V. F. Weisskopf, Zeits. f. Physik 90, 817 (1934).
[6] P. A. M. Dirac, Solvay Congress, 1933.

for the states represented by the Schrödinger functionals

$$\Phi(1_a 0_{r'} 1_\rho),\ \Phi(0_r 1_\rho),\ \text{first picture,} \quad (13a)$$

$$\Phi(0_{(\rho)} 0_{(a)} 1_{(r')}),\ \Phi(0_{(\rho)} 1_{(r)}),\ \text{second picture.} \quad (13b)$$

Here r denotes any positive energy state, while a prime indicates the exclusion of the state a occupied by the bound electron. The letters ρ, σ denote any negative energy state, while the indices n, α, β, γ, and δ are to be used for a complete set of states of any energy whatever. In the alternate picture, a positive energy state of a positive particle is represented by (ρ) and a negative energy state by (r), (s). The state whose vacancy constitutes our electron is denoted by (a).

Consider the expectation value

$$\Phi^*(1_a 0_{r'} 1_\rho) \sum_{\alpha\beta\gamma\delta} a_\alpha^+ a_\beta a_\gamma^+ a_\delta A_{\alpha\beta\gamma\delta}\, \Phi(1_a 0_{r'} 1_\rho).$$

Using the matrix elements[5] for the destruction and creation operators, we obtain

$$\sum_r A_{arra} + \sum_\rho A_{\rho\rho aa} + \sum_\rho A_{aapp} + \sum_\rho \sum_\sigma A_{\sigma\sigma\rho\rho} + \sum_\rho \sum_{r'} A_{\rho r' r' \rho}.$$

Subtracting the vacuum terms

$$\sum_\rho \sum_\sigma A_{\sigma\sigma\rho\rho} + \sum_\rho \sum_r A_{\rho rr\rho},$$

the self-energy of the electron in state a on the basis of the negative particle picture is

$$\sum_r A_{arra} + 2\sum_\rho A_{aapp} - \sum_\rho A_{appa} = \sum_n \pm A_{anna} + 2\sum_\rho A_{aapp},$$

where the upper or lower sign is to be taken for a positive or negative energy state, respectively. The first term represents an exchange term and diverges only logarithmically. The last term is the direct Coulomb energy of the electron in state a interacting with the sea of negative energy electrons and diverges quadratically. As mentioned above, the worst part of this divergence is removed by the process of symmetrization. On the basis of the alternate picture, we therefore calculate the expectation value

$$\Phi^*(0_\rho 0_a 1_{r'}) \sum_{(\alpha)(\beta)(\gamma)(\delta)} a_{(\alpha)}^+ a_{(\beta)} a_{(\gamma)}^+ a_{(\delta)} A_{(\alpha)(\beta)(\gamma)(\delta)} \Phi(0_{(\rho)} 0_{(a)} 1_{(r')}),$$

and obtain

$$\sum_{(r')}\sum_{(s')} A_{(r')(r')(s')(s')} + \sum_{(\rho)}\sum_{(r')} A_{(r')(\rho)(\rho)(r')} + \sum_{(r')} A_{(r')(a)(a)(r')}.$$

The vacuum term is

$$\sum_{(r)}\sum_{(s)} A_{(r)(r)(s)(s)} + \sum_{(r)}\sum_{(\rho)} A_{(r)(\rho)(\rho)(r)},$$

and the difference

$$\sum_{(r)} A_{(a)(r)(r)(a)} - \sum_{(\rho)} A_{(a)(\rho)(\rho)(a)} - 2\sum_{(r)} A_{(a)(a)(r)(r)} = \sum_{(n)} \pm A_{(a)(n)(n)(a)} - 2\sum_{(r)} A_{(a)(a)(r)(r)},$$

represents the self-energy of the electron in state a as calculated on the basis of the positive particle picture. The wave functions u_n and $u_{(n)}$ are identical for physical reasons, so that we may now drop the parentheses. Averaging the two results, we obtain

$$\sum_n \pm A_{anna} + \sum_n \mp A_{aann} = W_S + W_P. \quad (14)$$

The static term W_S is

$$W_S = \sum_n \pm A_{anna} = \tfrac{1}{2}\sum_n \pm \int\!\!\int d\mathbf{x} d\mathbf{x}'\, u_a^*(\mathbf{x}) u_n(\mathbf{x}) \times (e^2/|\mathbf{x}-\mathbf{x}'|) u_n^*(\mathbf{x}') u_a(\mathbf{x}'), \quad (15)$$

and by use of a Fourier representation for $1/|\mathbf{x}-\mathbf{x}'|$

$$\frac{1}{|\mathbf{x}-\mathbf{x}'|} = (1/2\pi^2)\int d\mathbf{k}\, \exp(i\mathbf{k}\cdot(\mathbf{x}-\mathbf{x}'))/\mathbf{k}^2, \quad (16)$$

may be written as

$$W_S = (e^2/4\pi^2)\int \frac{d\mathbf{k}}{k^2} \sum_n \pm \int d\mathbf{x} u_a^*(\mathbf{x}) \times \exp(i\mathbf{k}\cdot\mathbf{x}) u_n(\mathbf{x}) \int dx' u_n^*(\mathbf{x}') \times \exp(-i\mathbf{k}\cdot\mathbf{x}') u_a(\mathbf{x}'). \quad (17)$$

The polarization term $W_P(a)$

$$W_P(a) = \sum_n \mp A_{aann} = \frac{e^2}{2}\int d\mathbf{x} |u_a(\mathbf{x})|^2 \times \int \frac{d\mathbf{x}'}{|\mathbf{x}-\mathbf{x}'|} \sum_n \mp |u_n(\mathbf{x}')|^2, \quad (18)$$

may be written as

$$W_P(a)=\int d\mathbf{x}|u_a(\mathbf{x})|^2 ev(\mathbf{x}), \tag{19}$$

where the function $v(\mathbf{x})$ is the potential due to a charge density[7-9]

$$\rho(\mathbf{x})=(e/2)\sum_n \mp|u_n(\mathbf{x})|^2, \tag{20}$$

induced in the vacuum by the external electrostatic field. The energy W_P vanishes for a free electron.

The second-order electrodynamic self-energy $W_D(a)$ of the electron in state a, according to the electron picture, is given by the difference of the energy $W_D(1_a 0_r 1_\rho)$ for the electron in state a plus the vacuum electrons and the energy $W_D(0_r 1_\rho)$ of the vacuum electrons alone. The vacuum energy $W_D(0_r 1_\rho)$ is given by second-order perturbation theory, and involves the virtual emission and re-absorption of a light quantum of wave vector $\mathbf{k}$ and polarization type λ. There are two types of terms, represented by the following transition schemes:

$$\begin{pmatrix}\rho\to r+\mathbf{k}\\ r+\mathbf{k}\to\rho\end{pmatrix} \quad\text{and}\quad \begin{pmatrix}\rho\to\rho+\mathbf{k}\\ \sigma+\mathbf{k}\to\sigma\end{pmatrix}.$$

In the case of the energy $W_D(1_a 0_r 1_\rho)$, there are some additional transitions which the added electron can make, and some of the previously allowed transitions are prevented by the presence of the atomic electron in state a. One has then the following types of transitions:

$$\begin{pmatrix}\rho\to r'+\mathbf{k}\\ r'+\mathbf{k}\to\rho\end{pmatrix},\quad \begin{pmatrix}a\to r+\mathbf{k}\\ r+\mathbf{k}\to a\end{pmatrix},$$

$$\begin{pmatrix}\rho\to\rho+\mathbf{k}\\ \sigma+\mathbf{k}\to\sigma\end{pmatrix},\quad \begin{pmatrix}\rho\to\rho+\mathbf{k}\\ a+\mathbf{k}\to a\end{pmatrix},$$

$$\begin{pmatrix}a\to a+\mathbf{k}\\ \rho+\mathbf{k}\to\rho\end{pmatrix}.$$

The difference of the two corresponding energies is

$$-\int d\mathbf{k}\sum_{\lambda=1}^{2}\Big[\sum_r(|(r\mathbf{k}|\mathbf{H}_1|a)|^2/(E_r+\hbar ck-E_a))$$
$$-\sum_\rho(|(a\mathbf{k}|\mathbf{H}_1|\rho)|^2/(E_a+\hbar ck+E_a))$$
$$+2\sum_\rho((a|\mathbf{H}_1|a\mathbf{k})(\rho\mathbf{k}|\mathbf{H}_1|\rho)/\hbar ck)\Big],$$

which may be written as

$$-\int d\mathbf{k}\sum_{\lambda=1}^{2}\Big[\sum_n(\pm|(n\mathbf{k}|\mathbf{H}_1|a)|^2/$$
$$(|E_n|+\hbar ck\mp E_a))+2\sum_\rho((a|\mathbf{H}_1|a\mathbf{k})$$
$$\times(\rho\mathbf{k}|\mathbf{H}_1|\rho)/\hbar ck)\Big].$$

Symmetrization affects only the second term, and gives

$$W_D(a)=-\int d\mathbf{k}\sum_{\lambda=1}^{2}\sum_n$$
$$\times(\pm|(n\mathbf{k}|\mathbf{H}_1|a)|^2/(|E_n|+\hbar ck\mp E_a))$$
$$+\int d\mathbf{k}\sum_{\lambda=1}^{2}\sum_n$$
$$\times(\pm(a|\mathbf{H}_1|a\mathbf{k})(n\mathbf{k}|\mathbf{H}_1|n)/\hbar ck). \tag{21}$$

The last term can be written as

$$\int(d\mathbf{k}/k^2)\sum_{\lambda=1}^{2}\sum_n$$
$$\pm\int\int d\mathbf{x}d\mathbf{x}'u_a^*(\mathbf{x})\boldsymbol{\alpha}\cdot\mathbf{e}_{\mathbf{k}\lambda}u_a(\mathbf{x})$$
$$\times\exp(i\mathbf{k}\cdot(\mathbf{x}-\mathbf{x}'))u_n^*(\mathbf{x}')\boldsymbol{\alpha}\cdot\mathbf{e}_{\mathbf{k}\lambda}u_n(\mathbf{x}'),$$

which will be zero if the polarization current[7-9]

$$\mathbf{j}(\mathbf{x}')=e\sum_n\mp u_n^*(\mathbf{x}')\boldsymbol{\alpha}u_n(\mathbf{x}') \tag{22}$$

is zero. In the absence of an external vector potential, this current is in fact zero, so that the last term in Eq. (21) will henceforth be dropped. It should be noted that two physically different $\mathbf{k}$-spaces are involved in the expressions Eq. (17) and Eq. (21) for W_S and W_D.

[7] See reference 4, Eq. (40).
[8] E. A. Uehling, Phys. Rev. **48**, 55 (1935), W. Pauli and M. Rose, Phys. Rev. **49**, 462 (1936), and V. F. Weisskopf, Kgl. Danske Vid. Sels. Math.-Fys. Medd **14**, No. 6 (1936).
[9] R. Serber, Phys. Rev. **48**, 49 (1935).

III. COMPUTATION OF THE SELF-ENERGIES

We turn now to the evaluation of the expressions W_S, W_D, W_P for the self-energy. We shall pay particular attention to the static and dynamic terms W_S and W_D, as the polarization (Uehling) term W_P is directly related to the polarization charge density which has been computed by others.[7-9]

In the calculations to follow, relativistic units will be used throughout, in which $\hbar$, m, and c are taken equal to unity.

Our main interest, of course, is in the case of an electron moving in a Coulomb field for which $V=-e^2/r$. The integrals like

$$(n\mathbf{k}|\mathbf{H}_1|a)=-(ie/2\pi k^{\frac{1}{2}})\int d\mathbf{x}u_n^*(\mathbf{x})\boldsymbol{\alpha}\cdot\mathbf{e}_{\mathbf{k}\lambda}\times\exp(-i\mathbf{k}\cdot\mathbf{x})u_a(\mathbf{x})$$

occur in the theory of the relativistic photoelectric effect and have been studied extensively by Hall.[10] Because of their complexity, it seems hardly likely that we could perform the necessary further operations on them to evaluate such expressions as W_D. Even more must such a direct attack be ruled out for the case of an electron moving in a general potential field $V(\mathbf{x})$, for which the relativistic eigenfunctions $u_n(\mathbf{x})$ are not known. The only remaining method of approach seems to be to make an expansion of some kind. We observe that if the electron is free, the evaluation of the sums is a comparatively simple matter. Thus, if $u_a(\mathbf{x})$ is a plane wave of momentum $\mathbf{p}$, then

$$\int d\mathbf{x}u_n^*\boldsymbol{\alpha}\cdot\mathbf{e}\exp(-i\mathbf{k}\cdot\mathbf{x})u_a$$

is different from zero only if the momentum of the state n is $\mathbf{k}+\mathbf{p}$, and there are only four such states. In the case of a "weakly" bound electron, i.e., for

$$k\gg(a||\mathbf{p}||a),$$

one might expect that the matrix element above would have an appreciable value only when $|E_n|$ is of the order $E_k=+(1+k^2)^{\frac{1}{2}}$. We take advantage of this fact in the method of calculation used.

[10] H. Hall, Rev. Mod. Phys. 8, 358 (1936).

The sums over n can be performed, at least formally, by making use of the completeness of the solutions of the Dirac equation. Thus W_S can be written in the form

$$W_S=(e^2/4\pi^2)\int(d\mathbf{k}/k^2)\sum_n\int d\mathbf{x}u_a^*(\mathbf{x})\times\exp(i\mathbf{k}\cdot\mathbf{x})(H/|H|)u_n(\mathbf{x})\int d\mathbf{x}'u_n^*(\mathbf{x}')\times\exp(-i\mathbf{k}\cdot\mathbf{x}')u_a(\mathbf{x}'),\quad(23)$$

where

$$H=\boldsymbol{\alpha}\cdot\mathbf{p}+\beta+V\quad(24)$$

is the Hamiltonian of the unperturbed electronic motion, and $|H|$ the absolute value of the Hamiltonian, by which we mean an operator having the same eigenstates and spectrum as the Hamiltonian, except that its eigenvalues are taken to be positive. It can most conveniently be computed by representing it as $+(H^2)^{\frac{1}{2}}$. The equivalence of Eqs. (17) and (23) follows from the fact that $H/|H|$ is $+1$ when operating on a positive energy state and -1 when operating on a negative energy state. Using the completeness of the $u_n(\mathbf{x})$, we now find

$$W_S=(e^2/4\pi^2)\int(d\mathbf{k}/k^2)\int d\mathbf{x}u_a^*(\mathbf{x})\times\exp(i\mathbf{k}\cdot\mathbf{x})(H/|H|)\exp(-i\mathbf{k}\cdot\mathbf{x})u_a(\mathbf{x}),\quad(25)$$

so that the problem of computing W_S is reduced to that of finding the expectation value of the operator

$$(e^2/4\pi^2)\int(d\mathbf{k}/k^2)\times\exp(-i\mathbf{k}\cdot\mathbf{x})(H/|H|)\exp(+i\mathbf{k}\cdot\mathbf{x})$$

for the state a. We first note that for any polynomial function $f(\mathbf{p}, V)$

$$f(\mathbf{p}, V)\exp(+i\mathbf{k}\cdot\mathbf{x})u_a(\mathbf{x})=\exp(+i\mathbf{k}\cdot\mathbf{x})f(\mathbf{k}+\mathbf{p}, V)u_a(\mathbf{x}).$$

This theorem may then be used for any function $f(\mathbf{p}, V)$ such as $H/|H|$, for which a series expansion in $\mathbf{p}$ and V is valid. We therefore write

$$(H/|H|)\exp(i\mathbf{k}\cdot\mathbf{x})u_a(\mathbf{x})=\exp(i\mathbf{k}\cdot\mathbf{x})(H/|H|)_{\mathbf{k}+\mathbf{p}}u_a(\mathbf{x}),$$

where the notation

$$(\ )_{\mathbf{k}+\mathbf{p}}$$

means that the operator $\mathbf{p}$ is to be replaced by $\mathbf{k}+\mathbf{p}$ everywhere it appears within the brackets. One then has

$$W_S=(e^2/4\pi^2)\left(a\left|\int\frac{d\mathbf{k}}{k^2}(H/|H|)_{\mathbf{k}+\mathbf{p}}\right|a\right). \quad (26)$$

In an entirely similar manner, one can show that

$$W_D=-(e^2/4\pi^2)\left(a\left|\int(d\mathbf{k}/k)\sum_{\lambda=1}^{2}\boldsymbol{\alpha}\cdot\mathbf{e}_{\mathbf{k}\lambda}\right.\right.$$
$$\times\left\{\left(\frac{H}{|H|}+1\right)\Big/(|H|+k-E_a)\right.$$
$$\left.\left.+\left(\frac{H}{|H|}-1\right)\Big/(|H|+k+E_a)\right\}_{\mathbf{k}+\mathbf{p}}\boldsymbol{\alpha}\cdot\mathbf{e}_{\mathbf{k}\lambda}\right|a\right). \quad (27)$$

The evaluation of the terms W_S and W_D thus hinges on the expression of the operators

$$(1/|H|)_{\mathbf{k}+\mathbf{p}} \quad \text{and} \quad (1/(|H|+k\mp E_a))_{\mathbf{k}+\mathbf{p}}$$

in terms of operators whose expectation values can be readily obtained.

Turning now to this task, we write

$$\begin{aligned}(|H|)_{\mathbf{k}+\mathbf{p}}&=((H^2)^{\frac{1}{2}})_{\mathbf{k}+\mathbf{p}}=(((\boldsymbol{\alpha}\cdot\mathbf{p}+\beta+V)^2)^{\frac{1}{2}})_{\mathbf{k}+\mathbf{p}}\\&=((1+\mathbf{p}^2+\boldsymbol{\alpha}\cdot\mathbf{p}V+V\boldsymbol{\alpha}\cdot\mathbf{p}+2\beta V+V^2)^{\frac{1}{2}})_{\mathbf{k}+\mathbf{p}}\\&=(1+k^2+2\mathbf{k}\cdot\mathbf{p}+\mathbf{p}^2+2V(\boldsymbol{\alpha}\cdot\mathbf{k}+\boldsymbol{\alpha}\cdot\mathbf{p}+\beta)\\&\qquad+\boldsymbol{\alpha}\cdot\boldsymbol{\pi}V+V^2)^{\frac{1}{2}}, \quad (28)\end{aligned}$$

where $\boldsymbol{\pi}$ denotes an operator $\mathbf{p}$ which operates only on the quantity immediately following it (e.g., $\boldsymbol{\alpha}\cdot\mathbf{p}V=V\boldsymbol{\alpha}\cdot\mathbf{p}+\boldsymbol{\alpha}\cdot\boldsymbol{\pi}V$).

It is clear that the ratio of $(|H|)_{\mathbf{k}+\mathbf{p}}$ to $(1+k^2)^{\frac{1}{2}}$ approaches unity as k becomes large, which corresponds to our previous statement regarding the relationship between the magnitude of the matrix elements and the energy of the state n. Thus we expand

$$(1/|H|)_{\mathbf{k}+\mathbf{p}} \quad \text{and} \quad (1/|H|+k\mp E_a)_{\mathbf{k}+\mathbf{p}}$$

as follows:

$$\begin{aligned}(1/|H|)_{\mathbf{k}+\mathbf{p}}&=1/(E_k+\Delta_k)\\&=1/E_k-\Delta_k/E_k^2+\Delta_k^2/E_k^3-\cdots, \quad (29)\end{aligned}$$

$$\begin{aligned}(1/(|H|+k\mp E_a))_{\mathbf{k}+\mathbf{p}}&\\=1/(D_k^{\pm}+\Delta_k\mp w_a)&=1/D_k^{\pm}\\-(\Delta_k\mp w_a)/(D_k^{\pm})^2+\cdots, \quad (30)\end{aligned}$$

where

$$E_k=(1+k^2)^{\frac{1}{2}}, \quad (31)$$

$$\Delta_k=|H|-E_k, \quad (32)$$

$$D_k^{\pm}=E_k+k\mp1, \quad (33)$$

$$w_a=E_a-1. \quad (34)$$

It is, of course, also necessary to evaluate Δ_k by applying the binomial expansion

$$\begin{aligned}\Delta_k=|H|_{\mathbf{p}+\mathbf{k}}-E_k&=(E_k^2+\delta_{\mathbf{k}})^{\frac{1}{2}}-E_k\\&=\tfrac{1}{2}\delta_{\mathbf{k}}-\tfrac{1}{8}(\delta_{\mathbf{k}}^2/E_k)+\tfrac{1}{16}(\delta_{\mathbf{k}}^3/E_k^2)+\cdots, \quad (35)\end{aligned}$$

where

$$\begin{aligned}\delta_{\mathbf{k}}=2\mathbf{k}\cdot\mathbf{p}+\mathbf{p}^2+2V(\boldsymbol{\alpha}\cdot\mathbf{k}+\boldsymbol{\alpha}\cdot\mathbf{p}+\beta)\\+\boldsymbol{\alpha}\cdot\boldsymbol{\pi}V+V^2. \quad (36)\end{aligned}$$

All expansions indicated are to be carried to sufficiently high order so as to include all terms which are effectively of the fourth or lower order in v/c. The operator $\mathbf{p}$ is obviously of first order in v/c, V is of second order because of the virial theorem, while $\mathbf{k}$, β are of zeroth order. Since $\alpha_x^2=\alpha_y^2=\alpha_z^2=1$, $\boldsymbol{\alpha}$ must be regarded as a zero-order quantity until the expansion has been fully worked out.

The expansion of the operators in the manner indicated and the summation over the polarization direction $\lambda=1, 2$ is a straightforward but lengthy matter. This being completed, one is left with a sum of expectation values of various operators

$$\begin{aligned}&1, \beta, \boldsymbol{\alpha}\cdot\mathbf{p}, \beta\boldsymbol{\alpha}\cdot\mathbf{p}, \mathbf{p}^2, \beta\mathbf{p}^2, V, \beta V,\\&\boldsymbol{\sigma}\cdot\boldsymbol{\pi}V\times\mathbf{p}, \boldsymbol{\alpha}\cdot\boldsymbol{\pi}V, \beta\boldsymbol{\alpha}\cdot\boldsymbol{\pi}V, \boldsymbol{\pi}^2V, V\mathbf{p}^2, \mathbf{p}^2V, \boldsymbol{\pi}V\cdot\mathbf{p},\\&\mathbf{p}^4, \beta\mathbf{p}^4, V^2, \beta V^2, V\boldsymbol{\alpha}\cdot\mathbf{p}, \beta V\boldsymbol{\alpha}\cdot\mathbf{p},\\&\boldsymbol{\alpha}\cdot\mathbf{p}\mathbf{p}^2, w=E-1=\boldsymbol{\alpha}\cdot\mathbf{p}+\beta+V-1, w^2, \beta w,\end{aligned}$$

each multiplied by a combination of some fifty elementary integrals over k. The result of this calculation is given in Eq. (73) below. Before coming to it, we shall first discuss briefly the validity of the expansion used and the form in which the self-energy is expressed.

Assuming for the moment that $\mathbf{p}$ and V can be regarded as numbers less than unity (in relativistic units), then the expansions of

$$(1/|H|)_{\mathbf{k}+\mathbf{p}} \quad \text{and} \quad (1/(|H|+k+E_a))_{\mathbf{k}+\mathbf{p}},$$

(if carried far enough) are valid for all values of k, since E_k approaches unity and D_k^- approaches two as k goes to zero. On the other hand, D_k^+

approaches zero in this limit, so that one should examine the low k behavior for this case. It turns out that that part of

$$\Delta_k - w_a,$$

which does not approach zero as k approaches zero is of the order $(v/c)^2$. Therefore, in the term involving D_k^+ we shall carry our integrals down only to some intermediate wave number k_i, which, for convenience, we take to be of order $\alpha^{\frac{1}{2}}$. This term must then be given a separate treatment for the low k region $0 \lesssim k \lesssim k_i$. One would expect that the result is independent of the precise value of k_i, and this is indeed the case.

The assumption that $\mathbf{p}$ and V are always numbers less than unity is, of course, not valid. For example, in the case of the Coulomb field $V(\mathbf{x})$ becomes infinite at the origin. The region over which V is large, however, is small, so that the contribution to the expectation value from the region in which the expansion is invalid should be small. Again, in the case of the Coulomb field, $\mathbf{p}^2 u_a(\mathbf{x})$ becomes large compared to $u_a(\mathbf{x})$ for small $\mathbf{x}$. It should be observed that in the case of the Coulomb field this circumstance limits the expansion to the power of v/c here used, as the expected values of V^3, $\mathbf{p}^6$, $\pi^4 V$, etc., diverge for S states of the Coulomb field. Although the error introduced by this phenomenon is believed to be small, a numerical estimate would be desirable. We shall not, however, make such an estimate here, as the problem is a purely non-relativistic one.

In order to simplify the appearance and physical interpretation of our results, we have found it convenient to make use of various relationships between the expectation values of the Dirac operators which are valid to the order of v/c required. Thus one can write any solution of the Dirac equation as

$$u = \begin{pmatrix} \phi \\ \omega \end{pmatrix}, \tag{37}$$

where ϕ and ω are two-component wave functions satisfying

$$(\boldsymbol{\sigma}\cdot\mathbf{p}(1/(1+E-V))\boldsymbol{\sigma}\cdot\mathbf{p}+V+1-E)\phi=0, \tag{38}$$

$$\omega=(1/(1+E-V))\boldsymbol{\sigma}\cdot\mathbf{p}\phi, \tag{39}$$

so that for a positive energy state ω is of order v/c with respect to ϕ, which apart from terms of order $(v/c)^2$ is just a non-relativistic two-component Pauli-Schrödinger wave function. One can then see, for example, that

$$\begin{aligned}(a|\mathbf{p}^2-\beta\mathbf{p}^2|a) &= 2\int d\mathbf{x}((1/(1+E-V))\\ &\quad\times\boldsymbol{\sigma}\cdot\mathbf{p}\phi_a)^*\mathbf{p}^2(1/(1+E-V))\boldsymbol{\sigma}\cdot\mathbf{p}\phi_a\\ &\simeq\frac{1}{2}\int d\mathbf{x}\phi_a^*\mathbf{p}^4\phi_a\\ &\simeq\tfrac{1}{2}(a|\mathbf{p}^4|a),\end{aligned} \tag{40}$$

since $1-E$ and V are of order $(v/c)^2$, and $\int d\mathbf{x}\phi_a\mathbf{p}^4\phi_a$ and $(a|\mathbf{p}^4|a)$ differ only by a quantity of order $(v/c)^6$. One can therefore simplify the final result Eq. (73) by expressing all operators in terms of certain arbitrarily chosen ones which we have taken to be

$$\beta,\ \boldsymbol{\alpha}\cdot\mathbf{p},\ V,\ \pi^2 V,\ \beta\boldsymbol{\alpha}\cdot\boldsymbol{\pi}V,$$
$$V\mathbf{p}^2,\ \mathbf{p}^4,\text{ and } V^2.$$

Our reduction is obtained by using the following relations between expectation values

$$1\rightarrow\beta+\tfrac{1}{2}\boldsymbol{\alpha}\cdot\mathbf{p}-\tfrac{1}{8}\mathbf{p}^4+\tfrac{1}{4}\beta\boldsymbol{\alpha}\cdot\boldsymbol{\pi}V, \tag{41}$$

$$\mathbf{p}^2\rightarrow\boldsymbol{\alpha}\cdot\mathbf{p}+\tfrac{1}{2}\mathbf{p}^4+\tfrac{1}{2}\beta\boldsymbol{\alpha}\cdot\boldsymbol{\pi}V, \tag{42}$$

$$\mathbf{p}^2\rightarrow\boldsymbol{\alpha}\cdot\mathbf{p}+\tfrac{1}{2}\beta\boldsymbol{\alpha}\cdot\boldsymbol{\pi}V, \tag{43}$$

$$\beta V\rightarrow V-\tfrac{1}{2}V\mathbf{p}^2-\tfrac{1}{2}\beta\boldsymbol{\alpha}\cdot\boldsymbol{\pi}V, \tag{44}$$

$$\beta\boldsymbol{\alpha}\cdot\mathbf{p}\rightarrow 0, \tag{45}$$

$$\mathbf{p}^2 V\rightarrow V\mathbf{p}^2, \tag{46}$$

$$\boldsymbol{\pi}V\cdot\mathbf{p}\rightarrow-\tfrac{1}{2}\pi^2 V, \tag{47}$$

$$\boldsymbol{\alpha}\cdot\boldsymbol{\pi}V\rightarrow 0, \tag{48}$$

$$i\boldsymbol{\sigma}\cdot\boldsymbol{\pi}V\times\mathbf{p}\rightarrow\beta\boldsymbol{\alpha}\cdot\boldsymbol{\pi}V+\tfrac{1}{2}\pi^2 V, \tag{49}$$

$$V\boldsymbol{\alpha}\cdot\mathbf{p}\rightarrow V\mathbf{p}^2+\tfrac{1}{2}\beta\boldsymbol{\alpha}\cdot\boldsymbol{\pi}V, \tag{50}$$

$$\beta V\boldsymbol{\alpha}\cdot\mathbf{p}\rightarrow-\tfrac{1}{2}\beta\boldsymbol{\alpha}\cdot\boldsymbol{\pi}V, \tag{51}$$

$$\boldsymbol{\alpha}\cdot\mathbf{p}\mathbf{p}^2\rightarrow\mathbf{p}^4, \tag{52}$$

$$\beta\mathbf{p}^4\rightarrow\mathbf{p}^4, \tag{53}$$

$$\beta V^2\rightarrow V^2, \tag{54}$$

$$w=H-1\rightarrow\tfrac{1}{2}\boldsymbol{\alpha}\cdot\mathbf{p}+V+\tfrac{1}{8}\mathbf{p}^4-\tfrac{1}{4}\beta\boldsymbol{\alpha}\cdot\boldsymbol{\pi}V, \tag{55}$$

$$\beta w\rightarrow\tfrac{1}{2}\boldsymbol{\alpha}\cdot\mathbf{p}+V-\tfrac{1}{8}\mathbf{p}^4-\tfrac{1}{2}V\mathbf{p}^2-\tfrac{1}{4}\beta\boldsymbol{\alpha}\cdot\boldsymbol{\pi}V, \tag{56}$$

$$w^2\rightarrow\tfrac{1}{4}\mathbf{p}^4+V\mathbf{p}^2+V^2. \tag{57}$$

From these relations one finds that the total

contribution of the static and dynamic terms of the self-energy, apart from the low k contribution of the term involving D_k^+, is

$$(W_S+W_D)'=(\alpha/\pi)\left(a\left|\left(\frac{3}{2}\int_0^\infty (dk/E_k)+\tfrac{1}{4}\right)\beta\right.\right.$$
$$+\tfrac{1}{6}\boldsymbol{\alpha}\cdot\mathbf{p}+\tfrac{2}{3}\boldsymbol{\alpha}\cdot\mathbf{p}k_i+\tfrac{1}{4}\beta\boldsymbol{\alpha}\cdot\boldsymbol{\pi}V-(\tfrac{1}{3}\log(1/k_i)$$
$$\left.\left.-\tfrac{1}{3}\log 2+11/72)\pi^2 V\right|a\right). \quad (58)$$

In order to compute the low k contribution of the term involving D_k^+, it is convenient to take advantage of the essentially non-relativistic nature of this region and to make use of the previously discussed large and small component reduction Eq. (37). One then readily finds that the resultant expression has, to the order required, just the form of the non-relativistic self-energy, so that Bethe's[1] calculation may be used up to the frequency k_i. The contribution is

$$(\omega_{N.R.})_{k<k_i}$$
$$=(\alpha/\pi)(a|-\tfrac{2}{3}\mathbf{p}^2k_i-\tfrac{1}{3}(\log k_i/\bar{\epsilon})\pi^2V|a). \quad (59)$$

Adding the two, and observing that $(a|\mathbf{p}^2|a)$ is the same as $(a|\boldsymbol{\alpha}\cdot\mathbf{p}|a)$ to the order required, we find for the total contribution of W_S and W_D

$$W_S+W_D=(\alpha/\pi)\left(a\left|\left(\frac{3}{2}\int_0^\infty (dk/E_k)+\tfrac{1}{4}\right)\beta\right.\right.$$
$$+(\boldsymbol{\alpha}\cdot\mathbf{p}/6)+\tfrac{1}{4}\beta\boldsymbol{\alpha}\cdot\boldsymbol{\pi}V-\left(\tfrac{1}{3}\log\frac{1}{\bar{\epsilon}}\right.$$
$$\left.\left.\left.-\tfrac{1}{3}\log 2+11/72\right)\pi^2V\right|a\right), \quad (60)$$

and we note that the result is independent of the joining frequency k_i.

As previously mentioned, the direct Coulomb energy term can be expressed in terms of a polarization charge as follows:

$$W_P(a)=e\int d\mathbf{x}|u_a(\mathbf{x})|^2$$
$$\times\int d\mathbf{x}'\rho(\mathbf{x}')/|\mathbf{x}-\mathbf{x}'|, \quad (61)$$

where

$$\rho(\mathbf{x}')=(e/2)\sum_n \mp|u_n(\mathbf{x}')|^2 \quad (62)$$

is the induced charge density calculated by various authors. To the order required, this is found to be

$$\rho(\mathbf{x})=(e/6\pi^2)\nabla^2V\left(\tfrac{1}{6}+\int(k^2dk/E_k^3)\right)$$
$$+(e/60\pi^2)\nabla^4V, \quad (63)$$

from which one finds

$$W_P(a)=-(2e^2/3\pi)\left(\tfrac{1}{6}+\int(k^2dk/E_k^3)\right)$$
$$\times(a|V'|a)-(e^2/15\pi)(a|\nabla^2V|a). \quad (64)$$

The prime appearing on V' is used to indicate that the gauge of V' has been determined by the fact that it arises from an expression of the form

$$-1/4\pi\int d\mathbf{x}'\nabla^2V(\mathbf{x}')/|\mathbf{x}-\mathbf{x}'|. \quad (65)$$

We should like to point out that the expression for $\rho(\mathbf{x}')$ can be readily and neatly calculated by methods very similar to those used above in the case of the static and dynamic terms in the self-energy. To show this we first evaluate

$$\rho(\mathbf{x}',\mathbf{x}'')=-(e/2)\sum_n \pm u_n^*(\mathbf{x}')u_n(\mathbf{x}'')$$
$$=-(e/2)\sum_n u_n^*(\mathbf{x}')(H/|H|)u_n(\mathbf{x}'')$$
$$=-(e/2)\sum_n\sum_{\mu=1}^4\sum_{\nu=1}^4 (H/|H|)_{\mu\nu}$$
$$\times u_{n\mu}^*(\mathbf{x}')u_{n\nu}(\mathbf{x}''), \quad (66)$$

where the $u_{n\mu}$, $\mu=1,2,3,4$ are the components of u_n, and all operators in $H/|H|$ are to be taken with respect to $\mathbf{x}''$. Making use of the completeness relation

$$\sum_n u_{n\mu}^*(\mathbf{x}')u_{n\nu}(\mathbf{x}'')=\delta_{\mu\nu}\delta(\mathbf{x}'-\mathbf{x}''), \quad (67)$$

we obtain

$$\rho(\mathbf{x}',\mathbf{x}'')=-(e/2)\sum_\mu (H/|H|)_{\mu\mu}\delta(\mathbf{x}'-\mathbf{x}'')$$
$$=-(e/2)(\mathrm{Spur}H/|H|)_{\mathbf{x}''}\delta(\mathbf{x}'-\mathbf{x}''). \quad (68)$$

To evaluate this, we Fourier-analyze the delta-function

$$\delta(\mathbf{x}'-\mathbf{x}'')=(1/8\pi^3)\int d\mathbf{k}\exp(i\mathbf{k}\cdot(\mathbf{x}''-\mathbf{x}')), \quad (69)$$

TABLE I.

Quantity	State $2^2S_{1/2}$	$2^2P_{1/2}$	$2^2P_{3/2}$
$\nabla^2 V$	1	0	0
$i\beta\alpha\cdot\nabla V$	$-1/2$	1/6	$-1/12$

and find

$$\rho(\mathbf{x}', \mathbf{x}'') = (1/8\pi^3)\int d\mathbf{k}\exp(-i\mathbf{k}\cdot\mathbf{x}') \times(\mathrm{Spur}H/|H|)\exp(i\mathbf{k}\cdot\mathbf{x}''),$$

$$= (1/8\pi^3)\int d\mathbf{k}\exp(i\mathbf{k}\cdot(\mathbf{x}''-\mathbf{x}')) \times(\mathrm{Spur}H/|H|)_{\mathbf{k}+\mathbf{p}}\cdot 1(\mathbf{x}''), \quad (70)$$

when $1(\mathbf{x}'')$ is a constant equal to one. Since

$$\rho(\mathbf{x}') = \rho(\mathbf{x}', \mathbf{x}'), \quad (71)$$

we obtain, finally,

$$\rho(\mathbf{x}') = -(e/16\pi^3) \times\int d\mathbf{k}(\mathrm{Spur}H/|H|)_{\mathbf{k}+\mathbf{p}}\cdot 1(\mathbf{x}'). \quad (72)$$

The expression can now be readily reduced to the form Eq. (63) by expanding

$$(\mathrm{Spur}H/|H|)_{\mathbf{k}+\mathbf{p}}$$

in the manner used for the evaluation of the static and dynamic terms.

IV. INTERPRETATION OF RESULTS

The total expression for the self-energy is

$$W(a) = (\alpha/\pi)\left(a\left|\left(\frac{3}{2}\int(dk/E_k)+\tfrac{1}{4}\right)\beta - \left(\frac{2}{3}\int(k^2dk/E_k^3)+\tfrac{1}{9}\right)V' + (\boldsymbol{\alpha}\cdot\mathbf{p}/6) - (i/4)\beta\boldsymbol{\alpha}\cdot\nabla V + \left(\tfrac{1}{3}\log(1/\tilde{\epsilon}) - \tfrac{1}{3}\log 2 + (11/72) - (1/15)\right)\nabla^2 V\right|a\right), \quad (73)$$

where we have made use of the fact that $\boldsymbol{\pi} = -i\nabla$. We observe first of all that the worst divergence is logarithmic, and that the expression is invariant to the gauge of V.

We next see that the difference of the self-energies of the states $2^2S_{\frac{1}{2}}$ and $2^2P_{\frac{1}{2}}$ of the hydrogen atom does converge, since the expectation values of β, V', (and, therefore, $\boldsymbol{\alpha}\cdot\mathbf{p}$) are, respectively, equal for the two states. (These statements follow from the observation that neither a small change of charge nor mass of the electron will remove the degeneracy.) In order to calculate the numerical difference of $W(a)$ for the two states, we need the values of the expectation values of the remaining operators in Eq. (73). These are given in Table I[11] in units of $\alpha^2 Ry$. The energy difference is then

$$\Delta W = (\alpha^3 Ry/3\pi)[\log(1/\tilde{\epsilon}) - \log 2 + (23/24) - \tfrac{1}{8}], \quad (74)$$

which, using Bethe's revised values[12] for the constants $[(\alpha^3 Ry/3\pi) = 135.580$ Mc/sec., $\log(1/\tilde{\epsilon}) = 7.7169 - 0.0293]$, gives $\Delta W = 1052$ Mc/sec., and thus differs from the original guess by only a small amount. It should be admitted, however, that one cannot regard this energy difference as uniquely determined, since one is taking the difference of two infinite quantities.

With respect to the determination of the absolute value of the self-energy for a state, it is convenient to attempt a physical interpretation of the terms involved. In this context, it should be observed that even if the coefficients of the V' and β-terms were finite, the effect of these terms would be unobservable. This follows from the fact that they would manifest themselves as a

[11] It should be mentioned here that the expected value of $\nabla^2 V$ really diverges for the S states of the Coulomb field, since it then is equal to the square of the absolute value of the wave function at the origin. Since, however, our evaluation is being carried only to order $(v/c)^4$, one should be able to use the spatial dependence of the Schrödinger wave functions for the evaluation of operators which are themselves of fourth order. Thus, where Dirac wave functions are used, the divergent part is of higher order in v/c, and its neglect is consistent with the neglect of such divergent expressions as the expected value of p^6. If one rounds off the Coulomb potential at a radius considerably smaller than the classical electron radius, the contribution of the divergent part of $(S|\nabla^2 V|S)$ is still quite negligible. (If the charge is assumed to be evenly distributed over a sphere of radius a, then the ratio of the expected value of $\nabla^2 V$ for a Dirac S state to that for a Schrödinger S state is of the order $a^{-\alpha^2}\sim 1-\alpha^2\log a$.)

[12] H. A. Bethe, Pocono Conference, 1948.

modification in the real charge and mass of the electron, and thus be included in the observed charge and mass. We shall assume that these terms have been so included in the observed charge and mass and drop them from the self-energy expression. The term in $i\beta\boldsymbol{\alpha}\cdot\boldsymbol{\nabla}V$ is just of the form of the interaction of a Pauli-type intrinsic magnetic moment with a static potential V and can thus be interpreted as implying an additional electronic magnetic moment of $\alpha/2\pi$-Bohr magentons, while the term ∇^2V implies a correction to the external potential, or, more specifically, an additional short-range interaction between the electron and a point charge. The term in $\boldsymbol{\alpha}\cdot\mathbf{p}$ is not subject to a direct physical interpretation, and, in fact, must be regarded as having no physical significance. Thus if one applies the self-energy expression (73) (with the β- and V' terms omitted as explained above) to a free electron of momentum $\mathbf{p}$, only the term in $\boldsymbol{\alpha}\cdot\mathbf{p}$ contributes, yielding for the self-energy $(\alpha/\sigma\pi)[\mathbf{p}^2/(1+\mathbf{p}^2)^{\frac{1}{2}}]$. Now if the electron is to be regarded as a particle, the relativistic connection between the momentum and energy of a particle must be retained, so that the self-energy should have the momentum dependence appropriate to a mass correction, that is[13] $\sim 1/(1+\mathbf{p}^2)^{\frac{1}{2}}$ corresponding to the term in β already subtracted. The presence of the non-covariant term $(\alpha/\sigma\pi)[\mathbf{p}^2/(1+\mathbf{p}^2)^{\frac{1}{2}}]$, which is reminiscent of the stress terms in the classical self-energy, can be traced to the fact that the total self-energy is infinite, and can be avoided in the case of the free electron by paying proper attention to the domains of integration in the various $\mathbf{k}$-spaces.[14] That is, in order to keep the total self-energy finite it is necessary to integrate over a finite region of the light quantum space and the electron momentum space. If one integrates over a region which would be spherical for an electron at rest, a covariant result is obtained. One cannot, however, apply this prescription to a bound electron, so that some other means of modifying our self-energy expression must be found to give a covariant expression for the free electron. We proceed by subtracting some free electron operator from the operators contained in our self-energy expression such that the self-energy of a free electron is zero, thereby regarding the total self-energy as contained in the observed mass.

Such a procedure is, of course, not unique: we shall make the simplest subtraction, examine the resultant expression, and then investigate the nature of the lack of uniqueness. Thus if one simply drops the $(\alpha/\sigma\pi)\boldsymbol{\alpha}\cdot\mathbf{p}$ term from the self-energy, one obtains

$$W(a)=(\alpha/\pi)(a|-i\beta\boldsymbol{\alpha}\cdot\boldsymbol{\nabla}V/4+\Big(\tfrac{1}{3}\log(1/2\bar{\epsilon})+(11/72)-(1/15)\Big)\nabla^2V|a). \quad (75)$$

This expression can be interpreted as arising from an increase in the magnetic moment of the electron of $\alpha/2\pi$-Bohr magnetons and an additional interaction potential given by

$$\delta V_{\text{eff}}=\Big(\tfrac{1}{3}\log(1/2\bar{\epsilon})+(11/72)-(1/15)\Big)\nabla^2V. \quad (76)$$

These contribute 68 and 984 Mc/sec., respectively, to the level shift.

In accordance with our subtraction prescription we could, however, add any linear combination of free electron operators of order up to $(v/c)^4$ whose expectation value is zero for the free electron. There are seven such operators,[15] *viz.*, 1, β, $\mathbf{p}^2$, $\beta\mathbf{p}^2$, $\boldsymbol{\alpha}\cdot\mathbf{p}$, $\mathbf{p}^4$, $\beta\mathbf{p}^4$. The condition that a linear combination gives zero to order constitutes three constraints, so that there should be four linearly independent combinations giving zero for the free electron. A possible choice for these is the following:

$$\Omega_a=1-\beta-\tfrac{1}{2}\mathbf{p}^2-\boldsymbol{\alpha}\cdot\mathbf{p}+\beta\mathbf{p}^2+\tfrac{3}{8}\mathbf{p}^4, \quad (76a)$$

$$\Omega_b=\mathbf{p}^2-\beta\mathbf{p}^2-\tfrac{1}{2}\mathbf{p}^4, \quad (76b)$$

$$\Omega_c=\mathbf{p}^4-\beta\mathbf{p}^4, \quad (76c)$$

$$\Omega_d=\boldsymbol{\alpha}\cdot\mathbf{p}-\beta\mathbf{p}^2. \quad (76d)$$

The expectation values of the above combinations are all zero for the free electron. Their effect upon the self-energy of a bound electron depends upon their expectation values for a

[13] The energy of a particle of mass m and momentum p is $(m^2+\mathbf{p}^2)^{\frac{1}{2}}$. If m is modified by a quantity δm, then the energy to first order in δm is

$$(m^2+\mathbf{p}^2)^{\frac{1}{2}}+\delta m/(m^2+\mathbf{p}^2)^{\frac{1}{2}},$$

and the correction term with $m=1$, as is appropriate for the electron, is of the form given.

[14] A. Pais, Verh. d. K. Ned. Akad. v. Wet, Section 1, 19, No. 1 (1947).

[15] Operators of odd order in v/c have been ignored, as these are all zero for the bound electron.

bound electron. Those for Ω_a, Ω_b, and Ω_c are zero, so that their subtraction would have no physical consequences. On the other hand,

$$(a|\Omega_d|a) = -i(a|\beta\alpha\cdot\nabla V|a)/2, \qquad (77)$$

which is precisely the form of interaction of a magnetic moment with a static potential V. Thus, the lack of uniqueness of the subtraction prescription is just such as to make the magnetic moment correction indeterminate, while the correction to the potential is left uniquely determined. Now a purely magnetic measurement of the correction to the magnetic moment of the electron has been made by Kusch and Foley,[16] who obtain a value in good agreement with the value $\alpha/2\pi$-Bohr magnetons theoretically computed by Schwinger.[17] If we adopt this experimental and theoretical result, the $2^2S_{\frac{1}{2}}-2^2P_{\frac{1}{2}}$ separation becomes uniquely determined to be just the value 1052 Mc/sec. obtained above by a direct subtraction (74) of the self-energies for the two states.

[16] P. Kusch and H. M. Foley, Phys. Rev. **74**, 250 (1948), also J. E. Nafe and E. B. Nelson, Phys. Rev. **73**, 718 (1948).
[17] J. Schwinger, Phys. Rev. **73**, 416 (1948) and Pocono Conference, 1948.

PHYSICAL REVIEW VOLUME 75, NUMBER 3 FEBRUARY 1, 1949

Study of Phase Transitions by Means of Nuclear Magnetic Resonance Phenomena*

NELSON L. ALPERT**
Research Laboratory of Electronics, Massachusetts Institute of Technology, Cambridge, Massachusetts
(Received October 11, 1948)

Although the nuclear magnetic resonance condition generally depends only on the gyromagnetic ratio of the resonating nuclei, the width and amplitude of the resonance depend critically on the substance containing the resonating nuclei. A basic factor affecting the line width is the characteristic flipping time for the substance, i.e., the average time it takes a molecule to change its orientation appreciably. This fact has been applied in a study of a group of molecular solids which exhibit two or more phases in order to investigate the mechanisms of these transitions. Of the two mechanisms proposed, rotational and order-disorder, the former was eliminated in favor of the latter for HCl, HBr, HI, H_2S, and H_2Se, while free molecular rotation is shown to be plausible in CH_4 and CH_3D.

I. INTRODUCTION

THE first successful detection of radiofrequency transitions between Zeeman levels of nuclei in liquids and solids was announced by Purcell, Torrey, and Pound[1] and by Bloch, Hansen, and Packard[2] in 1946. It became apparent early in these investigations that the characteristics of a nuclear magnetic resonance depend directly on the material in which the resonating nuclei reside. This, coupled with the fact that the ratio of resonant frequency to magnetic field is a linear function of the nuclear g-factor, indicated three lines of research:

(a) The accurate measurement of nuclear g-factors.[3]

(b) An investigation of the interactions which affect the resonance characteristics, i.e., nuclear relaxation processes.[4]

(c) Study of internal properties of solids and liquids by means of nuclear magnetic resonance phenomena.[5–9] It is one phase of the last of these

* This research was supported in part by the Signal Corps, the Air Materiel Command, and the Office of Naval Research. The report given here is a condensation of a thesis submitted in partial fulfillment of the requirements for the degree of Doctor of Philosophy at the Massachusetts Institute of Technology, 1948.
** Now at Rutgers University, New Brunswick, New Jersey.
[1] E. M. Purcell, H. C. Torrey, and R. V. Pound, Phys. Rev. 69, 37 (1946).
[2] F. Bloch, W. W. Hansen, and M. Packard, Phys. Rev. 69, 127 (1946). F. Bloch, W. W. Hansen, and M. Packard, Phys. Rev. 70, 474 (1946).
[3] F. Bitter, N. L. Alpert, D. E. Nagle, and H. L. Poss, Phys. Rev. 72, 1271 (1947).
[4] N. Bloembergen, E. M. Purcell, and R. V. Pound, Phys. Rev. 73, 679 (1948), hereafter to be referred to as B.P.P.
[5] F. Bitter, N. L. Alpert, H. L. Poss, C. G. Lehr, and S. T. Lin, Phys. Rev. 71, 738 (1947).
[6] B. V. Rollin, Nature 158, 669 (1946).
[7] B. V. Rollin and J. Hatton, Nature 159, 201 (1947).

lines of research with which this investigation is chiefly concerned.

If a substance containing magnetic nuclei of magnetic moment μ and angular momentum $I\hbar$ is placed in a z-directed magnetic field, H_0, there will result a nuclear paramagnetism which may be found from Curie's law:

$$M_0 = N(g\mu_n)^2 I(I+DH_0)/3kT, \qquad (1)$$

where M_0 is the static magnetization, N the number of nuclei/cc, g the nuclear g-factor, μ_n the nuclear magneton, I the nuclear angular momentum in units of $h/2\pi$, k the Boltzmann factor, and T the absolute temperature. Now if a radio-frequency field is introduced in the $x-y$ plane with the Larmor frequency,

$$\nu_0 = \mu H_0/I\hbar \quad \text{or} \quad \omega_0 = \gamma H_0, \qquad (2)$$

where $\gamma = \mu/I\hbar$, a resonant absorption and dispersion will occur. For diamagnetic materials the ratio of ν_0 to H_0 generally depends only on the magnetic moment and angular momentum of the nuclei concerned, and the peak absorption will be found at the same resonance condition for the same nuclei, regardless of the material in which the nuclei reside. The width and magnitude of the nuclear magnetic resonance, however, are found to depend critically on the substance containing the resonating nuclei. More specifically, these properties are found to depend on two modes of interaction affecting the nuclei: (a) The interaction between the nuclei and the lattice containing them, expressed in terms of the spin-lattice or thermal relaxation time, T_1. It is the resultant interchange of energy which enables the nuclear system to attain thermal equilibrium at a temperature T and to attempt to maintain this equilibrium upon exposure to resonance radiation. (b) The magnetic interaction between the nuclei, which is expressed in terms of a spin-spin relaxation time, T_2. This effect manifests itself primarily in a broadening of the resonance line width. The experiments described below are chiefly concerned with this latter mode of interaction.

If a resonating nucleus is surrounded by magnetic nuclei there will be superimposed on H_0 a local magnetic field H_{loc}, which may be of the order of several gauss. The resonant condition is then $\omega_0 = \gamma(H_0 + H_{loc})$. Since H_{loc} depends on the orientations and positions of all neighbors, the result is a dispersion of the magnetic fields at the various nuclei about the applied H_0, the average field at the nuclei still being H_0. From the resultant broadening in the energy levels, $\Delta E = \hbar\gamma H_{loc}$, we may define a time T_2 on the basis of the uncertainty principle of quantum mechanics: $T_2 = \hbar/\Delta E = 1/|\gamma| H_{loc}$. It should be noted that H_{loc} represents a deviation of the magnetic field from an average H_0. Therefore, gradients in the magnetic field caused by magnetic field inhomogeneities serve also to broaden the line.***

Since the internuclear fields are expected to be of the order of a few gauss or more in magnitude, most solids fit well with this extremely elementary picture, giving resonance line widths of a few gauss or more. That this picture on the basis of a rigid lattice is inadequate becomes particularly obvious in the case of most liquids and gases and a few solids, where line widths of a small fraction of a gauss are found. The key to these narrower lines may be seen from the fact that no mode of spin-lattice relaxation is possible in the rigid lattice so far considered. A generally useful and satisfactory theory of both spin-lattice and spin-spin interactions has been developed by B.P.P.[4] On the basis of general lattice motion they derive fairly accurate values for T_1 and explain details of line narrowing.

Qualitatively, the resonance line width is reduced by an averaging out of the internuclear fields resulting from the lattice motion. This is particularly obvious in the extreme case of a nucleus residing in a freely rotating molecule, since rotational periods are much smaller than times associated with the nuclear resonance. In most cases of interest all orientations of the molecule are equally probable. As a consequence the internuclear fields essentially average out to zero, so that an extremely narrow line results. Actually, in the case of water a line width of 10^{-4} gauss is predicted. In practice it is impossible to observe this "true" line width since it would require, at a working field of 7000 gauss, a homo-

[8] B. V. Rollin, J. Hatton, A. H. Cooke, and R. J. Benzie, Nature 160, 437 (1947).
[9] G. E. Pake, J. Chem. Phys. 16, 327 (1948).

*** There are other factors which may contribute to the line width but which do not enter into the cases under study. A more complete discussion of this matter may be found in reference 4.

geneity of almost one part in 10^8 over the sample. Thus the line width in most liquids is determined entirely by the homogeneity of the magnet.

The theory referred to above approximates its description of the lattice motion by means of a single parameter τ_c. This so-called correlation time (or "flipping" time) is essentially the average time it takes for a molecule to change its position or orientation appreciably. This is very closely related, through a factor of the order of one, to the "characteristic relaxation time" introduced by Debye in his theory of polar molecules.[10] The effect of τ_c on T_2 and on the line width may be seen as follows:

Let us denote by T_2'' the spin-spin relaxation time in the limiting case of the rigid lattice. Thus, for this case, T_2'' represents the average lifetime of a nucleus in a particular energy state (or orientation). Now if $\tau_c \gg T_2''$, the slow variation of the internuclear fields during the "lifetime" of a nuclear orientation will have a negligible effect on the spin-spin interaction. Therefore we have

$$\textit{Case I:}\quad \tau_c \gg T_2''. \qquad T_2 = T_2'', \quad \Delta H = 1/\gamma T_2''. \tag{3a}$$

If, on the contrary, $\tau_c \ll T_2''$, considerable averaging out of the internuclear fields occurs during a normal nuclear level "lifetime." As a result the spin-spin interaction is greatly reduced, and the relaxation time increased accordingly. In this case it may be shown that, in general, the relaxation time varies inversely as the correlation time.

$$\textit{Case II:}\quad \tau_c \ll T_2''. \qquad T_2 \propto (1/\tau_c), \quad \Delta H \propto \tau_c. \tag{3b}$$

Thus it becomes apparent that the line width is a sensitive function of the correlation time.

On the basis of a simplified calculation, by taking into account the effect of only the nearest neighbor of a resonating nucleus, B.P.P. find for T_2 the relation:

$$(1/T_2)^2 = K \tan^{-1}(2\tau_c/T_2), \tag{4}$$

where K is a constant which includes the internuclear distance and other constants which are independent of frequency and of temperature. This has the properties discussed above. Namely, for $\tau_c \gg T_2$, $T_2 = (2/\pi K)^{\frac{1}{2}}$, which may be shown to be equal to T_2'', while for $\tau_c \ll T_2$, we find $T_2 = 1/2K\tau_c$. The form of a plot of $\log T_2$ *vs.* $\log \tau_c$ is immediately apparent. This is made up of two predominant portions, a horizontal line for $\tau_c \gg T_2''$ and a line whose slope is -1 for $\tau_c \ll T_2''$. If one reasons that the correlation time loses its "control" of T_2 when it reaches a value equal to T_2, one finds that the break between the horizontal and sloping part of this graph occurs near $\tau_c = T_2''/2^{\frac{1}{2}}$. Very little accuracy is lost if we approximate this plot by two straight lines, one horizontal and the other with slope -1, intersecting at $\tau_c = T_2''/2^{\frac{1}{2}}$.

Another factor which affects T_2 is the spin-lattice relaxation time. It may be seen that if the motion of the lattice transporting the nuclei has frequency components near ν_0, this motion is capable of inducing transitions between Zeeman levels. Although this picture is oversimplified, it indicates essentially the means of energy transfer between the lattice and the nuclei. T_1 is found to be $1/2W$, where W is the probability of an induced transition. Now if T_1 is comparable to T_2, the former will also serve to limit the lifetime of a nucleus in a particular state. Thus T_1 may also contribute to the line width. However, under the conditions of the experiments, one of two situations generally exists. Either $T_1 \gg T_2$, which is usually the case for broad lines, or $T_1 \cong T_2$ for the sample, and both are in the range of 0.01 second to several seconds. In the former case T_1 has no effect on the line width, while in the latter case the line width is determined by the homogeneity of the magnetic field, and T_1 does not influence the experimentally observed line widths for small r-f fields.

II. PHASE TRANSITIONS IN SOLIDS

Many solids undergo drastic changes in their physical properties at critical temperatures. Such transitions may be placed in one of two categories. The so-called first-order transitions occur at one particular temperature and are accompanied by a latent heat, usually as a result of a change in crystal symmetry. In contrast, second-order transitions are identified by λ-points with an anomalously high specific heat over the transition temperature range, generally of the order of a few degrees Kelvin. One class of solids

[10] P. Debye, *Polar Molecules* (Dover Publications, New York, 1945), reprinted.

showing second-order transitions is alloys. The order-disorder phenomenon responsible for the transitions in these substances is well understood. However, there is a large class of substances, including many molecular solids, which show second-order transitions whose mechanisms are not completely understood. These transitions may possibly be explained in terms of a change in molecular activity. It is this factor which points out the potentialities of studying this group of solids by the nuclear magnetic resonance experiment, since it has been shown that internal activity has a profound effect on the properties of the resonance. For the sake of completeness it should be noted that a few first-order transitions—e.g., in HCl—should also be of interest in any such investigation.

There are two conflicting theories to explain the transitions in question. One theory, put forward by Pauling[11] and Fowler,[12,13] associates the transition temperature with a change from rotational oscillation of the molecules or ionic groups below the critical temperature to a phase in which most of the molecules are freely rotating. The existence of λ-point transitions may be derived by statistical mechanics by assuming the rotation to be a cooperative phenomenon. That is, one considers that the rotation of a molecule is not independent of the motions of its neighbors and that the potential against rotation is a function of the degree to which its neighbors are rotating.

The second theory, developed by Frenkel[14] and Landau,[15] assumes that the transition is from an ordered to a disordered state. In this theory there is assumed a preferred orientation, occupied by a majority of the molecules, below the transition, while above the transition the molecules occupy with equal probability one of two, or more, equilibrium orientations. It should be noted that both below and above the transition the molecules flip between equilibrium orientations. The distinguishing factor between the ordered and disordered phases is that the molecules predominate in a preferred orientation in the ordered phase; however, in the disordered phase a preferred orientation ceases to exist.

It is quite possible that either of these mechanisms may be responsible in different cases.

Since the line width of the nuclear resonance depends on the average reorientation time of the molecule through τ_c, we see that it is potentially possible to gain information about these transitions and their associated mechanisms by means of a nuclear resonance in the substance in question. Let us now investigate the order of magnitude of the quantities involved, so as to determine what effect these mechanisms may be expected to have on the line width.

In general we should expect the line width in the rigid lattice to be three gauss or more. Since the gyromagnetic ratio γ is about 2.7×10^4 for protons, this indicates that T_2'' should be less than 12 microseconds. Now, as indicated in Section I, the line width is controlled by the molecular flipping time when τ_c is less than $T_2''/2^{\frac{1}{2}}$. Thus the line width is generally sensitive to τ_c for values of τ_c smaller than 8 microseconds. At 7000 gauss the limit of homogeneity of the magnet used during these experiments was roughly 0.2 gauss. Therefore the lowest values of τ_c which can be derived from line-width measurements would be in the range 0.05 to 0.5 microsecond.

We may obtain an idea of expected values of τ_c from Debye's *Polar Molecules*.[16] For liquid normal propyl alcohol he lists values from 26×10^{-10} second at -60°C to 0.9×10^{-10} second at $+20$°C for the characteristic reorientation time defined in his theory. Also, we should expect the reorientation time for the case of a free rotation in a solid to be of the order of a rotational period: 10^{-13} second or less. Therefore, it would be expected that, for rotating molecules in a solid, characteristic times of at most 10^{-10} second would be found.

Ice may be considered as an example of a solid with non-rotating molecules. A fairly rapid motion occurs at temperatures just below the freezing point, but the activity decreases quite rapidly as the temperature is decreased. From experiments on the dielectric constant of ice at radio-frequencies Debye gives values of 2.7 micro-

[11] L. Pauling, Phys. Rev. **36**, 430 (1930).
[12] R. H. Fowler, Proc. Roy. Soc. London **A149**, 1 (1935).
[13] R. H. Fowler, *Statistical Mechanics* (The Macmillan Company, New York, 1936), second edition, Ch. 21.
[14] J. Frenkel, *Kinetic Theory of Liquids* (Oxford University Press, London, 1946), Ch. 2.
[15] L. Landau, Physik. Zeits. Sowjetunion **11**, 26, 545 (1937).
[16] Reference 10, p. 108.

seconds at -5°C and 18 microseconds at -22°C for the reorientation time as defined in his development. Undoubtedly a considerable variation in these values would occur for different substances, but the above would lead us to expect values in the microsecond range. It should be noted that this range is precisely that in which the line width is effective in measuring τ_c.

The marked difference between the values of τ_c for rotation and non-rotation, a factor of at least 10^4, should be carefully noted. In addition, it is important that in the case of non-rotation τ_c may possibly fall in a range in which it directly affects the observed line width, while for rotation τ_c is so small that the observed line width must, in all practical cases, be only as narrow as the homogeneity of the magnet permits.

The expected effect of phase transitions on line widths may now be discussed on the basis of the expected values of T_2'' and τ_c. For the case of a rotational transformation, the line should be broad, typical of most solids, below the transition; upon reaching the transition, where free rotation becomes predominant, one should expect a rapid decrease, over the range of the transition, to a narrow line limited in width by magnet inhomogeneity.

The picture in the case of an order-disorder transition is not so clear cut, since there may be *little or no change* in τ_c at such a transition. Even in this case there may be some sharp change in the line width at the transition temperature, since the critical temperature is frequently accompanied by a change in lattice constants or in crystal structure. The crystal structure generally becomes more symmetrical in the highest temperature phase. This would result in a change in T_2'' even if τ_c does not decrease to the range in which it affects T_2. A discontinuous decrease of τ_c at the transition may, of course, contribute to a change in line width. In any case one might expect a decrease of τ_c with increasing temperature, which may or may not reveal itself in the line-width measurements. As Frenkel points out,[14] τ_c should be a function of the type

$$\tau_c = \tau_{c0} \exp(U/kT), \qquad (5)$$

where τ_{c0} is the period of the rotational oscillations which would occur under the influence of the local electric field and U is the activation energy required to reorient a small group of molecules. Of course U itself may be a complicated function of the temperature T.

To summarize, if a moderate change, or zero change, in line width occurs at the transition, this must be identified with the order-disorder mechanism. On the contrary, if a rapid change to a very narrow line occurs at the transition, the rotational transformation mechanism may be indicated. However, the order-disorder mechanism is not completely ruled out on the basis of this evidence alone.

A third mechanism which applies to a few cases, for example, rochelle salt, is the so-called displacive transition. In this case the unit cell of the crystal suffers a small distortion during which a new symmetry element appears or disappears. Although this type of transition has not yet been studied experimentally by the method proposed here, it is expected that this would show very little effect on the nuclear resonance line width.

Essentially complete lists of substances which exhibit phase transitions may be found in review articles by Eucken[17] and by Smyth.[18] As one would expect on the basis of the mechanisms introduced to explain the transitions, these transitions are found primarily in substances composed of light molecules or of internal groups which would have low moment of inertia.

Pauling[11] proves that for the hydrogen molecule and the methane molecule the eigenfunctions and energy levels, even in the lowest quantum state, closely approximate those for a freely rotating molecule. The case of hydrogen has recently been studied by Rollin and collaborators[8] by the nuclear resonance method. Other substances which show transitions include: the hydrogen halides, except for the lightest member of the group, HF; the H_2X group, with the exception of the lightest member, H_2O; the XH_3 group, also except for the lightest member, NH_3; a number of ammonium salts, including the ammonium halides; and a multitude of organic molecules.

---

[17] A. Eucken, Zeits. f. Elektrochemie **45**, 126 (1939).
[18] C. P. Smyth, Chem. Rev. **19**, 329 (1936).

III. APPARATUS AND CRYOGENY

The circuit used is essentially the one described by B.P.P. The water-cooled electromagnet used for most of these experiments was designed by F. Bitter and constructed in the Research Laboratory of Electronics shop. The magnet is fitted with detachable pole pieces eight inches in diameter and a gap of $2\frac{1}{4}$ inches. The pole faces are shimmed to minimize field gradients at the center of the gap. To satisfy the demands of current constancy—one part in 10^5 or better—the magnet was usually run from a bank of submarine storage batteries. The d.c. field is generally modulated at 60 or 30 cycles through the use of separately wound inner layers of the magnet coils.

A General-Radio 605-B signal generator was used in most of the experiments. In order to minimize unwanted frequency and amplitude modulation on the r-f carrier, the power supply of the r-f generator was replaced by a well-filtered and regulated d.c. power supply. Most of the experiments were carried out at 30 Mc in a magnetic field of about 7000 gauss. Narrow and intense resonances were most easily displayed on an oscilloscope, using a magnetic-field sweep several times the line width. For less intense resonances the sweep was reduced to a small fraction of a line width and final amplification was obtained by means of a 30-cycle, twin-T, narrow-band amplifier with a lock-in feature.[19] The output of this instrument is proportional to the slope of the resonance curve. In this case the absorption component of the resonance is more generally used, and the width measured is the distance between the inflection points, i.e., between the peak deflections of the output meter. If one assumes a line shape resembling a universal resonance curve, as results from Bloch's development,[20] for example, the above definition of line width is $3^{\frac{1}{2}}$ times the distance between half-value points, which is normally defined as the line width.†

The temperatures which must be obtained in order to study practically all of the phase transitions of interest fall in the range from about 20°K to room temperature. Preliminary low temperature experiments were carried on in the $9\frac{1}{2}$-inch gap between the unshimmed poles of the M.I.T. cyclotron magnet. These experiments were carried on in glass Dewars with appropriate liquid baths as the low temperature reservoir. In many cases the liquid had to be discarded just before making observations for one of two reasons: (a) Proton-containing liquids around the r-f coil gave appreciable signals. (b) A boiling effect, due to the lack of complete rigidity in the r-f coil, caused a large increase in background noise. Also, by removing the liquid and allowing the temperature to drift upward, it was possible to cover any temperature range desired. However, these methods were not generally suitable for quantitative measurements because: (a) The bridge balance was very sensitive to small changes in temperatures. (b) The continuous drift in temperature left the temperature and thermal equilibrium of the sample very much in doubt, particularly in regions of high specific heats in the vicinity of phase transitions.

The above work indicated the requirements on the cryostat used for most of the quantitative work. This was designed to fit in a glass Dewar specially made for use in the small electromagnet. This Dewar is narrow at the bottom in order to fit conveniently in the gap, and flares out at the top in order to provide a greater volume for a liquid reservoir.

The cryostat operates on the principle of a variable heat leak between a thick-walled copper pot containing the sample at the bottom and a reservoir containing a suitable liquid in the wide part of the Dewar. The heat leak is controlled by means of a heater placed just above the copper pot. The pot and the reservoir are connected by thin-walled brass tubing, which represents a compromise between too slow a heat leak on the one hand and a too rapid loss in liquid on the other. A copper tube was placed from the top of the reservoir to the top of the pot with a heater wound over almost its entire length. This was used to keep the entire gas column above the pot at a temperature at least as high as that of the pot, in order to prevent convection currents. The space between the copper tube and the reservoir

[19] R. H. Dicke, Rev. Sci. Inst. **17**, 268 (1946).
[20] F. Bloch, Phys. Rev. **70**, 460 (1946).
† Bloch makes certain approximations which lead to the assumed line shape. This line shape is only an approximation, however. Since there is no completely adequate theory for line shape, any definition of line width is arbitrary to a certain degree.

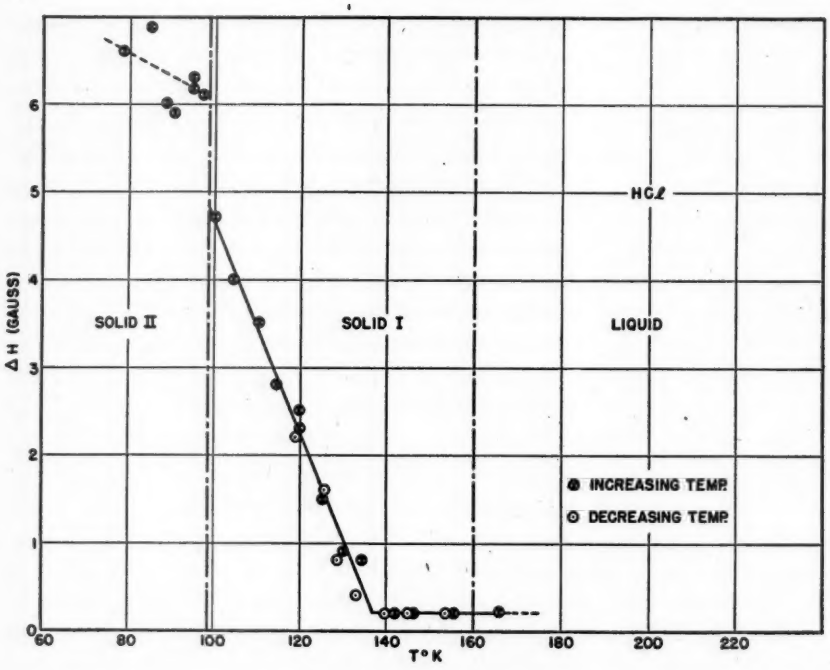

FIG. 1. Line width *vs.* temperature for hydrogen chloride.

was filled with an insulating material. The reservoir was made vacuum tight to permit pumping on the liquid and to enable convenient removal of explosive and noxious vapors. In addition, the construction of the cover was such that the space in the Dewar, but outside the reservoir, could be evacuated, so that the cryostat could be made adaptable for use with liquid hydrogen.

Resistance thermometers were used to determine temperature with one wound about midway along the copper pot and the other in the gas column several inches above the pot. Resistance was measured by means of a Leeds and Northrup Wheatstone Bridge (Type "*S*" testing set). This was found to be quite adequate for the purpose of the experiments above 80°K. Since the lower resistance thermometer reads the average temperature of the pot rather than the temperature of the sample, the time-dependent relationship between these was checked by placing a thermocouple in the position of the sample. As a result, a waiting period of the order of 20 minutes was adopted after changes in temperature of the order of 5 to 10K°. Generally, two or more readings of line width were taken over a time of 10 or more minutes after the waiting period, and data were not accepted until these could be repeated to within the estimated accuracy of the readings. To check this procedure, line-width data were usually taken in the direction of increasing as well as decreasing temperature. Practically no cases were found of hysteresis resulting from a lack of thermal equilibrium.

Those samples which are gases at room temperature were condensed through a capillary opening into thin-walled glass ampules dipped in liquid nitrogen. After the sample was collected, the ampule was sealed by applying a small, hot flame to the capillary. The seal was then worked around into a hook so that the sample could be suspended from a string for ease in storing the samples and transferring them to the cryostat. The ampules were stored in liquid nitrogen. An outline of the chemical preparation of the samples is given in the appendix.

IV. RESULTS AND DISCUSSION

Those substances which have been studied in some detail include (a) normal and heavy methane, CH_4 and CH_3D; (b) the hydrogen halides, HCl, HBr, and HI; (c) the H_2X group, H_2S and H_2Se. In addition, some preliminary results will be reported for ammonium chloride and for natural and synthetic rubber.

4a. The Methanes

It was the exploratory work with normal methane which gave the first indication of the possible

application of this method to the study of phase transitions. No work has been done at hydrogen temperatures, the range of interest for these substances, since the construction of the cryostat. Therefore, the results for these solids were obtained entirely during the exploratory experiments.

Normal methane shows a single λ-point transition at 20.5K°, occurring over a range of 3K°. Its melting point is at 90.6°K. The methane crystal is cubic both above and below the λ-point, and the transition shows some hysteresis.††

A line width of the order of 0.2 gauss was observed just above 77.4°K and 20.4°K. Since the lower temperature observation was believed to be above the λ-point, one experiment was carried on in liquid helium. Under these conditions a 10-gauss resonance was observed. Although no explicit temperature measurements were taken, the helium was known to have boiled away rapidly, since a drift in r-f balance conditions shortly after filling indicated a drifting temperature. There was no marked change in the appearance of the resonance for approximately 30 minutes. Then, within a period of less than one minute, during which the bridge was being rebalanced, the resonance became narrow, as had been observed above 20.4°K. We therefore conclude that there was a transition in the line width from about 10 gauss to roughly 0.2 gauss in a range of order of less than 1K°. The corresponding transition in τ_e is therefore from greater than 2 microseconds to 0.03 microsecond *or less*. As was pointed out in Section II, this behavior is what would be expected in the case of a rotational transformation. However, the possibility that this is an order-disorder transition accompanied by a decrease in the flipping time to less than 0.03 microsecond is not excluded.

In the case of CH_3D two λ-points are found, at 15.5°K with a range of 2°, and at 22.6°K with a range of 3°. The crystal structure of this solid has not been investigated, to the knowledge of the author. The melting point of deuterated methane is also at 90.6°K.

A line-width behavior very similar to that observed in normal methane was found at the higher temperature λ-point. No investigation was carried on below 20.4°K. In this case a resonance of the order of 3 gauss in width was observed very near 20.4°K. This line narrowed to less than 0.3 gauss in a very small temperature range slightly above 20.4°K, which was believed to be the transition temperature. This change in line width represents a change in τ_e from greater than 5 microseconds below the transition to less than 0.3 microsecond above the transition.

As is the conclusion for CH_4, the behavior of the nuclear resonance line width in CH_3D in the vicinity of its upper λ-point is what one would

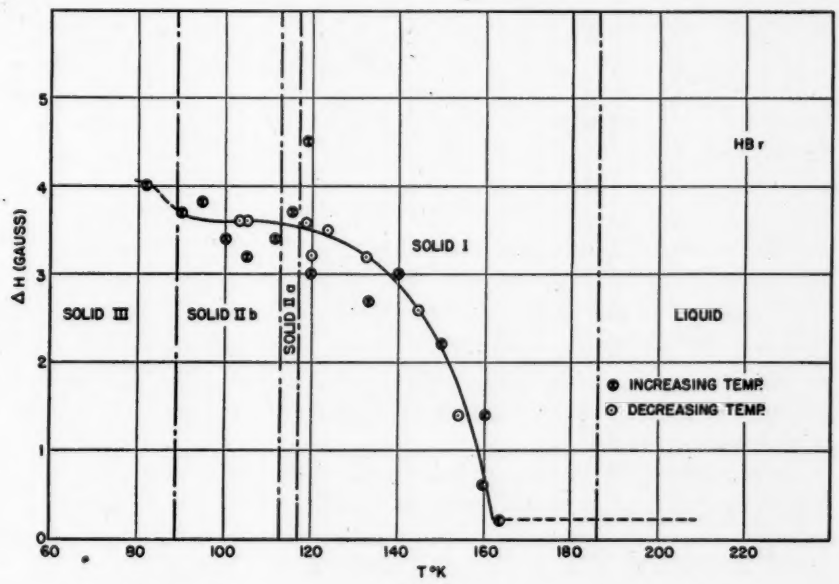

FIG. 2. Line width *vs.* temperature for hydrogen bromide.

†† Data concerning transition temperatures, etc., are from references 17 and 18.

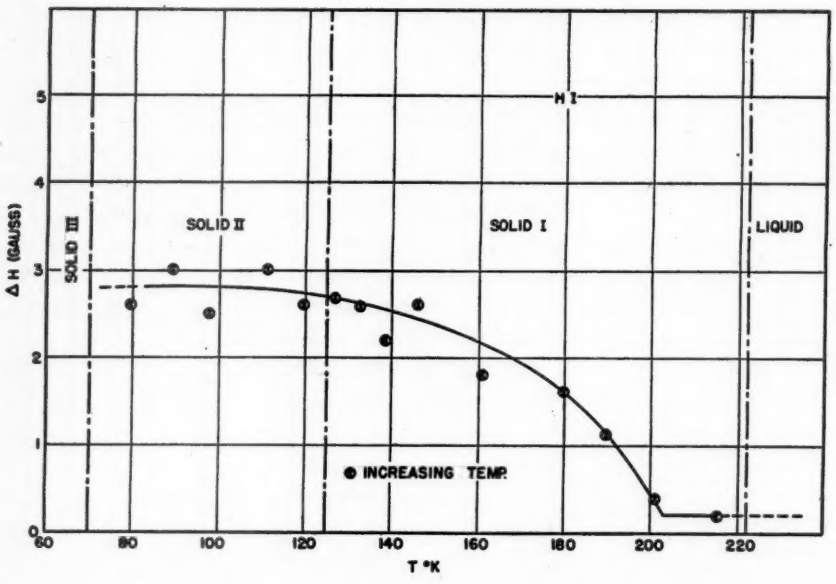

FIG. 3. Line width *vs.* temperature for hydrogen iodide.

expect for a rotational transformation. However, the possibility of its being an order-disorder transition is not absolutely eliminated. Although observations were not carried down to the lower λ-point, by process of elimination one would expect this to be an order-disorder transition.

4b. The Hydrogen Halides

HCl shows a first-order transition at 98.36°K which is accompanied by a change in crystal structure from cubic in the higher temperature modification to a less symmetrical structure at lower temperatures. HCl melts at 158.9°K.

The resultant curve of line width *versus* temperature, shown in Fig. 1, divides into three sections. In the comparatively short temperature range investigated below the transition the line width appears to be decreasing slowly with increasing temperature. This line width is probably a measure of the rigid-lattice line width, and the temperature variation may then be attributed to slight changes in the lattice constants with temperature. It would be difficult to prove this assumption until an accurate rigid-lattice line width can be computed for the lower temperature modification.

An apparently sharp drop in line width at the transition temperature constitutes the boundary between the first and second portions of the graph. In the temperature range from 98.4°K to about 135°K the graph indicates almost a perfectly linear decrease in line width with the temperature. In this case we are almost certainly in the range where ΔH is proportional to τ_e, which implies a linear decrease in τ_e from about 3 microseconds at 100°K to about 0.08 microsecond at 135°K. It is likely that the sharp drop at the transition is due at least in part to a change in the rigid-lattice line width accompanying the change in crystal structure. There is also some possibility that this may be associated with a small discontinuity in the characteristic flipping time.

Beyond 135°K the observed line width is determined entirely by the homogeneity of the magnetic field. This limiting line width is roughly 0.2 gauss at a resonant field of 7000 gauss. No change in the amplitude of the resonance, as observed on the oscilloscope, was noted upon melting the sample. There is little to be gained by speculating as to the variation of τ_e above 135°K, although it should be noted that the extreme possibility of free molecular rotation setting in below the melting point is not ruled out by these data. However, this does not imply a rotational transformation, for which case free molecular rotation sets in at the transition. Therefore, there is no doubt that this line-width variation fits in with what would be expected for the order-disorder transition mechanism. The possibility of a rotational transformation is completely eliminated.

Hydrogen bromide has λ-points at 89°K, with

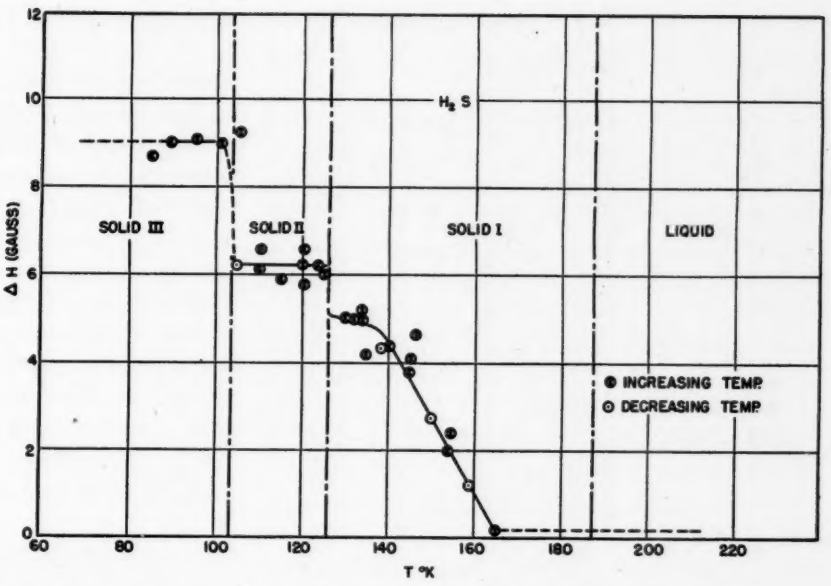

FIG. 4. Line width *vs.* temperature for hydrogen sulfide.

a 3° range, and at 113° and 117°K, with a 2.5° and 1.5° range, respectively. A change from a less symmetrical structure to a cubic structure occurs at the lowest transition. Hysteresis is found at all three transitions. HBr melts at 186.2°K.

Referring to the line width *versus* temperature graph in Fig. 2, we see that there may be a slight change in line width at the lowest transition. However, in the temperature range between 90° and about 140°K, the line-width curve is characterized by a very slow decrease with increasing temperature. It is believed that in this range we are measuring the rigid-lattice line width. It would therefore appear that τ_c has become sufficiently small to take control of the line width in the vicinity of 140°K. Above this temperature the line width responds similarly to what was found in the higher temperature modification of HCl. Between 140° and about 160°K this line width drops very rapidly from about 3 gauss to the observable limit of about 0.2 gauss, the drop representing, on the basis of our interpretation, a decrease in τ_c from roughly 5 microseconds to about 0.3 microsecond. Again there is a range of somewhat over 20K° in the solid state in which the observed line width depends only on the homogeneity of the magnetic field. As in the case of HCl, the possibility of a rotational transformation at any of the λ-points is clearly eliminated, while the data satisfy the implications of the order-disorder mechanism.

The remaining member of the hydrogen halide series, hydrogen iodide, has two λ-transitions at 70° and 125°K, each with a range of 5°. HI is tetragonal (face-centered) above 70°K, while no data seem to be available for the lowest temperature modification.

The line width *versus* temperature data, shown in Fig. 3, are almost identical in character to those found for HBr. In this case the investigation has not been carried to the lowest temperature modification. For HI the line width is almost constant from 80°K to about 150°K, and drops rapidly from about 2.5 gauss to the observable limit of about 0.2 gauss between 150° and about 200°K. This represents an assumed decrease in τ_c from about 6 microseconds to roughly 0.5 microsecond. Again there is a temperature range of somewhat over 20K° in the solid state in which the observed line width is determined entirely by the homogeneity of the magnetic field. As is the case for HCl and HBr, the data clearly deny the Pauling-Fowler interpretation of the λ-points in favor of the Frenkel-Landau interpretation.

4c. Hydrogen Sulfide and Hydrogen Selenide

The lighter substance of the two, H_2S, shows phase transitions at 103.6°K and at 126.2°K. The former is a λ-transition with a range of 0.9K° and some hysteresis, while the latter is apparently a first-order transition, sharp and showing

no hysteresis. The intermediate-temperature modification is known to be cubic. H_2S melts at 187.6°K.

The graph of the line width *versus* temperature data for H_2S, as shown in Fig. 4, may be interpreted in much the same way as the results for the hydrogen halides. In the lowest temperature modification the line width is apparently constant and is probably the rigid-lattice line width for this phase. A sharp drop in line width occurs in the vicinity of 103.6°K, the lower transition temperature, and the line width is constant in the range of the intermediate-temperature modification, leading us again to interpret this as the rigid-lattice line width for this phase. At the upper transition temperature another small discontinuity in line width apparently occurs followed by a sharp break in the slope at about 135°K. If we interpret this as the temperature at which τ_c becomes effective in narrowing the line, this indicates an approximately linear variation in τ_c from 3 microseconds to 0.1 microsecond between 135° and 165°K. Again there is a range of about 20K° in the solid state in which the observed line width is limited only by the homogeneity of the magnetic field. As is the case with the hydrogen halides, the above behavior eliminates the possibility of a rotational transformation and indicates the order-disorder mechanism as the source of the transitions.

Hydrogen selenide shows two phase transitions in the solid state. The one at 82.3°K is a λ-point with a range of 7° and showing some hysteresis, while the upper transition at 172.5°K is sharp with no hysteresis, and may be a first-order transition, similar to H_2S. Hydrogen selenide is known to be cubic in its two higher temperature modifications. The melting point is at 207.4°K.

The nuclear resonance data for protons in H_2Se, shown in Fig. 5, have somewhat different characteristics from those described for the previous cases. There is some decrease in line width at the lower transition. However, the drastic increase in line width between 110° and about 140°K, and the subsequent decrease between 140° and 172°K, have no precedence. If one assumes that the line width is proportional to τ_c in this range, then the indicated variation in τ_c is very startling. It was noted in Section II that τ_c should be proportional to $\exp(U/kT)$, where U is the activation energy required to reorient a small group of molecules. Thus the variation in the case of H_2Se indicates that the barrier against reorientation would have to increase drastically between 110° and 140°K, so as to more than compensate for the inverse temperature depend-

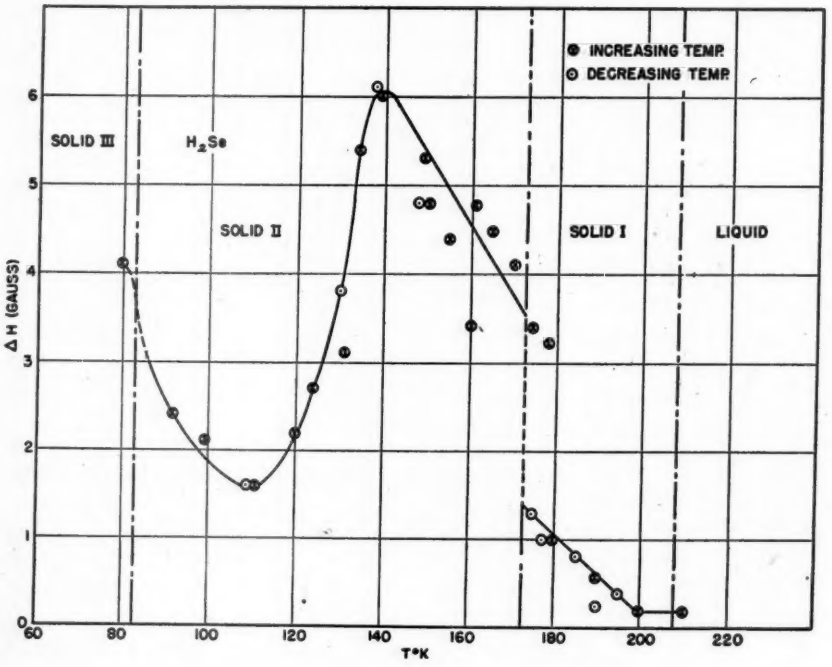

FIG. 5. Line width *vs.* temperature for hydrogen selenide.

ence in the exponential. It is difficult to see how this could happen.

Although there is a considerable dispersion in the data in the vicinity of the upper transition, there seems to be a discontinuous decrease in the line width at this temperature to the comparatively narrow width of about 1.4 gauss, followed by a decrease to the observable limit of 0.2 gauss at 200°K, in this case only about 8K° below the melting point. It is apparent, in spite of the strange behavior noted above, that the rotational mechanism is clearly eliminated by the data in favor of the order-disorder mechanism.

One factor which may have contributed to the strange results in the case of H_2Se is the possibility of the presence of some HCl as impurity.

4d. Preliminary Results for Ammonium Chloride and for Rubber-Like Materials

In both cases data were taken only during the exploratory experiments.

In the case of NH_4Cl, which has a λ-point at 242.8°K, a line width of about 5.5 gauss was found at room temperature and somewhere in the vicinity of the λ-point. At nitrogen temperature a line width of 18 gauss was observed. As in the other cases, this definitely indicates that this is an order-disorder type of transition,[21] and not a rotational transformation, as has frequently been assumed.[18]

In natural, unvulcanized rubber a narrow line was observed, limited only by the homogeneity in the magnetic field. Therefore, the possibility of extremely short flipping times for the methyl side groups or for the hydrogen bonds, for example, is quite plausible. However, there is an apparent decrease in the number participating in this motion as the temperature is decreased, since the amplitude of the resonance decreases drastically while there is no change in the other characteristics of the resonance. A small, narrow pip is still visible at dry-ice temperature, about −78°C. Vulcanization had no effect at room temperature, while carbon loading did seem to broaden the resonance slightly. As was expected, a sample of GR-S synthetic rubber gave only a broad resonance.

[21] A. W. Lawson, Phys. Rev. 57, 417 (1940).

4e. Summary of the Results

We have indicated and applied a method capable of distinguishing the mechanism of those λ-points, as well as a few first-order transformations, for which the transitions may be attributed to a change in molecular reorientation time. In the experimental studies it was shown in most cases that the transitions cannot possibly be associated with the onset of molecular rotation but satisfy, instead, the conditions of an order-disorder transformation. Those substances which fall into this classification are HCl, HBr, HI, H_2S, H_2Se, and NH_4Cl. In a few cases the results indicate the plausibility of a rotational transformation, although the order-disorder mechanism is not absolutely eliminated for these transitions. These exceptional solids are CH_4 and CH_3D at the upper transition, as well as natural rubber, for which internal rotation is shown to be reasonable but is not proved unquestionably.

The experimental data for the methanes, in particular, should be made more quantitative under better conditions of temperature control. In addition, measurements of the spin-lattice relaxation time T_1 may possibly eliminate the ambiguity in these rare cases. This follows from the fact that T_1 is also a function of the characteristic flipping time,[4] with the advantage that no limitations will be imposed in the direction of short flipping times by the homogeneity of the magnetic field. However, the measurement of T_1 is much more difficult than the measurement of line width, or T_2, which has been shown to be adequate in most cases.

ACKNOWLEDGMENTS

The author is deeply indebted to Professor F. Bitter for his guidance and encouragement in the carrying out of this research. He is also grateful to Professor L. Tisza for indicating the problem and for his invaluable discussions of its theoretical background. The author also wishes to thank other members of the nuclear resonance project, in particular C. G. Lehr, who contributed much to the design of the r-f apparatus. In addition, the author acknowledges the use of the facilities of the Research Laboratory of Electronics and the aid and services of many of its staff members, especially C. S. Pearsall and his

staff, who prepared chemically many of the solids studied.

APPENDIX

Following is a brief outline of the methods by which the commercially unavailable samples were produced. In all cases at least one stage of fractionation was carried on before condensation into the ampules.

a. Hydrogen Chloride

Hydrogen chloride was prepared by dropping concentrated sulfuric acid on a mixture of hydrochloric acid and sodium chloride. The gas was dried by passing it through four tubes of P_2O_5. It was collected in a 100-ml flask in a liquid nitrogen trap.

b. Hydrogen Bromide

Forty-eight percent hydrobromic acid was dropped slowly onto a mixture of freshly ignited sand and phosphoric pentoxide. The resulting gas was passed through two tubes of red phosphorus to remove free bromine, and through three tubes of P_2O_5 to remove water vapor. The gas was first collected in a 100-ml flask (drawn down in the neck) submerged in a liquid nitrogen bath.

c. Hydrogen Iodide

Hydrogen iodide was prepared by the substitution reaction $NaI+H_3PO_4 \rightarrow HI\uparrow +NaH_2PO_4$. Moderate heat was applied. The apparatus was completely covered with aluminum foil to prevent decomposition of the hydrogen iodide by light. Free iodine was removed by freezing out in a $\frac{3}{4}$-inch Pyrex coil in a $-30°C$ trap. The temperature of the trap was maintained by regulating a dry air flow through a glass-wool-packed U-tube immersed in liquid nitrogen. This temperature was easily kept to within $\pm 1C°$. Further traces of iodine were removed by passing the gas through two tubes of red phosphorus. Moisture was removed by passing the gas through three tubes of P_2O_5. The gas was collected in two U-tubes in liquid nitrogen baths. The HI first condensed into the U-tubes as a pure white solid. It was observed then that after a few seconds' exposure to light a progressive discoloration of the solid HI took place, probably due to decomposition of the HI. Although considerable effort was made to prevent exposure to light during the fractionation, some decomposition did take place. The finished frozen gas therefore shows some discoloration, presumably due to free I_2.

d. Hydrogen Selenide

Hydrogen selenide was made by dropping dilute HCl slowly onto freshly made aluminum selenide: $Al_2Se_3+(3+x)H_2O \rightarrow 3H_2Se+Al_2O_3 \cdot xH_2O$. The aluminum selenide was prepared by mixing 50 grams of finely divided precipitated selenium with 30 grams of aluminum powder that had been washed with acetone and ether: $2Al+3Se \rightarrow Al_2Se_3$. Five grams of the mixture were placed in a fire-clay crucible and ignited with glowing magnesium ribbon. Every few seconds three grams of the mixture were added to the glowing mass in the crucible. The aluminum selenide was stored in a vacuum desiccator until used. Dilute hydrochloric acid was slowly dropped from the dropping funnel onto the freshly made aluminum selenide. The evolved hydrogen selenide passed through a drying train of two tubes of $CaCl_2$ and three tubes of phosphorus pentoxide. It was collected in a 100-ml flask in a liquid nitrogen bath. Metaphosphoric acid was used to lubricate the ground-glass joints in the glass system.

e. Deuterated Methane

The methyl deuteride was prepared by the Grignard reaction: $CH_3I+Mg \rightarrow CH_3MgI$; $CH_3MgI+D_2O \rightarrow CH_3D\uparrow +MgI(OD)$, carried on in dibutyl ether as solvent. The dibutyl ether and methyl iodide were first carefully dried and redistilled. The heavy water was dropped slowly on to the methyl magnesium iodide. The gas resulting from the reaction passed through concentrated sulfuric acid to remove the dibutyl ether, and then through three tubes of P_2O_5 for drying. In this case the gas was condensed directly into the ampules.

PHYSICAL REVIEW VOLUME 75, NUMBER 3 FEBRUARY 1, 1949

High Frequency Gas Discharge Breakdown in Helium*

A. D. MacDonald and Sanborn C. Brown
Research Laboratory of Electronics, Massachusetts Institute of Technology, Cambridge, Massachusetts

(Received October 26, 1948)

Breakdown electric fields in low pressure helium at high frequencies have been theoretically predicted and experimentally verified. The energy distribution of electrons is derived from the Boltzmann transport equation, taking into account all significant removal processes. The distribution function is expanded in spherical harmonics and the resulting second order linear differential equation is solved in terms of the confluent hypergeometric function. This distribution function combined with kinetic theory formulas permits calculation of the ionization rate and the electron diffusion coefficient. From these the high frequency ionization coefficient is determined. Through the diffusion equation this ionization coefficient is related to breakdown electric fields. Thus breakdown electric fields are predicted theoretically without using any gas discharge data other than experimental values of the excitation potential and collision cross section of helium. Breakdown electric fields are measured for helium in microwave cavities of various sizes with a large range of pressure. The theoretical electric fields, involving no adjustable parameters, are checked within the maximum experimental error of 6 percent.

I. INTRODUCTION

WHEN a high frequency electric field is applied to a gas, breakdown occurs when the number of electrons produced by ionization equals the number lost by diffusion.[1] The ionization rate and the diffusion coefficient will be computed theoretically on the basis of kinetic theory. These enable us to predict high frequency ionization coefficients and breakdown electric fields. The electron distribution function is determined by setting up the electron continuity equation, accounting for production and loss of electrons in phase space. The distribution functions so determined are used in standard kinetic theory formulas in order to find ionization rates and diffusion coefficients. The results are expressed in terms of the high frequency ionization coefficient ζ.[1]

II. SPHERICAL HARMONIC EXPANSION

The phase space continuity equation (Boltzmann transport equation) for electrons may be written

$$P=\frac{\partial f}{\partial t}+\bar{v}\cdot\nabla f+\bar{a}\cdot\nabla_v f,^{2,3} \tag{1}$$

where f is the electron energy distribution function, P is the production rate of electrons per unit phase space and may be expressed in terms of f by finding the energy changes in electrons for elastic and inelastic collisions; $\bar{v}$ the velocity, $\bar{a}$ the acceleration, t the time, and ∇_v the gradient operator in velocity space.

Collisions with gas atoms tend to disorder any non-random motion of the electrons so that f is almost spherically symmetric. Thus if f is expanded in spherical harmonics $f=f_0+(\bar{v}\cdot\bar{f}_1)/v+\cdots$,[4] the spherically symmetrical term f_0 is predominant. The $\bar{f}_1$ term represents a vector drift term from which the current may be calculated. The series then is rapidly convergent and we consider only those cases where the first two terms suffice to calculate the properties of the system.

III. THE DIFFERENTIAL EQUATION FOR f_0

Consider the electric field as sinusoidal in time; on expansion, Eq. (1) becomes[3]

$$P_0=\frac{\partial f_0}{\partial t}+\frac{v}{3u}\frac{\partial}{\partial u}(u\bar{E}\cdot\bar{f}_1)+\frac{v}{3}\nabla\cdot\bar{f}_1 \tag{2}$$

and

$$\bar{P}_1=\frac{\partial\bar{f}_1}{\partial t}+v\nabla f_0+v\bar{E}\frac{\partial f_0}{\partial u}, \tag{3}$$

* This work has been supported in part by the Signal Corps, the Air Materiel Command, and ONR.

[1] M. A. Herlin and S. C. Brown, Phys. Rev. **74**, 291 (1948).

[2] S. Chapman and T. G. Cowling, *The Mathematical Theory of Non-Uniform Gases* (Cambridge University Press, Teddington, 1939), Chap. 3.

[3] P. M. Morse, W. P. Allis, and E. S. Lamar, Phys. Rev. **48**, 412 (1935).

[4] H. Margenau, Phys. Rev. **73**, 303 (1948), Eq. (26).

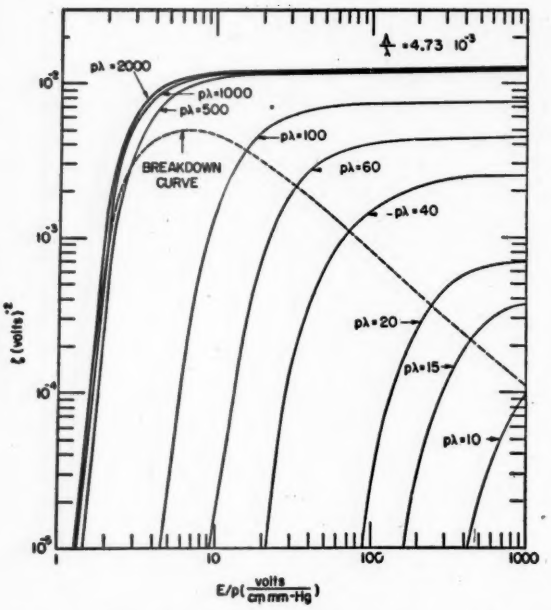

FIG. 1. The high frequency ionization coefficient ζ computed as a function of E/p from Eq. (19). The breakdown curve is indicated by the dashed line; it is determined by setting $\zeta=1/\Lambda^2E^2$.

provided P is expanded $P=P_0+(\bar{P}_1\cdot\bar{v})/v$, and the electric field is represented by $\bar{E}$. An energy variable u is introduced by setting $mv^2/2e=u$, where e is the electronic charge and m is the mass of the electron.

Elastic collisions may be considered as instantaneous processes and the energy loss therefrom may be treated by putting equivalent loss terms $P_{0,el}$ and $\bar{P}_{1,el}$ in the equation. Morse, Allis, and Lamar[3] have shown that

$$P_{0,el}=2\frac{m}{M}\frac{v}{u}\frac{d}{du}\left(\frac{u^2f_0}{l}\right) \tag{4}$$

and

$$\bar{P}_{1,el}=-\frac{v}{l}\bar{f}_1 \tag{5}$$

l being the electronic mean free path, and M the mass of the atom.

In low pressure helium, recombination is not a significant electron removal process at breakdown. Ionizations and excitations have no angular dependence and therefore make a contribution to P_0 only; we represent this contribution due to inelastic collisions by $P_{0,in}$.

The electric field E is represented by $E_0e^{j\omega t}$ where ω is the radian frequency. In the gas, the energy transfer by the field to the electrons depends on E^2 so that the root mean square field is all that is required. There follows directly from Margenau's analysis[5] an expression for $\bar{E}\cdot\bar{f}_1$ which is the same as that obtained by considering an effective field E_e defined by

$$E_e^2=E^2\frac{(v/l)^2}{(v/l)^2+\omega^2}, \tag{6}$$

where E is the r.m.s. value of the applied field.

The differential equation for f_0 then becomes

$$P_{0,in}+\frac{2m}{M}\frac{v}{u}\frac{d}{du}\left(\frac{u^2f_0}{l}\right)=\frac{lv}{3\Lambda^2}f_0-\frac{v}{3u}\frac{d}{du}\left\{lu\frac{df_0}{du}\cdot\frac{E^2(v/l)^2}{(v/l)^2+\omega^2}\right\}. \tag{7}$$

Here ∇^2f_0 has been replaced by $-(1/\Lambda^2)f_0$ using the diffusion equation.[1] The factor $1/\Lambda^2$ depends on the geometry of the discharge container, and is the characteristic value in the solution of the diffusion equation; Λ is then the characteristic diffusion length. The mean free path l equals $1/pP_c$ if p is the pressure and P_c the probability of collision per cm of path per mm of pressure. There now remains to specify the functional forms of P_c and $P_{0,in}$, to complete the formulation of the equation. Excitation will be effectively eliminated by the introduction of mercury vapor.

IV. EXPRESSION FOR THE COLLISION CROSS SECTIONS

A good approximation for P_c in helium is $P_cu^{\frac{1}{2}}=\text{constant}=43(\text{volt}^{\frac{1}{2}}/\text{cm}\times\text{mm Hg})$.[6] The experimental curve departs from this form for u less than 4 volts and P_c is roughly constant from $u=0$ to $u=4$. Most of the collisions the electron makes with gas atoms occur after the electron has an energy of 4 ev, so this discrepancy has a small effect on the breakdown field. The solution of the equation will be carried out assuming $P_cu^{\frac{1}{2}}=\text{constant}$ over the whole range of electron energies, and will be corrected in Section VI by finding the distribution function required when this range of constant mean free path is considered.

[5] H. Margenau, Phys. Rev. **73**, 303 (1948), Eq. (27).
[6] R. B. Brode, Rev. Mod. Phys. **5**, 257 (1933).

Helium has a metastable level at 19.8 volts and transitions from this level to the ground state by radiation are forbidden. Since metastable states have mean lives of the order of thousands of microseconds, practically every helium atom which reaches an energy of 19.8 volts will collide with a mercury atom and lose its energy by ionizing the mercury. Therefore each inelastic collision will produce an ionization and the effective ionization potential u_i will be the first helium excitation potential plus a small overshoot energy due to the fact that the most probable energy at excitation is higher than the excitation energy. (The amount of this overshoot is calculated in Section VII.) Then $P_{0,in}$ may be assumed zero for $u<u_i$ and infinite for $u>u_i$. Physically this means that there will be no electrons with an energy above that corresponding to $u=u_i$. This condition on the electron population provides a boundary value for the differential equation which we now solve for $u<u_i$, with f_0 zero for $u=u_i$.

V. SOLUTION OF THE EQUATION AND EVALUATION OF ζ

Equation (7) becomes, on inclusion of results of Section IV, in the region where $u<u_i$

$$u\frac{d^2f_0}{du^2}+\frac{df_0}{du}\left[\frac{\mu u}{\beta}+\frac{3}{2}\right]+f_0\left[\frac{3}{2}\frac{\mu}{\beta}-\frac{u}{\beta}\right]=0, \quad (8)$$

where

$$\mu=\frac{3m}{M}\cdot\frac{m}{e}\cdot\frac{\Lambda^2}{\tau^2},$$

and

$$\beta=\frac{1}{\sigma}\left(\frac{E\Lambda}{\omega\tau}\right)^2.$$

τ is the mean free time, $1/\tau=2.37(10^9)p$ (in mm Hg),[6] and

$$\sigma=1+\left(\frac{1}{\tau\omega}\right)^2.$$

For convenience we transform to a dimensionless independent variable by letting

$$w=\frac{\mu}{\beta}\left(1+\frac{4\beta}{\mu^2}\right)^{\frac{1}{2}}u=\frac{\mu b}{\beta}u, \quad (9)$$

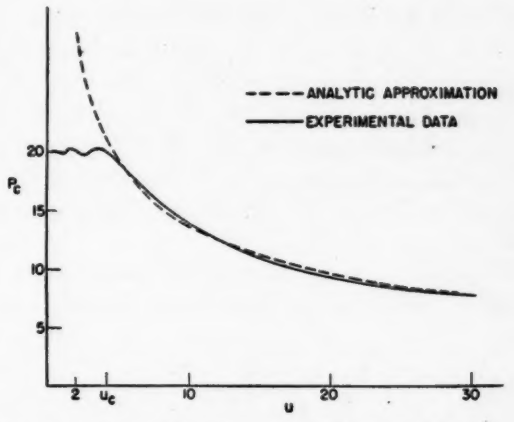

FIG. 2. The probability of collision of electrons in helium at 1 mm of Hg pressure. Brode's experiment is compared with the approximation of this paper.

and transform the dependent variable by

$$f_0=(g)\exp\left[-\frac{1}{2}\left(\frac{1}{b}+1\right)w\right]. \quad (10)$$

Then

$$w\frac{d^2g}{dw^2}+\frac{dg}{dw}\left(\frac{3}{2}-w\right)-\alpha g=0, \quad (11)$$

where

$$\alpha=\frac{3}{4}\left(1-\frac{1}{b}\right).$$

Equation (11) is the confluent hypergeometric equation[7] and its solutions may be written

$$g_1=M(\alpha;\tfrac{3}{2};w),\ g_2=w^{-\frac{1}{2}}M(\alpha-\tfrac{1}{2};\tfrac{1}{2};w).^8 \quad (12)$$

For brevity we will use the notation

$$M(\alpha;\tfrac{3}{2};w)=M_1(w) \quad (13)$$

and

$$w^{-\frac{1}{2}}M(\alpha-\tfrac{1}{2};\tfrac{1}{2};w)=M_2(w). \quad (14)$$

Then the distribution function f_0 is given by

$$f_0=[M_1(w)+CM_2(w)]\exp[-w(1-2/3\alpha)], \quad (15)$$

where the constant C is determined by the boundary condition that the distribution function go to zero at $u=u_i$; therefore

$$C=-\frac{M_2(w_i)}{M_1(w_i)}.$$

---

[7] E. Jahnke and F. Emde, *Funktionen Tafeln* (Teubner, Leipzig, 1933), p. 275.

[8] A. D. MacDonald, "Properties of the confluent hypergeometric function," Technical Report No. 84, Research Laboratory of Electronics, M.I.T., Cambridge, Massachusetts.

Having determined the distribution function we are in a position to calculate the high frequency ionization coefficient ζ. By the use of standard kinetic theory formulas and the distribution function expressed in Eq. (15) we calculate the quantities $n\nu$ and nD. The ratio of these quantities divided by the square of the electric field is ζ.

The kinetic theory formula for the number of inelastic collisions per electron per second, ν, is

$$n\nu = -4\pi\frac{2e^2}{m^2}\int_{u_i}^{\infty}\frac{u}{v}P_{0,in}du, \tag{16}$$

where $P_{0,in}$ is the production rate of electrons per unit volume of phase space due to inelastic collisions.

The integral in Eq. (16) is an improper integral but $P_{0,in}$ is transformed through Eq. (7) to a function of f_0 and u. The resulting rigorous expression is integrated by parts. The integration, subject to the condition that f_0 and df_0/du are zero for $u=\infty$, yields

$$n\nu = -\frac{2\pi}{3}\left(\frac{E}{\omega}\right)^2\frac{1}{\sigma\tau}\left(\frac{2e}{m}\right)^{5/2}\left[u^{3/2}\frac{df_0}{du}\right]_{u=u_i}. \tag{17}$$

Similarly the diffusion coefficient for electrons, D, is

$$nD = \frac{2\pi\tau}{3}\left(\frac{2e}{m}\right)^{5/2}\int_0^{u_i} f_0 u^{3/2}du. \tag{18}$$

The expression for f_0 from Eq. (15) is substituted in the integrand and the integrations performed. The integrals have been evaluated for arbitrary values of the parameters involved.[8]

On carrying out the integrations in Eq. (18), and dividing Eq. (17) by the resulting expression we have the high frequency ionization coefficient

$$\frac{1}{\zeta}=\frac{DE^2}{\nu}=(E\Lambda)^2[M_1(w_i)\exp(-\tfrac{2}{3}\alpha w_i)-1]. \tag{19}$$

The form of Eq. (18) has been simplified by using the fact that the expression

$$M_1'(w_i)M_2(w_i)-M_2'(w_i)M_1(w_i)$$

is the Wronskian of the differential Eq. (11) and its value is $\frac{1}{2}w_i^{-\frac{1}{2}}\exp w_i$. At breakdown $\nu/D=1/\Lambda^2$, so we see from Eq. (19) that the breakdown electric fields may be determined by solving the equation

$$M_1(w_i)\exp(-\tfrac{2}{3}\alpha w_i)=2. \tag{20}$$

For helium, the numerical values of the variables involved in terms of experimental parameters are

$$w_i=\frac{0.820(10^4)u_i}{(E\lambda)^2}b\left(1+\left(\frac{p\lambda}{79.6}\right)^2\right) \tag{21}$$

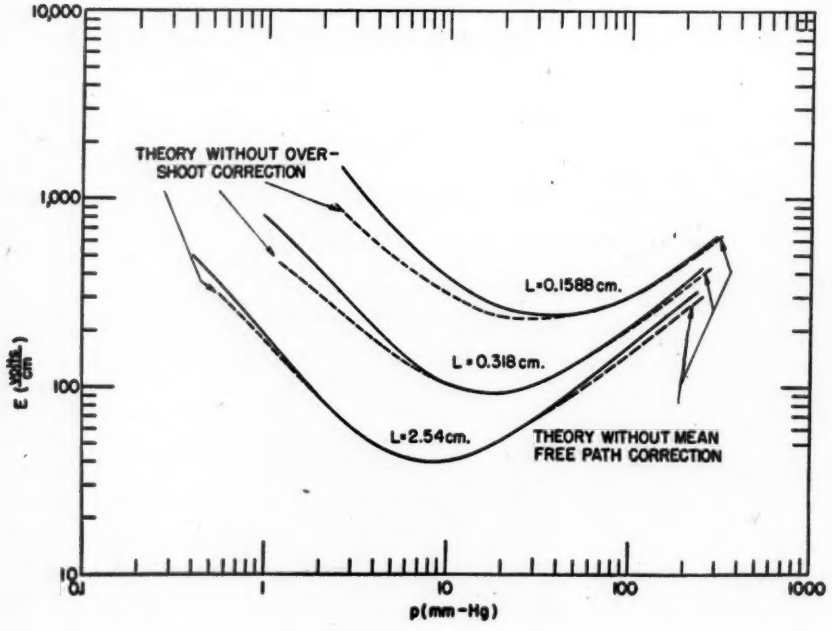

FIG. 3. Theoretical $E-p$ curves illustrating the effect of the correction factors of Sections VI and VII. The broken lines indicate theoretical fields without corrections. The $\frac{1}{8}$-inch cavity is omitted to avoid confusing the diagram.

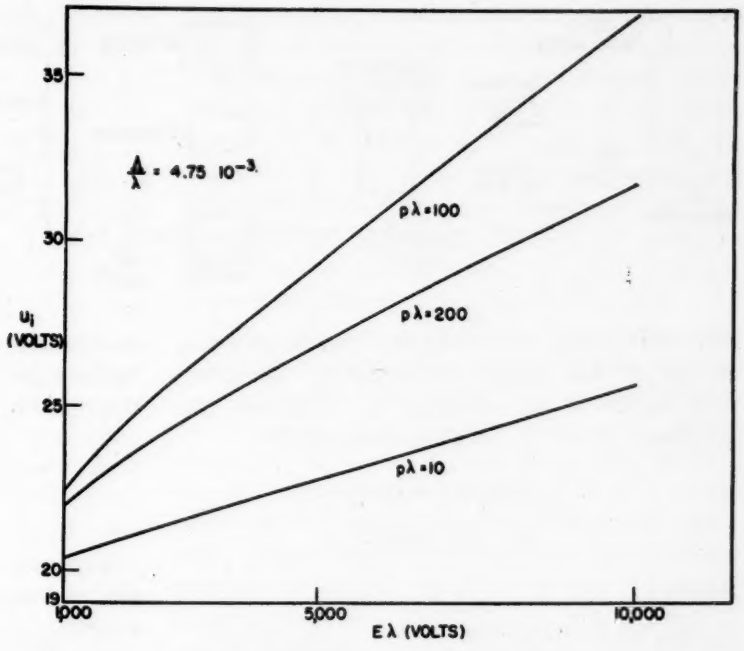

FIG. 4. The effective ionization potential as a function of $E\lambda$ at a constant Δ/λ.

$$b=\left[1+\frac{(E\lambda)^2}{(p\Delta)^2}\frac{3.77(10^{-4})}{\left[1+\left(\frac{p\lambda}{79.6}\right)\right]^2}\right]^{\frac{1}{2}} \tag{22}$$

$$\alpha=0.75\frac{b-1}{b}, \tag{23}$$

where λ is the free space wave-length of the electric field in cm, E is the r.m.s. value of the electric field in volts per cm, p is the pressure in mm of Hg and Δ is in cm.

A plot of ζ *vs.* E/p is given in Fig. 1, computed from Eq. (19). Tables of the functions involved are available.[8] The breakdown electric field may be determined from Fig. 1 by finding the curve through those points where $\zeta=1/\Delta^2E^2$.

VI. CORRECTION FOR FLAT PORTION OF P_e CURVE

From Fig. 2 we see that our approximation for P_e is inaccurate for electron energies below 4 ev, and therefore in those cases where there are many electrons with low energies, a small correction term may be applied. The low energy electrons are most important in determining breakdown fields when E/p is small and there are many more collisions per second than oscillations of the field per second, because under these conditions, the relative number of low energy electrons is large. For energies below 4 ev, Eq. (6) may be simplified by neglecting ω^2 in comparison with $(\nu/l)^2$, and by using the fact that l is constant. The solution may be carried out in the manner of Section V and f_0 is then given by

$$f_0=A[M(a;1;y)+BW(a;1;y)]\exp(-y), \tag{24}$$

where M is the confluent hypergeometric function, W is the second solution for integral values of the second parameter,[8,9]

$$a=\frac{1.54}{(p\Delta)^2},$$

and

$$y=71.2\left(\frac{p}{E}\right)^2\left(\frac{u}{u_i}\right)^2,$$

and both functions in Eq. (24) are tabulated.[8]

Again we use a more concise notation for the confluent hypergeometric function by setting

$$M(a;1;y)=M_3(y)$$

and

$$W(a;1;y)=W_3(y).$$

The energy at which P_e changes from a constant to a $u^{-\frac{1}{2}}$ trend is seen from Fig. 2 to be that corresponding to $u_e=u_i/5$. The distribution

[9] W. J. Archibald, Phil. Mag. 26, 419 (1938).

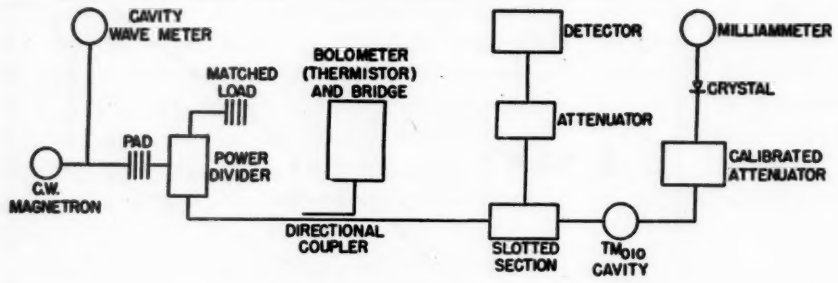

FIG. 5. Block diagram of the experimental microwave equipment.

functions in Eqs. (15) and (24) must be smoothly joined at this energy. By equating the values and slopes of the distribution functions, the constants A and B are determined to be

$$B=\frac{RM_3(y_c)-M_3'(y_c)}{W_3'(y_c)-RW_3(y_c)} \tag{25}$$

where

$$R=\frac{M_1'(w_c)+CM_2'(w_c)+2/3\{M_1(w_c)+CM_2(w_c)\}}{M_1(w_c)+CM_2(w_c)}, \tag{26}$$

and

$$A=\frac{[M_1(w_c)+CM_2(w_c)]\exp[-w_c(1-\frac{2}{3}\alpha)]}{[M_3(y_c)+BW_3(y_c)]\exp(-y_c)}. \tag{27}$$

This distribution function then modifies the value of the integral for nD and also the expression for ζ in Eq. (19).

The amount of this correction for various cavity sizes and pressures is illustrated in Fig. 3, which shows the correction to be appreciable only for high pressures, and in no case to be more than a few percent.

VII. CORRECTION FOR OVERSHOOT

The probability of excitation is not infinite at the first excitation potential so that some electrons reach energies above this value before exciting helium atoms. This overshoot in energy is most noticeable at low pressures when the energy gained between collisions is large. To find the energy at which the distribution function goes to zero, we insert the measured values[10] of the excitation function as a loss term in Eq. (8). The excitation function is linear in energy at energies close to the excitation potential. Using Maier-Leibnitz's experimental excitation function[10] for h_x, we may write

$$h_x=\frac{P_x}{P_c}=h_1(w-w_x)=\frac{(u-19.8)u^{\frac{1}{2}}}{623}. \tag{28}$$

Equation (8) now written in the reduced form and including h_x is

$$\frac{d^2g}{du^2}-Ig=0, \quad f_0=(u^{\frac{1}{2}}g)\exp\left(-\frac{\mu u}{2\beta}\right), \tag{29}$$

where

$$I=\frac{1}{\beta}\left[1+\frac{M}{m}\frac{\mu}{2}h_1-\frac{1}{u}\left(\frac{M}{m}\frac{\mu}{2}h_1u_x+3\mu\right)-\frac{3\beta}{16u^2}\right]. \tag{30}$$

For $u>u_x$, I may be seen on inspection to be a slowly varying function so we may solve Eq. (30) approximately and obtain

$$g=\exp(-(I)^{\frac{1}{2}}u). \tag{31}$$

Equation (31) combined with Eq. (29) gives the distribution function above the excitation potential; and this distribution function should be fitted to that of Eq. (15). However, the distribution function is small in this region and we may determine a voltage at which the distribution function goes to zero by extrapolating Eq. (31) linearly and choosing that voltage where it cuts the axis as the ionization potential. The extrapolation of Eq. (31) yields

$$u_i-u_x=\frac{g}{g'}=(I)^{\frac{1}{2}}. \tag{32}$$

The effective ionization potential is plotted in Fig. 4 for helium as a function of $E\lambda$ with several values of $p\lambda$, for one value of Λ/λ. A more

[10] H. Maier-Leibnitz, Zeits. f. Physik 95, 499 (1935).

rigorous treatment in which Eq. (29) is solved exactly[8] is possible but does not alter the value of u_i in Fig. 4 significantly.

VIII. EXPERIMENTAL PROCEDURE

A block diagram of the microwave apparatus used in the experiment is shown in Fig. 5. A continuous-wave tunable magnetron in the 10-cm wave-length region supplies up to 150 watts of power into a coaxial line leading to the measuring equipment. A cavity wavemeter receives a small signal from a probe in the line. The power incident on the cavity is varied by a power divider. A directional coupler provides a known fraction of the incident power to a thermistor element whose resistance, measured by a sensitive bridge, indicates power incident on the cavity. A slotted section of line with a movable probe measures the standing wave ratio and voltage minimum, the probe signal going to a detector with a wave-guide-beyond-cutoff attenuator. The cavities resonate in the TM_{010}-mode in the 10-cm wave-length region, and are coupled to the coaxial transmission line by a coupling loop. A second coupling loop provides a transmitted signal to an attenuator, crystal and meter. The electric field is calculated by standard microwave methods.[11,12] The unloaded Q of the cavity is calculated from standing wave measurements. The power absorbed in the cavity is determined by the measured incident power and the standing wave ratio. The absorbed power is related to the stored energy through the unloaded Q and the electric field is determined from the known field configuration and the stored energy. It is convenient to calibrate the transmitted signal network in terms of incident power measurements to measure the field.

Care was taken to obtain high gas purity. The cavities were made of oxygen-free high conductivity copper and all joints were silver soldered. The coupling loops were made of copper, Kovar and glass. The cavity was connected through Kovar to an all-glass system including a three-stage oil diffusion pump and a liquid-nitrogen trap. Spectroscopically pure helium and distilled mercury were used. Each cavity was baked out for several days at 400°C and the whole vacuum system carefully outgassed before each run. The mercury pool which introduced the mercury vapor also served to seal the cavity from the liquid air trap during each breakdown field measurement. The possible effect of direct ionization of mercury in the breakdown process has been investigated theoretically. For the density of mercury used it was found to be not significant

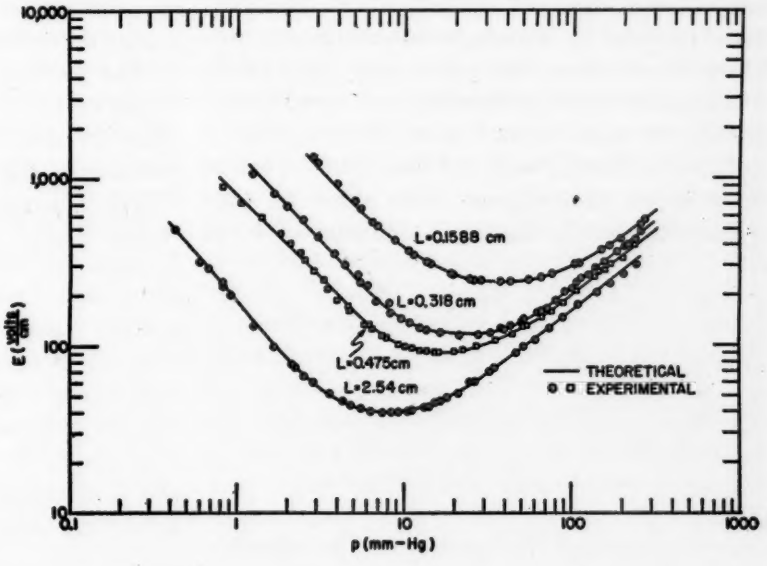

FIG. 6. Experimental breakdown electric fields compared with those theoretically predicted.

[11] C. G. Montgomery, *Microwave Techniques* (McGraw-Hill Book Company, Inc., New York, 1947).
[12] S. C. Brown *et al.*, "Methods of measuring the properties of ionized gases at microwave frequencies," Technical Report No. 66, Research Laboratory of Electronics, M.I.T., Cambridge, Massachusetts.

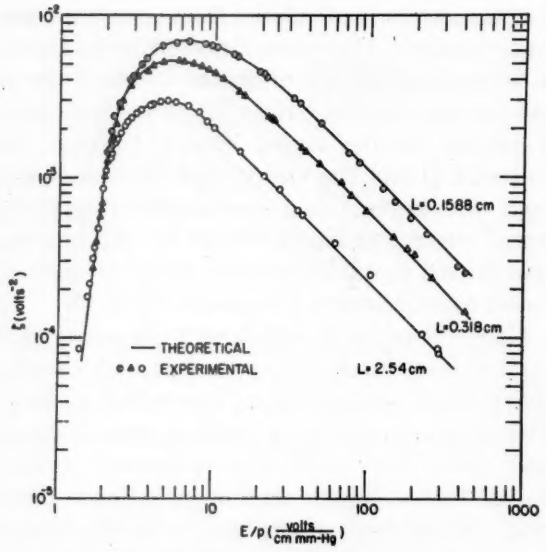

FIG. 7. Experimental ionization coefficient compared with theoretically predicted coefficients. The ½-inch cavity is omitted to avoid confusing the diagrams.

in the range of pressures and container sizes used in the experiment.

The breakdown experiment consists of filling the cavity with the gas at a measured pressure, increasing the magnetron power until the crystal current reaches a maximum and drops suddenly to a much lower value. The drop indicates that the gas has broken down and the maximum current indicates the breakdown field. The electrons required to initiate the discharge are provided by a radioactive source near the cavity. The breakdown measurements were reproducible within an experimental error of less than 5 percent in electric field and less than 1 percent in pressure. Experiments were done on four cylindrical cavities having a diameter of 8.140 cm and heights of 0.1588, 0.3175, 0.4760, and 2.540 cm. The cavity whose height was great enough so that it could not be considered a parallel plate system was computed using a non-uniform field theory.[13]

Figure 6 presents the experimental and theoretical E *vs.* p curves. ζ *vs.* E/p curves computed from the experimental data are compared with theory in Fig. 7.

IX. CONCLUSIONS

The high frequency ionization coefficient has been calculated theoretically on the basis of the electron continuity equation, considering diffusion to the container walls as the only removal process. It is expressed in terms of $E\Lambda$, $p\lambda$, and $p\Lambda$. The high frequency ionization coefficient has been derived theoretically in Eq. (19). The ionization coefficient had been previously related to breakdown fields through the diffusion equation.[1]

Equation (20), containing no adjustable gas discharge data or constants, and involving only the excitation potential and collision cross section of helium, enables us to predict breakdown electric fields. It has been derived from the electron velocity distribution function given by kinetic theory, and the diffusion equation. The agreement between theory and experiment over a wide range of pressure and container size variation verifies the correctness of the approach.

The authors wish to acknowledge the many valuable ideas contributed by Professor W. P. Allis in numerous discussions leading to the solution of this problem.

[13] M. A. Herlin and S. C. Brown, Phys. Rev. **74**, 1650 (1948).

On the Scattering of Protons in Hydrogen

C. L. CRITCHFIELD AND D. C. DODDER
Department of Physics, University of Minnesota, Minneapolis, Minnesota
(Received October 25, 1948)

Results of the recent proton-proton scattering experiments at the University of Minnesota in which measurements were made at angles in the laboratory system from 8° to 45° using incident proton energies of from 2.4 to 3.5 Mev, are used to calculate phase shifts for the interaction. *S*-wave scattering is found which agrees with previous work in corresponding to the potential of an attractive rectangular well of radius e^2/mc^2 and depth 10.5 Mev, or to a Yukawa-type potential with a meson of mass in the neighborhood of 300 electron masses. An anomaly which remains at the smaller angles is not removed by a careful treatment of the geometry of the scattering chamber, but is tentatively accounted for with a combination of repulsive *p*-wave scattering and a systematic experimental error of approximately one percent. The *p*-wave phase shifts are several times larger than those expected from a repulsive rectangular well of the same dimensions as the well for the *s*-wave scattering.

PRECISE measurements of the intensity with which protons are scattered by gaseous hydrogen have been extended by Blair, Freier, Lampi, Sleator, and Williams[1] to higher energies of bombardment and to smaller angles of scattering than those measured hitherto.[2] The general method of the experiment, however, is the same as that used by Tuve *et al.*, at the Department of Terrestrial Magnetism, and Herb *et al.*, at Wisconsin.

This method is to direct a narrow beam of protons from an electrostatic generator through a scattering chamber filled with hydrogen gas and to count the protons that emerge from a small volume at the center of the chamber along a line forming an angle θ with the axis of the incident beam. Apertures are placed along the axis of the detector window so that only those rays forming a narrow "beam" will be counted and the volume of gas effective in scattering is determined by the intersection of the incident beam with the detecting "beam." Since the scattering geometry can be very closely defined in this way and since the energy can be controlled quite accurately in the electrostatic machines, the method used in these experiments leads to results that are valid to about one percent. In the work at Minnesota the energy of the bombarding protons has been advanced from 2.4 Mev, the highest energy used at Wisconsin, to 3.5 Mev and the scattered intensity was measured at 8°, 10° and 12.5°, as well as in the range 15°–45° which was studied in preceding work.

The method of theoretical reduction of data on proton-proton scattering appears in the literature in the classic work of Breit[3] and his collaborators. This method is adopted here in its essential features but with certain modifications in application. In the first place, since new data were gathered at angles of scattering smaller than those previously used, we had to compute the Coulomb scattering and interference terms for arguments not appearing in existing tables. We did this by substituting directly into the formula for the differential cross section at the particular energies and angles concerned in the experiments of reference 1. Secondly, the great care taken by the experimenters to eliminate errors in alignment makes it unnecessary to consider corrections that are of first order in such errors. However, special attention is paid to "second order geometry," the corrections arising from the finite width and height of the incident and scattered beams.

The notation introduced in Breit's work will be adopted, for the most part, in the presentation of the fundamental scattering formula. The "phase shift" due to nuclear forces in singlet *S* collisions of two protons will be denoted by K_0,

[1] Blair, Freier, Lampi, Sleator, and Williams, Phys. Rev. 74, 553 (1948).
[2] Herb, Kerst, Parkinson, and Plain, Phys. Rev. 55, 998 (1939). References to the earlier work are listed here.
[3] Cf. especially G. Breit, H. M. Thaxton and L. Eisenbud, Phys. Rev. 55, 1018 (1939). A complete list of background references appears in that paper.

and k and η have the meanings

$$k=(Mv/2\hbar) \quad \eta=(e^2/\hbar v)$$

where M is the mass of the proton, v the velocity of the bombarding proton upon entering the scattering volume and $\hbar$ and e have their conventional significance. Using the fundamental constants reported by Birge[4] we obtain

$$k\eta=1.7352\times10^{11}\ \text{cm}^{-1} \quad \eta=.15806/E_{\text{Mev}}^{\frac{1}{2}} \quad (1)$$

where E_{Mev} is the energy per proton in millions of electron volts, in the incident beam. The velocities of bombardment are small compared with that of light and relativistic effects amount to only a few tenths of a percent. The differential cross section for scattering $\sigma(\theta)$ as measured in the laboratory at the angle θ, may be written

$$\sigma(\theta)=(\cos\theta/k^2)f(\theta). \quad (2)$$

Neglecting relativistic effects as well as nuclear phase shifts in collisions of angular moments greater than zero, the function $f(\theta)$ takes the well-known form:

$$\begin{aligned}f(\theta)=\eta^2\{&\csc^4\theta+\sec^4\theta\\&-\sec^2\theta\csc^2\theta\cos(\eta\ln\tan^2\theta)\}\\&-2\eta\{\csc^2\theta\cos(K_0+\eta\ln\sin^2\theta)\\&+\sec^2\theta\cos(K_0+\eta\ln\cos^2\theta)\}\sin K_0\\&+4\sin^2K_0. \quad (3)\end{aligned}$$

In computing $f(\theta)$ for the various values of η, θ, and K_0 it was found convenient to transform to a new notation:

$$\begin{aligned}&\xi=(8\eta/1-\cos4\theta)\\&a=\eta[2+\cos(\eta\ln\tan^2\theta)]\\&b=\cos^2\theta\cos(\eta\ln\sin^2\theta)+\sin^2\theta\cos(\eta\ln\cos^2\theta)\\&c=-\cos^2\theta\sin(\eta\ln\sin^2\theta)\\&\qquad-\sin^2\theta\sin(\eta\ln\cos^2\theta) \quad (4)\end{aligned}$$

so that:

$$\begin{aligned}f(\theta)=\xi^2&+4\sin^2K_0-\xi\\&\times\{a+b\sin2K_0+2c\sin^2K_0\}. \quad (5)\end{aligned}$$

Equation (5) can be solved for $2K_0$ with the result:

$$2K_0=\sin^{-1}\left\{\frac{\xi^2-\xi(a+c)+2-f(\theta)}{\xi b}\times\cos\left(\tan^{-1}\frac{2-\xi c}{\xi b}\right)\right\}-\tan^{-1}\frac{2-\xi c}{\xi b}. \quad (6)$$

[4] R. J. Birge, Rev. Mod. Phys. 13, 233 (1941).

The measurements required in order to determine K_0 from Eq. (6) are those of the energy, E_{Mev}, the angle of scattering θ, and a value of $f(\theta)$, which is calculated from the observed $\sigma(\theta)$. In practice, however $\sigma(\theta)$ is not observed directly since the differential cross section is a function of the angle of scattering and the latter is not defined exactly by the system of apertures. Since the correction for "second order geometry" becomes of increasing importance as the measured angle of scattering is diminished, an attempt is made here to refine the formula for this correction.

We assume that the incident beam of protons is accurately defined by the small circular (Nylon) "source" window that separates the scattering chamber from the accelerating tube and by a second circular aperture placed between the window and the center of the chamber. The line of centers of the circles forms the axis of the incident beam and the planes of the circles are taken perpendicular to this axis. The optical rays forming the incident beam then form a family of conical bundles, each member of the family originating on a particular element of area, $dudv$, of the source window. This description of the incident beam relies on the supposition that the accelerator side of the Nylon window is bombarded by a uniform current density of protons and that the the protons in passing through the Nylon are scattered sufficiently to supply all the conical rays that pass through the second aperture with the same current. In fact, multiple scattering in the window is adequate to give an essentially uniform distribution of emergent protons within the angles concerned. However, subsequent scattering of the protons from the rectilinear paths by collisions in the gas is a possible source of departure of the description of the actual beam from the model we have assumed. Since the effect of multiple scattering in the gas decreases to zero as the density of the gas decreases to zero, we should rather assert that the ray description of the incident beam holds only in the limit of very low density of gas. The over-all effect of gas density on the observed cross section was tested (cf. reference 1) and found to be negligible at the pressures used in obtaining the data. On this basis, therefore, we assume that the description

of the paths of the protons by straight lines is adequate for computing the geometrical corrections.

A model similar to that for the incident beam is assumed for the family of trajectories that pass through the window of the detector. The detector window is circular and the normal at its center is assumed to intersect the axis of the incident beam at a certain angle, θ. This normal is the axis of the scattered beam and the intersection with the axis of the incident beam is the center of the scattering volume. Between the detector window and the scattering volume is placed a rectangular aperture, normal to and centered on the axis of the scattered beam. The long sides of the rectangle are perpendicular to the plane of scattering, i.e., the plane formed by the incident and the scattered axis. The optical rays that may enter the detector then form a family of pyramidal bundles, each member of the family being designated by having the apex of the pyramid on a certain element of area, $d\xi d\zeta$ on the detector window. The long side of the rectangular aperture is long enough so that every pyramid with apex on the detector window encompasses the entire section of the incident beam. Hence the scattering volume is defined by the intersection of cones with pyramids with axes inclined at an angle near θ and such that the lines of intersection form complete ellipses on the broad faces of the pyramids.

If a proton in the incident beam collides with a proton in the gas within the volume of intersection defined above it may be detected. The intensity of protons originating on the source window in an area $dudv$, scattered in the volume $dxdydz$ and detected on the area $d\xi d\zeta$ of the counter window is

$$d^7I = I_0 N_0 \frac{\sigma(\phi)}{R^2 S^2} \cos\theta_R \, dudvdxdydzd\xi d\zeta \qquad (7)$$

where

I_0 is the intensity (per cm²) emerging from source window
R is vector distance from scattering volume $dxdydz$ to detecting area $d\xi d\zeta$
N_0 is the density of hydrogen nuclei in the gas
S is vector distance from source area $dudv$ to scattering volume $dxdydz$
ϕ is the angle of scattering for the particular paths **R** and **S** (i.e., $\cos\phi = \mathbf{R}\cdot\mathbf{S}/RS$)
$\sigma(\phi)$ is the differential cross section at angle ϕ
θ_R is the angle between R and normal to detecting window.

The measured intensity for a given setting of the detector is the sevenfold integral of Eq. (7). In general, ϕ will be a function of all seven independent variables $\mathbf{R}=\mathbf{R}(x, y, z, \xi, \zeta)$ and $\mathbf{S}=\mathbf{S}(x, y, z, u, v)$ and $\theta_R=\theta_R(x, y, z, \xi, \zeta)$. However, ϕ differs from θ and θ_R differs from zero only by infinitesimal angles, and **R** and **S** differ from R_0 and S_0 only by infinitesimal lengths, where R_0 and S_0 are the distances from the scattering center to the center of the detector window and to the center of the source window, respectively. Since the integral of Eq. (7) cannot be calculated in closed form it is necessary to expand ϕ, $\sigma(\phi)$, $\cos\theta_R$, R^2, and S^2 in ascending powers of the infinitesimal departures from their principal values and perform the integration on the individual terms. For the purposes of analysis of the proton-proton scattering one requires only the leading terms and the terms of one and two higher orders of infinitesimals.

The limits of integration of Eq. (7) are as follows: $dudv$ is to be integrated over the circular area of the source window the radius of which will be denoted by c. Similarly, $d\xi d\zeta$ is integrated over the detector window the radius of which is a. On the other hand, the limits on the $dxdydz$ integration are complicated functions of u, v, ξ, ζ, and are not, in the least way, convenient. In order to obtain an integration over the scattering volume for which the limits are formally independent of the source point and the detecting point we make a transformation so as to describe the scattering point x, y, z, as the intersection of one of the incident rays with a plane formed of detecting rays. The plane is taken parallel to the long side of the rectangular aperture and is then uniquely specified by the detecting point ξ, ζ, and by giving its angle with the corresponding plane through the scattering axis. Actually, if the rectangular aperture stands the distance H before the detector window, a convenient way of describing the angle of the plane is through the parameter t such that the angle is arctan t/H. The limits of integration of the variable t are then evidently $\pm$ the half-width of the rectangular slit, provided the thickness of the aperture walls may be neglected. (The effect of aper-

TABLE I. Calculation of S-wave phase shift K_0.

	$E=2.42$ Mev				$E=3.04$ Mev			
θ	$\Delta_2(\theta)$	$\sigma_{obs}(\theta)$ Barns	$f(\theta)$	K_0	$\Delta_2(\theta)$	$\sigma_{obs}(\theta)$ Barns	$f(\theta)$	K_0
25°	0.0004	0.528	1.699	48°11′1	0.0004	0.483	1.952	51°15′4
30°	0.0001	0.528	1.778	48°37′2	0.0001	0.469	1.984	50°51′4
35°	−0.0001	0.503	1.791	48° 9′6	0.0000	0.450	2.013	50°37′6
40°	−0.0001	0.475	1.809	48° 1′6	−0.0001	0.425	2.033	50°18′7
45°	−0.0001	0.446	1.840	48°21′2	−0.0001	0.402	2.083	51° 1′8
	Average $K_0=48°16′1$				Average $K_0=50°49′0$			
	$E=3.27$ Mev				$E=3.53$ Mev			
θ	$\Delta_2(\theta)$	$\sigma_{obs}(\theta)$ Barns	$f(\theta)$	K_0	$\Delta_2(\theta)$	$\sigma_{obs}(\theta)$ Barns	$f(\theta)$	K_0
25°	0.0003	0.473	2.057	53°34′1	0.0002	0.442	2.075	52°38′1
30°	0.0001	0.450	2.048	51°38′5	0.0001	0.428	2.103	52°13′4
35°	0.0000	0.441	2.122	52° 5′3	0.0000	0.418	2.171	52°35′8
40°	−0.0001	0.410	2.100	51°32′7	−0.0001	0.397	2.205	52°44′0
45°	−0.0001	0.380	2.118	51°33′1	−0.0001	0.366	2.202	52°38′7
	Average $K_0=51°52′7$				Average $K_0=52°34′0$			

ture thickness has been checked experimentally, cf. reference 1.) This half-width is called w. The incident ray needed to define an intersection point with the plane may be specified by giving the point (u, v) on the source window and by giving the point in the plane of the circular aperture (that defines the incident beam) through which the ray passes. It was found convenient to use polar coordinates for this point, ρ the radius from the center of the aperture and ψ the angle from the plane of scattering. The limits on ρ are zero and the radius of the circular aperture which is denoted by b.

The procedure in integrating Eq. (7) is then to substitute for x, y, z in terms of t, ρ, ψ, defined above and replace $dxdydz$ by $[\partial(x,y,z)/\partial\rho,\psi,t)]\times d\rho d\psi dt$, whereupon the integration becomes straight forward. The type of calculation is so evident that we omit the details and present the result with a tabulation of the symbols:

$$I=\frac{I_0N_0\sigma(\theta)2\pi^3wa^2b^2c^2}{L^2HR_0\sin\theta}\Big\{1-\frac{b^2+c^2}{2L^2}-\frac{w^2}{2H^2}-\frac{3}{8}\frac{a^2}{H^2}-\frac{3}{8R_0^2}\Big[a^2+\frac{b^2S_0^2+c^2G^2}{L^2}\Big]+\frac{\cot^2\theta}{4R_0^2}\times\Big[a^2+\frac{b^2}{L^2}(R_0+S_0\sec\theta)^2+\frac{c^2}{L^2}(R_0+G\sec\theta)^2\Big]+\cot\theta\frac{\sigma'(\theta)}{\sigma(\theta)}\Big[\frac{a^2}{8R_0^2}-\frac{a^2}{4HR_0}+\frac{b^2(S_0^2-R_0^2)+c^2(G^2-R_0^2)}{8L^2R_0^2}\Big]+\frac{\sigma''(\theta)}{\sigma(\theta)}\Big[\frac{a^2}{8H^2}+\frac{w^2}{6H^2}+\frac{b^2+c^2}{8L^2}\Big]+\text{higher order terms}\Big\}$$

where

L is distance from source window to circular aperture

S_0 is distance from source window to scattering center

$G=S_0-L$ is from circular aperture to scattering center

H is distance from detector window to rectangular aperture

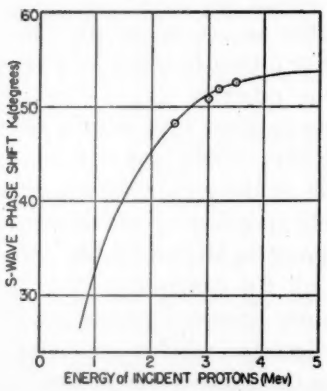

FIG. 1. S-wave phase shift K_0 in degrees is plotted against energy E_p of incident protons in Mev. Values of K_0 determined from experimental cross sections for the proton-proton scattering are shown as open circles. The solid line represents the values of K_0 corresponding to a nuclear potential well of depth 10.5 Mev and range e^2/mc^2 as calculated by Thaxton and Hoisington.

R_0 is distance from detector window to scattering center
θ is measured angle of scattering
$2w$ is width of rectangular aperture
a is radius of detector window
b is radius of circular aperture
c radius of source window
$\sigma(\theta)$ is Eq. (2) evaluated at θ
$\sigma'(\theta)$ is first derivative by θ evaluated at θ
$\sigma''(\theta)$ is second derivative by θ evaluated at θ.

If we denote the curly brackets in Eq. (8) by $\{1+\Delta_2(\theta)\}$ and write the factor in terms of the number of protons registered per second in the incident beam, n,

$$n=(\pi^2b^2c^2/L^2)I_0$$

the expression for the measured intensity becomes

$$I=nN_0\frac{2\pi wa^2}{HR_0\sin\theta}\sigma(\theta)\{1+\Delta_2(\theta)\}. \qquad (9)$$

Through Eqs. (9) and (8) the value of $\sigma(\theta)$ may be computed from the observed I and subsequently $f(\theta)$ and K_0 can be determined. Owing to the fact that quite small apertures were used in the experiments reported in reference 1, the corrections for second order geometry are quite small, amounting to only 2 percent at the smallest angle of scattering.

In Table I we present the results of calculations for angles of scattering larger than 20°. These larger angles were used to obtain the values of K_0 because they are most sensitive to the S-wave anomaly (cf. Breit reference 3) and because the lower angles are more sensitive to errors in voltage, etc., as well as to effects of higher angular momentum. The "observed" differential cross section is that computed from the yield without geometrical correction, i.e.,

$$\sigma_{obs}(\theta)=\sigma(\theta)\{1+\Delta_2(\theta)\}. \qquad (10)$$

In Fig. 1, the average values of K_0, shown in Table I are plotted against the energy of bombardment as open circles. The solid line shown in Fig. 1 represents the theoretical prediction for K_0 as calculated by Hoisington and Thaxton[5] for a nuclear potential well of constant depth of 10.5 Mev and range e^2/mc^2. The phase shifts due to a Yukawa potential corresponding to a mass of around 300 electron masses are also in this region.[6] These potentials are those which fit the experiments on proton-proton scattering below 2.4 Mev. It is evident that the new experimentally determined values of K_0 are satisfactorily accounted for.

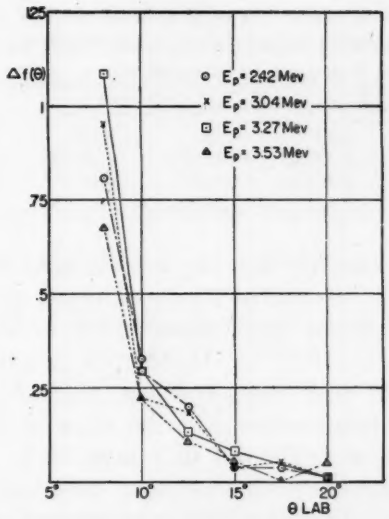

FIG. 2. $\Delta f(\theta)=f(\theta)_{obs}-f(\theta)_{calc}$ is plotted against θ_1, the angle of scattering in the laboratory system, for each value E_p of incident proton energy. The calculated values of $f(\theta)$ correspond to values of K_0 determined from the cross sections at the scattering angles from 25° to 45°.

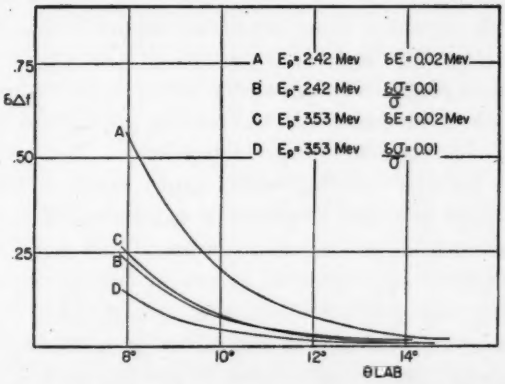

FIG. 3. $\delta\Delta f(\theta)$, the change in the value of $f(\theta)$ which would result from a change in the value of experimentally determined quantities, is plotted against scattering angle in the laboratory system for bombarding energies of 2.42 and 3.53 Mev. $f(\theta)$ is shown corresponding to systematic errors of 0.02 Mev in measurement of bombarding energy and of 1 percent in measured cross section. Other errors in experimental values will produce similar effects.

[5] L. E. Hoisington and H. M. Thaxton, Phys. Rev. 56, 1196 (1939), Fig. 2.

[6] Private communication from Professor Gregory Breit, who has calculated the phase shifts corresponding to mesons of various masses. A paper of his on the subject is forthcoming.

TABLE II.

Values of P-wave phase shift in radians for:
(a) rectangular potential well of range e^2/mc^2 and depth 10.5 Mev,
(b) corresponding to observed cross section.

E in Mev		2.42	3.04	3.27	3.53
K_1	(a)	−0.00302	−0.00413	−0.00460	−0.00515
	(b)	−0.00794	−0.0112	−0.0125	−0.0395

The possibility that the $p-p$ S-wave scattering can be accounted for by a meson potential function with a meson mass of 326, in. was put forward in 1939 by Hoisington, Share, and Breit.[7] At that time, however, the only independent measurements of the mass of mesons in cosmic rays showed that mass to be about 200M. Recently, independent evidence of a meson in cosmic rays with mass in the neighborhood of 300M has been found.[8,9] Furthermore, these heavier mesons are created by nuclear bombardment with the 184-in. cyclotron at Berkeley indicating that they are probably associated with nuclear forces. It is quite possible, therefore, that the proton-proton scattering is directly associated with the properties of a neutral π meson.

The values of K_0 from Table I were used with Eq. (5) to compute $f_{calc}(\theta)$ due to Coulomb and s-wave scattering (Table II) at angles from 8° to 20°. A comparison of the results with the values of $f(\theta)$ obtained from the observations of $\sigma_{obs}(\theta)$ and Eqs. (10) and (2) is plotted as a function of angle in Fig. 2. The difference between the values is seen to increase with decreasing angle, and to show no marked energy dependence. Two possible factors which might cause such a discrepancy are: the presence of scattering of particles with higher angular momenta, and possible systematic experimental errors in energy, cross section or related measured quantities. The angular dependence of the effect of such errors in energy and cross section is plotted in Fig. 3 for the $E=3.53$ Mev and 2.42 Mev. The amount of error is taken to be that of probable error estimated by the experimenters. The observed anomaly in $f(\theta)$ is also shown for comparison. It is seen that the effect of such errors decreases more rapidly with increasing angle than does the anomaly.

On the other hand the discrepancy does not show the increase with increasing energy to be expected of nuclear p-wave scattering. Thus attempts to explain the difference in terms of either alone are not successful. It has been possible, however, to choose a combination of p-wave scattering with phase shifts varying as $E^{\frac{1}{2}}$ and systematic experimental error to account for the anomaly with some consistency. The relative amounts of the two effects are not very precisely determined by the available data. However, the choice made gives results which are plausible. The systematic experimental error which seems to fit is one of about one percent. The p-wave shifts are shown in Table II. Also shown are values of the p-wave phase shifts obtained by extrapolation of the calculations of Thaxton and Hoisington[6] on the basis of a rectangular repulsive well of range e^2/mc^2 and depth 10.5 Mev.

The results of the analysis presented above are that the S-wave phase shifts fit very well with the interpretations previously found for those at lower energy. Especially interesting among these interpretations is the one that appears to connect the proton-proton forces with the new π-meson. However, the S-wave phase shifts are not adequate to account for the observed scattering at angles of 15° and below. In fact, the discrepancies at small angles do not appear to originate from any one source but can be understood as a systematic error in the energy scale of about one percent superposed upon a small, negative P-wave phase shift. The magnitude and sign of the P-wave shift are within reason but the error in energy or other related quantity is very difficult to understand. It must be kept in mind, however, that measurements of scattering at small angles are very sensitive to geometry so that the discrepancies might possibly arise through some undetected effect of this type. In any event the numerical values for K_1 are not accurate.

ACKNOWLEDGMENTS

We should like to thank Professor Williams and the members of the Minnesota electrostatic

[7] L. E. Hoisington, S. S. Share, and G. Breit, Phys. Rev. 56, 884 (1939).
[8] C. M. G. Lattes, G. P. S. Occhialini, and C. F. Powell, Nature 60, 453 (1947).
[9] E. Gardner and C. M. G. Lattes, Science 107, 270 (1948).

generator group for their cooperation in obtaining results especially suitable for the type of calculations used here, including their exceedingly careful elimination of other conceivable causes of the anomaly for which an interpretation is given above. We are also indebted to Professor Breit for sending us the values of the *S*-wave phase shifts corresponding to Yukawa meson potentials. This work was supported in part by the Office of Naval Research.

PHYSICAL REVIEW VOLUME 75, NUMBER 3 FEBRUARY 1, 1949

An Investigation of Bremsstrahlung by Means of the Nuclear Isomerism of Indium*

WALTER C. MILLER AND BERNARD WALDMAN
Department of Physics, University of Notre Dame, Notre Dame, Indiana

(Received October 4, 1948)

The metastable state of In^{115} has been used as a detector of a narrow energy band in the continuous x-ray spectrum produced by a monoenergetic electron beam on gold targets. The thin target x-ray isochromat ($h\nu = 1.04$ Mev) has been investigated in the neighborhood of the short wave-length limit. This isochromat is finite at the threshold and constant for at least 400 kev. This in agreement with Guth's theory and verifies the assumption that the excitation of In^{115*} is a line absorption. Both the thin target and thick target x-ray excitation curves for In^{115} have been obtained in the region from 1.0 to 2.6 Mev. The thin target curve exhibits a step-like character from 1.0 to 1.9 Mev. The thick target curve below 2.0 Mev exhibits straight line segments as expected from the thin target curve, but above 2.0 Mev there are no straight line segments, in good agreement with the thin target data and theory. Activation levels have been found at 1.04 ± 0.02 Mev and at 1.42 ± 0.02 Mev. The over-all cross section (per electron incident on a 34 mg/cm² gold target) is 10^{-34} cm² in the region of the threshold. Evidence is presented for the existence of a lower activation level between 0.8 and 0.9 Mev with an over-all cross section (for a similar target) of the order of 10^{-36} cm².

INTRODUCTION

THE x-ray excitation of the isomeric state of indium (In^{115*}) was first observed almost ten years ago.[1,2] The early work of Collins and Waldman[3] indicated that new information could be obtained about (a) the character of the continuous x-ray spectrum (bremsstrahlung) produced by a monoenergetic electron beam and (b) some nuclear energy levels of the excited nucleus. The latter is exemplified by the work of Waldman and Wiedenbeck[4] on indium and by Wiedenbeck[5] on many other elements.

The first conclusive evidence of nuclear isomerism in a stable nucleus was reported by Goldhaber, Hill, and Szilard.[6] They found that the 4.1-hour negative electron activity of indium could be produced by fast neutrons but not by slow neutrons; in fact, there seemed to be a threshold for the process. This activity was assigned to a metastable state of In^{115} excited by the neutron impact and designated by In^{115*}. They postulated that this metastable state can be reached by a spontaneous transition from a higher energy activation level, and that the negative electron activity may be the internal conversion electrons from the gamma-ray transition, In^{115*} to In^{115}. Lawson and Cork[7] have shown that the energy of the gamma-ray is 338 kev and the conversion coefficient is 0.5.

A. Activation by X-Rays

Pontecorvo and Lazard[1] produced In^{115*} by irradiation with x-rays of 1.85-Mev maximum

* The results of this paper were presented at the M.I.T. Accelerator Conference on June 8, 1948.

[1] B. Pontecorvo and A. Lazard, Comptes Rendus 208, 99 (1939).

[2] Collins, Waldman, Stubblefield, and Goldhaber, Phys. Rev. 55, 507 (1939).

[3] G. B. Collins and B. Waldman, Phys. Rev. 59, 109 (1941).

[4] B. Waldman and M. L. Wiedenbeck, Phys. Rev. 63, 60 (1943).

[5] M. L. Wiedenbeck, Phys. Rev. 67, 92 (1945); Phys. Rev. 68, 1 (1945); Phys. Rev. 67, 267 (1945); Phys. Rev. 68, 237 (1945).

[6] M. Goldhaber, R. D. Hill, and L. Szilard, Nature 142, 521 (1938); Phys. Rev. 55, 47 (1939). See also M. Dode and B. Pontecorvo, Comptes Rendus 207, 287 (1938).

[7] J. L. Lawson and J. M. Cork, Phys. Rev. 57, 982 (1940).

energy from an impulse generator. Independently, Collins, Waldman, Stubblefield, and Goldhaber[2] using x-rays from the Notre Dame electrostatic generator found the threshold for the x-ray excitation to be 1.35±0.1 Mev. Later Waldman, Collins, Stubblefield, and Goldhaber[8] reported a more accurate threshold of 1.2±0.1 Mev. Their excitation curve, i.e., activity *vs.* energy of electrons producing the x-rays, had a sharp break or change of slope at 1.55±0.1 Mev, and they postulated the presence of a second activation level at this energy. Collins and Waldman[3] studied the excitation of indium by x-rays produced in a thin (23 mg/cm²) gold target. This excitation showed a rise in activity at the threshold, followed by a flat plateau up to 1.55 Mev, followed by another sharp rise. Unfortunately, the errors were large in this experiment, and little confidence was placed in the results. The cross section was estimated to be 10^{-33} cm². Waldman and Wiedenbeck[4] carried the excitation to higher energies with a pressure electrostatic generator and found evidence for activation levels at 1.12 Mev, 1.55 Mev, 2.13 Mev, and 2.64 Mev. A decay curve for In^{115*} was followed for 24 hours, and the half-life was found to be 4.42±0.02 hours. In 1943, Korsunsky, Walther, Ivanov, Zypkin, and Ganeko[9] published the results of their work on indium. They irradiated indium with x-rays up to 1.6 Mev produced in a thin (8.9 mg/cm²) target of gold backed by a thick target of beryllium. The activity produced by the beryllium backing was subtracted from that produced by the composite target to give the activity caused by the thin gold. The threshold was found at 1.07±0.05 Mev in good agreement with the Notre Dame value. However, their thin target excitation curve is a smooth curve showing neither plateaus nor straight segments. These results agree with the Bethe-Heitler theory, but this theory does not hold near the threshold.

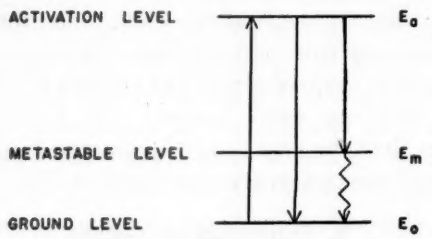

ENERGY LEVEL DIAGRAM

FIG. 1. Energy level diagram.

B. Activation by *p*, *α*, *e*, *n*, and *d*

Barnes and Aradine[10] produced In^{115*} by proton bombardment and estimated the cross section to be 10^{-29} cm² at 5.8 Mev. Lark-Horovitz, Risser, and Smith[11] produced this activity with 16-Mev alpha-particles. Collins and Waldman[12] excited In^{115*} with 1.3-Mev electrons and estimated the cross section to be about 10^{-33} cm². Waldman and Wiedenbeck[4] determined the excitation curve for this electron excitation. Recently Cohen[13] found evidence of a threshold for the neutron activation of In^{115*} at approximately 1 Mev and a cross section at 2.2 Mev of 3.6×10^{-25} cm². Following Guth's suggestion[14] of the possibility of inelastically scattering deuterons by a "polarization" process, Miller and Waldman[15] attempted to produce In^{115*} with 2-Mev deuterons. This activity was not detected thus setting an upper limit for the cross section for this process at 10^{-30} cm².

C. Activation of In^{113*}

Indium has one other stable isotope, In^{113}, which also exhibits nuclear isomerism.[16] Since its abundance is 4.5 percent, the 105-min. activity of In^{113*} is not easily detected in the presence of the 4.4-hour activity. Recently, Dunworth and Pontecorvo,[17] after irradiating indium with very intense 2-Mev x-rays, obtained the composite decay curve for both isotopes, from which the

[8] Waldman, Collins, Stubblefield, and Goldhaber, Phys. Rev. 55, 1129 (1939).
[9] Korsunsky, Walther, Ivanov, Zypkin, and Ganeko, J. Phys. 7, 129 (1943).
[10] S. W. Barnes and P. W. Aradine, Phys. Rev. 55, 50 (1939).
[11] K. Lark-Horovitz, J. R. Risser, and R. N. Smith, Phys. Rev. 55, 878 (1939).
[12] G. Collins and B. Waldman, Phys. Rev. 57, 1088 (1940).
[13] S. G. Cohen, Nature 161, 475 (1948).
[14] E. Guth, Phys. Rev. 68, 279 (1945); Phys. Rev. 68, 280 (1945).
[15] W. C. Miller and B. Waldman, University of Notre Dame, January 15, 1947 Progress Report to Office of Naval Research, Contract N6-ori-83, Task Order II.
[16] S. W. Barnes, Phys. Rev. 56, 414 (1939).
[17] J. V. Dunworth and B. Pontecorvo, Proc. Camb. Phil. Soc. 43, 123 (1947).

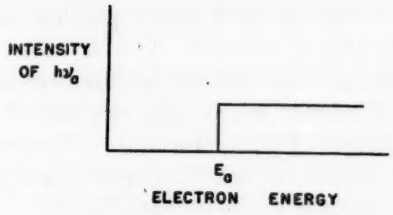

FIG. 2. Thin target isochromat.

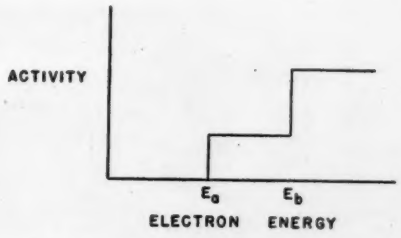

FIG. 3. Thin target excitation curve.

4.4-hour activity was subtracted leaving the 105-min. activity.

The aim of this investigation is to study the process of nuclear excitation by x-rays. This process consists of (a) the production of x-rays by monoenergetic electrons incident on a gold target and (b) the subsequent excitation of indium by these x-rays. In order to simplify the first process x-rays were produced in a thin gold target, however, thick gold targets were also used.

THEORY

Nuclear isomerism in a stable nucleus requires the existence of two energy states of the nucleus: one, the ground state; the other, the metastable state of measurable lifetime. This lifetime may be accounted for by a relatively large spin difference between the metastable and ground states. For a change of spin of 4 units, the lifetime may be from one second to many years and is a highly forbidden transition. The theory of the dependence of lifetime on energy and spin change has been reviewed by Wiedenbeck.[18] Since the transition from metastable to ground state is forbidden, so, also, is the inverse process. Thus, in order to excite a nucleus into its metastable level, it is necessary to raise it into an activation level by absorption of energy E_a, from which it can drop either to the ground level with emission of energy $h\nu_a=E_a$ or to the metastable level with emission of energy E_a-E_m (Fig. 1).

Guth[19] has proposed an energy level diagram for indium in which the spin of the ground state is 9/2, the spin of the metastable state is 1/2, and the spin of the activation state is 5/2. Thus, the transition from metastable state to ground state involves a spin change of four units, whereas the transition from ground to activation state and that from activation state to metastable state both involve spin changes of two units.

The excitation of indium to the activation level may be (a) a line absorption (b) a Raman effect (c) a photo-effect. It is assumed to be a line absorption ($h\nu_a=E_a$) which is detected by virtue of the activity of the metastable level into which it may fall. If indium is irradiated with a continuous spectrum of x-rays, the activity is a measure of the intensity of that line in the spectrum equal to the activation energy. Since an isochromat is the intensity of a line of fixed energy ($h\nu_a$) as a function of electron beam energy E, the shape of the excitation curve in passing the activation energy reveals the shape of the corresponding isochromat.

The wave mechanical theory of the production of bremsstrahlung in the non-relativistic region has been given by Sommerfeld,[20] Sommerfeld and Maue,[21] and Weinstock[22] and confirmed experimentally by Nicholas,[23] Kulenkampff,[24] and the Stanford group under Kirkpatrick.[25] In the relativistic region the Bethe-Heitler theory applies

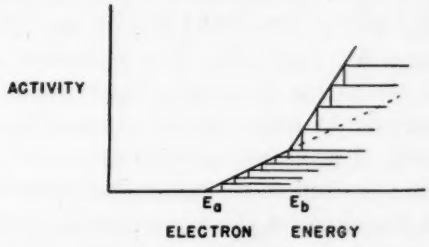

FIG. 4. Thick target excitation curve.

[18] M. L. Wiedenbeck, Phys. Rev. 69, 567 (1946).
[19] E. Guth, Phys. Rev. 59, 325 (1941).
[20] A. Sommerfeld, Ann d. Physik 11, 257 (1931).
[21] A. Sommerfeld and A. W. Maue, Ann. d. Physik 23, 589 (1935).
[22] R. Weinstock, Phys. Rev. 61, 584 (1942); 64, 276 (1943).
[23] W. W. Nicholas, Bur. Stand. J. Research 2, 837 (1929).
[24] H. Kulenkampff, *Handbuch der Physik* 23, 2 (1933).
[25] K. Harworth and P. Kirkpatrick, Phys. Rev. 62, 334 (1942).

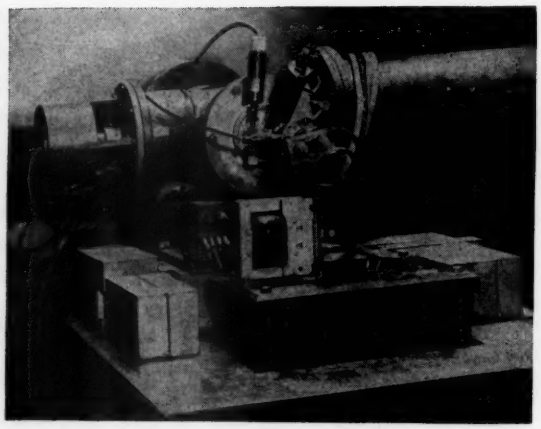

FIG. 5. Rocking target assembly.

within the Born approximation. Since it breaks down at the short wave-length limit (i.e., threshold) Guth[19] has calculated a correction factor to be applied at the threshold. This results in an isochromat which is finite at the threshold and independent of electron energy E in the immediate vicinity of the threshold. His calculations show that an isochromat of $h\nu_a=1.1$ Mev should be constant within 2 percent if E is raised from the threshold to 1.4 Mev.

In the excitation of indium by thin target bremsstrahlung, the energy of the activation level is the energy of the isochromat $E_a=h\nu_a$. As the beam energy is increased, this isochromat should remain constant (Fig. 2), and, consequently, the excitation curve should remain constant. If indium has a second activation level at a higher energy E_b, a second isochromat, $h\nu_b=E_b$, will be detected; and it should have the same flat character. The excitation curve should show this isochromat superimposed on the first; or, in other words, a step-like curve consisting of two plateaus (Fig. 3).

In the excitation of indium by thick target x-rays, the shape of the excitation curve reveals the shape of the thick target isochromat. If the thick target is assumed to be a summation of thin targets, then it is reasonable to assume that the thick target isochromat will be an integral of the thin target isochromat. The excitation curve should have a positive slope from the threshold up to the energy E_b, at which point the height of the infinitesmal thin target steps increases, resulting in a more positive slope as shown in Fig. 4.

If Φ is the cross section for the production of quanta of energy $h\nu_a$ by one electron of energy E' in a target of thickness dx and N atoms/cm³, then the number $n(h\nu_a,E')$ of quanta produced in a thick target is given by Eq. (1).

$$n(h\nu_a,E')_{\text{thick}}=\int\Phi N dx=\int_{h\nu_a}^{E'}\frac{\Phi N dE}{(-dE/dx)}. \quad (1)$$

Assuming Φ and $(-dE/dx)$ are constant over the energy interval $h\nu_a$ to E' then (1) can be integrated

$$n(h\nu_a,E')_{\text{thick}}=\frac{N\Phi}{(-dE/dx)}(E'-h\nu_a). \quad (2)$$

Thus the thick target isochromat is a straight line of positive slope.

EXPERIMENTAL PROCEDURE

A. Irradiation

The thin target x-rays were produced by bombarding a gold foil 34 mg/cm² thick with the electrons accelerated by the Notre Dame Pressure Electrostatic Generator. The activity produced in the indium was sufficiently low that it was advantangeous to place it close to the gold.

The fact that the electrons after passing through the gold could activate as well as melt the indium presented a serious difficulty. A strong magnetic field was placed between the

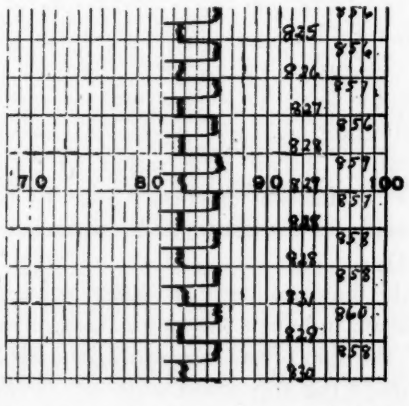

FIG. 6. Brown record of beam current. Full scale is 125 microamperes, and each horizontal line represents 20 seconds. The square wave appearance is due to the reflection of the incident electrons by the gold foil. The small numbers at the right are the estimations of the current for integration.

gold and the indium to prevent the electrons from reaching the indium. This was unsuccessful because the electrons were deflected before reaching the gold in spite of the fact that a magnetic shield was used. A second attempt consisted in placing the indium on the outside of a long evacuated thin-walled aluminum cylinder, coaxial with the beam, the gold foil forming one base of the cylinder, the electron collector forming the other base. This would allow the electrons to be collected at some distance from the indium which was placed near the gold end of the cylinder. The gold scattered enough electrons so that the walls of the cylinder became hot and melted the indium. A water jacket placed around the aluminum cylinder prevented this, but the indium activity was then too small, and the x-rays produced in the aluminum could not be taken into account.

The method finally used was a subtraction process in which the electrons passing through the gold were absorbed by a carbon disk one-half inch thick backed by a one-sixteenth-inch sheet of aluminum. Two such carbon-aluminum absorbers were placed in a water cooled mount with the gold foil on the face of one and indium foils on the backs of both. An electromagnet, energized automatically, rocked first one and then the other of these absorbers into the electron beam with a twenty-second period (Fig. 5). The activity of the indium irradiated by the x-rays produced in the carbon was subtracted from the activity caused by the x-rays produced in the gold plus carbon. The irradiation times were measured by Standard Electric Timers controlled by micro-switches on the rocker, and both samples received the same irradiation time within one percent. The cross-irradiation, i.e., the irradiation of the non-exposed indium foil by the x-rays produced in the exposed target assembly, was negligibly small.

A criterion for a "thin" target is that activity be proportional to thickness. When the 34-mg/cm² gold foil was replaced by a 20-mg/cm² foil, the activity was decreased to approximately 60 percent.

In the thick target experiment the x-rays were produced by stopping the electron beam in a 1.6-mm gold target at the bottom of a copper

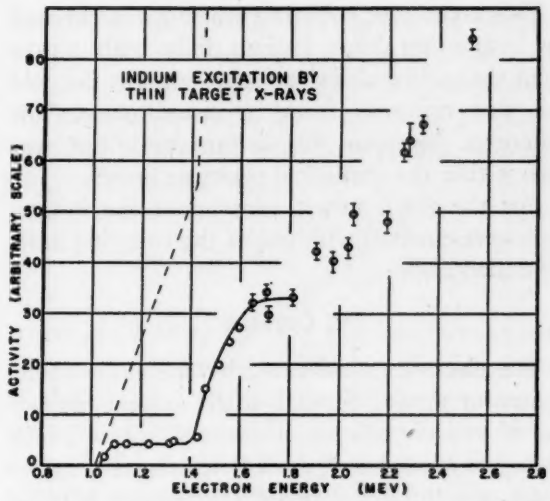

FIG. 7. Thin target excitation curve for indium[115]. Errors in activity and in voltage are less than size of circles unless otherwise indicated. To convert *activity* to *over-all cross section* multiply ordinate by 2×10^{-35} cm² for 34-mg/cm² gold target. Dotted curve is first portion of thick target curve (Fig. 8) to same scale.

Faraday cage. The indium foils were placed on the outside of this cage in line with the beam.

B. Counting

Pure indium metal was rolled into sheets of thickness 0.01 inch, and disks of diameter $\frac{15}{16}$ inch were punched from this sheet. This thickness (185 mg/cm²) is greater than the range of the conversion electrons to be detected. The activity of the two indium foils was measured simultaneously by two similar thin end-window Geiger tubes and scalers. Each foil was counted first on one scaler for 1000 seconds and then on the other scaler for 1000 seconds. This cross-over technique has the advantage that it is unnecessary to know the sensitivity or the geometry of each counter before subtracting the data. It is only necessary that these factors remain constant during the course of the experiment. It can be shown that the difference in activity of the two foils is proportional to the difference between the geometrical mean of the counts from one foil on both scalers and the geometrical mean of the counts from the other foil. The proportionality constant depends on the irradiation time and the delay times as well as the sensitivities of the Geiger tubes. These times were held constant and the same Geiger tubes were used for the entire experiment.

This cross-over counting scheme was checked by irradiating both indium foils with x-rays from the carbon absorbers only—that is, the gold foil was removed from its usual place. The difference between the indium activities was zero within the statistical counting errors.

For the thick target experiment the indium foils were counted with one of the counting units described above.

C. Current

The electrons accelerated by the electrostatic generator passed through a slit system consisting of two circular apertures, the first a $\frac{1}{4}$-inch hole, the second a $\frac{5}{16}$-inch hole, about 9 inches apart and through a one-mil aluminum window onto the rocking target assembly. The current to the target must be measured by a low impedance device since the ionization of the air presents a relatively low impedance leakage path to ground. A multirange sensitive microammeter has a resistance of about 2000 ohms, and this introduces an error of about 10 percent in measuring the target current. This difficulty was overcome by using a Brown recording potentiometer (three-millivolt full scale) to measure the voltage developed by the target current in flowing through a small precision resistor of about 25 ohms. A further advantage of this device is the record obtained. As a result of the motion of the rocker and the reflection of the electrons from the gold foil, it is quite apparent which target is being irradiated at a particular time (Fig. 6).

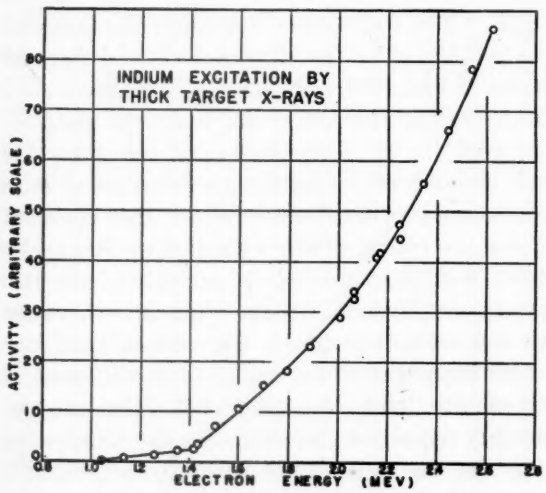

FIG. 8. Thick target excitation curve for indium[115]. To convert *activity* to *over-all cross section* multiply ordinate by 3×10^{-34} cm^2.

The record of the current to each target was integrated by estimating each ten-second interval and summing for each target to obtain the total charge incident on that target. The charge for the gold-carbon target was adjusted for the reflection mentioned above. The mean counts obtained from each indium foil were normalized by the appropriate charge before subtracting the data.

For the thick target experiment the Brown record was integrated with a planimeter whose accuracy was checked on a standard area and found to be ±0.3 percent. The counts obtained from the foil were normalized by this charge.

D. Voltage

The energy of the electrons depends on the potential of the high voltage terminal of the electrostatic generator. This potential was measured by a null type generating voltmeter in which the electric field resulting from the terminal is balanced by a field produced by a battery. The battery voltage was measured to 0.1 percent by a potentiometer. The off-balance of the terminal potential was detected by a gated vacuum tube voltmeter and recorded on an Esterline-Angus recorder. With this device a change in sphere potential of ±5 kv can be detected. The voltmeter was calibrated[26] by determining the photodisintegration thresholds of beryllium and deuterium and accepting Stephens'[27] values of 1.63 and 2.187 Mev, respectively. These values have an accuracy of about ±20 kev so the absolute accuracy of our voltmeter is no better than this.

The output of the voltmeter operates a stabilizing control of the belt charging supply. This stabilizer consists of two parts, a variable impedance circuit similar to Hanson's[28] to compensate for fast changes and a motor driven Variac to compensate for slow changes. With this device a stability of ±5 to 10 kv can be maintained for long irradiations.

---

[26] B. Waldman and W. C. Miller, Phys. Rev. **74**, 1225 (1948).
[27] W. E. Stephens, Rev. Mod. Phys. **19**, 19 (1947).
[28] A. O. Hanson, Rev. Sci. Inst. **15**, 57 (1944).

RESULTS AND DISCUSSION

From the above discussion it can be seen that the errors, except statistical errors in counting, have been reduced to less than one percent. For the thin target experiment where the activity is low, these statistical errors are large. These are increased by the subtraction process so that the total errors are between four and ten percent (standard deviation). For the thick target experiment, the statistical errors are not greater than 2.5 percent and in most cases are about 1 percent.

A. Thin Target

Figure 7 is a plot of the thin target excitation in the region from 1.0 to 2.6 Mev. This shows the sharp threshold and a plateau followed by another sharp rise and a subsequent plateau. The flat portion of this curve indicates that the thin target x-ray isochromat is also constant, at least within 400 kev of the threshold. This is in excellent agreement with Guth's theory and verifies his assumption that *the excitation of indium is a line absorption.* The threshold is at 1.04 ± 0.02 Mev, and the sharp rise indicates an activation level at 1.42 ± 0.02 Mev. These values are lower than those of Waldman and Wiedenbeck[4] (1.12 ± 0.03 and 1.55 ± 0.03 Mev, respectively) because of the lower background counters (8 counts per minute) used in this experiment. The activity just above threshold would not be detected with higher background counters. Above 1.9 Mev the data do not warrant drawing a curve. There is an indication of other steps, but it is not strong. Possibly there are many levels lying close together which cannot be resolved by the method used in this experiment. Or perhaps the thin target isochromat is not flat for more than 500 kev. If it does not remain flat, the sharp rises due to other activation levels would be somewhat masked.

The over-all cross section (i.e., per electron incident on a 34-mg/cm² gold target) at the first plateau is 10^{-34} cm² within an order of magnitude. This over-all cross section σ is the product of two factors

$$\sigma = n(h\nu_a,E)_{\text{thin}} \cdot \sigma_{h\nu_a}, \tag{3}$$

where $n(h\nu_a,E)_{\text{thin}}$ is the number of quanta of energy $h\nu_a$ produced by one electron of energy E in a target of thickness dx and N atoms/cm³, and $\sigma_{h\nu_a}$ is the cross section for the production of the metastable nuclei by a quantum of energy $h\nu_a$. The number of 1.04-Mev quanta, $n(h\nu_a,E)$, as given by Guth[19] is

$$n(h\nu_a,E)_{\text{thin}} = A\frac{Z^2r_0^2}{137}\frac{d(h\nu)}{h\nu_a}Ndx, \tag{4}$$

where $A=3.44$ at 1.1 Mev and $d(h\nu)$ = the width of the level. Since $n(h\nu_a,E)$ is a linear function of the target thickness dx (for a thin target), the over-all cross section, σ, is also a linear function of the x-ray target thickness. Using this value of σ Guth has calculated the width of the 1.04-Mev activation level to be 4 millivolts. Using Eq. (4) one finds that the number of quanta of energy 1.04 Mev in a 0.004-ev width is 10^{-12}. Thus $\sigma_{h\nu_a}$ is of the order of 10^{-22} cm², a value to be expected for a resonance process.

The experimental verification of Guth's theory (Eq. (4)) permits one to calculate the number of 1.04-Mev quanta per incident electron in the energy range 1.0 Mev to 1.4 Mev. This can be extended to thick targets by Eq. (1). In order to determine numbers of quanta of energy other than 1.04 Mev, the slowly varying factor A in Eq. (4) must be evaluated.

B. Thick Target

Figure 8 is a plot of the thick target excitation in the same energy region. As would be expected from the thin target curve and Eq. (2), this excitation curve is a straight line of positive slope from the threshold at 1.04 ± 0.02 Mev to 1.42 ± 0.02 Mev. At this point there is a sudden change of slope corresponding to the sharp rise in the thin target curve. Above this energy the evidence for straight line portions is no more striking than that for more steps in the thin target curve. There are three reasons why one should not expect more straight line segments: (a) the stopping power $(-dE/dx)$ in Eq. (1) is not constant and independent of electron energy in the region above 2 Mev; (2) the thin target isochromat may not be independent of electron energy for more than 500 kev, and the integration of Eq. (1) would not yield a straight line of positive slope; (3) there may be many levels

lying close together which cannot be resolved. Thus, even if there were no levels above 1.42 Mev, and even if the thin target isochromat were completely independent of energy, *one cannot expect a straight line excitation curve above 2 or 2.5 Mev.*

The cross section for the thick target excitation is given by an expression similar to Eq. (3) where $n(h\nu_a,E)_{\text{thin}}$ is replaced by $n(h\nu_a,E')_{\text{thick}}$ from Eq. (2). In the region where the thick target excitation is a straight line, the ratio of the thick target cross section to the thin target cross section is

$$\frac{\sigma_{\text{thick}}}{\sigma_{\text{thin}}}=\frac{n(h\nu_a,E')_{\text{thick}}\cdot\sigma_{h\nu}}{n(h\nu_a,E)_{\text{thin}}\cdot\sigma_{h\nu}}$$

$$=\frac{\int N\Phi dx}{N\Phi\Delta x}=\frac{E'-h\nu_a}{(-dE/dx)\Delta x}, \quad (5)$$

where Δx is the thickness of the thin target. Using the average value of the stopping power in the region from 1.0 to 1.4 Mev of 10^7 volts/cm and $(E'-h\nu_a)$ equal to 400 kev, one finds this ratio should be about 19. A portion of the thick target excitation curve is plotted (dotted line) in Fig. 7 to the same scale as the thin target excitation. At 1.4 Mev the ratio is about 11, which is good agreement with theory when one considers the difference in angular distribution of the x-rays from thick and thin targets.

C. Lower Activation Level

Since the completion of the above experiments, further attempts were made to activate indium below 1 Mev. Five-hour irradiation with a 100 microampere beam of 880-kev electrons on the thick gold target resulted in very weak activity (twice background) of approximately 4.4 hours half-life. Correspondingly higher activity was found at 930 kev. The activity at 800 kev was not greater than 10 percent of background. This is an indication of another activation level below 1.0 Mev, and it may be the level at 873 kev reported by Lawson and Cork.[7] Assuming that this level is at 873 kev, one can estimate the cross section for thin target x-rays using the method of Eq. (5). This results in an over-all cross section of the order of 10^{-36} cm^2 per electron incident on a 34 mg/cm^2 gold target. Activation in this energy region is being investigated at the present time.

D. Self-absorption

Since the excitation of indium is a line absorption, one might expect to observe self-absorption. This was attempted using indium absorbers up to 1-cm thick. Replacing indium by a neighboring element, tin, resulted in an equivalent absorption. Thus, the absorption in indium can be completely accounted for by the usual Compton and photoelectric effects.

The very weak self-absorption is due to the large doppler width (0.7 ev) as compared to the radiation width (0.004 ev). This point has been discussed by Guth.[19]

ACKNOWLEDGMENTS

We wish to thank our former colleagues, G. B. Collins, J. R. Feldmeier, G. C. Wick, M. L. Wiedenbeck, and especially our present colleague E. Guth for stimulating discussions.

This work was supported by a grant from the Fredrick Gardner Cottrell Fund of the Research Corporation and by the joint program of the Office of Naval Research and Atomic Energy Commission.

PHYSICAL REVIEW VOLUME 75, NUMBER 3 FEBRUARY 1, 1949

88-Mev Gamma-Ray Cross Sections

JAMES L. LAWSON
Research Laboratory, General Electric Company, Schenectady, New York
(Received October 18, 1948)

Total cross sections for 88-Mev gamma-rays have been measured in 6 elements by absorption methods to a statistical accuracy of about 1.5 percent. The results expressed in cm^2/gram are 0.0107, 0.0252, 0.0471, 0.0665, 0.0909, and 0.0973 for the elements Be, Al, Cu, Sn, Pb, and U, respectively. Values appear generally lower than predictions of existing theory by a factor proportional to Z^2.

Ratios of pair formation cross sections in different elements have been obtained in a few cases; these data can be used together with the total cross section to obtain non-pair cross sections (presumably Compton scattering). The cross section so obtained at 88 Mev agrees within the experimental accuracy of about 15 percent with the Klein-Nishina prediction for Compton scattering.

INTRODUCTION

EXPERIMENTS have been performed with the gamma-radiation of the 100-Mev betatron in an effort to determine the cross sections for gamma-ray absorption and scattering and to determine the energy spectrum of the radiation. In this paper, the results of some experiments undertaken to determine accurately the cross sections at approximately 90 Mev will be presented; detailed surveys of spectra will be left to future reports.

When this work was started over a year ago it was clear that at least in some cases the theoretical cross section for gamma-rays was in rough agreement with experiment. Semiquantitative information existed from cosmic-ray shower experiments, but perhaps the best evidence came from cloud-chamber experiments by Delsasso, Fowler, and Lauritsen[1] who not only obtained rough information on the total cross section for absorption of 17-Mev radiation but on the individual pair and Compton scattering cross sections. An attempt was therefore made in this work to obtain good statistical accuracy within reasonable limits of effort and to extend the observations to the highest practicable gamma-ray energy currently available.

The total cross section for gamma-rays is probably best determined by measuring the transmission and hence absorption coefficient in particular materials. The measurement of this absorption coefficient at high energies is not as easy as might first be suspected. If one considers the Bremsstrahlung radiation produced by a high energy electron accelerator; e.g., the 100-Mev betatron, one must devise a detector which is sensitive only to the portion of the radiation having the required energy. The pair-detecting spectrum analyzer mentioned below is such a device; the total number of pairs found in a given (small) energy interval is a linear measure of the total number of gamma-quanta in that interval. However, the reduction in intensity near the middle of the Bremsstrahlung energy spectrum caused by intervening absorbing materials is *not* a measure of the true absorption coefficient for that energy. It is a measure of the combined effects of true absorption and scattering (total cross section) and the *increase* of intensity in that interval caused by the scattering of higher energy quanta. This latter effect of the degrading of the spectrum is difficult to evaluate; it depends upon many factors including the particular geometry chosen, etc. However, if one measures the reduction in intensity sufficiently near the upper end point of the Bremsstrahlung spectrum, the degradation of the spectrum can be neglected. This is equivalent to saying that any process for scattering or absorbing the radiation appreciably will reduce the energy enough to fall outside the selected energy region. One needs to know how much of the upper end of the spectrum can be safely used; a large amount is desirable for statistical and stability reasons, but a small amount is desirable to keep degradation correction low. An upper

[1] L. Delsasso, W. Fowler, and C. C. Lauritsen, Phys. Rev. 51, 391 (1937).

TABLE I. Fractional reconverted energy E_c for 100-Mev Bremsstrahlung.

E_c	Compton effect	Pair-Bremsstralung
95 Mev	0.004	0.001
90	0.012	
85	0.019	0.001
80	0.027	0.004
70		0.015

limit to the correction due to degradation can be estimated by making certain assumptions. We shall assume the Bremsstrahlung spectrum given by Heitler[2] with an upper energy limit of approximately 100 Mev. Two processes of absorption; e.g., Compton effect and pair production, are assumed to be appreciable near the upper end point. It will be assumed that the detector responds to radiation above a critical cut-off energy, E_c. We calculate specifically the fraction of initial Bremsstrahlung intensity lying above E_c that is reconverted to radiation of energy greater than E_c for the two absorption processes under consideration. This is a direct indication of the error to be expected in using intensity observations for a calculation of the absorption coefficient. In the case of Compton scattering, one merely calculates the differential cross section for scattering into various energy intervals and compares this with the appropriate total cross section. For the pair process, however, one first must consider the spectrum of electrons and positrons produced from the Bremsstrahlung spectrum. Then one calculates the radiated intensity from these charged particles.

The result of these calculations, shown in Table I, gives specifically the fraction of incident radiation above E_c taking place in the process which is reconverted to energy also above E_c. The table has been constructed for an initial Bremsstrahlung spectrum having an upper limit of 100 Mev.

The permissible cut-off energy for the detector depends upon the final accuracy desired, the ratio of Compton to pair cross section and, of course, on the validity of the above calculations. It is believed that the above figures represent larger errors than are actually found because they neglect the effect of ionization loss (which tends to reduce the energy of the charged particles and hence eliminate them from the energy region under consideration) and they neglect the very important influence of geometrical factors. For example, in the experiments to be described, an angular deflection for a scattered photon of greater than 0.01 radian results in its loss by "geometrical capture;" this effect turns out to greatly reduce the errors shown in Table I; e.g., for a cut-off of 80 Mev the fractional reconverted energy for the Compton effect is reduced to 0.0023 or less than one-tenth the value shown.

These considerations indicate that if one chooses the detector cut-off energy at 80 Mev (for 100-Mev radiation) one can use the results to compute the absorption coefficient with a systematic error of less than $\frac{1}{2}$ percent. This is substantially what has been done in the following experiments; the actual effective cut-off has been placed at about 82 Mev, and it is believed that the systematic error from spectral degradation is less than $\frac{1}{2}$ percent.

In addition to the measurement of total cross section by this absorption method the determination of the individual contributions due to pair formation and Compton scattering has been attempted. This was done very nicely in a cloud chamber by Delsasso, Fowler, and Lauritsen at lower energies[1] by measuring the ratio of electrons to positrons ejected from a radiator illuminated by a monochromatic gamma-ray. This technique cannot be applied directly in this work because the efficiency of collection for a Compton electron is not only different from that of an electron member of a pair but extremely hard to determine. Consequently, the approach has been to measure the ratios of pair cross sections for different materials; this is done by determining the relative numbers of pairs ejected from weighed targets of different materials with known relative gamma-ray dosages. This information allows one to approximately separate the pair formation and Compton scattering; this can be easily seen by writing the ratio of total cross sections in two materials,

$$\frac{\sigma^I}{\sigma^{II}}=\frac{\sigma_p{}^I}{\sigma_p{}^{II}}\frac{(1+\alpha^I)}{(1+\alpha^{II})}. \qquad (1)$$

In this equation the superscripts refer to the

[2] W. Heitler, *The Quantum Theory of Radiation* (Oxford University Press, London, 1944), p. 170.

particular material chosen, σ is the total cross section and σ_p the pair cross section. The symbol, α, denotes the ratio of non-pair to pair cross section (theoretically the ratio of Compton scattering to pair formation). Of course this equation is energy dependent, but at a given energy the individual total cross sections can be measured by absorption and the ratio of pair cross sections by the ratio of pairs ejected from pair-forming targets. Furthermore, if one makes material *II* of high atomic number, Z, and chooses a high energy, e.g., 90 Mev the quantity α^{II} can be almost neglected. For example, for Pb at 90 Mev α^{Pb} is theoretically about 0.02; this figure can be assumed without much discomfort even though the theory is in question. Therefore, one can determine essentially α^I by Eq. (1), and if material I is of low Z, this quantity can be determined with fair accuracy. This clearly allows, with the measured value of σ^I, a check on the value of $\sigma_p{}^I$ and, of course, the non-pair part of the cross section. It is obvious that even a rough indication of Compton scattering at an energy of 90 Mev is a sensitive check on the Klein-Nishina formula.

EXPERIMENTAL TECHNIQUE

The radiation used in these experiments is that given by the 100-Mev betatron operated at full energy; this is presumably the Bremsstrahlung radiation whose spectrum is shown in Heitler[2] and with an upper energy limit of 100 Mev. The radiation is emitted in short bursts lasting a few microseconds which are repeated at a uniform rate of 60 per second. The fact that the peak gamma-ray intensity is so large compared with the average rate imposes severe limitations on the detecting equipment; these limitations fortunately can be overcome by careful design and (generally) complicated and extensive circuitry.

It has been shown that the total cross section for gamma-ray absorption can be obtained by measuring the attenuation of the 100-Mev Bremsstrahlung radiation in various materials; the important consideration is to detect only that part of the radiation lying above perhaps 80 Mev in energy. At these energies it is currently believed that the incident photons are absorbed either by (Compton) scattering by electrons or by forming electron-positron pairs in the fields of the nucleus and electrons.[3] The Compton effect could be used as an energy-selective means of detection but, unfortunately, the energy of the ejected electron is not a unique indication of the gamma-ray energy.[4] On the other hand, the total energy of a pair is substantially the energy of the gamma-ray responsible for its production; this feature makes the detection of pairs quite suitable for energy selection.[5]

The easiest system for the detection of high energy pair particles appears to be a set of counters suitably arranged in or around an energy-separating magnetic field. With only a pair of counters, one generally runs into confusion of multiple pairs unless one operates the system at a distressingly low recording rate. An array of counters allows an enormously increased recording rate for two reasons. First, a much greater fraction of all pairs formed are recorded and, second, if the efficiencies are high enough, multiple pairs formed in the target can be detected (by the simultaneous discharge of more than two electron or positron counters) and therefore eliminated in the final recording. A qualitative calculation shows that the use of a multiple counter array in the experiments to be described has resulted in a time saving for data collection of several years. Furthermore, it has resulted in a much clearer understanding of the various "dirt" effects in the apparatus.

The experimental procedure which has been used is to measure the relative intensity of high energy radiation by means of the high energy pairs formed in a thin gold radiator (usually 0.002-inch thick). The intensity attenuation obtained by interposed blocks of various materials is then used to compute the cross sections. The average effective energy of the radiation is

---

[3] The photoelectric effect is negligible in all elements at these energies.

[4] The angle of ejection could be used also, but the angles involved are so small that they appear difficult to evaluate.

[5] The pairs formed in the field of the electrons may actually emerge as *triples*, i.e., the electron causing pair formation may itself be ejected with considerable momentum. However, the usual case is that the energy of this third particle will lie below mc^2, and can be screened out by appropriate stopping materials. Furthermore, in the experiments using pair-forming materials, high atomic number Z is chosen so that nuclear pair formation greatly predominates.

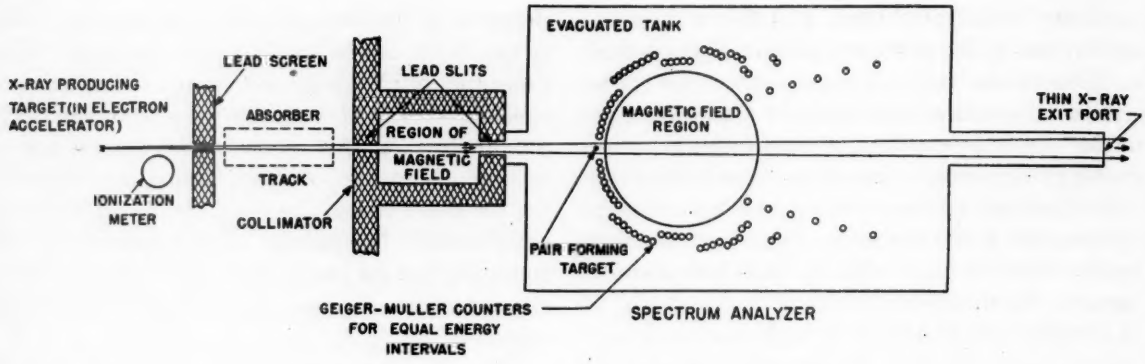

FIG. 1. Schematic diagram of equipment.

computed from the theoretical shape of the Bremsstrahlung spectrum and the expected energy resolution of the pair-forming spectrometer. The assumption of Bremsstrahlung shape can be checked by the intensity ratios found experimentally in adjacent energy channels; the agreement is good enough to assure proper average energy determination to about one percent. This average energy in the experiments to be reported is 88 ± 1 Mev. This inaccuracy in energy is unimportant as cross sections probably do not vary rapidly in this range.

The radiation from the betatron is subject to intensity fluctuations and also requires collimation; the complete experimental equipment is shown schematically in Fig. 1. The beam passes in order through an ionization radiation meter, absorber track, collimator, and pair-detecting spectrum analyzer. The radiation meter in front of the absorber rack is designed to measure the total incident dose during a typical run. It will be noticed that the meter is situated just outside the main beam and also that between the meter and absorbing rack there is placed a thick lead absorber. The purpose of this arrangement is to make the radiation meter insensitive to radiation scattered back from the absorbing blocks; this requirement is obvious if one wishes to have a reading proportional to the incident dose in which the proportionality constant is independent of the presence of absorbing blocks. For the particular geometry chosen the influence of absorber scattering on the meter reading was tested by using a given dense absorber in the two extreme positions on the rack. The ratio of pairs (see discussion below) in the spectrum analyzer to the radiation meter reading was essentially independent of absorber position; this measurement was sufficient to insure a maximum meter correction of less than 0.5 percent for any absorber in the track.

The collimator furnishes a clean gamma-ray beam which does not appear to produce appreciable secondary effects from the various parts of the spectrum analyzer.

The pair-forming spectrum analyzer consists of a thin pair-forming target and a curious array of Geiger-Müller counters about a (circular) magnetic field region. There are many possible field and counter arrangements; the one which has been chosen was designed for pair spectrum measurements up to energies of 200 Mev and is so arranged that each electron (or positron) group of counters represents 15-Mev energy intervals. It is important to note that the region of magnetic field must be large enough that the magnetic deflection between adjacent intervals exceeds comfortably the angular electron or positron scattering in the pair-forming target. This condition requires a magnet structure whose size is not greatly influenced by the highest energy under surveillance; an adequate magnet weighs 5 or 10 tons.[6]

One of the troublesome features of the entire experiment was the nature of the betatron radiation itself. Considerable time was spent in getting a clean x-ray beam; in the early stages of operation the radiation would arise from two

[6] For lower energies where semicircular focusing is feasible, wide-angle particle scattering is permissible; this desirable feature, however, cannot be extended into the several hundred-Mev range without monstrous magnet structures.

or three well separated spots in the betatron. It is clear that the excellence of collimation depends upon a small initial source of radiation. Fortunately, this difficulty finally disappeared when the proper target was installed in the betatron. Secondly, the intensity of the beam would fluctuate enormously from pulse to pulse. There was no obvious cure for this defect, but careful dosage monitors were used for calibrations.[7] Thirdly, the position of the collimated x-ray beam would slowly change due to betatron temperature. These changes, while ordinarily considered negligible, materially altered the ratio of pairs produced from a given target to the monitor dose reading. Therefore, it was necessary to make interpolated short runs (usually 10 min.) for most measurements. Finally, in the measurement of pairs near the upper limit of the spectrum, it is obvious that small changes in betatron energy would cause serious fluctuations in number; actually a one percent change in energy would generally give about a six percent change in pair counting rate. The betatron energy fluctuates with the power supply line voltage and, because of the high Q circuit, also with the line frequency. It was fortunately possible to control the energy to about 0.1 percent by continuously watching the mega-voltmeter and providing appropriate manual corrections.

In the actual use of the spectrum analyzer, one is always confronted with the background correction. The determination of background rates is a very important consideration. At very low recording rates, the background of chance "pairs" from coincident random single events may be negligible, but the statistical accuracy available from these low pair-recording rates is correspondingly poor. At reasonable rates, the background corrections are quite important, and, in the experiments reported here, have been determined usually to within 10 percent. The various background effects have been separated in two or three ways. First, the measured quantities during a normal run are not only the spectrum of pairs, but the spectrum of single events and the number of multiple events. A "single" is defined as an event in which only one counter of given sign (positron or electron) is discharged; a "multiple" is an event where at least two counters of the same sign are discharged. From this information, it is possible to calculate the background correction for pairs. This can be seen as follows.

Let us assume that counters are discharged by one of two mechanisms—either by true pair particles from the pair-forming target or by random single events, whether or not these singles be caused by room background of scattered radiation, cosmic rays, or by fragments of true pairs (the other member of the pair does not, for some reason, produce a corresponding discharge in a counter—it may be lost by geometry, absorption, or scattering). Denote for these two mechanisms probabilities (per betatron pulse) p_l and s_j^- and s_k^+, where p_l is the probability for a recorded pair in the lth energy interval, s_j^- is the probability of recording an electron single in the jth energy channel and s_k^+ is the corresponding probability for the kth positron channel. The actual recorded rates for "zero" events (no discharges), Z, electron singles, S_j^-, positron singles, S_k^+, and pairs, P_l, will then evidently be

$$Z=e^{-\phi} \tag{2}$$

where ϕ denotes the sum of all the p_l, s_j^- and s_k^+.

$$S_j^-=Z(e^{s_j^-}-1) \tag{3}$$

$$S_k^+=Z(e^{s_k^+}-1) \tag{4}$$

$$P_l=Z[p_l+\delta_l+\sum(e^{s_j^-}-1)(e^{s_k^+}-1)] \tag{5}$$

where δ_l involves higher terms in p_l. Equations (3) and (4) contain the curious exponential factor; this is necessary to take into account the events in which two or more random events occur in the same counter channel actually registering as a single. The summation term in Eq. (5) is the "background" term for pairs; the summation must be made over all energy combinations j and k adding up to the energy interval l. From these equations, it is clear that the probabilities p, s^-, and s^+ can be easily calculated from the observed rates Z, S^-, S^+ and P.

This mathematical formulation can be trusted only as far as the original assumptions can be justified, i.e., that only the two stated processes

[7] The fluctuations are still troublesome because the calibrated monitor reads only the average intensity. For many of the measurements, one needs to know the mean intensity, mean square intensity, mean cube intensity, etc.

contribute towards counter discharges. This has actually been tested by a sample experiment without the pair-forming target and determining a calculated chance pair spectrum (the summation term of Eq. (5)). This has been compared with the measured "pair" spectrum and the agreement has been excellent for all high energy pair channels. Tests have also been made of the way in which the net p_l varies with target thickness, and, although this is complicated by particle scattering in the target, it is found that p_l is proportional to target thickness. Nevertheless, in the cross-section experiments to be reported, the background correction has been held to less than 10 percent of the true pairs; this is done simply by limiting the intensity of x-ray beam.

DESCRIPTION OF EQUIPMENT

A detailed description of the equipment in this paper is not necessary; however, a few points of interest can be mentioned. The dose integrating meter at the front of the absorber rack consists of an argon-filled ion chamber connected to a vacuum condenser having a capacitance of about 10^{-9} farad. The storage time constant of this condenser is noteworthy; even with a one-mg radium source one foot away the leakage time constant was measured to be greater than 50 years. Connections to the storage condenser are made in the vacuum at the beginning and end of the run. For reading the condenser potential a Dersham electrometer is used as a null device; the condenser voltage is balanced by an external accurately measured potential. In this way an accuracy of 5 mv is obtained even when reading potentials up to 10 volts. The ion chamber is specially made to have constant sensitivity even when the collector changes potential.

The collimator consists essentially of two thick (about 10 inches) lead slits with an intervening region of magnetic field. The first slit defines the beam aperture and the magnetic field sweeps all charged particles aside. The second lead slit does not quite touch the beam; it is designed to remove only the (wide) secondary radiation produced at the first slit. The entire collimator is, of course, evacuated.

The spectrum analyzer tank is shown schematically in Fig. 1; the actual box is shown in Fig. 2. It is essentially a large evacuated box containing the Geiger-Müller tubes and pair-forming target. While the Geiger-Müller tubes can be operated very easily in an induction of 5000 gauss[8] the tubes associated with the electronic amplifier must be located well out of the magnetic field. The leads in the evacuated tank to the individual Geiger-Müller channels must be mutually shielded; low capacity coaxial tubes are satisfactory. The target consists of a thin 8-mm ribbon of the selected material; actually a target rack containing several elements is used. Selection of the desired element is made by an external control.

An important part of the spectrum analyzer is the magnetic field. In this model a moderate flux density (4000 gauss) was used with a large (2-foot diameter) pole face. The field was controlled automatically by a device using the proton resonance principle described by Purcell *et al.*[9] In this control apparatus the frequency of the radio signal instead of the value of magnetic field was modulated over the resonance; this necessitated the construction of a balanced bridge nearly insensitive to frequency and microphonics. Such a bridge was actually made and is in use but the author cannot recommend this procedure for general use. Nevertheless the control apparatus was finally made reliable and could easily control the field to 0.01 percent over long periods of time. The chief trouble encountered in its actual use with the betatron was the microphonics from the high noise level (about 105 db) in the betatron room during x-ray generation.

The Geiger-Müller counter information from preamplifiers located at the spectrum analyzer tank is fed to an analyzing circuit by means of several coaxial cables. The analyzing circuit only gives an output coincident with the betatron x-ray pulse. The circuit puts directly on registers

[8] The operation of the Geiger-Müller tubes in a magnetic field was investigated by shining light through an end seal liberating photoelectrons from the cathode. The counting rate and pulse shape from this source was found independent of magnetic induction at least up to 5000 gauss. The photoelectrons are ideal for this test. They are liberated in numbers independent of magnetic flux and are at the same time of very low energy and far from the anode, so that they are most easily influenced by magnetic fields.

[9] E. M. Purcell, H. C. Torrey, and R. V. Pound, Phys. Rev. 69, 37 (1946).

the spectrum of single events of both signs, spectrum of pairs, and number of multiple events. This operation unfortunately requires about 200 vacuum tubes and associated parts.

In spite of the large number of tubes required (about 500) for proper operation of the entire equipment the overall electronic reliability has been very gratifying. Electronic failures have prevented operation for less than one percent of scheduled time; the chief reasons for this record are conservative ratings on components and built-in test equipment.

EXPERIMENTAL RESULTS

Total Cross Section

The total cross section for 88-Mev gamma-rays has been obtained by absorption methods in 6 elements—Be, Al, Cu, Sn, Pb, and U. The preparation of the absorbing samples was found quite difficult because of the purity requirement (varies with the element but ought to be at least 99.5 percent) and the degree of homogeneity required. For example, in one of the early aluminum castings which had been rolled to decrease porosity, the measured sample density was about 0.5 percent too low; this led to the discovery of an internal longitudinal cavity which would have completely invalidated an absorption measurement. The final samples have, however, been carefully checked for density, uniformity and purity; in all cases except that for Be the purity has been higher than 99.85 percent. In the case of Be, the purity is not known precisely; the chief contaminant is oxygen and is believed to contribute about 0.5 percent by weight. All other contaminants total less than 0.5 percent, including the effective porosity factor. The exact oxygen content is now being determined.

The absorbing samples were designed to provide two transmission factors of about 0.3 and 0.1. The smaller figure gives more accurate statistical results, but the larger figure was used in a few instances to provide a check. In no case was there observed a discrepancy in measured absorption coefficient with the two absorber thicknesses.

The determination of an absorption coefficient at one energy for a given material to an accuracy of about two percent requires an operating time of about one day. During this run, the intensity is usually adjusted in the betatron so that at least one counter in the array is discharged on about one-half of the betatron bursts; of these events about one-third are true pairs and the rest are background single events. The background singles are largely caused by scattered low energy radiation (perhaps one to 10 Mev) in the betatron room. It is perhaps surprising that the amount of this softer radiation in the room is so high; however, it probably is caused chiefly by the betatron electron beam after striking the target which causes the main x-ray beam. In the figures which have already been quoted, the spectrum analyzer counter array is already shielded from the room by about one ton of lead arranged to give the lowest effective singles background per recorded pair.

The results of several measurements made on various absorbing samples is shown in Table II, and a weighted average of the individual measurements on each material is given. The cross section is quoted for convenience both in cm^2 per gram and in cm^2 per atom. The errors which are quoted are in all cases the probable statistical error and do not include possible systematic errors. It is believed, however, that for all cases, except that for Be, the systematic error is so small that it will not affect the result. In the case for Be, a correction of -0.7 ± 0.3 percent is shown because of contamination; it is clear that a small contamination of a heavy element in a light element is much more serious than a small contamination of a light element in a heavy

FIG. 2. Spectrum analyzer.

TABLE II. Experimental values of total cross section at 88 Mev.

Sample	Approx. transmission	cm²/g	cm²/atom	Probable statistical error	Date
Be	0.28	0.0107_8	0.161×10^{-24}	1.2%	7/15/48
(corrected for contaminant)		*0.0106_9*	*0.160×10^{-24}*	*1.5%*	
Al	0.4	0.0247	1.10×10^{-24}	13.5%	11/24/47
	0.4	0.0271	1.21×10^{-24}	11.0%	11/25/47
	0.18	0.0256	1.15×10^{-24}	3.5%	12/15/47
	0.18	0.0249	1.11×10^{-24}	4.7%	5/11/47
	0.075	0.0251	1.12×10^{-24}	1.8%	5/13/47
weighted average		*0.0252*	*1.128×10^{-24}*	*1.5%*	
Cu	0.12	*0.0471*	*4.971×10^{-24}*	*1.5%*	5/21/48
Sn	0.08	0.0662	13.1×10^{-24}	2.2%	5/13/48
	0.08	0.0695	13.7×10^{-24}	2.4%	5/21/48
	0.08	0.0664	13.1×10^{-24}	1.7%	5/27/48
	0.08	0.0654	12.9×10^{-24}	1.6%	5/28/48
weighted average		*0.0665*	*13.11×10^{-24}*	*0.95%*	
Pb	0.4	0.0868	29.8×10^{-24}	13.0%	11/24/47
	0.1	0.1010	34.7×10^{-24}	13.0%	11/24/47
	0.4	0.0720	24.8×10^{-24}	17.0%	11/25/47
	0.1	0.0910	31.3×10^{-24}	11.0%	11/25/47
	0.14	0.0919	31.6×10^{-24}	3.7%	12/10/47
	0.14	0.0900	30.9×10^{-24}	3.3%	12/12/47
	0.14	0.0910	31.3×10^{-24}	2.2%	5/11/48
weighted average		*0.0909*	*31.27×10^{-24}*	*1.6%*	
U	0.1	*0.0973*	*38.46×10^{-24}*	1.1%	7/16/48

element. It can be seen that the results are internally consistent even though they were obtained with a variety of absorbers. Some of the early results were obtained in the latter part of 1947 with a different counter geometry in the spectrum analyzer. The change in geometry was not required for absorption measurements but was necessary in order to improve the low energy interval efficiency for spectrum measurements.

It does not appear profitable to attempt a much more accurate statistical result except perhaps for a single test case. In order that the systematic errors be kept smaller than the statistical error one must operate at a correspondingly low intensity; the result appears to be that in order to halve the listed errors an increase in operating time of about tenfold is required.

Ratios of Pair Cross Sections

The ratios of pair cross sections at 88 Mev in different elements has been measured by counting directly the ratios of 88 Mev pairs ejected from weighed targets of the test elements with equal x-ray bombardment. The accuracy with which a ratio is determined is not as high as for the total cross section chiefly because the statistics are not as favorable, energy fluctuations in the betatron are more serious, and scattering corrections in the spectrum analyzer are more important. The statistics can be improved slightly by considering larger energy intervals; this procedure is probably quite safe since the ratio of pair cross sections in two elements is not expected to be violently dependent on energy. The chief expected variation with energy comes from the different screening corrections applied principally at the high energies. For this reason the experimental results will be quoted in two ways; no subscript will signify the value obtained directly at 88 Mev, while the subscript, w, will signify the result at 88 Mev of the best theoretical curve through the experimental points above 50 Mev. This theoretical curve is not a constant only because of screening; however, in practice the screening corrections are very small.

In this experiment one must be quite sure that the measured number of pairs is proportional to the pairs actually produced. For targets of different thicknesses, the angular distribution of pair fragments varies because of multiple scattering in the target itself; unless the efficiency of the spectrum analyzer is independent of this scattering one can easily obtain incorrect pair cross-section ratios. The procedure used in the following experiments has been to first choose targets sufficiently thin that these scattering corrections are small; this is tested by observing directly the correspondence between observed pairs and target thickness. Second, the test targets were made thick enough to give about the same theoretical multiple scattering; this thickness incidentally gives nearly the same yield of pairs. This was not quite possible in the case of a heavy element for mechanical reasons, but was sufficiently well approximated that corrections are negligible.

It was hoped that information could be obtained on the same elements for which total cross sections were obtained, but it was clear from Eq. (1) that the principal information was to be obtained on light elements in comparison with a

TABLE III. Ratio of pairs ejected from equal target weights.

Combination	Date	R	error	R_w	error
Be/Au	8/ 5/48	0.089	3%	0.093	2.0%
Al/Au	8/18/48	0.2665	2.6%	0.274	1.0%
Cu/Au	8/12/48	0.482	3%	0.505	1.5%
Be/Cu	8/ 6/48	0.1875	3%	0.192	1.2%

TABLE IV. Experimental values of α at 88 Mev.

Element	Combination	α	error	α_w	error
Be	Be/Au	0.38	0.05	0.32	0.04
Al	Al/Au	0.082	0.05	0.052	0.04
Cu	Cu/Au	0.116	0.06	0.07	0.04
Be	Be/Cu	0.29	0.05	0.26	0.04

single heavy element. An attempt was made to construct a thin radiator of lead for the comparison heavy element, but for the required thickness of about 10^{-3} cm the mechanical properties of such a foil were inadequate. Consequently a foil was made of pure gold (99.97 percent) of about the proper thickness. This foil is strong and fairly uniform. Pure foils were also made of Be, Al, Cu, and Sn for these experiments. The chief problem in the construction of a suitable foil appears to be the determination of thickness in a specified region. This was done by cutting a large sheet of the material into uniform pieces around the region under consideration and plotting the measured density contours. In this way the effective thickness of the target was determined to about one percent even though some of the foils were thin as 0.001 cm.

The results of several measurements are shown in Table III which lists the ratios, R, of pairs ejected per unit weight of target. As already explained, the symbol R_w represents the 88-Mev value obtained by the best fit for data above 50 Mev.

This information can be used in Eq. (1) to determine the experimental ratio of non-pair to pair cross sections at 88 Mev if one first finds the total cross section in Au and then assumes a value for α for the heavier element. The total cross section in Au can be inferred from the value found in Pb; the only assumption is that the cross section in cm² per atom is a smooth function of atomic number, Z. This interpolation procedure yields an "experimental" total cross section in Au of 0.0896 cm² per gram ± 1.6 percent. For the two heavier elements, Au and Cu, appearing in Table III, the theoretical values of α at 88 Mev have been assumed (see discussion below); these are 0.024 for Au and 0.06 for Cu. The result is shown in Table IV, where for convenience the combination is shown from which the determination was made.

COMPARISON OF EXPERIMENTAL RESULTS WITH THEORY

The theory of gamma-ray absorption is not yet complete so that precise comparison with experiment is impossible. However, the theory of Compton scattering is complete and yields the Klein-Nishina formula[10] easily evaluated for any energy and material. The theory of pair formation in the field of the nucleus exists,[11] but the numerical values available are limited by the accuracy of reading some curves not designed for high precision.[12] Furthermore, this theory has led to curves of cross-section values as a function of Z;[13] these curves are, however, calculated under the assumptions of the Fermi-Thomas atomic model and the Born approximation. It is unfortunate that in the case of heavy elements one distrusts the Born approximation and in the case of light elements one distrusts the Fermi-Thomas atom. In fact, Wheeler and Lamb have shown[14] that in the elements hydrogen and nitrogen the results using the Fermi-Thomas model can differ appreciably from those obtained using the exact wave functions. Consequently, there does not appear to be any theoretical numerical values for pair formation which can be compared precisely to the experimental results. Therefore, for definiteness in the following discussion the theoretical pair cross section will be defined as that obtained by the Fermi-Thomas atom and Born approximation; it is hoped that in the future some pertinent numerical theoretical values for exact wave functions become available.

In addition to pair formation in the field of

[10] See, for example, reference 2, p. 157.
[11] H. Bethe and W. Heitler, Proc. Roy. Soc. **146**, 83 (1934).
[12] See, for example, reference 11, p. 93.
[13] See, for example, reference 2, p. 201. These cross-section curves are apparently not very accurate; they have recently been recalculated and plotted by P. V. C. Hough who has furnished the author with the new curves.
[14] J. A. Wheeler and W. E. Lamb, Phys. Rev. **55**, 858 (1939).

TABLE V. Theoretical cross sections at 88 Mev.*

	Be		Al		Cm	
	cm²/g	cm²/atom	cm²/g	cm²/atom	cm²/g	cm²/atom
Pairs (nucleus)	0.005928	0.0888×10^{-24}	0.02035	0.9113×10^{-24}	0.04186	4.418×10^{-24}
Pairs (electron)	0.001565	0.0234×10^{-24}	0.00167	0.0748×10^{-24}	0.00153	0.161×10^{-24}
Compton scatt.	0.00240	0.0359×10^{-24}	0.00261	0.1169×10^{-24}	0.00247	0.261×10^{-24}
Total	0.00989	0.1482×10^{-24}	0.02463	1.103×10^{-24}	0.04586	4.840×10^{-24}
$\alpha_{theor.}$		0.321		0.118		0.057

	Sn		Pb		U	
	cm²/g	cm²/atom	cm²/g	cm²/atom	cm²/g	cm²/atom
Pairs (nucleus)	0.06511	12.83×10^{-24}	0.09803	33.72×10^{-24}	0.1068	42.21×10^{-24}
Pairs (electron)	0.00138	0.27×10^{-24}	0.00127	0.44×10^{-24}	0.0012	0.49×10^{-24}
Compton scatt.	0.00228	0.45×10^{-24}	0.00214	0.74×10^{-24}	0.0021	0.83×10^{-24}
Total	0.06877	13.55×10^{-24}	0.1014	34.90×10^{-24}	0.1101	43.53×10^{-24}
$\alpha_{theor.}$		0.0343		0.0237		0.0193

* There is also shown in this table, labeled $\alpha_{theor.}$, the ratio of cross sections for Compton scattering and pair production.

the nucleus there is, especially in light elements, pair formation in the field of the electrons. Wheeler and Lamb[14] have calculated the cross section for this process, with the usual assumption of Fermi-Thomas atom and Born approximation (which should be very good for electrons), and in addition neglecting the effect of high-momentum transfers to the electron. They have also furnished exact results for hydrogen which deviate appreciably from the Fermi-Thomas hydrogen atom. There appear in the literature other papers dealing with pairs formed in the field of the nucleus[15] but for definiteness the Wheeler and Lamb treatment will be considered here. In addition to the Compton effect and pairs formed in the fields of the nucleus and electrons, there are conceivably other processes which might contribute to the total cross section. Hamilton and Peng[16] have found that the scattering of a light quantum by the nuclear meson charge cloud can give a substantial cross section up to 1000 Mev; however, effects of this type of scattering at 90 Mev are not calculated[17] and in the following discussion will be assumed negligible. The possible contribution of gamma-nucleon cross section is not known, but information exists on some absolute cross sections which indicates that at energies near the resonance the cross section can be as large as the Compton effect.[18] However, it appears likely that in most elements the contribution above 50 Mev is small.

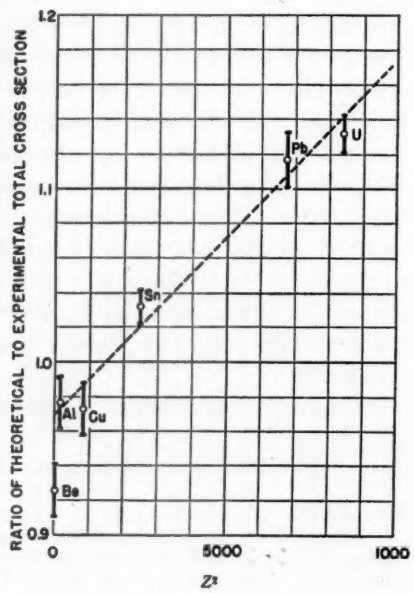

FIG. 3. Ratio of theoretical to experimental cross section *vs.* the square of atomic number.

We have therefore three processes which theoretically contribute appreciably to the total cross section. The cross sections for these at 88

[15] First mention was by F. Perrin, Comptes Rendus **197**, 1100 (1933); K. M. Watson, Phys. Rev. **72**, 1060 (1947) (results do not agree with Wheeler and Lamb); P. Nemirovsky, J. Phys. U.S.S.R. **11**, 94 (1947) (considers only energies <3 Mev); A. Borsellino, Helv. Phys. Acta **20**, 136 (1947); V. Vortruba, Phys. Rev. **73**, 1468 (1948).

[16] Hamilton and Peng, Proc. Roy. Ir. Acad. **49A**, 197 (1944).

[17] Such calculations would probably not be very significant anyway because of present uncertainties in meson theories.

[18] J. L. Lawson and M. Perlman, Phys. Rev. **74**, 1190 (1948).

Mev are shown in Table V; for convenience the cross sections are listed both in cm^2 per gram and cm^2 per atom.[19]

We may now compare the experimental and theoretical total cross sections from Tables II and V. Discrepancies clearly exist especially for heavy elements; this fact leads one to suspect the failure of the Born approximation in giving the proper theoretical result. One would expect the failure of the Born approximation to be proportional to $(Z/137)^2$; consequently a plot of the ratio of theory to experiment *vs.* Z^2 should be linear.[20] Such a plot is shown in Fig. 3 where the ordinate is expanded for easy visibility. The errors shown on the points are the probable statistical errors of the experimental results only; the error associated with the theoretical values is probably caused mainly by the theoretical approximations used. It is clear that the curve in Fig. 3 is mainly linear in Z^2 indicating that the present theory gives a larger cross section than is actually measured by about $Z^2/500$ percent. It is surprising that at lower energies (<3 Mev) the result of exact calculation[21] gives a correction of opposite sign. It is not clear whether or not at high energies the size and sign of the correction can be inferred from the low energy results. It is hoped that when exact calculations of pair production in heavy elements are made available this discrepancy can be understood.

The intercept of the curve in Fig. 3 for small Z^2 is approximately unity indicating that the theoretical predictions for pair production and Compton scattering are approximately correct. The experimental results are actually somewhat larger than those from theory possibly because of slight theoretical failure, experimental inaccuracy, or perhaps because of some other contributing process. The experimental point for Be is unfortunately distinctly off the linear plot. It was suspected that this might be in part caused by the Fermi-Thomas model. Exact calculations have now been made by R. Ehrlich and H. Hurwitz,[22] using the known wave functions for Be, to check this possibility. The exact results increase the theoretical cross section to 0.00996 cm^2 gram which accounts for only about 0.2 of the discrepancy.

With respect to the ratio of non-pair to pair cross sections, the values of α obtained by experiment in Table IV can be compared to those obtained theoretically in Table V. In no case does a large discrepancy occur; indeed it is highly reassuring that even for the most sensitive case of beryllium agreement within the experimental error exists. This is an indication that the Klein-Nishina formula for Compton scattering is correct within perhaps 15 percent at energies of 88 Mev.

CONCLUSIONS

It has been shown that at an energy of 88 Mev the experimental cross sections for gamma-ray absorption are nearly those predicted by theory. Discrepancies occur of magnitude proportional to Z^2 and, in addition, some discrepancy exists in the measured case of beryllium. The Compton scattering cross section at 88 Mev has been approximately verified by the combined use of total cross sections and ratios of pair cross sections. It is encouraging that observed discrepancies have been small; in fact they are probably caused mainly by known approximations in present theory.

It is a pleasure to acknowledge the cooperation of the betatron group, and especially the services of the operators, McNamara and Martin. The sample of uranium was kindly fabricated and furnished by the Metallurgical Section of the Knolls Atomic Power Laboratory. It is a privilege to acknowledge the help of R. Ehrlich and H. Hurwitz, who not only have shown continued interest and activity in the theoretical treatment of radiation problems, but have materially

[19] The author is indebted to Miss E. Coe who has performed the appropriate numerical integrations of the screening functions given in Bethe and Heitler and in Wheeler and Lamb. The numbers shown in this table are accurate integrations but probably cannot be trusted to better than one percent because of possible inaccuracies in the screening functions. They differ slightly from the values calculated independently by P. V. C. Hough, e.g. for lead a difference of nearly 2 percent exists.

[20] The plot should strictly not be quite linear because the failure of the Born approximation applies only to the part of the cross section caused by pairs in the nuclear field. However, it happens that where Z^2 is appreciable the contribution to cross section by other processes is very small (see Table V).

[21] Hulme and Jaeger, Proc. Roy. Soc. 153, 443 (1936).

[22] R. Ehrlich and H. Hurwitz, private communication.

assisted in computations pertinent to the spectrum analyzer equipment itself. Finally, it must be obvious that the success of experiments involving extensive equipment depends upon painstaking tests and circuit development; without the able assistance of C. M. Bishop, the equipment used in these experiments would not have been built and operated satisfactorily.

This work was made possible through the Office of Naval Research Contract N7-ONR-332.

PHYSICAL REVIEW VOLUME 75, NUMBER 3 FEBRUARY 1, 1949

The Angular and Lateral Spread of Cosmic-Ray Showers*

JANE ROBERG** AND L. W. NORDHEIM
Department of Physics, Duke University, Durham, North Carolina

(Received October 4, 1948)

The mean square angular and lateral spreads in showers have been evaluated for electrons as well as photons as functions of their energy. Analytical expressions have been obtained for high and medium energies down to the critical shower energy. The calculations have been extended by numerical methods for air down to low energies (~4 Mev). Radiative effects and ionization losses have been taken into account simultaneously for all energies, and we believe that no factors of physical significance have been omitted.

1. INTRODUCTION

THE calculation of the sidewise spread of a shower constitutes a problem of importance comparable to the evaluation of its development in depth. Particularly, the discussion of the nature of large air showers cannot be carried out without knowledge of their lateral evolution.

The first treatment of this problem has been given by Euler and Wergeland.[1] These authors discussed the mechanism of the spreading and its general features. Their numerical results, as pointed out by Bethe[2] and by the present authors[3] were, however, quite unsatisfactory and gave an extension of showers far too small. L. Landau[4] set up diffusion equations for the sidewise development in extension of the well-known Landau-Rumer[5] treatment of shower theory. However, his results are invalidated by numerical errors. The most extensive investigation was made by G. Molière.[6] Unfortunately, only an abbreviated version of his work is available. Molière uses an extension of Landau's method and carries it through to an actual evaluation of the radial density distribution in a shower. Because of the complications of the process, he is forced to neglect ionization losses for energies higher than the ionization limit and he takes low energy electrons into account according to a rather inadequate method, as he points out himself. His function will thus be subject to later revision. An evaluation of the mean square angular spread of electrons as function of energy has been given by S. Z. Belenky.[7] He starts with the Landau diffusion equations and obtains from them a set of integro-differential equations for various moments of the distribution. They are evaluated with the help of the method of Tamm

* This paper is based on the Ph.D. Thesis by Jane Roberg, Duke University, 1942. Its publication has been delayed because of the war. The results have been announced previously at several meetings of the Am. Phys. Soc. and have been communicated privately on request.

** Now at Yale University.

[1] H. Euler and H. Wergeland, Astrophys. Nor. 3, 165 (1940); Naturwiss. 28, 41 (1940).

[2] H. A. Bethe, Phys. Rev. 59, 684 (A) (1941).

[3] L. W. Nordheim, Phys. Rev. 59, 929 (A) (1941); Jane Roberg, Phys. Rev. 62, 304 (A) (1942).

[4] L. Landau, J. Phys. U.S.S.R. 2, 234 (1940).

[5] L. Landau and G. Rumer, Proc. Roy. Soc. A166, 213 (1938).

[6] G. Molière, Naturwiss. 30, 87 (1942); more fully reported in W. Heisenberg, *Cosmic Radiation* (Dover Publications, New York, 1946).

[7] S. Z. Belenky, J. Phys. U.S.S.R. 8, 9 (1944).

and Belenky.[8] His values differ rather markedly from those obtained here, as will be discussed later.

The presently reported investigation was carried out simultaneously and independently from Molière's and Belenky's work and is, in some respects, complementary to the previous investigations. We have not attempted to evaluate the distribution function itself, but concentrated our efforts on the determination of the mean square momenta under adequate consideration of the low energy region. We believe that no effect of significance has been omitted in our calculations, and that they can serve thus as standard against which calculations of the distribution function can be measured.

In addition to the momenta of electrons, we have also calculated the momenta of photons of all energies which differ significantly from the electron distribution. Our formulas can be considered as applicable to all materials for energies above the characteristic energy of shower theory. Calculations for lower energies have been carried through for air for reason of its particular importance for the discussion of large showers. We have extensively used the results of Richards and Nordheim,[9] quoted henceforth as R.N., and we refer to this paper for a discussion of units and cross sections.

2. GENERAL THEORY

We choose the customary units of shower theory. The unit of energy is the energy E_j, at which radiation and ionization losses are equal. The unit of length is the radiation length, that is, the distance at which one electron would lose the energy E_j, if it were subject only to ionization losses. The specific energy losses for radiation and for ionization are then

$$(dE/dt)_{\text{rad}}=E;\quad (dE/dt)_{\text{ion}}=\beta=1. \quad (2.1)$$

The values of these units for some materials are given in Table I.

We denote the energy of an electron by E, the energy of a photon for easy distinction by K. We write further the function that describes the longitudinal development of a shower under neglection of its sidewise spread as

$f(E, E', t)dE'$ = number of electrons at a depth t in the interval dE' due to a primary of energy E,

$g(E, K, t)dK$ = corresponding number of photons.

Table I. Units of shower theory for various materials.

	Air	Water	Al	Fe	Pb
Radiation length	300 m	43 cm	9.8 cm	1.8 cm	0.51 cm
Critical energy	86 Mev	111 Mev	52 Mev	25 Mev	6.7 Mev

According to Euler and Wergeland,[1] the only important source of deflection is the multiple Coulomb scattering of the shower electrons by the nuclei of the traversed material. This effect gives on a path dt a mean square angular deflection in one particular direction of magnitude

$$d\vartheta^2=(E_s/E)^2dt, \quad (2.2)$$

where E_s, a characteristic scattering energy, is in good approximation, for all materials[10]

$$E_s=mc^2(2\pi 137)^{\frac{1}{2}}=15 \text{ Mev}. \quad (2.3)$$

We refer all our calculations to one coordinate normal to the longitudinal direction of the shower. Due to the axial symmetry, the total mean square deviation in a radial direction will be twice the value thus calculated. Otherwise E_s has to be assumed to have a value $\sqrt{2}$ times as large as in Eq. (2.3) or 21 Mev.

The extension of the path of particles due to their deviation from straight lines can be neglected for small angular deflections, i.e., in this approximation the influence of scattering on the functions $f(E, E', t)$ and $g(E, K, t)$ does not have to be considered. This has been verified by an extensive investigation by S. Belenky.[11]

The *angular mean square deviation of electrons* of energy E at a distance t from the origin of the shower due to a primary electron of energy E_0 can then be evaluated as follows. The contribution of an electron of energy E' in an intermediate position, a distance t' backwards from the end point, to the total at t will be

$$d\vartheta^2(E, t)=(E_s/E')^2dt'f(E', E, t-t'),$$

[8] I. Tamm and S. Z. Belenky, J. Phys. U.S.S.R. 1, 177 (1939).

[9] J. A. Richards and L. W. Nordheim, Phys. Rev. 74, 1106 (1948).

[10] Compare B. Rossi and K. Greisen, Rev. Mod. Phys. 13, 262 (1941).

[11] S. Belenky, J. Phys. U.S.S.R. 8, 347 (1944).

and the average over all possibilities then gives

$$f(E_0, E, t)\vartheta^2(E, t) = \int_0^t \int_E^{E_0} f(E_0, E', t-t') \times (E_s/E')^2 f(E', E, t')dt'dE'. \quad (2.4)$$

An exactly similar argument gives for the mean square lateral deviation

$$x^2(E, t) = \frac{1}{f(E_0, E, t)} \int_0^t \int_E^{E_0} f(E_0, E', t-t') \times (E_s/E')^2 t'^2 f(E', E, t')dt'dE'. \quad (2.5)$$

The *angular distribution of quanta* is equal to the distribution of their parent electrons. Since all photons are ultimately produced by electrons and can be considered as being destroyed by absorption, we can express the photon distribution $g(E_0, K, t_0)$ in terms of the electron distribution as follows:

$$g(E_0, K, t) = \int_0^t \int_K^{E_0} f(E_0, E, t-t') \times \sigma(E, K)e^{-\delta t'}dEdt', \quad (2.6)$$

where $\sigma(E, K)$ is the cross section for production of a photon of energy K by an electron of energy E, and δ is the total absorption coefficient for the photon. The angular mean square deviation of the photons is then obtained by averaging over the contributions of the parent electrons according to the genetic relationship Eq. (2.6), i.e.,

$$\vartheta^2(K, t) = \frac{1}{g(E_0, K, t)} \int_0^t \int_K^{E_0} f(E_0, E, t-t') \times \sigma(E, K)e^{-\delta t'}\vartheta^2(E, t-t')dEdt'. \quad (2.7)$$

For the calculation of the *lateral spread of photons* one has to take into account the extension of the path length of the parent electron by the photon. We can still express the lateral deviation by an average, as in Eq. (2.7),

$$x^2(K, t) = \frac{1}{g(E_0, K, t)} \int_0^t \int_K^{E_0} f(E_0, E, t-t') \times \sigma(E, K)e^{-\delta t'}x^2(E, t-t', t')dEdt', \quad (2.8)$$

but we have to replace the deviation, Eq. (2.5), by the "prolonged" scattering

$$x^2(E, t, t'') = \frac{1}{f(E_0, E, t)} \int_0^t \int_E^{E_0} f(E_0, E', t-t') \times f(E', E, t')\left(\frac{E_s}{E'}\right)^2 (t'+t'')^2 dE'dt', \quad (2.9)$$

with the difference to Eq. (2.5) that the lever arm for sidewise deflection is increased by a constant addition t''.

The above equations are exact, but unwieldy. A considerable simplification can be achieved for high energy showers. The principal contribution to the scattering of an individual shower particle will come from the last few radiation lengths of his ancestors, due to the factor $(E_s/E)^2$ in the scattering cross section. In a large shower this depth will be small compared to the total longitudinal extension of the shower. Thus, the dependence on the upper limit of the integration will disappear asymptotically in taking the average of all quantities over the longitudinal coordinate of the shower according to the definitions

$$f(E) = \int_0^\infty f(E_0, E, t)dt, \quad (2.10)$$

$$\vartheta^2(E) = \frac{1}{f(E)} \int_0^\infty \vartheta^2(E_0, E, t)f(E_0, E, t)dt, \quad (2.11)$$

and so on.

The function $f(E)$, Eq. (2.10), is called the track length distribution, or normal distribution. It has been determined for all energies in R.N.[9]

Our formulas for the scattering averaged over the longitudinal extension of the shower can now be written as

$$\vartheta^2(E) = \frac{1}{f(E)} \int_0^\infty \int_K^\infty f(E')f(E', E, t) \times (E_s/E')^2 dE'dt, \quad (2.12)$$

$$\vartheta^2(K) = \int_K^\infty f(E')\sigma(E', K)\vartheta^2(E')dE' \times \left[1 \Big/ \int_K^\infty f(E')\sigma(E', K)dE'\right], \quad (2.13)$$

$$x^2(E, t) = \frac{1}{f(E)} \int_K^\infty \int_0^\infty f(E')f(E', E, t) \times (E_s/E')^2 (t'+t)^2 dt'dE'. \quad (2.14)$$

The mean square angular scattering of a shower electron is then

$$x^2(E)=x^2(E,0). \tag{2.14a}$$

Finally we have a prolonged lateral photon scattering,

$$x^2(K,t)=\frac{\int_0^\infty\int_K^\infty f(E')\sigma(E',K)x^2(E',t'+t)e^{-\delta t'}dE'dt'}{\int_0^\infty\int_K^\infty f(E')\sigma(E',K)e^{-\delta t'}dE'dt'}. \tag{2.15}$$

The use of these longitudinally averaged values corresponds to the physical situation insofar that we will not know, in general, where an observed shower originated. Since the energy distribution in a large shower near its maximum is the same as the track length distribution, the above formulas will also be correct for the shower maximum, where there is the best chance of observing it.

It is possible and useful for later considerations to express the scattering of electrons in terms of their photon ancestors. We introduce the track length distribution of photons,

$$g(K)=\int_0^\infty g(K,t)dt, \tag{2.16}$$

and, further, the straggling function $f_0(E',E,t)$, which denotes the probability that an electron of energy E' arrives at the distance t with the reduced energy E. The angular deflection of the shower electrons can then be expressed as follows:

$$\vartheta^2(E)=\frac{\int_{E'}^\infty dK\int_E^\infty dE'\int_0^\infty dt'g(K)\sigma(K,E')[\vartheta^2(K)+\vartheta_0^2(E',E,t')]f(E',E,t')}{\int_{E'}^\infty dK\int_E^\infty dE'\int_0^\infty dt'g(K)\sigma(K,E')f(E',E,t')}. \tag{2.17}$$

Here $\vartheta_0^2(E',E,t)$ stands for the angular deflection the electron obtains as an individual from its birth at energy E' to observation with energy E at distance t'.

In order to describe the lateral deflection in an analogous manner, we have to introduce the prolonged deflection both for photons and for electrons. The expressions obtained are

$$x^2(K,t)=\frac{\int_E^\infty dE'\int_0^\infty dt'f(E')\sigma(E',K)x^2(E',t'+t)e^{-\delta t'}}{\int_E^\infty dE'\int_0^\infty dt'f(E')\sigma(E',K)e^{-\delta t'}}, \tag{2.18}$$

$$x^2(E,t)=\frac{\int_{E'}^\infty dK\int_E^\infty dE'\int_0^\infty dt'g(K)\sigma(K,E')[x^2(K,t'+t)+x_0^2(E',E,t'+t)]f(E',E,t')}{\int_{E'}^\infty dK\int_E^\infty dE'\int_0^\infty dt'g(K)\sigma(K,E')f(E',E,t')}. \tag{2.19}$$

Here again $x_0^2(E',E,t'+t)$ denotes the lateral deviation obtained by an electron as an individual when slowed down from the energy E' to E in the distance t' with the extension of the lever arm by a fixed constant t. The actual mean square deviations in the shower are again given

TABLE II. Normal energy distribution in a shower; air. $f(E)=\varphi(E)/E^2$.

E/E_j	∞	10	7	5	3	2	1.5	1
$f(E)$	$1/E^2$	0.0086	0.0166	0.030	0.073	0.145	0.23	0.42
$\varphi(E)$	1	0.86	0.81	0.75	0.65	0.58	0.52	0.42

E/E_j	0.75	0.5	0.3	0.2	0.15	0.1	0.05
$f(E)$	0.62	0.97	1.61	2.25	2.8	3.7	5.5

by $x^2(K,0)$ and $x^2(E,0)$. The two equations, (2.18) and (2.19), form a simultaneous system of integral equations, which can be solved by an iteration process, as will be shown in Sections 5 and 6.

The mean square angular and lateral deviations for electrons as well as photons have now been expressed in terms of the functions which describe the longitudinal development of a shower, i.e., the normal distribution $f(E)$ and the general shower functions $f(E,E',t)$ and $g(K,K',t)$. The problem reduces thus to the finding of suitable approximations for these functions that permit the evaluation of Eqs. (2.12) to (2.15) or (2.18) to (2.19). We divide the whole energy spectrum into three regions: (a) high energies, where ionization losses can be entirely neglected, (b) intermediate energies where ionization can be considered as a small correction, and (c) low energies where ionization predominates over radiation effects. The division between (b) and (c) is made at the critical energy of shower theory, where ionization and radiation losses are equal.

3. HIGH ENERGIES

We consider firstly the high energy region where ionization losses can be completely neglected. The track length distribution is then given[12] by

$$f(E)=1/E^2. \tag{3.1}$$

We require further the shower functions $f(E',E,t)$ for small values of the distance t and for values of the primary energy E' which is not much larger than E. The only available form which gives a good approximation for the beginning of small showers is the development of Bhabha and Heitler,[13] quoted henceforth as B.H. Their formulas, as described in appendix I, are based on an adequate approximation for high energies. The evaluation of the actual distribution functions by the Bhabha-Heitler method is complicated and can only be done approximately. It is remarkable, however, that the scattering integrals containing their functions can be integrated in closed form.

B.H. decompose the distribution function into a series

$$f(E',E,t)=\sum_0^\infty f_n(E',E,t). \tag{3.2}$$

The first term f_0 represents the probability that the primary electron E' itself has reached a depth t with an energy E. The term f_1 represents the number of second generation electrons, i.e., particles that have been created by an intermediate photon, and f_n represents electrons of the n'th generation, i.e., with n intermediate photons. The series (3.2) will obviously converge since the total number of electrons above a given energy remains finite.

Inserting Eqs. (3.1) and (3.2) into the integrals (2.12), (2.14), we obtain for the angular and prolonged lateral scattering

$$E^2\vartheta^2(E)=\int_0^\infty\int_E^\infty (dE'/E'^2)\sum_0^\infty f_n(E',E,t') \times(E_s/E')^2dt', \tag{3.3}$$

$$E^2x^2(E,t)=\int_0^\infty\int_E^\infty (dE'/E'^2)\sum_0^\infty f_n(E',E,t') \times(E_s/E')^2(t'+t)^2dt'. \tag{3.4}$$

They are composed of terms of the general form

$$(1/E^4)I_m^n(E)=\int_0^\infty\int_E^\infty (dE'/E'^4) \times f_n(E',E,t')t'^m dt'. \tag{3.5}$$

The integration gives, as shown in the appendix,

$$\begin{aligned} I_0^n&=1/(2\times 12^n),\\ I_1^n&=[1/(2\times 12^n)][((n+1)/2)+(n/\delta)],\\ I_2^n&=[(n+1)/(2\times 12^n)]\\ &\quad\times[[(n+2)/4]+(n/\delta)+(n/\delta^2)], \end{aligned} \tag{3.6}$$

where $\delta=7/9$ is the absorption coefficient for photons.

[12] L. W. Nordheim and M. H. Hebb, Phys. Rev. **56**, 494 (1939).
[13] H. J. Bhabha and W. Heitler, Proc. Roy. Soc. **159**, 432 (1937).

The summation over n can be carried out in closed form, according to Eq. (A16) with the result that

$$I_0=\sum_0^\infty I_0^n=0.545,$$

$$I_1=\sum_0^\infty I_1^n=0.362, \tag{3.7}$$

$$I_2=\sum_0^\infty I_2^n=0.642.$$

Inserting the values into Eqs. (3.3) and (3.4), we obtain

$$\vartheta^2(E)=0.545(E_s/E)^2, \tag{3.8}$$

$$x^2(E,t)=(0.642+0.724t+0.545t^2)(E_s/E)^2. \tag{3.9}$$

The lateral scattering of electrons is obtained, of course, by taking $t=0$. The scattering integrals for photons, Eqs. (2.13) and (2.15), can now be evaluated with the help of Eqs. (3.8) and (3.9) with the result

$$\vartheta^2(K)=0.181(E_s/K)^2, \tag{3.10}$$

$$x^2(K)=(1/3)(I_2+(2/\delta)I_1+(2/\delta^2)I_0)\times(E_s/K)^2=1.126(E_s/K)^2. \tag{3.11}$$

4. INTERMEDIATE ENERGIES

Our next step will be the consideration of intermediate energies, where ionization losses have to be taken into account, but are not yet predominant. We solve this problem again by the standard integrals, Eqs. (2.12) to (2.15), but we introduce suitable modifications in the shower functions $f(E)$, $g(K)$, and $f(E', E, t)$.

The normal distribution $f(E')$ has been determined numerically for all energies by R.N.[9] There it was written as

$$f(E')=\varphi(E')/E'^2, \tag{4.1}$$

where $\varphi(E')$ is a slowly varying function of E'. It is tabulated for air in Table II. The form (4.1) is not practical here, since φ is only given numerically, and we try to find an analytical approximation. It is most essential that the latter is good in the neighborhood of the energy E for which the scattering is to be evaluated. We write

$$f(E')=(1/E'^2)+q(E)/E'^3, \tag{4.2}$$

with

$$q(E)=-E[1-\varphi(E)]. \tag{4.3}$$

This means that we take a different formula for every E value, so that we have always the correct value for $E'=E$. It would, in principle, be possible to improve the approximation by adding terms with higher negative powers in E'. However, the error in Eq. (4.3) is already less than 10 percent for all values of E', even if we take E as low as E_j.

We have, furthermore, to correct the functions $f_n(E', E, t)$ in the development, Eq. (3.2). Let us first consider the straggling function f_0. We assume now that the electron looses through ionization the energy β (or E_j) per radiation length or βt on the length t. If this loss is small compared to the loss by radiation, then we may neglect the change in radiation loss resulting from the electron energy is also reduced by ionization. We take thus as corrected straggling function

$$f_0(E', E, t)_{\text{corr}}=f_0(E', E+\beta t, t). \tag{4.4}$$

In other words, the function f_0 is to be calculated not for the final energy value, but for the energy $E''=E+\beta t$ which the electron would have had without ionization loss.

In the higher functions f_n, which represent the contribution of n'th generation particles, the ionization losses of the ancestor electrons will be relatively unimportant due to the large reduction of energy at every transformation. It will be sufficient, therefore, to consider this effect only over the last lap of the path, i.e., for the final electron after its production by a photon. We call this distance t' and decompose the function f_n as follows:

$$f_n(E', E, t)=\int_0^t dt' h_n(E', E, t', t), \tag{4.5}$$

where the function $h_n(E', E, t', t)$ gives the distribution of n'th generation electrons at t which have been created at a distance t' backwards. The function h_n can also be obtained by the Bhabha-Heitler method, as shown in the appendix. In analogy to Eq. (4.4) we take as the corrected function

$$f_n(E', E, t)_{\text{corr}}=\int_0^t dt' h_n(E', E+\beta t', t', t). \tag{4.6}$$

In order to have uniform formulas we write Eq.

(4.4) in the same form with

$$h_0(E', E, t', t) = f_0(E', E, t)\delta(t-t'). \quad (4.7)$$

Equations (2.12) and (2.14) for the angular and prolonged lateral scattering for electrons*** become now, on substitution of Eqs. (4.2), (3.2), and (4.6),

$$(\varphi(E)/E^2)\vartheta^2(E) = \int_0^\infty dt'' \int_0^{t''} dt' \times \int_{E+\beta t'}^\infty dE' \left(\frac{1}{E'^2} + \frac{q(E)}{E'^3}\right)(E_s/E')^2 \times \sum_0^\infty h_n(E', E+\beta t', t', t''), \quad (4.8)$$

$$(\varphi(E)/E^2)x^2(E, t) = \int_0^\infty dt''(t''+t)^2 \int_0^{t''} dt' \times \int_{E+\beta t'}^\infty dE'[(1/E'^2)+(q(E)/E'^3)] \times (E_s/E')^2 \sum_0^\infty h_n(E', E+\beta t', t', t''). \quad (4.9)$$

The general term of this integral is of the form

$$E^{-(s+2)}\, {}^sJ_m^n(E) = \int_0^\infty dt'' t''^m \int^{t''} dt' \times \int_{E+\beta t'}^\infty \frac{dE'}{E'^{s+2}} h_n(E', E+\beta t', t', t''), \quad (4.10)$$

where $m=0$, 1, or 2 and $s=2$ or 3. They are evaluated in the appendix. On introduction of the definition

$${}^sJ_m = \sum_{n=0}^\infty {}^sJ_m^n, \quad (4.11)$$

we obtain

$$\vartheta^2(E) = (E_s/E)^2(1/\varphi(E))[{}^2J_0(E) - (1-\varphi(E))\, {}^3J_0(E)], \quad (4.12)$$

$$x^2(E, t) = (E_s/E)^2(1/\varphi(E)) \times \{[{}^2J_2(E) - (1-\varphi(E))\, {}^3J_2(E)] + 2t[{}^2J_1(E) - (1-\varphi(E))\, {}^3J_1(E)] + t^2[{}^2J_0(E) - (1-\varphi(E))\, {}^3J_0(E)]\}. \quad (4.13)$$

The photon momenta are again obtained from Eqs. (2.13) and (2.15). Upon introduction of Eqs. (4.12) and (4.13), they take the form

$$\vartheta^2(K) = \left(E_s^2 \Big/ \int_K^\infty f(E)dE\right) \int_K^\infty (dE/E^4) \times [{}^2J_0(E) - (1-\varphi(E))\, {}^3J_0(E)], \quad (4.14)$$

$$x^2(K, t) = \left(E_s^2 \Big/ \int_K^\infty f(E)dE\right) \int_K^\infty (dE/E^4) \times \{{}^2J_2(E) - (1-\varphi(E))\, {}^3J_2(E) + (2/\delta)[{}^2J_1(E) - (1-\varphi(E))\, {}^3J_1(E)] + (2/\delta^2)[{}^2J_0(E) - (1-\varphi(E))\, {}^3J_0(E)]\}. \quad (4.15)$$

The evaluation of these integrals has been carried out numerically, except for the high energy tail (above $E>10E_j$) where a series development has been used. The results of these calculations are contained in Table III.

It may be remarked that the methods developed here would also make possible the evaluation of the higher moments of the distribution. It also would be possible, in principle, to carry out similar calculations for other longitudinal positions than the maximum in the shower, as long as the variation of the primary distribution $f(E)$ can be neglected within the distance from the point of observation which contributes to the scattering. Such calculations have not been carried out.

5. LOW ENERGIES, ANGULAR SCATTERING

The approximations made in the preceding section are satisfactory for energies down to about the ionization limit E_j. Below this energy our functions $f_n(E', E, t)$ (Eq. (4.5)), loose their validity. Also, the cross sections for most processes become different functions of energy, and new effects, such as the Compton effect, come into play.

In order to offset these difficulties, we may here neglect the straggling of electrons, i.e., we can assume that every electron with $E<E_j$ loses its energy in a continuous fashion according to the law

$$dE/dt = E+E_j, \quad (5.1)$$

where the first term E represents the radiative losses and the second the ionization losses. This means that the path length, or range between

*** In the subsequent equations the letter s is used in two different connotations. As a subscript to the energy, i.e., E_s, it signifies the characteristic scattering energy, while as a superscript, i.e., E^s, it signifies an exponent.

two energies E' and E, is given by

$$R(E', E) = \log[(E'+E_j)/(E+E_j)], \quad (5.2)$$

or that the energy expressed as function of distance is

$$E(t) = (E'+E_j)e^{-R} - E_j.$$

The function $f_0(E', E, t)$ reduces to a function of two variables only (E' and E, or E' and t). An approximation that is more easily handled is obtained by development of the log in Eq. (5.2), i.e.,

$$R(E', E) \simeq (E'-E)/(E+E_j), \qquad E' = E+(E+E_j)R. \quad (5.2a)$$

The assumption of a definite range-energy relation as in Eq. (5.2) or (5.2a) permits the direct evaluation of the scattering of an individual electron, i.e., of the functions $\vartheta_0^2(E', E, t')$ and $x_0^2(E', E, t'+t)$ in Eqs. (2.17) and (2.19).

It is then possible to solve directly the integral equations (2.12), (2.17), and (2.18), (2.19) by an iteration process similar to the method used by R.N.[9] for the determination of the energy distribution. We refer to this paper for a discussion of cross sections and for the values of a number of auxiliary functions.

The method will be best illustrated by the discussion of the actual procedure.

We decompose the electronic distribution into two groups

$$f(E) = f_0(E) + f_1(E), \quad E \leqslant E_j, \quad (5.3)$$

where f_0 is the number of electrons which have been decelerated as individuals from higher energies and f_1 is the number which have been created by photons at energies below E_j. f_0 and f_1 are numerically given by R.N.[9]

The angular scattering can be decomposed in a similar manner, i.e., in obvious notation:

$$\vartheta^2(E) = [1/f(E)][f_0\vartheta_0^2(E) + f_1\vartheta_1^2(E)]. \quad (5.4)$$

The contribution ϑ_0^2 will be the sum of the deviation the electron acquires on its path from E_j to E plus the known amount it inherited at E_j. Thus,

$$\vartheta_0^2(E) = \int_0^{R(E_j, E)} (E_s/E(t))^2 dt + \vartheta^2(E_j). \quad (5.5)$$

The first part can be evaluated as follows:

$$\int_0^R (E_s/E(t))^2 dt = \int_E^{E_j} (E_s/E')^2 (dt/dE) dE$$
$$= \int_E^{E_j} (E_s/E')^2 [dE/(E'+E_j)]$$
$$= (E_s/E_j)^2 [(E_j/E) - 1 - \log[(E+E_j)/2E]]. \quad (5.6)$$

The function $\vartheta_1^2(E)$ can be expanded in a similar manner:

$$\vartheta_1^2(E) = \left[1 \Big/ \int_E^{E_j} h(E')dE'\right] \int_E^{E_j} dE' h(E') \times \left\{ \int_E^{E'} (E_s/E'')^2 [dE''/(E''+E_j)] + \vartheta_2^2(E') \right\}. \quad (5.7)$$

Here $h(E')dE'$ denotes the number of electrons produced in dE' by quanta, a function computed in R.N.[9] The first term on the right-hand side of Eq. (5.7) represents thus the deviation acquired on their path by electrons which have been created with energies $E' < E_j$. The second term $\vartheta_2^2(E')$ is the angular deviation inherited by these electrons from their parent quanta.

We note that by definition

$$f_1(E) = [1/(dE/dt)] \int_E^{E_j} h(E')dE' = [1/(E+E_j)] \int_E^{E_j} h(E')dE'. \quad (5.8)$$

The first term of Eq. (5.7) can then be brought into the easily integrable form

$$\int_E^{E_j} dE' h(E') \int_E^{E_j} (E_s/E'')^2 [dE''/(E''+E_j)]$$
$$= \int_E^{E'} (E_s/E'')^2 [dE''/(E''+E_j)] \int_{E''}^{E_j} h(E')dE'$$
$$= \int_E^{E_j} (E_s/E'')^2 f_1(E'')dE''.$$

The evaluation of $\vartheta_2^2(E')$ requires the knowledge of the scattering of the parent quanta, which

TABLE III. Mean square angular and lateral spread of shower electrons and photons as function of energy.

E/E_j or K/E_j	$x^2(E)$	$X^2(E)$	$x^2(K)$	$X^2(K)$	$\vartheta^2(E)$	$\theta^2(E)$	$\vartheta^2(K)$	$\theta^2(K)$
∞	$0.642(E_s/E)^2$	$0.214(E_s/E)^2$	$1.13(E_s/K)^2$	$0.38(E_s/K)^2$	$0.545(E_s/E)^2$	$0.182(E_s/E)^2$	$0.181(E_s/K)^2$	$0.060(E_s/K)^2$
10	0.49	0.18	0.95	0.32	0.47	0.16	0.16	0.054
7	0.46	0.17	0.88	0.285	0.44	0.15	0.15	0.050
5	0.43	0.16	0.80	0.260	0.42	0.14	0.14	0.047
3	0.40	0.140	0.71	0.220	0.38	0.13	0.12	0.040
2	0.33	0.125	0.62	0.195	0.34	0.11	0.11	0.036
1.5	0.30	0.105	0.55	0.175	0.31	0.095	0.095	0.034
1	$0.25(E_s/E_j)^2$	$0.085(E_s/E_j)^2$	$0.46(E_s/E_j)^2$	$0.155(E_s/E_j)^2$	$0.27(E_s/E_j)^2$	$0.085(E_s/E_j)^2$	$0.085(E_s/E_j)^2$	$0.029(E_s/E_j)^2$
0.75	0.28	0.120	0.64	0.255	0.34	0.135	0.110	0.043
0.5	0.39	0.165	0.80	0.42	0.69	0.22	0.145	0.062
0.4	0.46	0.190	1.30	0.53	0.97	0.28	0.170	0.076
0.3	0.60	0.235	1.75	0.72	1.40	0.35	0.23	0.100
0.2	0.86	0.31	2.55	1.02	2.40	0.57	0.38	0.145
0.15	1.13	0.48	3.4	1.30	3.4	0.80	0.50	0.185
0.10	1.6	0.46	4.7	1.8	6.7	1.23	0.68	0.26
0.05	2.8	0.64	7.4	2.7	12.8	2.3	1.25	0.40

in turn is determined by

$$\vartheta^2(K)=\frac{\int_K^\infty f(E)\sigma(E,K)\vartheta^2(E)dE}{\int_K^\infty f(E)\sigma(E,K)dE}. \quad (5.9)$$

The contribution to $\vartheta^2(E)$ from ϑ_2^2 must evidently be small, since the angular deviations of photons are small and $\vartheta_2^2(E)$ refers in addition to photons of energies larger than E_j. We can carry out the simultaneous determination of $\vartheta^2(K)$ and of $\vartheta_2^2(E)$ by an iteration process, i.e., we evaluate $\vartheta^2(K)$ with a $\vartheta^2(E)$ not yet containing the $\vartheta_2^2(E)$ terms, and then use this function to determine $\vartheta_2^2(E)$. The evaluation of Eq. (5.9) could then be corrected again and so on. It was found, however, by estimates based on this procedure that the contribution from $\vartheta_2^2(E')$ is entirely negligible.

The evaluation of Eq. (5.9) was carried out with the cross sections given by R.N. The results of the calculations are contained in Table III.

6. LOW ENERGIES, LATERAL SCATTERING

The lateral scattering of electrons and photons can be treated by the method of the preceding section, with the added complication that the "prolongation" of the lever arm by subsequently added path lengths has to be taken into account. We will deal throughout with the "prolonged" scattering expressions $x^2(E,t)$, $x^2(K,t)$ from which the actual scattering is obtained by taking $t=0$.

We write the expression for the prolonged photon scattering as follows (cf. Eq. (2.15)):

$$x^2(K,t)=\frac{\int_K^\infty f(E)\sigma(E,K)\bar{x}^2(E,t)dE}{\int_K^\infty f(E)\sigma(E,K)dE}, \quad (6.1)$$

where we introduced the "averaged" prolonged electron scattering,

$$\bar{x}^2(E,t)=\int_0^\infty x^2(E,t'+t)\delta e^{-\delta t'}dt'. \quad (6.2)$$

We decompose $x^2(E,t)$ again as in the preceding section:

$$x^2(E,t)=[1/f(E)][f_0x_0^2(E,t)+f_1x_1^2(E,t)], \quad (6.3)$$

where the first term contains the contribution of electrons decelerated from E_j as individuals and the second term those produced with energies below E_j. For the first part one finds

$$x_0^2(E,t)=\int_E^{E_j}[(R(E',E)+t)^2/(E'+E_j)]\times(E_s/E')^2dE'+x^2(E_j,R(E',E)+t), \quad (6.4)$$

where $R(E',E)$ is the range of the electrons between the energies E' and E (cf. Eq. (5.2)). It is clear that $x_0^2(E,t)$ is a quadratic function in t. It follows then from Eq. (6.2) that

$$\bar{x}_0^2(E,t)=(E_s/E_j)^2[a(E)+2b(E)t+c(E)t^2], \quad (6.5)$$

where a, b, c, are functions of E that can be obtained from Eqs. (6.2) and (6.4).

For the actual computation we have used the approximation, Eq. (5.2a). We find, with $R_0=(E_0-E)/(E+E_j)$, for the prolonged scattering of an electron between the energies E_0 and E:

$$x_0^2(E_0, E, t)$$

$$=\int_E^{E_0}[(R(E', E)+t)^2/(E'+E_j)](E_s/E')^2dE'$$

$$=\int_0^{R_0}(R+t)^2(E_s/E(R))^2dR$$

$$\simeq E_s^2\int_0^{R_0}\left[\frac{R+t}{E+(E+E_j)R}\right]^2dR$$

$$=(E_s/E_j)^2[E_j/(E+E_j)]^2$$

$$\times\{[1-(E^2/E_0^2)-2(E/E_0)\log(E_0/E)]$$

$$+2t[\log(E_0/E)-(1-(E/E_0))]$$

$$+t^2(1-(E/E_0))(1+(E_j/E))\}. \quad (6.6)$$

As the next step we evaluate a first approximation to the photon momentum $x_0^2(K, t)$ from Eq. (6.1), using the previously found expression (6.5) for $E<E_j$ for the electron scattering at $E<E_j$ in place of the not yet determined full expression (6.3). For $E>E_j$, of course, the results from Section 4 have been used. We obtain again a quadratic function in t,

$$x_0^2(K, t)=(E_s/E_j)^2$$
$$\times[A(K)+2B(K)t+C(K)t^2], \quad (6.7)$$

where A, B, C, are numerically obtained functions of the photon energy K. It turned out that these functions do not have to be corrected again, and the results of this calculation for $t=0$ are given in Table III as our final results.

It remains to compute the contribution $x_1^2(E, t)$ of the electrons which have been produced with energies $E'<E_j$. It can be written as

$$x_1^2(E, t)=\int_E^{E_j}dE'\int_{E'}^{\infty}dKg(K)\sigma(K, E')$$

$$\times[x_0^2(K, R(E', E)+t)+x_0^2(E', E, t)]$$

$$\times 1\Big/\int_E^{E_j}dE'\int_{E'}^{E}g(K)\sigma(K, E')dK. \quad (6.8)$$

TABLE IV. Comparison of shower spreads at high energies obtained by various authors (notations as in Table III).

	$(E/E_s)^2x^2(E)$	$(E/E_s)^2x^2(K)$	$(E/E_s)^2\vartheta^2(E)$	$(E/E_s)^2\vartheta^2(K)$
Euler-Wergeland	0.074		0.33	
Molière	0.835	1.314	0.6	0.2
Belenky	0.94			
Janossy	0.724		0.570	
Roberg-Nordheim	0.642	1.13	0.545	0.181

Here $g(K)$ is the energy distribution of photons, $\sigma(K, E')$ the production cross section for electrons, for which we have to add pair production and Compton effect, and $x_0^2(E', E, t)$ the contribution to the scattering of the electron after it has been created, as determined in Eq. (6.6). All functions in Eq. (6.8) are then known.

In order to simplify the evaluation of Eq. (6.8), we have assumed that every electron E' is created in the average by a quantum of definite energy K. For Compton electrons of not too low energies we can assume without much error that they have the same energy as their parent photons. The average energy K_{Av} of the photon which gives the correct scattering inheritance to a pair electron E' is defined by the relation

$$x^2(K_{Av})=\frac{\int_{E'}^{\infty}g(K)\sigma_p(K, E')x^2(K)dK}{\int_{E'}^{\infty}g(K)\sigma_p(K, E')dK},$$

where σ_p is the differential cross section for pair production. If we assume that $x^2(K_{Av})$ is proportional to K^{-n} and $g(K)$ to K^{-m}, we find, since $\sigma_p(K, E')\sim K^{-1}$,

$$(K_{Av})^{-n}=\int_E^{\infty}K^{-(m+n+1)}dK\Big/\int_0^{\infty}K^{-(m+1)}dK$$

$$=[m/(m+n)]E^{-n},$$

or

$$K_{Av}=[1+(n/m)]^{1/n}E=\alpha E. \quad (6.9)$$

The value of α is fairly insensitive to the exponents. At very high energies, we would have $n=2$, $m=2$, and $\alpha=\sqrt{2}$. At very low energies $n\sim 1$, $m\sim 1$, $\alpha=2$. We choose as a suitable average value $\alpha=\sqrt{3}=1.73$. The evaluation of Eq. (6.8) reduces then to single integrals of the

general form

$$\int_{\alpha E}^{E_j} h_p(\alpha E')x_0^2(\alpha E', R)dE', \qquad (6.10)$$

where $h_p(E')$ is the number of pair electrons produced per interval dE', a function determined by R.N.[9], and x_0^2 is to be taken from Eq. (6.7).

The process could be repeated, i.e., one could go back with the new value of $x_1^2(E)$ into Eq. (6.3) and then re-evaluate the photon scattering from Eq. (6.1). However, as mentioned before, this turned out to be unnecessary. We also have left out of our calculations the knock-on electrons and post-Compton photons, since their contribution to the mean square deviations could be estimated to be negligible.

Our calculations have been extended down to energies of $0.05E_j$ or $\sim$4 Mev, the lower limit to which the auxiliary functions $f(E)$, $g(K)$ have been given by R.N.[9] For the final results see Table III.

7. DISCUSSION

Our results are collected in Table III which gives the mean square deviations of electrons and photons as function of their energy. The symbols have the following meaning:

$x^2(E)$ = mean square lateral spread of electrons of energy E,
$x^2(K)$ = mean square lateral spread of photons of energy K,
$\vartheta^2(E)$ = mean square angular spread of electrons of energy E,
$\vartheta^2(K)$ = mean square angular spread of photons of energy K.

The capitalized letters denote the same quantities averaged over all energies in a shower larger than a given lower limit, for instance,

$$X^2(E) = \int_E^\infty x^2(E')f(E')dE' \times 1 \Big/ \int_E^\infty f(E')dE'. \qquad (7.1)$$

$X^2(E)$ gives thus the total spread of a shower as measured by an arrangement that records only particles above a given energy E.

The units of energy and length are those of shower theory (cf. Table I). Angles are measured in radians. The critical scattering energy E_s (cf. Eq. (2.3)) has to be taken as 21 Mev for evaluation of radial deviations, and equal to $21/\sqrt{2}$ Mev = 15 Mev for deviations in one particular direction normal to the shower axis.

The mean square deviations are obtained from Table III by multiplying the figures in the upper half ($E/E_j \geqslant 1$) by $(E_s'/E)^2$, in the lower half ($E/E_j \leqslant 1$) by $(E_s/E_j)^2$.

Table III should be used in conjunction with Table I of R.N.,[9] which gives the corresponding energy distribution functions in a large shower. The energy distribution for electrons is also reproduced in Table II, Section 4, of this paper.

The first row in Table III represents asymptotic values for high energies under complete neglection of ionization losses. They have been obtained (cf. Section 3) without any further neglection from the shower theory in the form of Bhabha and Heitler.[13] The values down to $E/E_j = 1$ have been obtained from the formulas of Section 4, using asymptotic cross sections for high energies. The results are valid as far as these cross sections are a satisfactory approximation. The low energy part has been calculated for air. The results should, however, have at least qualitative validity for other materials.

It is to be noted, of course, that the forward progress of a shower will be stopped for energies such that the root mean square angular deflection of electrons becomes of order unity. Our calculations are actually based on the assumption that the scattering angles are small. $(\vartheta^2(E))^{\frac{1}{2}}$ reaches the value 0.5 for air at $E/E_j = 0.2$ or $E = 16$ Mev, and for lead at $E/E_j = 3.7$ or $E = 25$ Mev and the value unity for air at $E/E_j = 0.05$ or $E = 4$ Mev, and for lead at $E/E_j = 1.8$ or $E = 12$ Mev. We can take the latter values as a rough measure of the energy below which electrons do not show any preference for the forward direction. Using the results of R.N., we find that for air about $\frac{1}{6}$ of the electron track length is contained in this low energy, non-directional part while this fraction increases to 80 percent for lead.†

The root mean square lateral deviation of electrons with $\vartheta^2(E) \sim 1$ can be considered as a rough measure of the total radius of a large shower. This radius is for normal air about 120 m, for

† The position of the shower maximum will not be affected much, since it depends mainly on the particles of high energy, compare S. Belenky, reference 11.

lead about 0.45 cm. The root mean square deviation for all shower electrons above these energies is less, namely, ~60 m for air or 0.3 cm for lead. Spreads of this order of magnitude are sufficient to explain observations on large air showers; compare f.i. the investigation by Cocconi[14] and collaborators.

The general behavior of the spread as function of energy is similar to that found by Euler and Wergeland[1] and by Molière,[6] and it gives, as shown by these authors, a qualitative explanation of the general features of showers. For example, photographs of showers penetrating several lead plates often show quite clearly that electrons with larger angular spread are more easily absorbed. Furthermore, electrons emerging from lead with a pronounced forward direction must have energies at least of order 20 to 30 Mev. The root mean square radial deviation of all electrons of this and higher energies is only about 1.5 mm. Thus, lead showers seem to diverge virtually from single points.

An interesting feature of our results is that the angular deviations of photons are smaller than those of electrons of the same energy while their radial deviation is larger. The reason for this behavior is that a photon inherits its angular deflection from a higher energy electron parent. For the lateral deflection this effect is overcompensated by the comparatively long mean free path of photons.

During the last years, calculations on the spread of showers have been given by various authors, and it seems to be of importance to compare their results with ours and to assess their accuracy.

Table IV gives the results for the mean square deviation at high energies under total neglection of ionization losses.

The original Euler-Wergeland[1] theory contains a serious underestimate of the spread. The results of the other authors are in rough agreement, the differences being due to the use of different forms of the shower theory and different approximations for the cross sections. Molière uses simplified cross sections and his method, based on Landau's[4] general equations, cannot be judged completely from the short available abstracts.

Belenky's[7] value has been obtained after correction of a factor in his equations which made the mean square deviation four times too large. He uses the Tamm-Belenky[8] formalism to evaluate correct diffusion equations.

Janossy,[15] in his recent book, evaluates our Eqs. (2.12) and (2.14) in an elegant and simple way, using the full asymptotic cross sections. His values have to be considered as the best ones today. His method, unfortunately, does not seem to yield itself to the inclusion of ionization losses. Our values are obtained from a rigorous evaluation of the Bhabha-Heitler theory, the difference to Janossy being due to the basic approximations underlying their formulas.

Data on $x^2(E)$ for lower energies under inclusion of ionization losses have been given by Belenky and Janossy. Belenky's curve, as judged from a very small graph, gives approximately the correct reduction due to ionization at the critical energy. It is, however, considerably too flat, i.e., it gives too little reduction at higher energies and too small a spread at lower energies. The sharp upturn of our values for very low energies is the result of the comparatively long range of low energy photons, an effect that is neglected in the Tamm-Belenky formalism. Janossy gives plausibility arguments for the rough interpolation formula

$$x^2(E)=0.724(E_s/(E+E_j))^2. \qquad (7.2)$$

This formula gives a reduction somewhat too high at energies in the neighborhood of E_j and also fails to give the upturn at very low energies.

The only serious attempt to obtain the full density distribution averaged over all electron energies as function of distance from the shower axis is due to Molière.[6] He neglects ionization losses for all energies above the critical energy E_j, while our Table III shows that this effect reduces $x^2(E)$ by a factor ~2.5 at E_j. The number of electrons in the neighborhood of E_j is also reduced by a similar factor. The contribution of electrons with $E \gtrsim E_j$ is thus very considerably overestimated by Molière. On the other hand, he considers in the low energy region only those electrons that have been slowed down from higher energies (our contribution f_1, compare

[14] G. Cocconi, A. Loverdo, and V. Tongiorgi, Phys. Rev. 70, 846 (1946).

[15] L. Janossy, *Cosmic Rays* (Oxford University Press, London, 1948).

TABLE V. Values of ${}^sK_m(E)$ for $s=2$ and 3; $m=0, 1, 2$.

$\beta b/2E$	${}^2K_0(E)$	${}^2K_1(E)$	${}^2K_2(E)$	${}^3K_0(E)$	${}^3K_1(E)$	${}^3K_2(E)$
1/2	0.370	0.151	0.0679	0.315	0.109	0.0415
2/5	0.421	0.187	0.105	0.363	0.143	0.0607
1/3	0.463	0.222	0.134	0.404	0.175	0.0810
1/4	0.531	0.282	0.173	0.471	0.234	0.122
1/7	0.656	0.438	0.308	0.602	0.375	0.235
1/10	0.730	0.551	0.330	0.66	0.384	
1/20	0.835	0.69	0.55	0.792	0.619	
1/50	0.93	0.86	0.81	0.91	0.83	0.705
0	1	1	1	1	1	1

Section 5). This underestimates the number as well as the individual deviations in the low energy range. It would seem thus that a more accurate calculation should give a somewhat stronger compression of the shower core coupled with a larger sidewise dispersion from the lower energy region. The outmost part of the shower is, according to Molière, due to single scattering through comparatively large angles†† which gives asymptotically for large distances r from the shower axis a decrease of density as r^{-3}. This latter result cannot be strictly correct since it would result in a divergent mean square deviation and it is also physically clear that finally there must be an exponential cut-off.

It is thus difficult to judge how good an approximation Molière's density function represents. In order to obtain a rough criterium, we have calculated the mean square radial moment of Molière's distribution, cutting it off at about two radiation lengths, from where on he has a pure $1/r^2$ law. The result is an $X^2(E)=1.14(E_s/E_j)^2$, while our value for a lower energy cut-off of 4 Mev has the numerical factor 0.64. Molière thus overestimates somewhat the extension of showers and his curve has more qualitative than quantitative significance. The theoretical interpretation of experimental data on large showers is, however, inherently of very rough character. Use of Molière's results will thus probably not lead to a seriously distorted picture.

APPENDIX

The Bhabha-Heitler formula and evaluation of the scattering integrals. Bhabha and Heitler[13] (abbreviated as B.H.) use for the probability of emission of a quantum K by an electron E the formula

$$\sigma(E, K)dKdl=\log 2(dK/K)dl. \tag{A1}$$

Their unit of length is thus connected with the one used here through

$$l\log 2=t. \tag{A2}$$

They write for the probability of pair production in dl

$$\sigma(K)dl=\alpha dl. \tag{A3}$$

Their value for the absorption coefficient of photons is then

$$\alpha=(7/9)\log 2=\delta\log 2. \tag{A4}$$

B.H. express their energies by a logarithmic variable

$$y=\log(E'/E), \tag{A5}$$

where E' is an initial and E a final energy. The total number of electrons plus positrons produced by a primary E' having an energy $\geqslant E$ at a depth l is then expressed in a series

$$F(E', E, l)=F(y, l)=F_0+\sum_{n=1}^{\infty}F_n. \tag{A6}$$

F_0 is the probability that the primary electron has arrived with an energy $\geqslant E$. It is given by the "straggling function" $W(l, y)$ of B.H. (Eq. (6) or Eq. (34) of reference 12).

$$F_0(y, l)=\int_0^y (e^{-\eta}\eta^{l-1}/\Gamma(l))d\eta. \tag{A7}$$

The terms F_n give the numbers of electrons at l with energy $\geqslant E$ which had been produced from the primary with n intermediate quanta. According to B.H.'s formula (reference 13, top of p. 442), it can be written as

$$F_n(y, l)=(2\alpha\log 2)^n e^{-\alpha l}\int_0^l dl' \times\int_0^{l-l'}\frac{dl''e^{\alpha(l'+l'')}l''^n(l-l'-l'')^{n-1}}{(n-1)!(n-1)!} \times\int_0^y\frac{(y-y')^{n-1}}{(n-1)!}F_0(y', l'+l''+n)dy'. \tag{A8}$$

In comparing this expression with the one in B.H., it is to be noted that our F_n is twice the B.H. f_n which represents the number of electrons of one charge only. Further, the formula quoted above (B.H., p. 442) represents f_{n+1}. Tracing the deviation of this formula back to B.H., Eq. (21), and the developments on p. 440, one verifies that the variable l' in Eq. (A8) denotes the distance an electron of the n'th generation has traveled as an individual after it had been created by the immediate ancestor photon. In order to express this dependence explicitly, we write

$$F_n(y, l)=\int_0^l H_n(y, l', l)dl', \quad n\geqslant 1. \tag{A9}$$

For $n=0$, i.e., the straggling of an individual electron, l' is, of course, equal to the total path l, and we write

$$H_0(y, l', l)=F_0(y, l')\delta(l-l'). \tag{A10}$$

The scattering integrals. In Section 4 we had introduced the differential distribution function of electrons

$$f_n(E', E, t)=\partial F_n(E', E, t)/\partial E.$$

†† In the evaluation of the mean square as in this paper the single scattering is included through proper choice of the scattering constant E_s.

In order to take into account ionization losses, we approximated the f_n by Eq. (4.6)

$$f_n(E', E, t)_{\text{corr}} = \int_0^t h_n(E', E+\beta t', t', t)dt'.$$

Here $h_n(E', E'', t', t)$ is the probability under neglection of radiation losses that an electron of the n'th generation arrived at t with the energy E'' after having been created the distance t' backwards. The functions h_n are given by

$$h_n(E', E'') = \partial H_n/\partial E'' = (1/E'')(\partial H_n/\partial y). \quad \text{(A11)}$$

The identification $E = E'' - \beta t$ gives then the modification of the distribution by ionization losses.

The mean square scattering deviation requires the evaluation of the integrals

$$E^{-(s+2)}\, {}^sJ_m^n = \int_0^\infty t^m dt \int_0^t dt' \times \int_{E+\beta t}^\infty (dE'/E'^{s+2}) h_n(E', E+\beta t', t', t), \quad \text{(A12)}$$

where m is 0, 1 or 2, s is 2 or 3, and n goes from 0 to ∞. Upon introduction of the unit length, Eq. (A2), we obtain

$${}^sJ_m^n = (\log 2)^{m+1} \int_0^\infty l^m dl \int_0^l dl' \times \int_0^\infty [e^{-(s+1)y}(\partial H_n/\partial y_n)dy/(1+(\beta l'/E)\log 2)^{s+2}], \quad \text{(A13)}$$

where the H_n are given by Eqs. (A7) to (A10). The expressions (A13) are sixfold integrals. They can be evaluated by one of the so-called "simple calculations" by suitable changes of the order of integration and introduction of new variables.††† The results are as follows:

$${}^sJ_m^0 = (m!/2^{m+1}) b\, {}^sK_m, \quad (m \text{ any value}),$$

$${}^sJ_0^n = [b^{n+1}/2[(s+1)(s+2)]^n]\, {}^sK_0, \quad n = 1, 2, \cdots,$$

$${}^sJ_1^n = \frac{b^{n+1}}{2[(s+1)(s+2)]^n}\left\{n\left(\frac{1}{\delta}+\frac{b}{2}\right){}^sK_0 + \frac{b}{2}\,{}^sK_1\right\},$$

$${}^sJ_2^n = \frac{b^{n+1}}{2[(s+1)(s+2)]^n} \times \left\{\left(\frac{n(n+1)}{\delta^2}+\frac{n^2 b}{\delta^2}+\frac{n(n+1)}{4}b\right){}^sK_0 + bn\left(\frac{1}{\delta}+\frac{1}{2}\right){}^sK_1 + \frac{b}{2}\,{}^sK_2\right\}, \quad \text{(A14)}$$

where

$${}^sK_m(E) = \frac{1}{m!}\int_0^\infty \frac{e^{-x}x^m dx}{[1+(x\beta b/2E)]^{s+2}}, \quad \text{(A15)}$$

$$b = \log 4/\log(s+2).$$

All the $K(E)$ go to unity in the limit $E \to \infty$. The ${}^sJ_m^n$ reduce for $\beta = 0$ to the I_m^n given in Eq. (3.6). The integrals ${}^sK_m$ can be evaluated for large E by expansion of the denominator which leads to a semiconvergent series. They can also be expressed in terms of the exponential integral and thus be computed. Values are given in Table V.

The summations over n can be carried out in closed form with the help of the summation formulas

$$\sum_0^\infty z^n = 1/(1-z); \quad \sum_1^\infty n z^n = z/(1-z)^2;$$

$$\sum_1^\infty n^2 z^n = z(z+1)/(1-z)^3. \quad \text{(A16)}$$

We denote the sums so obtained by

$${}^sJ_m = \sum_{n=0}^\infty {}^sJ_m^n. \quad \text{(A17)}$$

The expressions of these quantities in terms of the integrals K follow.

For $s=2$:

$$\begin{aligned} {}^2J_0 &= 0.545\, {}^2K_0, \\ {}^2J_1 &= 0.273\, {}^2K_1 + 0.0885\, {}^2K_0, \\ {}^2J_2 &= 0.273\, {}^2K_2 + 0.0885\, {}^2K_1 + 0.281\, {}^2K_0. \end{aligned}$$

For $s=3$: (A18)

$$\begin{aligned} {}^3J_0 &= 0.450\, {}^3K_0, \\ {}^3J_1 &= 0.194\, {}^3K_1 + 0.0348\, {}^3K_0, \\ {}^3J_2 &= 0.167\, {}^3K_2 + 0.030\, {}^3K_1 + 0.100\, {}^3K_0. \end{aligned}$$

††† See J. Roberg, Ph.D. Thesis, Duke University, 1942, for all details of this and subsequent calculations.

The Application of a Magnetic Lens Spectrometer to the Measurement of Gamma-Radiation from Zn^{65} and Co^{60}

ERLING N. JENSEN, L. JACKSON LASLETT, AND WILLIAM W. PRATT
*Institute for Atomic Research and Department of Physics, Iowa State College, Ames, Iowa**

(Received September 29, 1948)

A thin magnetic lens spectrometer for the investigation of gamma-ray spectra is described. The effect of the thickness of the radiator used for the production of photoelectrons and the influence of the earth's magnetic field are reported. Based on a calibration of the instrument by means of annihilation radiation and the F line of ThB, energy values of 1.10_6 Mev for the gamma-ray of Zn^{65}, and 1.15_5 and 1.31_7 Mev for the two lines of Co^{60} are obtained. The probable error is estimated as 0.5 percent.

I. INTRODUCTION

THE use of a thin magnetic lens spectrometer for the study of beta- and gamma-radiations has been reported by several investigators.[1–4] The flexibility of such an instrument and, if iron-free, the convenience of its linearity have been previously indicated.[1] It is the purpose of this paper to describe briefly a magnetic lens spectrometer which we have constructed, to present the results of studies to determine the corrections which should be made to data obtained with it, and to give the energies found for the gamma-radiations from Zn^{65} and Co^{60}.

II. DESCRIPTION OF SPECTROMETER

The spectrometer is shown in Figs. 1 and 2. The design is similar to that employed by previous workers,[1–3] save that the instrument is mounted with its axis parallel to the magnetic field of the earth and, to minimize scattering, the chamber proper has been constructed of aluminum tubing. To preserve linearity, nonferromagnetic materials have been used throughout.

The spectrometer chamber is 7 inches in diameter and 40 inches long, evacuated by means of a two-stage oil diffusion pump backed by a mechanical pump. The baffles, shown in Fig. 2, are of micarta, ½-inch thick, except for the gamma-ray shields, which are of lead sheathed with aluminum. Baffle *C*, which is adjustable by means of a brass rod passing out of the chamber through a Wilson seal, serves to delimit the electrons analyzed and so, for a given diameter of source and counter window, determines the intensity and resolution obtained. The lead shield surrounding the counter is primarily for the purpose of absorbing scattered gamma-radiation and was designed to lie within the shadow of the lead shield in the center of the spectrometer. An indication of the small extent of electron scattering obtained with the arrangement described is seen from the fact that, with no current in the coil, the counting rates obtained with and without a 10 microcurie beta-ray source in the instrument were, respectively, 21.1 ± 0.4 and 20.7 ± 0.2 cts/min.

Radioactive sources are mounted on Lucite holders at the end of a brass tube which enters the upper end of the spectrometer through a Wilson seal and through a 2½-inch gate valve modified to be suitable for vacuum service. The counter is mounted within a similar brass tube at the lower end of the instrument, where Wilson seals are again used to facilitate assembly and adjustment. The counter was originally used with a mica window of 4 mg/cm² surface density; for the ThB measurements a 1.1 mg/cm² window was used and for the most recent work a thin Formvar-polystyrene film ($\cong$0.3 mg/cm²) was employed.

The coil for producing the magnetic field consists of 2799 turns of No. 12 single cotton-covered enameled copper wire, wound on a form consisting of a brass hub and two aluminum

* Paper No. 42 from the Institute for Atomic Research. Work performed at the Ames Laboratory of the Atomic Energy Commission.

[1] M. Deutsch, L. G. Elliott, and R. D. Evans, Rev. Sci. Inst. 15, 178 (1944).

[2] W. Rall and R. G. Wilkinson, Phys. Rev. 71, 321 (1947).

[3] L. C. Miller and L. F. Curtiss, J. Research Nat. Bur. of Standards 38, 359 (1947).

[4] E. A. Quade and D. Halliday, (*a*) Phys. Rev. 72, 181(A) (1947); (*b*) Rev. Sci. Inst. 19, 234 (1948).

castings. Every fourth layer of wire is followed by a copper sheet, 0.030-inch thick, provided with 12 tabs which are soldered to water-cooled brass blocks mounted on the exterior surface of the castings. The completed coil has an inside radius of 9.9 cm, an outside radius of 28.3 cm, and an axial length of 10 cm. When the full number of turns is used with 220 volts across the coil, a focal length of 25 cm is obtained for electrons of approximately 3.4 Mev energy.

The focusing current for the coil is provided by a 2 kw motor-generator set. To stabilize the current, a portion of it is passed through a bridge circuit which has as one of its elements a 60-watt tungsten lamp bulb to serve as a non-linear resistance. Changes in the coil current affect the balance of the bridge and the resulting error-signal, when amplified, is used to correct the generator field. The magnetic field is thereby maintained constant within a probable error of 0.1 percent. The coil current is measured by means of a series resistance and a potentiometer.

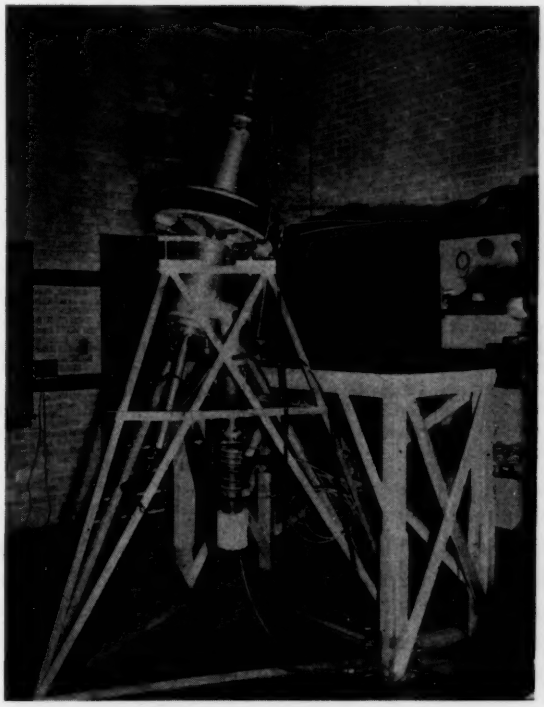

FIG. 1. The magnetic lens spectrometer, aligned with its axis parallel to the magnetic field of the earth.

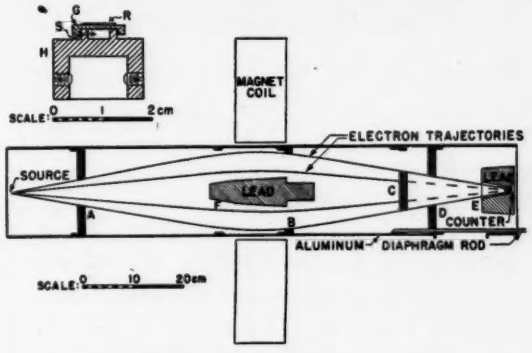

FIG. 2. Diagram of spectrometer chamber. *Insert:* Source holder.

III. DETERMINATION OF GAMMA-RAY ENERGIES

A. General Method. In the work described in this paper, the gamma-ray energies were determined by a study of the spectra of photoelectrons produced in radiator foils. For calibration, use was made of photoelectrons produced by the annihilation radiation from Zn^{65} and of conversion electrons from ThB (F line). Each gamma-ray source S (Fig. 2), a few mm thick, was mounted in a Lucite holder H and covered by an aluminum cap G, which carried the radiator R.

The spectra obtained from Zn^{65} and Co^{60} sources are shown in Figs. 3 and 4. In addition to the photoelectric conversion lines generated in the lead by gamma- and annihilation radiation, a broad distribution of Compton electrons is also obtained.

To permit an accurate determination of the energies of the photoelectrons ejected from the radiator, attention must be given to the effect of radiator thickness and to the influence of the earth's magnetic field, which is in the direction of the spectrometer axis.

B. Effect of the Magnetic Field of the Earth. For a focusing field of a *given shape* the momentum of the focused electrons will quite generally be proportional to the strength of the field and, if the field in question is proportional to the coil current, we may write for this momentum

$$P = I \cdot F, \tag{1}$$

where I is the current in the coil and F is dependent upon the shape of the field. In the presence of an additional magnetic field H, superposed upon that produced by the coil current, F may be regarded as a function of the ratio H/I, since the shape of the field would remain un-

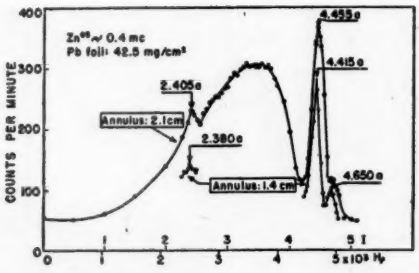

FIG. 3. Spectrum of Zn^{65}, showing the photoelectric-conversion peaks produced in a lead radiator by annihilation radiation and the 1.11 Mev gamma-ray, in addition to the broad distribution of Compton electrons. The sharper peaks shown separately were obtained with an adjustment which permitted the K and L lines to be resolved. The annulus is the width of the electron beam at the center of the spectrometer.

changed if H and I were to vary in a mutually proportional manner. The relation between the current I_1 required to focus electrons of a given energy in the presence of the field H, and the current I_0 required in its absence may therefore be written,

$$I_1F(H/I_1)=I_0F(0). \tag{2}$$

One then finds, to a first approximation, that

$$I_1-I_0=-HF'(0)/F(0), \tag{3}$$

indicating that this difference is independent of the energy of the electrons. This is in agreement with the conclusions of Quade and Halliday,[4b] who have shown experimentally that for their spectrometer very little error is made by applying Eq. (3) to electron energies as low as 10 kev.

In the use of the spectrometer, it is the current necessary to focus electrons in the *absence* of an external field which is to be taken as proportional to the momentum, so the difference I_1-I_0 must be determined and applied as a correction. This correction is most readily found by observing the change in the focusing current required when the current in the coil is reversed. It is, however, of interest to note that an approximate calculation, described in the Appendix, leads to a value for the correction which is independent of the energy and is in good numerical agreement with that found empirically. When all the turns on the focusing coil are employed, the current required to focus a particular conversion line is found to change by 0.012 amp when the current is reversed, so the correction then to be applied because of the presence of the magnetic field of the earth has been taken as ± 0.006 amp.

C. Effect of Radiator Thickness. The photoelectrons ejected from a radiator will, for a particular gamma-ray energy, have energies which depend upon the depth of the point from which they originate. The momentum distribution of the emergent electrons will, to a first approximation, be rectangular, with a width equal to the momentum loss associated with a full traversal of the radiator foil.** Figure 5(A) shows a momentum distribution of this type, which extends from a momentum P_a to the maximum momentum P_m. The result of the combination of this distribution function with the transmission curve of the spectrometer must be considered and will indicate the manner by which the experimental data may be corrected in cases for which the effect of radiator thickness is not completely negligible. The result of an analysis of this character will be applicable with equal validity to internal conversion lines which arise from a source of non-vanishing thickness.

The transmission curve of a magnetic lens spectrometer has been investigated by Deutsch

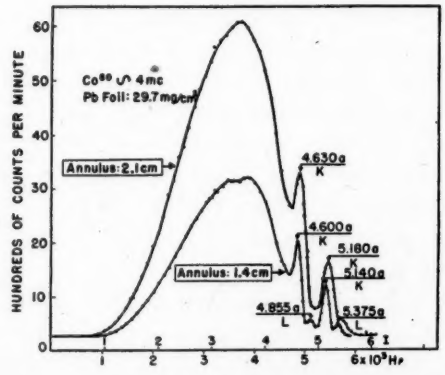

FIG. 4. Spectrum of Co^{60}, showing the photoelectric-conversion peaks produced in a lead radiator by the two gamma-rays present.

** To a higher order of approximation it might be supposed that, because of the change of the rate of momentum loss as the electrons lose energy in the foil, a *trapezoidal* distribution should be considered. In addition, the *scattering* of electrons in their passage through the foil would cause the distribution to drop and tail off on the low momentum side. An approximate analysis of these phenomena, as well as the experimental results reported here, indicates, however, that these effects are not of importance in the energy range with which we are concerned in the present paper. At lower energies scattering will certainly play a prominent role [cf. Bethe, Rose, and Smith, Proc. Am. Phil. Soc. **78**, 573 (1938)].

et al.[1] and has approximately the shape of an isosceles triangle for the case in which the image and counter windows have the same size. As the current is changed in the coil of the spectrometer, the width of the transmission curve will vary in direct proportion to the momentum of the electrons which it passes. For a triangular transmission curve, we therefore take the half-width b as equal to a constant K multiplied by the momentum P_0 corresponding to the point of maximum transmission. This is illustrated by Fig. 5(B). The constant K evidently serves as a measure of the resolution of the instrument. When, in order to obtain the expected line shape, we pass such a transmission curve across the momentum distribution for the electrons, there are two cases to consider. The first of these is that for which the momentum spread of the electrons is less than the full width of the transmission curve, as illustrated by Fig. 5(C); the other is that for which the momentum spread is greater than the width of the transmission curve and is shown in Fig. 5(D).

In the case of a *thin* radiator, specifically one for which the momentum spread P_m-P_a is less than $2b$, the maximum transmission is found to occur when

$$P_0\cong(P_a+P_m)/2, \tag{4}$$

neglecting terms small compared to P_m-P_a. Thus

$$P_m\cong P_0+a/2, \tag{5}$$

where

$$a\equiv P_m-P_a. \tag{6}$$

The effect of radiator thickness is, therefore, to give maximum transmission at a momentum which is less than the maximum momentum of the electrons by an amount which is equal in a first approximation to one-half the momentum loss experienced by electrons which traverse the full thickness of the radiator.

For a thick radiator, for which $P_m-P_a>2b$, maximum transmission is to be expected when the transmission curve lies just inside the momentum distribution, if terms in K^2 are neglected. Thus

$$P_m\cong P_0(1+K), \tag{7}$$

where

$$K=b/P_0. \tag{8}$$

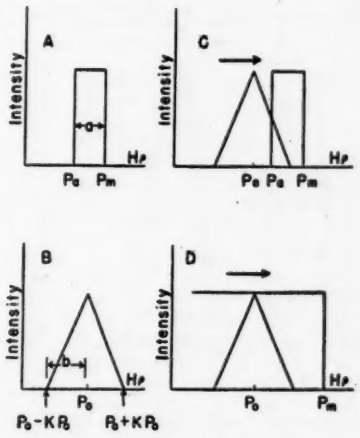

FIG. 5. Momentum distribution and transmission curve of spectrometer, as assumed for the purposes of the analysis given in the text.

In determining, from the current corresponding to maximum transmission, the upper limit of the momentum distribution of electrons generated by an unknown gamma-ray, the factor $(1+K)$ may be absorbed into the calibration constant of the spectrometer *provided* the radiator thickness is such that Eq. (7) is applicable. It should be noted that, owing to the variation of the rate of momentum loss, a radiator which can be correctly regarded as a thin foil for high energies may, on the other hand, be effectively a thick foil at lower energies. We shall, therefore, apply the correction indicated by Eq. (7) in an *explicit* fashion in those cases to which it applies. In analyzing the data reported in this paper, we have based the energy determinations on the positions of the *maxima* of the curves obtained, subject to the corrections indicated above, since the maximum appears to be the point most accurately located for every line.

The complete line shape which results from a combination of a rectangular momentum distribution and a triangular transmission curve has been calculated for the case that a/P_m, the relative momentum spread from the radiator, is 0.03 and the resolution of the spectrometer is such that $K=0.021$. The calculated curve is represented by the broken line in Fig. 6 and may be compared with the solid line, which gives the results experimentally obtained under these conditions with photoelectrons produced in lead by Zn^{65} radiation ($P_m\cong4800$ gauss-cm). The

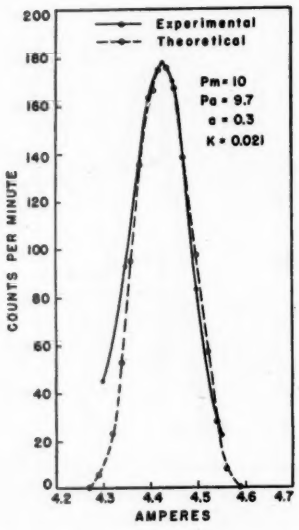

FIG. 6. Resultant line shape obtained with electrons for which $P_m \simeq 4800$ gauss-cm. The dotted curve represents the line shape calculated for $a/P_m = 0.03$ and $K = 0.021$; the solid curve represents the shape obtained experimentally under comparable conditions.

two curves were made to fit at their peaks and it is felt that their shapes are in satisfactory agreement. The somewhat larger counting rate obtained experimentally on the low momentum side of the line may be ascribable to straggling and scattering phenomena, the importance of which is indicated, for example, by the work of White and Millington.[5]

An experimental study was made of the positions of the points of maximum intensity when various radiator thickness are used. For this purpose the 1.1 Mev gamma-ray of Zn^{65} was again used, with the results shown in Figs. 7 and 8. It is seen that, in agreement with our previous discussion, the shift of the peaks obtained with thin foils is proportional to the thickness of the radiator, but becomes constant when the foil thickness exceeds a value of approximately 65 mg/cm². The slope of the initial part of the curve in Fig. 8 corresponds to 1.7_5 gauss-cm/mg-cm^{-2}. The theoretical rate of energy loss in lead, as obtained from a formula given by Heitler,[6] is 1.0 Mev/gm-cm^{-2} for electrons of the energy with which we are concerned here. This theoretical energy loss corresponds to a momentum loss of 3.5 gauss-cm/mg-cm^{-2} and, when compared with the slope of the experimental curve, affords confirmation of the statement that the peaks should be shifted by an amount which is half the momentum loss associated with a full traversal of the radiator foil.

The horizontal portion of the curve of Fig. 8 occurs at a current value which is 2.3 percent below the extrapolated value for zero foil thickness. This implies that $K = 0.023$, which is consistent with the expected resolution for the spectrometer at the time the data were obtained. The break in the curve of Fig. 8 occurs, as expected, at a radiator thickness for which $a = 2b$. Similar data obtained with a lower energy gamma-ray, for which the photoelectrons have an energy of 0.177 Mev, indicate that the break occurs for a foil thickness between 6.6 and 11.3 mg/cm². In this case the condition $a = 2b$ would imply a thickness of 10 mg/cm².

IV. RESULTS

The photoelectric conversion lines obtained with lead radiators were measured for the Zn^{65} and Co^{60} radiations at each of two settings of the adjustable baffle. For these baffle positions, the radial width of the effective aperture at the center of the spectrometer assumed the values 2.1 and 1.4 cm. The resolution of the spectrometer was characterized by $K = 0.023$ and $K = 0.021$ in these two cases. As may be seen from Figs. 3 and 4, lines were obtained from both the K and L shells of the lead in the second series of measurements.

For calibration, the F line of ThB and the photoelectric line produced by the Zn^{65} annihilation radiation were measured at each of the two adjustments of the instrument. For the two adjustments the calibrations from the annihilation radiation and the F line of ThB agree to 0.1 percent and 0.3 percent, respectively. The ThB sample was deposited on an aluminum foil 0.00025 inch thick and mounted on the Lucite source holder by means of a thin Formvar-polystyrene film. The line obtained with this source is shown in Fig. 9.

The results of the measurements are summarized in Table I. Lines which are similar in character and for which the intensity measurements are made with equal precision can, presumably,

[5] B. A. White and B. A. Millington, Proc. Roy. Soc. (London) **A120**, 701 (1928).

[6] W. Heitler, *The Quantum Theory of Radiation* (Oxford University Press, London, 1936), p. 219.

be located with the same *relative* accuracy, although the lines are of different momenta and occur at different current values. In the work reported here, however, the data obtained were such that the location of the various lines could not be determined in all cases with the same relative accuracy; accordingly, the estimated weighting factors indicated in Table I were applied to the current/momentum ratios.

In calculating, from the data of Table I, the momenta of the photoelectrons generated in the lead radiator by the Zn^{65} gamma-ray, a correction of 74 gauss-cm was taken as appropriate to the foil thickness employed. For the Co^{60} determinations the correction was assigned the values 51 and 64 gauss-cm for the thinner and thicker Pb radiators, respectively. The correction made for the Th radiator was 48 gauss-cm and that for the U foil was 70 gauss-cm. Upon converting from the resulting momenta to the corresponding energy values and adding the binding energy appropriate to the photoelectric process involved, the gamma-ray energies shown in the final column of Table I resulted. Averaging for each line the energy values so found, taking into account the weights assigned to the individual determinations and to the calibration measurements, the following gamma-ray energies are obtained:

Zn^{65}, 1.10_6 Mev;
Co^{60}, I, 1.15_5 Mev;

and

Co^{60}, II, 1.31_7 Mev.

A conservative estimate of the probable error for the values of the gamma-ray energies is ± 0.5 percent. The constant of the spectrometer has the values 1063 and 1074 gauss-cm/amp. for the two adjustments used.

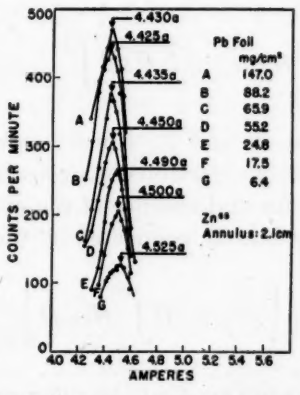

FIG. 7. Photoelectric lines obtained from the 1.11 Mev gamma-ray of Zn^{65} with various thicknesses of the lead radiator.

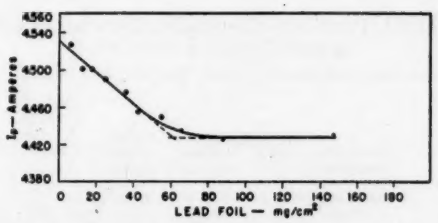

FIG. 8. Current values corresponding to the peaks of the lines of Fig. 7, as a function of radiator thickness. The results of additional data, not shown in Fig. 7, are included. In determining the slope of the line, the points designated by the heavy solid circles were given half the weight of those marked by open circles.

It is that seen the value found for the energy of the Zn^{65} radiation is below the energy for either of the Co^{60} gamma-rays. Because of the possible interest[7] in the use of these radiations as standards, a direct comparison of the energies was felt to be desirable. To this end a source with *both* activities was put into the spectrometer. As reported[8] previously, the individual peaks in the composite spectrum were readily identified and indicated that the gamma-ray from Zn^{65} is of lower energy than either of the Co^{60} lines.

The energies found for the Co^{60} gamma-rays are in good agreement with those given by Miller and Curtiss,[3] although somewhat higher than the values of Deutsch *et al.*[7] The energy found for the Zn^{65} gamma-ray is lower than the value given in an early report by Deutsch,

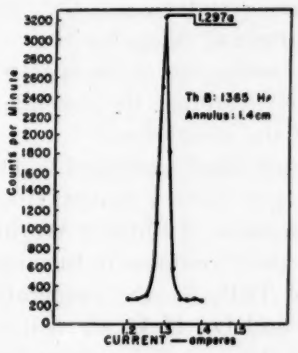

FIG. 9. The *F* line of ThB.

[7] M. Deutsch, L. G. Elliott, and A. Roberts, Phys. Rev. 68, 193 (1945).
[8] E. N. Jensen, L. J. Laslett, and W. W. Pratt, Phys. Rev. 73, 529 (1948).

TABLE I. Positions of conversion lines measured in magnetic-lens spectrometer.

Line	Momentum (gauss-cm)	Aperture width (cm)	Radiator thickness (mg/cm²)	Coil current (amp.)*	Relative weight (of curr./momentum ratio)	Gamma-ray energy (Mev)
Annih.	2608/1.023**	2.1	42.5 Pb	2.401 (av.)	5	
ThB	1385†		Negligible	1.303	10	
Zn^{65} (K)			42.5 Pb	4.454††	20	1.10₈
Co^{60}, I (K)			29.7 Pb	4.624	10	1.15₀
Co^{60}, II (K)			29.7 Pb	5.174	10	1.31₇
Annih.	2608/1.021**	1.4	42.5 Pb	2.374	3	
ThB	1385†		Negligible	1.291	10	
Zn^{65} (K)			42.5 Pb	4.409	10	1.10₈
(L)			42.5 Pb	4.644	5	1.10₈
Co^{60}, I (K)			42.0 U	4.501	10	1.16₀
(K)			28.5 Th	4.524	10	1.15₈
(K)			37.0 Pb	4.583	10	1.15₆
(K)			29.7 Pb	4.594	10	1.15₆
(L)			29.7 Pb	4.849	5	1.16₂
Co^{60}, II (K)			42.0 U	5.011	10	1.31₆
(K)			28.5 Th	5.045	10	1.31₄
(K)			37.0 Pb	5.104	10	1.31₅
(K)			29.7 Pb	5.134	10	1.32₁
(L)			29.7 Pb	5.369	5	1.32₁

* 0.006 amp. has been subtracted from the observed current values to correct for the magnetic field of the earth.

** Since the radiator is *thick*, in the sense $a>2b$, for electrons of the energy with which we are concerned here, the momentum value of 2608 gauss-cm corresponding to 0.5108 Mev must be divided by $1+K$ to correct for radiator thickness.

† C. D. Ellis, Proc. Roy. Soc. (London) **A138**, 318 (1932).

†† Obtained from the sloping portion of the curve of Fig. 8, so that data obtained with several foil thicknesses are, in effect, included.

Roberts, and Elliott[9] and that obtained by Mandeville and Fulbright[10] through a study of Compton electrons.

V. ACKNOWLEDGMENTS

We should like to indicate our gratitude to Dr. J. M. Keller for helpful discussions on the theory of the spectrometer and to Dr. A. F. Voigt for his invaluable contribution in the preparation of the radioactive sources. Acknowledgment should also be made to Messrs. R. B. Leachman and R. C. Skar for constructing the Geiger-Müller counters, to the staff of the College Instrument Shop for their cooperation during the construction of the spectrometer, and to Mr. E. R. Rathbun for assistance with the operation of the instrument.

We are particularly indebted to Dr. F. N. D. Kurie and Capt. W. H. Ferguson (U. S. N., Ret.) of the Department of Physics, Washington University, for their kindness in furnishing us with a sample of ThB. By the cooperation of Mrs. G. W. Fox and Dr. P. H. Carr, it was possible to transport this sample by air to Ames in a few hours.

[9] M. Deutsch, A. Roberts, and L. G. Elliott, Phys. Rev. **71**, 389(A) (1942).

[10] C. E. Mandeville and H. W. Fulbright, Phys. Rev. **64**, 265 (1943).

APPENDIX: APPROXIMATE CALCULATION OF THE CORRECTION FOR THE MAGNETIC FIELD OF THE EARTH

The solution of the differential equations for the trajectories of paraxial electrons in an axial magnetic field $H_z=H_0/[1+(z/a)^2]$ has been given by Glaser.[11] When the object distance and image distance are equal ($u=v=2f$), the focal length f may be written

$$f=\Lambda[H\rho]^2\Big/\int_{-u}^{u}H_z^2dz, \qquad \text{(i)}$$

where Λ is a numerical coefficient, calculable in terms of f/a, which takes on values extending from $\Lambda=4$ for f/a large (thin lens) to π^2 for f/a small (solenoid). Here $[H\rho]$ serves as a measure of the momenta of the electrons in question in terms of their radius of curvature in a uniform magnetic field.

Assuming that to a field of the shape mentioned above, there is added a small constant axial field H, one can attempt to fit the resultant field in an approximate way to an equation of the original form and so obtain new values, H_0' and a' for the parameters. In this way we find that $H_0'-H_0\cong 8H/7$ and $a'-a\cong(12a/7)(H/H_0)$.

Introducing a constant A which connects the current in the coil with the magnetic field produced, so that

$$\int_{-u}^{u}H_{\text{coil}}^2dz=AI^2, \qquad \text{(ii)}$$

we then write the approximate relation for the *total* field as

$$\int_{-u}^{u}H_z^2dz\cong AI^2+2H\int_{-u}^{u}H_{\text{coil}}dz. \qquad \text{(iii)}$$

The currents I_1 and I_0, which are respectively required to focus electrons of a given momentum in the presence and absence of the external field, are then, by Eq. (i), connected by the relation

$$\frac{AI_0^2}{\Lambda(f/a)}=\left[AI_1^2+2H\int_{-u}^{u}H_{\text{coil}}dz\right]\frac{1}{\Lambda(f/a')}. \qquad \text{(iv)}$$

From this it follows that the difference I_0-I_1 is

[11] W. Glaser, Zeits. f. Physik **117**, 285 (1941).

approximately

$$I_0-I_1=H\left[\left(\frac{1}{A}\right)\int_{-u}^{u}(H_{\text{coil}}/I)dz + (6/7)(I/H_0)\frac{d\ln\Lambda}{d\ln(f/a)}\right]. \quad \text{(v)}$$

Through the use of Eqs. (i) and (ii) an approximate value of A is readily estimated experimentally by fucusing electrons of known energy, while H_0/I and $\int_{-u}^{u}(H_{\text{coil}}/I)dz$ may be calculated from the geometry of the coil, the latter quantity being given closely by $4\pi/10$ times the number of turns on the coil.

For the spectrometer described in the present paper, the following values apply when all the turns on the coil are employed:

$f=25$ cm, $a\cong 13.6$ cm, $f/a=1.84$,

$\Lambda=5.1$, $d\Lambda/d(f/a)=-0.65$, $\dfrac{d\ln\Lambda}{d\ln(f/a)}=-0.23$,

$A=2.27\times10^5$ gauss^2-cm/amp.^{2},

$H_0/I=93.5$ gauss/amp.,

$\int_{-u}^{u}(H_{\text{coil}}/I)dz=3230$ gauss-cm/amp.,

and $H=0.56$ gauss.

With the substitution of these values in Eq. (v) we find $I_0-I_1=0.007$ amp., in close agreement with the correction found experimentally.

PHYSICAL REVIEW VOLUME 75, NUMBER 3 FEBRUARY 1, 1949

The Magnetic Susceptibility of BeO

CLYDE A. HUTCHISON, JR.
Argonne National Laboratory and the Institute for Nuclear Studies, University of Chicago, Chicago, Illinois

(Received October 15, 1948)

The molal magnetic susceptibility of pure BeO is found to be -11.93×10^{-6} (c.g.s. units) at 24.8°C.

I. INTRODUCTION

THE value of the molal magnetic susceptibility of BeO is given in the standard reference sources as 0.0×10^{-6} based on the work of Meyer.[1] (The values -2.8×10^{-6} and -1.9×10^{-6} at two field strengths have also been found by Huttig and Kittel.[2]) However, it has been pointed out by Angus[3] that application of Slater's[4] screening constants in slightly modified form to the calculation of the diamagnetic susceptibilities of Be^{+2} and O^{-2} ions gives -11.39×10^{-6} [5] as the sum of the two. Since there was no apparent reason for this discrepancy, a measurement of the susceptibility of BeO has been made.

[1] Meyer, Ann. d. Physik **69**, 236 (1899).
[2] G. F. Huttig and H. Kittel, Gazz. Chim. Ital. **63**, 833 (1933).
[3] W. R. Angus, Proc. Roy. Soc. London **A136**, 579 (1932).
[4] John C. Slater, Phys. Rev. **36**, 57 (1930).
[5] Angus's value of -11.60×10^{-6} has been corrected, taking into consideration newer values of certain constants.

II. EXPERIMENTAL PROCEDURE

The Gouy method has been employed for the measurement of the magnetic susceptibility of BeO powder.

The sample of "Fluorescent Grade" BeO powder was prepared by the Clifton Products Company, Inc., Painesville, Ohio, by ignition of a mixture of $Be(OH)_2$ and $BeSO_4$ in a process designed to give a product with a very low im-

TABLE I. Impurities in BeO sample.

Impurity	Parts per million
Ag	1
Al	10
Ca	<50
Cu	<10
Fe	< 1
Mg	10
Mn	< 0.5
Ni	<10
Pb	< 2
Si	20
Sn	< 2

TABLE II. Magnetic susceptibility of BeO.

ρ g cm^{-3}	$F_{BeO}\times10^6$ g	Temp. °C	$\chi_{BeO}\times10^6$ c.g.s. units	$\chi_{molal}\times10^6$
0.500	5466	24.9	−0.479	−11.98
0.533	5825	24.7	−0.476	−11.91
0.540	6173	24.8	−0.495	−12.38
0.559	5954	24.8	−0.462	−11.56
0.561	6156	24.8	−0.475	−11.88
		Average	−0.477 ±0.008	−11.93 ± 0.19

TABLE III. Magnetic susceptibility of BeO.

Approximate field strength $\times10^{-4}$ oersted	$F_{BeO}\times10^6$ g	Temp. °C	$\chi_{BeO}\times10^6$ c.g.s. units	$\chi_m\times10^6$
1.24	6156	24.8	−0.475	−11.88
1.07	4715	25.1	−0.481	−12.03
0.81	2703	24.9	−0.483	−12.08

purity content. Table I gives the results of spectrographic analysis of the sample used.

The sample was found by ignition at 800–850°C to contain 1.22 percent H_2O.

The powder was packed in a Pyrex tube, the lower half of which was evacuated. The weighings were made in an atmosphere of N_2 at temperatures from 24.7 to 24.9°C. The sample tube had an inside mean cross-sectional area of 0.323 cm^2 with a ~2 percent variation over the length of the tube. The mean density of the sample was determined by weighing combined with cathetometric measurement of the length of the sample. The length used was ~16 cm. The tube was calibrated magnetically by weighing when filled with degassed water at 24.7°C and at a magnet current (thermionically controlled) of 8.83 amperes (approximately 1.24 $\times10^4$ oersted), the value used for the measurements on BeO. The values of Auer[6] for the susceptibility of water were employed.

The magnetic susceptibility of BeO was calculated by use of the following expression:

$$\chi_{BeO}=\frac{1}{m_{BeO}}\left\{\frac{1}{\rho}\left[F_{BeO}\frac{\chi_{H_2O}\rho_{H_2O}}{F_{H_2O}}-\left(1-\frac{\rho}{3.01}\right)\kappa_{air}\right]-\chi_{H_2O}m_{H_2O}\right\},$$

where the meanings of the symbols are as follows:

χ_{BeO} = gram susceptibility of BeO.
m_{BeO} = fraction BeO in the sample (0.9878).
ρ = density of BeO-air mixture in sample tube.
F_{BeO} = the force exerted by the field on the BeO sample corrected for the force on the tube (−0.000042 g as determined by weighings in which the upper half of the tube was filled with N_2).
χ_{H_2O} = gram susceptibility of H_2O at 24.7°C.
ρ_{H_2O} = density of H_2O at 24.7°C.
F_{H_2O} = force exerted by field on H_2O at 24.7°C (−0.018094 g).
κ_{air} = cm^3 susceptibility of air [$(2.52\times10^{-3}/T^2)$ where T is the absolute temperature].
m_{H_2O} = fraction H_2O in the sample (0.0122).

3.01 g cm^{-3} is the theoretical x-ray density of BeO and is employed to correct for the presence of air in the sample tube.

The results of measurements on five separate fillings of the tube are summarized in Tables II and III.

Two additional measurements on the fifth sample were made at magnet currents of 7.00 amperes (approximately 1.07×10^4 oersted) and 5.00 amperes (approximately 0.81×10^4 oersted).

III. CONCLUSIONS

The lack of appreciable variation of susceptibility with field strength and the results of spectrographic analysis indicate that the measurements were made on a quite pure sample. The value, -11.93×10^{-6}, of the molal susceptibility is in relatively good agreement (4.7 percent deviation) with the value -11.39×10^{-6} which results from the calculation of the sum of the susceptibilities of Be^{+2} and O^{-2} by use of Angus's modification of Slater's screening constants for determining the mean squares of the orbital radii.

[6] E. C. Stoner, *Magnetism and Matter* (Methuen and Company, Ltd., London, 1934), p. 552.

PHYSICAL REVIEW VOLUME 75, NUMBER 3 FEBRUARY 1, 1949

Multiple Compton Scattering

W. R. FAUST AND M. H. JOHNSON
Nucleonics Division, Naval Research Laboratory, Washington, D. C.

(Received September 7, 1948)

An experimental and theoretical investigation has been made of the γ-radiation in water produced by a uniform distribution of radioactive cobalt. The intensity and spectral distribution of the radiations are determined essentially by the multiple Compton scattering that takes place in the liquid. An approximate quantitative treatment is presented in which the multiple scattering is considered as a succession of steps which are the same for every emitted γ-ray. Although the method is quite crude, the numerical results both for the absolute counting rate of a submerged counter and for the effect of shielding around the counter are in close agreement with experiment.

I. INTRODUCTION

WHILE much experimental work[1] has been done on the scattering of γ-radiation, the study of multiple scattering has been neglected. In the arrangements usually considered, a plane parallel beam falls upon a target. The geometrical factors thereby introduced make an analysis of the results difficult.[2]

A substantial simplification is possible by use of a γ-ray source which is homogeneously distributed throughout an infinite medium. The effect of multiple scattering then manifests itself in the intensity and spectral distribution of the radiation which is the same at every point in the medium. In the next section of this paper, we will show that these quantities can be related, in a simple way, to the strength of the source and the density of electrons in the medium. In Section III an equally simple experimental arrangement is described which effectively provides a γ-ray source distributed throughout an infinite medium. In Section IV the measurements of intensity and spectral distribution are compared with the theoretical values.

II. THEORY

Suppose that there are η-γ-ray sources per cubic cm distributed throughout a uniform medium and that each source emits λ-quanta of energy E_0 per second. Each quantum is scattered many times by the electrons of the medium,[3] losing energy in each scattering process according to the familiar Compton formula, until it is finally absorbed photoelectrically. The quanta existing in the medium can then be divided into groups which are determined by the number of scatterings experienced, i.e., quanta in the k'th group have been scattered k times. The quanta in each group will be distributed in energy about some mean energy, E_k.

Every quantum will travel a mean distance, l, between scattering processes. This distance depends upon the energy and can be computed from the well-known Klein-Nishina formula.[4] It is plotted as a function of the energy for the electron density of water (3.37×10^{23} electrons/cm^3) in Fig. 1. It is inversely proportional to the electron density.

The Klein-Nishina cross section, σ, can be decomposed into the sum $\sigma_a+\sigma_s$ where σ_s/σ is the fraction of incident energy given to the scattered quantum while σ_a/σ is the fraction of incident energy given to the recoil electron. The ratio σ_s/σ can be obtained by integrating the scattered intensity as given by the Klein-Nishina formula over all angles and dividing the result by the product of the total cross section and the incident energy. A graph of this ratio against energy is shown in Fig. 2.

We will now assume that each quantum passes through a succession of energy values given by the mean energies of the various groups. Thus the actual problem is replaced by one in

[1] A. H. Compton and S. K. Allison, *X-Rays in Theory and Experiment* (D. Van Nostrand Company, Inc., New York, 1930), Ch. III.

[2] Hirshfelder, Magee, and Hull, Phys. Rev. **73**, 8 (1948).

[3] It is assumed that the energy E_0 is sufficiently low that pair production is negligible.

[4] W. Heitler, *The Quantum Theory of Radiation* (Oxford University Press, London, 1944), Ch. III.

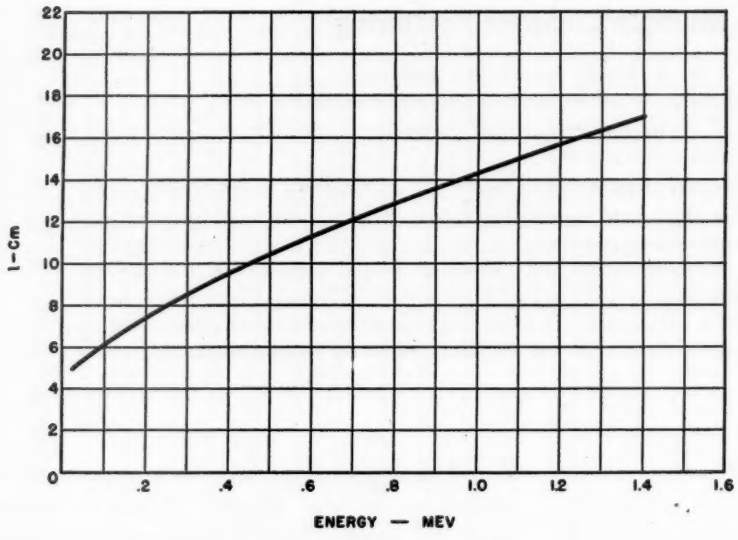

FIG. 1. Mean distance, l, between scatterings.

which all quanta of the kth group have the mean energy E_k. The accuracy of this procedure will be discussed in Section IV. With this assumption the mean energy of the $k+1$st group is determined from the energy of the kth group by

$$E_{k+1}=(\sigma_s/\sigma)E_k, \tag{1}$$

where σ_s/σ is evaluated for the energy E_k. The succession of energy values determined by Eq. (1) for an initial energy $E_0=1.2$ Mev is given in Table I.

A detector immersed in the medium will, according to an obvious definition of efficiency, ϵ, register quanta of the kth group at a rate R_k given by

$$R_k=\int_{\Delta E_k}\epsilon(E)dE\int\bar{F}_k\cdot d\bar{\sigma}, \tag{2}$$

where $\bar{F}_k$ is the incident flux of quanta of the k'th group, and ΔE_k is an energy interval that contains all quanta of the k'th group. The surface integral is extended over the active surface of the detector. It may be readily evaluated for a detector of axial symmetry whose area projected perpendicularly to the axis of symmetry is A. Let $N_k=\int n_k dE$ where n_k is the number of quanta of the kth group per unit energy interval generated in each cubic cm per second. Then it is readily shown that

$$\int\bar{F}_k\cdot d\bar{\sigma}=\frac{\pi}{4}n_k l A. \tag{3}$$

Substituting Eq. (3) in (2) and summing over k, we find

$$R=\sum_0^\infty R_k=\frac{\pi}{4}A\sum_0^\infty\int_{\Delta E_k}\epsilon n_k l dE$$

$$=\frac{\pi A}{4}\sum_0^\infty N_k l_k\epsilon_k. \tag{4}$$

In the last step the assumption that all quanta of the kth group have the same energy has been used, and the subscripts on l and ϵ mean that values of these quantities at the energy E_k are to be used.

Usually the photoelectric absorption of the detector walls causes the response of the detector to vanish at an energy sufficiently high that the photoelectric absorption of the medium is negligible. Then, in the region of interest, N_k is constant and must be equal to $\eta\lambda$, the number of quanta emitted by the γ-ray source per cm^3

TABLE I. Scattered energies.

Energy Mev	σ_s/σ	d	dl_{Al}	dl_{Pb1}	dl_{Pb2}
1.2	0.545	106	105	100	95
0.654	0.63	37	36.2	34.6	32.1
0.412	0.64	17	16.5	12.4	9.3
0.284	0.73	11	10.5	6.0	3.42
0.207	0.79	9.5	9.0	3.24	1.17
0.164	0.825	10.5	9.9	2.38	0.57
0.135	0.845	11	10.3	1.55	0.24
0.113	0.86	12	11.2	1.01	0.09
0.098	0.875	12	11.1	0.22	
0.086	0.89	11	10.1		
		237	229	161.4	141.1

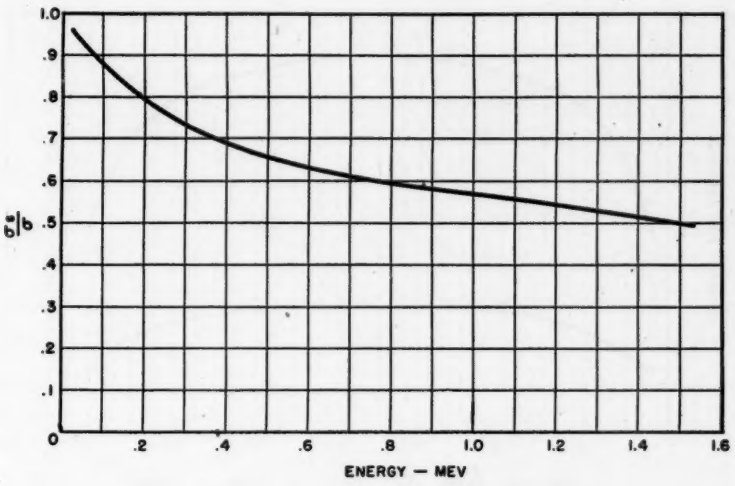

FIG. 2. Fraction of incident energy, σ_s/σ, transmitted to the scattered quantum.

per sec. Hence, Eq. (4) may be written as

$$R=(\pi A/4)\eta\lambda\sum_{0}^{m} l_k\epsilon_k. \qquad (5)$$

The upper limit of the sum is determined by setting E_m equal to the energy at which the detector ceases to respond.

Equation (5) is the desired relation between the intensity of the radiation, the source strength, and the properties of the medium. Of course it also involves the properties of the detector through the quantity ϵ. If we were only interested in the flux of γ-radiation through a cylinder, ϵ_k should be set equal to unity. The various terms in the sum of Eq. (5) correspond to the mean energies of the successive groups. Hence, the part of the response that arises from quanta in a given energy interval is comprised by the terms in this sum which lie within this energy interval. Hence, Eq. (5) also contains the spectral distribution of the radiation.

III. EXPERIMENT[5]

A homogeneously distributed source of γ-radiation may be realized by dissolving a salt of radio-isotope in water. We have used Co^{60}, which emits two γ-rays per disintegration of 1.2-Mev mean energy. Thus the number of γ-rays emitted per cm^3 per second is $2\eta\lambda$, which should replace $\eta\lambda$ in our previous equations.

A Cu Geiger-Müller counter of $\frac{1}{32}$-in. wall thickness, 1-in. diameter and 8.83-in. effective length was used for a detector. The anode was a 3-mil tungsten wire, and the tube was filled with a five to one ratio of argon to ether to a pressure of 30 cm Hg. The efficiency was measured with several standard sources with the results shown in Table II. The last column of the table gives the results of Bradt *et al.*[6] for a Cu counter, and our values differ by less than the experimental error. Bradt's results for a Cu tube are shown in Fig. 3.

Measurements were first made of the background counting rate at different positions in a

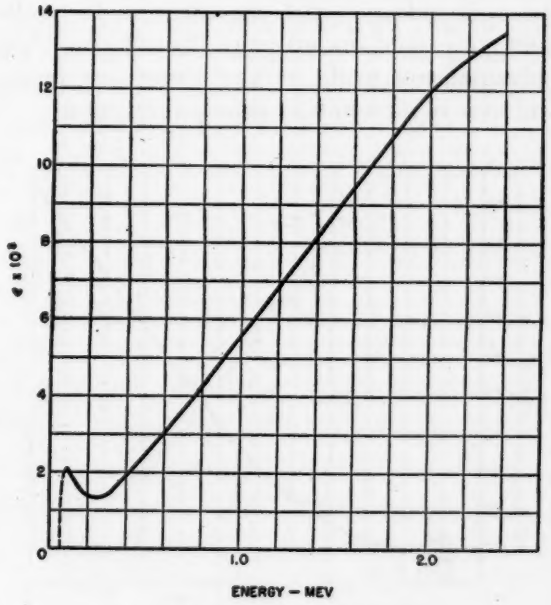

FIG. 3. Efficiency of a Cu counter.

[5] We are indebted to C. Fiddler for assistance in the experimental work.

[6] H. Bradt, *et al.* Helv. Phys. Acta 19, 77 (1946).

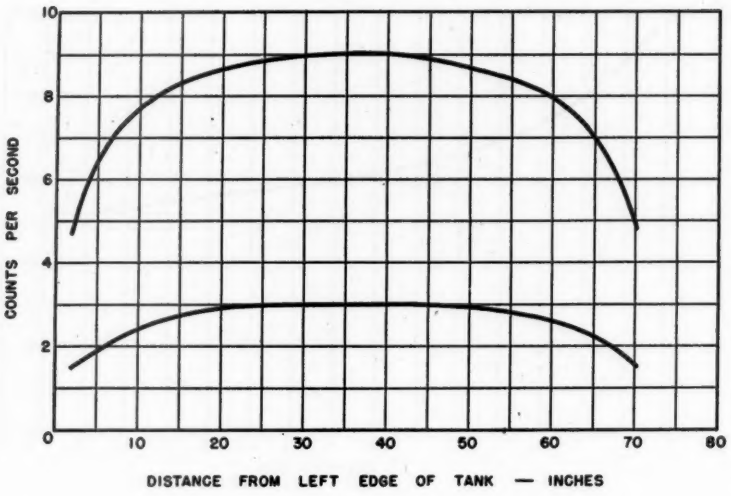

FIG. 4. Counting rate at points within the tank.

tank 6′ in diameter and 6′ high filled with water. These measurements were repeated with two concentrations of Co^{60}, whose activity was measured before being put in solution. One concentration had a specific activity of 4.0 $\mu\mu C$ (10^{-12} curies) per cm^3, the other 11.9 $\mu\mu C$ per cm^3.

For the larger Co^{60} concentration $2\eta\lambda$ is $2\times11.9\times10^{-12}\times3.7\times10^{10}=0.88$ γ-ray per second per cm^3. The results with background subtracted are shown in Fig. 4. The ordinates are precisely in the ratio of the specific activities. The flat portion of the curves at the center of the tank indicates that the effect at the walls does not extend inward more than 60 cm. Thus measurements made at the center are representative of an infinitely extended medium.

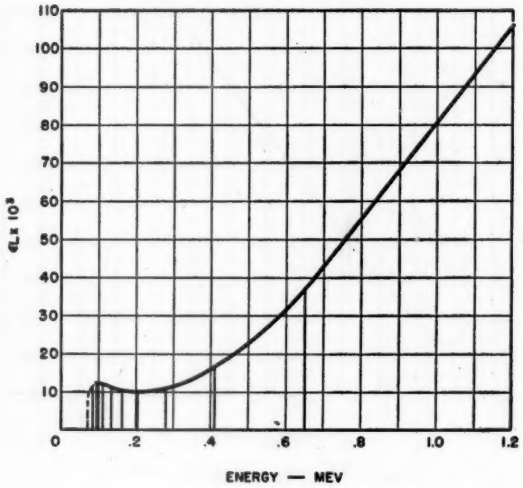

FIG. 5. Product of efficiency and path length.

The counter was always enclosed by an aluminum shield (0.4 g/cm²) to protect it from the water. The effect of introducing additional shields around the counter are shown in Table III. These measurements were made to obtain some information about the spectral distribution of the radiation.

IV. DISCUSSION

The counting rate can readily be determined from Eq. (5). The numerical values for the factors before the summation have been given in the previous section. The summation may be effected graphically by plotting ϵl against energy, as shown in Fig. 5. The values of $\epsilon_k l_k$ for energies of the scattered quanta given in Table I are represented by the ordinates of the figure and

TABLE II. Efficiency of copper counter.

Source	Mean energy of γ-rays-Mev	Measured efficiency	Bradt, *et al.*
Co^{60}	1.2	0.70%	0.68%
RaC*,	0.78	0.39%	0.40%
X-rays	0.12	0.14%	0.14%

* The mean energy and γ-ray spectrum is given by C. D. Ellis and G. H. Aston in Proc. Roy. Soc. **A129**, 180 (1930).

TABLE III. Effect of shielding on submerged counter.

Shield	Counts/sec.	Experimental reduction in counting rate	Calculated reduction in counting rate
Lead—0.8 g/cm²	6.52±0.10	(27±3)%	29.5%
Lead—1.6 g/cm²	6.17±0.15	(31±5)%	38%
Al—0.8 g/cm²	8.52±0.14	4.5±3%	7%
No shield	8.92±0.14	0	0

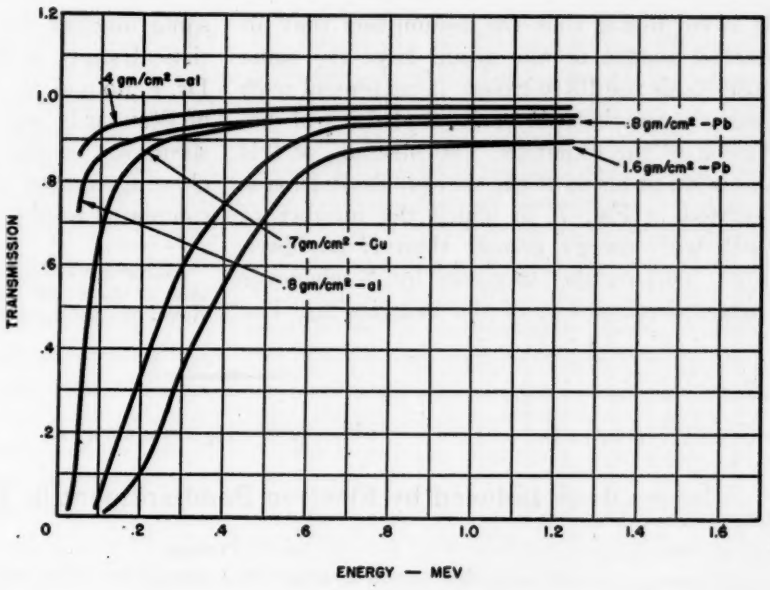

FIG 6. Transmission of shields.

their sum, including the attenuation introduced by the 0.4-g/cm aluminum shield, is 0.229 cm. From Eq. (5) we find for the 11.9-$\mu\mu C$/cm³ concentration of Cl^{60} that the counting rate should be 9.04/sec., which is 1.3 percent higher than the observed value in Table II.

The effect of introducing shields around the counter may be understood from the transmission curves shown in Fig. 6. They are computed from the known mass absorption coefficients[7] of the various metals used. The efficiency of a counter with a shield around it is now reduced at each energy by the transmission coefficient for this energy. It will be noted that the mass absorption coefficient includes scattering as well as photoelectric absorption. Our use of this coefficient should overestimate the effect of shielding because not all of the quanta scattered in the shield are deflected through a large enough angle to miss the counter. The error is small for Pb shields where photoelectric absorption is predominant. If the indicated calculation is made for 0.80-g/cm² and 1.60-g/cm² lead shields, $\epsilon_k l_k$ is found to be 0.161 cm and 0.141 cm, giving 29.5 percent and 38 percent reduction in the counting rate. Similarly, a 0.80-g/cm² Al shield gives a 7 percent reduction. Comparison with experiment is shown in Table III.

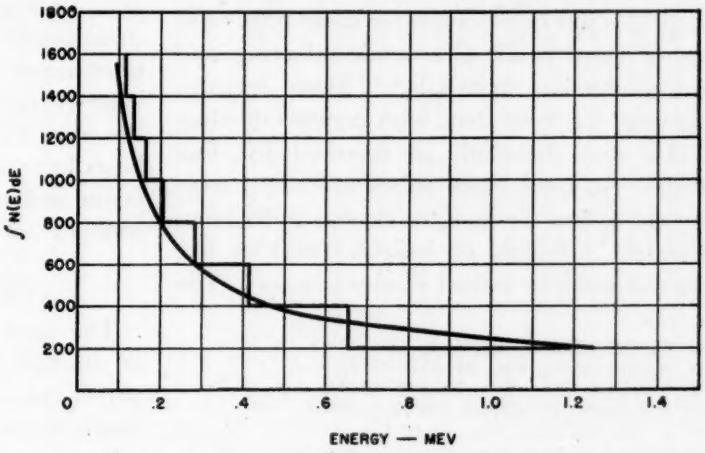

FIG. 7. Energy distribution of quanta.

[7] A. H. Compton and S. K. Allison, *X-Rays in Theory and Experiments* (D. Van Nostrand Company, Inc., New York, 1936), Appendix IX.

It is surprising that the assumption that all scattered quanta of one group have the same energy yields results so closely in agreement with experiments on both intensity and spectral distribution of the radiation. The meaning of this assumption in terms of the energy distribution is illustrated in Fig. 7, in which the number of quanta with energy greater than E has been plotted. This number increases by N whenever E passes through one of the energies E_k. The same number has been computed from a statistical study of 200 calculated γ-ray tracks by Dr. Fano and Mr. Karr[8] at the National Bureau of Standards and is also shown in Fig. 7. The similarity of the two curves accounts for the close agreement between our experimental and calculated results.

[8] We are indebted to Dr. Fano and Mr. Karr for permission to quote the results of their work on an Office of Naval Research contract.

PHYSICAL REVIEW VOLUME 75, NUMBER 3 FEBRUARY 1, 1949

Conductivity Induced by Electron Bombardment in Thin Insulating Films

L. PENSAK
Radio Corporation of America, RCA Laboratories, Princeton, New Jersey
(Received September 24, 1948)

When thin films of insulating material are bombarded by high velocity electron beams that can penetrate through the thickness of the film, steady currents can be obtained that are as much as 100 times that in the bombarding beam. These currents vary with the gradient across the film and are proportional to the fraction of the beam energy absorbed in the film. Typical data obtained with amorphous silica are presented, together with a description of the experimental procedures that were used.

INTRODUCTION

ALTHOUGH considerable work has been done with the bombardment of insulators by electron beams, most of it has been related to emission of secondary electrons. Relatively few papers have dealt with the problem of the currents induced by the bombarding beam, even though this has been known for some time,[1] and most of these dealt with semiconducting and photo-conductive materials.[2–4] More recently some work has been done with crystals of silver chloride and diamond, as reported by Van Heerden.[5] In these cases pulses of current were observed to flow through the crystal under bombardment by pulses of ionizing particles like alpha-particles[6] or pulsed electron beams.[7] The magnitudes of these currents are very sensitive to the structure of the crystal.

An effect has been found, however, which is not dependent on the crystalline structure and has been found in all of the several insulating films tried to date. Among these are silica, magnesium fluoride, electrolytic aluminum oxide, and mica. It was found that electrons can flow continuously through thin films of the insulator when bombarded by an electron beam of sufficient velocity to penetrate through the thickness of the film. These currents have been observed to be as large as 100 times that of the bombarding beam and are proportional to the energy absorbed from the bombarding beam.

EXPERIMENTAL PROCEDURE

The tests described below refer to thin films of amorphous silica on Nichrome base metal plates two inches square. The films were in the range of thickness from 2500A to 15,000A and were prepared by heating the plates in an atmosphere of ethyl silicate vapor, which decomposes

[1] A. Becker, Ann. d. Physik **13**, 394 (1904).
[2] R. Kronig, Phys. Rev. **24**, 377 (1924).
[3] R. Frerichs, Phys. Rev. **72**, 594 (1947).
[4] E. S. Rittner, Phys. Rev. **73**, 1212 (1948).
[5] P. J. Van Heerden, *The Crystal Counter* (N. V. Noord-Hollandsche Uitgevers Maatschappij, Amsterdam, 1945).
[6] A. J. Hearn, Phys. Rev. **23**, 524 (1948).
[7] K. G. McKay, Phys. Rev. **74**, 1606 (1948).

at high temperature to form silica. This process* was chosen for the tests because it provided films that were much better insulators than could be obtained by the evaporation of fused quartz from tungsten filaments. Other insulating films, such as aluminum oxide, magnesium fluoride, and barium borate were tried as examples of readily available materials and were found to show the effect of bombardment induced conduction, but no comparable data has as yet been taken.

In order to perform the measurements, the targets were set up in an evacuated envelope which was equipped with two cathode-ray guns, so spaced as to permit the deflection of the beams by standard television deflection yokes, as shown in Fig. 1. The target was connected to a video amplifier which ultimately drove the grid of a standard kinescope whose deflection yoke was driven in synchronism with those of the test tube. The decoupling filter shown in the Fig. 1 was designed to permit the application of d.c. voltages to the target plates. The meter marked "microampere No. 1" reads only the current striking the target and meter marked "microampere No. 2" reads only the current that passed through the insulating film to the base metal. Some care was taken with close-fitting mica shields to prevent electrons from reaching the base metal by any path other than through the film.

When one of the cathode-ray guns is turned on at comparatively low voltage (600 to 1000 volts), there is no appreciable penetration through the film, and the operation is as one would expect from the well-known phenomena characterizing the behavior of insulators under an electron bombardment. Because the secondary emission ratio is greater than unity, the surface is held at approximately the potential of the collector, which in this case is the wall coating. This potential is independent of that applied to the base metal, which can now be adjusted to provide a predetermined potential drop across the film. Any charges that leak through the film will also be removed by the scanning beam. In addition, the beam generates a television-type signal as it scans over the surface by a mechanism similar to that in the iconoscope.[8] This signal, when viewed in the kinescope, produces a uniform picture when the surface is at equilibrium. However, any deviation from that potential, for any reason, shows up as a light or dark area. This provides a two-dimensional check on the surface potential.

Under such conditions the data of Fig. 2 were obtained. The target metal potential was set with respect to the collector at the values shown on the figure, and the beam current was varied. Some small leakage currents were found which varied directly with the beam current and were found to be relatively independent of the beam voltage over the range of 500 to 800 volts. The crossing of two of the lines is assumed to be an artifact because of the difficulty of obtaining reproducible measurements with the small currents involved.

Figure 3 shows how the leakage current varied with target voltage, keeping the beam current and beam voltage fixed. For the range of data shown the current is an exponential function of the target voltage. The dashed portion of the

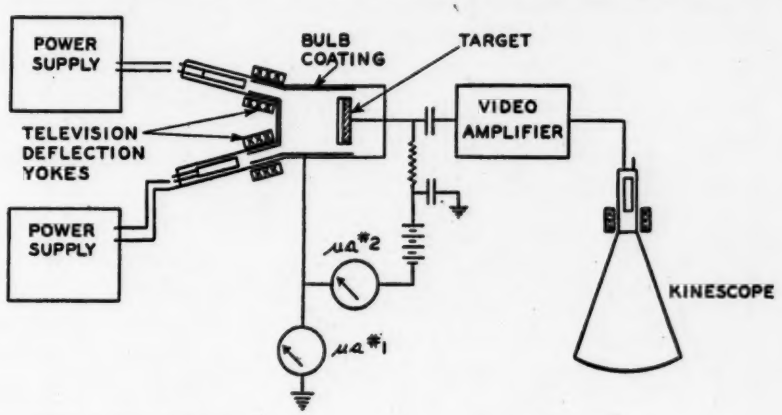

FIG. 1. Arrangement of apparatus.

* Developed by H. B. Law of the RCA Laboratories Division.
[8] Zworykin, Morton, and Flory, Proc. I.R.E. 25, 1071 (1937).

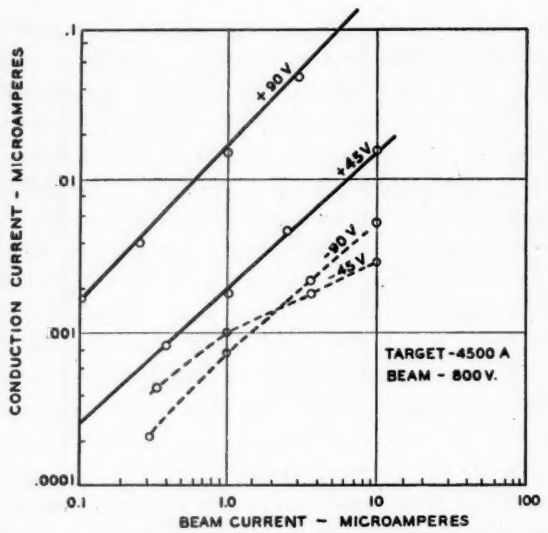

FIG. 2. Conduction current as a function of beam current.

curve is extrapolated to indicate an expected approach to zero current at zero target voltage.

A possible explanation of these small currents is that there are flaws in the film through which base metal shows and that secondary emission can be obtained from it when it is negative. Because the percentage area involved is small, the observed currents would be small. When the metal is positive the bare areas can act as collectors of redistributed secondary electrons that originate in the insulator, and in this case the current can be appreciably larger than with the negative voltage. The exponential character, however, is not explained. This effect was not further investigated because it was of less interest than the larger order effect described below.

An interesting phenomenon was observed in attempting to take measurements with negative target voltage appreciably greater than those indicated. As the gradient exceeded 2×10^6 volts per centimeter, occasional sparking was observed in the kinescope as a burst of electrons emanating from a point and spraying over the region around it, causing this region of the surface to become highly negative until it was again charged up by the beam.

Figure 4 shows the beginnings of the increased conduction resulting from the increasing penetration by the beam. The curves are similar to those of Fig. 2, except that the film is only 2500A thick. Increasing the beam voltage now shows an increased conduction current through the film. It is readily apparent, however, that as the conduction current approaches an appreciable fraction of the beam current the surface potential begins to drift towards the base metal potential. This is more obvious in the case where the film approaches a good conductor. The loss of surface potential sets a limit to measurements of this type with high velocity beams.

For this reason a two-beam technique was devised that permitted extending the range of

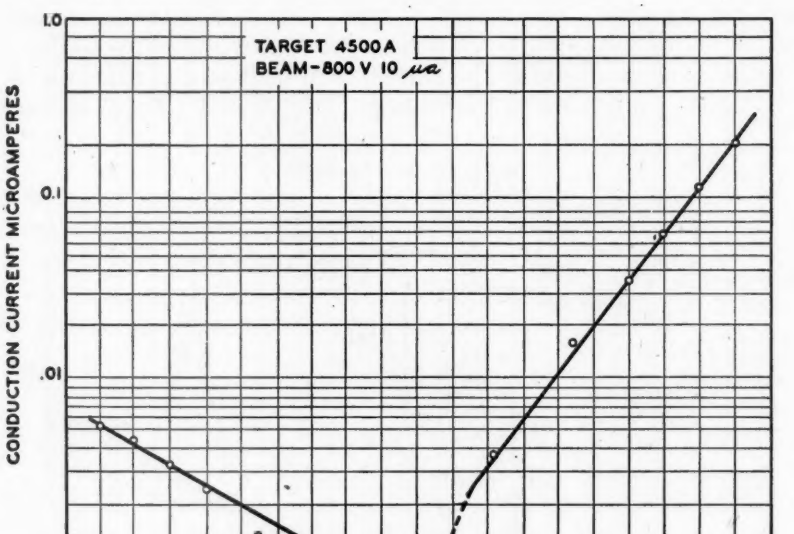

FIG. 3. Conduction current as a function of target voltage.

measurements in the following manner. The one beam was set at a fixed voltage low enough so that the conduction effect due to it was suitably small. The current in this beam was made large enough to be well in excess of any conduction currents that might be generated by the second beam whose voltage was varied over the desired range. The currents in this second beam were held to a small enough value so that its conduction effects would not require going beyond the practical limits for the first gun. Typical values that illustrate this principle are:

	Volts	Current	Cond. current
Beam 1	800	10 ua	0.1 ua
Beam 2	10,000	0.02 ua	1.0 ua

It is apparent that the low voltage beam current was well in excess of the total conduction current through the film, and so the surface potential was held at collector potential. For this reason the potential drop across the film was still known and controlable.

For purposes of describing the experimental data without reference to specific currents, the term "conduction ratio" was applied to the ratio of the conduction currents to the beam current that excited it. For example, the conduction ratio of the beam 2 above would be 50.

Figure 5 shows a typical set of data as the voltage of the second beam was varied. The solid line curves are for the positive voltages applied to the base metal, and the dashed lines are for negative voltages. It is apparent that the conduction ratio rises very rapidly with increasing voltage at the lower beam voltages, reaching a maximum and then tapering off slowly. Increasing the potential drop across the film increased the conduction ratio at any given voltage. The ratio was also larger for positive voltages, which is the direction of gradient such as to pass electrons from the bombarded surface through the film to the base metal.

Figure 6 shows the effect with different thicknesses of film. The curves are marked with the thickness in angstrom units, and for each film a positive gradient was set at the value of 10^6 volts per centimeter. The second beam voltage was varied as above. Although these curves are rather flat, some rough conclusions can be drawn. First it is to be noted that the voltage at the maximum

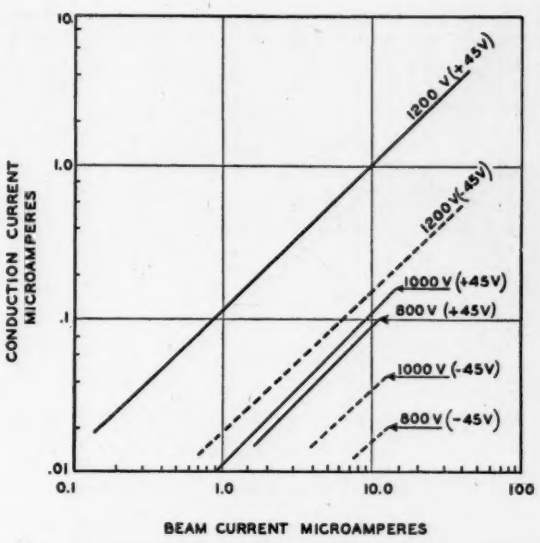

FIG. 4. Increased conduction due to the increasing penetrating of the beam.

increases with film thickness. In particular, this voltage increases approximately with the square root of film thickness, as would be expected from the Thomson-Whiddington law. Secondly, the increasing conduction ratios at the maxima indicate an increased conduction effect with increased film thickness. Again as a rough approximation, the magnitude of the increase is proportional to the voltage at the maximum. For example, the 2500A film can be said to have a maximum conduction ratio of 9 at a beam voltage of 6 kv. The 9000A curve shows a maximum at

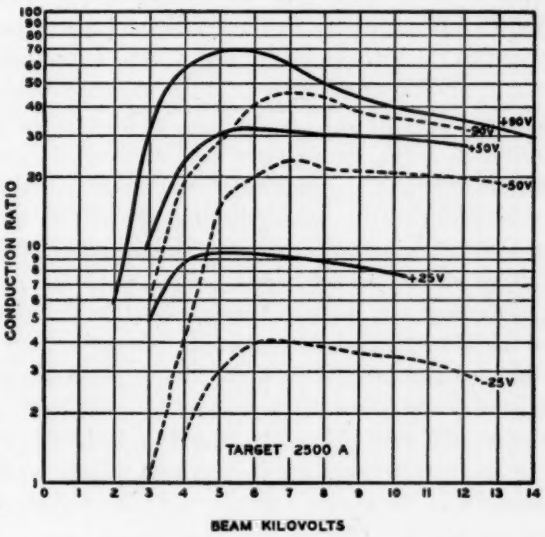

FIG. 5. Typical data with the two-beam technique.

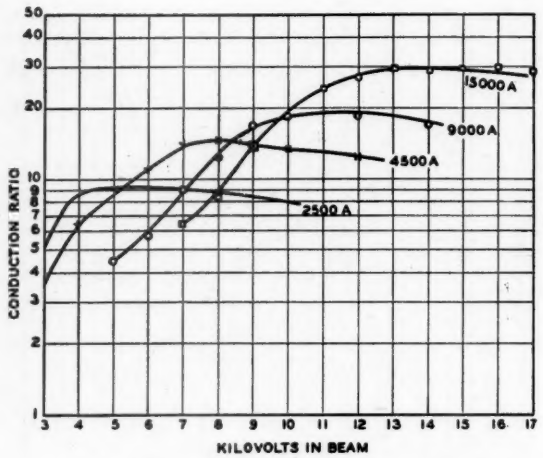

FIG. 6. Effects of varying the film thickness.

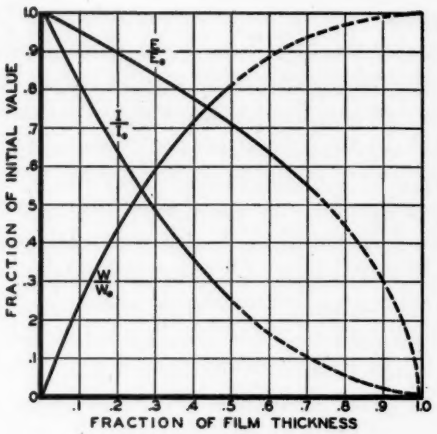

FIG. 7. Power losses in thin film.

12 kv, which is double the previous voltage, and the conduction ratio is approximately 19, which is slightly over double that of the thinner film. This appears to indicate that the conduction effect is proportional to the beam energy absorbed in the film.

The indication of the proportionality of the effect with absorbed beam energy can be supported by a different consideration. We can calculate the energy losses in a thin film by a beam of electrons as the beam velocity exceeds that required for penetration. The Thomson-Whiddington law indicates that the range of electrons goes up with the square of the voltage. Experimental data of Terrill[9] indicate that the current in a beam falls off exponentially with depth of penetration. Both these laws were transposed to the form shown in Fig. 7, which assumes a film thickness of unity and an electron beam velocity just able to penetrate it. The latter is obtained from the Thomson-Whiddington law which defines the range or the maximum depth of penetration by extrapolating the initial loss of voltage on penetration into the material. The falling off of current and voltage are plotted as fractions of the initial value against the fraction of the film thickness penetrated. The dashed portions of the curves indicate the regions where experimental data have not been available to verify the laws involved. Based on these two curves, a third curve was obtained which is the product of the loss of current and loss of voltage and is therefore the loss of power with penetration into the film. This indicates the interesting fact that 80 percent of the power is lost in the first half of the range of penetration.

It is a relatively simple matter to compute from this power curve what the energy loss is as a function of beam voltage for a given film thickness, as the voltage is increased to values above that required for penetration. The solid line of Fig. 8 is such a curve for one of the thicknesses used. In this case the range voltage is 6.3 kv, so that for all lower values all of the beam energy is absorbed. This part of the curve is therefore a straight line with a 45° slope. The line starts to curve when the voltage begins to exceed that for which the range is the film thickness, but the total energy absorbed continues to rise with voltage because the energy loss occurs primarily in the first half of the range. The absorbed energy decreases at still higher voltages because the range increases with the square of the voltage so that the fraction of the beam energy absorbed begins to decrease faster than the increase in the initial energy.

The experimental data for this film were plotted as dashed lines, using an arbitrary scale chosen only for purposes of comparing curve shapes. We find once more that the broad maxima prevent an accurate matching, but the similarity is very suggestive.

The locations of the maxima in the experimental and calculated curves are close enough to be within experimental error, whereby a further check is provided on the theory of penetra-

[9] H. M. Terrill, Phys. Rev. **24**, 616 (1924).

tion. Also, the similarity of slopes after the maxima points to the proportionality of the effect with absorbed energy. This relationship would then appear to be substantiated by the measurements on a single film as well as by the comparison of a range of thicknesses. The differences occur primarily in the low voltage region where the unknown factor of incomplete penetration would be expected to cause a reduction of the conduction effect.

CONCLUSIONS

The excitation of conduction current by a penetrating electron beam has been found in all insulating materials tested. This indicates that the effect is not critically dependent on the crystal structure of the material. It is, therefore, possible to obtain an elementary picture of the phenomenon based primarily on the fact that almost all of the energy of a high speed electron on penetrating into a solid body is given up to the bound electrons by collision processes. These bound electrons are thereby made free to migrate in the direction of an applied gradient. If it is assumed that the energy required to free a bound electron is of the order of 10 to 20 electron volts, then a 10,000-volt primary electron should excite from 500 to 1000 low velocity electrons. These electrons are subject to trapping by several mechanisms, including that of capture by the positive ions that were also generated. It is not likely that the steady state current observed means that any electrons have gone through the entire thickness of the film. It is more reasonable to assume that the electrons freed near the front surface go part way into the interior and then become trapped, thus building up a space charge. If the beam penetrates beyond this point, the electrons freed in the interior leave positive ions that reduce the space charge. There is thus a progressive travel of current as a series of jumps of electrons along the path of the penetrating beam. If penetration is complete, then a steady current can be observed. Otherwise, on incomplete penetration, the build-up space charge rapidly reduces the current to those low values which represent that fraction of the excited electrons that can escape the traps and migrate through the unpenetrated region. This fraction falls off rapidly with increasing length of unpenetrated path. The experimental data in the voltage range below that of the maximum conduction ratio (see Fig. 8) indicates a rapid falling off of the conduction effect with decreasing voltage where penetration is incomplete. This picture of the process also indicates why the effect falls off with increasing voltage after the maximum. The total number of electrons excited is proportional to the absorbed energy, and the current through the film should be proportional to the number of excited electrons.

When the base metal is negative, it is possible

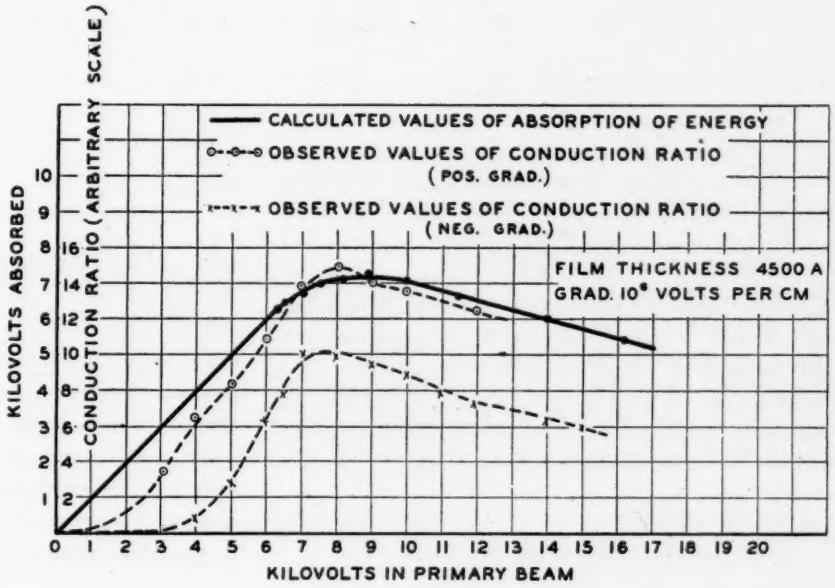
CALCULATED VALUES OF ABSORPTION OF ENERGY
OBSERVED VALUES OF CONDUCTION RATIO (POS. GRAD.)
OBSERVED VALUES OF CONDUCTION RATIO (NEG. GRAD.)
FILM THICKNESS 4500 A
GRAD. 10⁶ VOLTS PER CM
KILOVOLTS ABSORBED
CONDUCTION RATIO (ARBITRARY SCALE)
KILOVOLTS IN PRIMARY BEAM
0 1 2 3 4 5 6 7 8 9 10 11 12 13 14 15 16 17 18 19 20

FIG. 8. Energy loss as a function of voltage.

to assume a similar process, but dealing with the travel of holes instead of electrons. Because the mobility of holes is appreciably less than that of electrons, there should be observed a more rapid decrease of conduction current with decreasing penetration. This too is supported by the curve for negative gradient in Fig. 8. The recovery of full insulation after removal of the penetrating beam, with both types of conduction, is to be expected. No current should flow on the mere application of a gradient without a means of exciting the electrons in the interior.

This simple theory leaves unexplained, however, the observation in the data of Fig. 6, that the conduction ratio is proportional to the beam voltage at the maximum regardless of the film thickness. It is to be expected that, on doubling the beam voltage, the number of excited electrons is doubled, but the path length is increased four times. If the range of excited electrons is constant, the increased path length should result in a decrease of current in spite of the increased number of excited electrons in the thicker film. The fact is that current increases, and in an amount that indicates no appreciable loss due to the increased film thickness.

SUMMARY

An apparently new type of conduction effect has been found which occurs on fairly complete penetration through an insulator film and seems to be present in an uncritical manner in each of several insulator materials tried. The conduction currents can exceed the penetrating beam current by many times, and the insulation recovers completely after the penetrating beam is removed. The effect is shown to be proportional to the amount of beam energy absorbed.

ACKNOWLEDGMENT

The author wishes to express his appreciation of the value of many profitable discussions with Dr. A. Rose and of the encouragement and support by Dr. L. E. Flory.

PHYSICAL REVIEW VOLUME 75, NUMBER 3 FEBRUARY 1, 1949

The Recording of Electron Tracks in Photographic Emulsions*

R. H. HERZ
Kodak Research Laboratories, Kodak Ltd., Wealdstone, Harrow, England.
(Received October 14, 1948)

Four different methods of obtaining electron tracks in nuclear-track plates are described. Electron tracks have been produced by x-rays, by natural radioactive decay, by exposures in an electron microscope, and by feeble, induced radioactivity. A first attempt at establishing the range-energy relationship of electrons has been made from length measurements of electron tracks produced by heterogeneous and monochromatic x-rays at various kilovoltages and by monoenergetic electrons in an electron microscope. Some considerations are given on the sensitivity of the nuclear-track plate used in these experiments.

I. INTRODUCTION

SINCE the introduction of the Kodak Nuclear-Track Emulsion, Type NT2a,[1] which permits the recording of electron tracks, studies have been made of such tracks produced in various ways. Apart from the interest which these photographs have simply as records of electrons, they provide data for estimating the relation between the length of the track and the electron energy, and also the sensitivity of the plates to electrons. Accurate determination of these properties would require a source of monoenergetic electrons (the energy of which can be varied). Since such an apparatus was not available, measurements have been made from electron records produced by exposure to x-rays generated at different voltages. A few measurements were also made with mono-

* Communication No. 1204-H from the Kodak Research Laboratories.
[1] R. W. Berriman, Nature 161, 432 (1948).

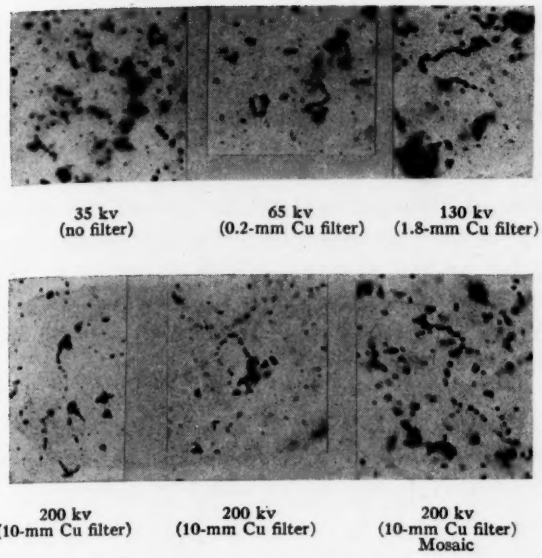

FIGS. 1–6. (Reading from top left to bottom right.) Tracks of electrons released by x-rays at various kilovoltages. Magnification, 2200×.

energetic electrons produced in the electron microscope. Accurate measurements are being carried out by means of an electron spectrograph by M. A. S. Ross and B. Zajac of the University of Edinburgh.

II. RECORDING OF ELECTRON TRACKS BY VARIOUS METHODS

A. Electron Tracks Produced by X-Rays of Increasing Hardness

If NT2a Plates are exposed to x-rays, electrons are released from the silver bromide grains and leave tracks in the emulsion which are visible under the microscope. Heavily filtered heterogeneous x-rays have been used, and for each quality of x-rays electron tracks of different lengths have been obtained, as described in Section III. As the kilovoltage is increased, the quantum energy of the x-radiation is increased and electrons of higher energy are produced, leaving tracks of increasing lengths in the emulsion. Typical electron tracks obtained with various kilovoltages of x-rays are shown in the photomicrographs (Figs. 1–6). The exposure conditions for the tracks of electrons released at 35, 65, 130, and 200 kilovolts are given in Table I.

The plates were all processed for 20 minutes at

TABLE I.

kv	Filtration (in mm Cu)	mA	Exposure time (in seconds)
35	Inherent filtration of x-ray tube	0.5	2
50	0.05	0.5	2
65	0.2	1.5	2
69*	Selective filter of $CaWO_4$		
100	1.3	4.0	2
130	1.8	5.0	2
200	10.0	4.0	7

* Monochromatic K_α-radiation of platinum.

65°F in Kodinol Developer,** using the following formula:

	Metric	British
Kodinol Developer (concentrated)	100 cc	8 fluid oz.
Potassium bromide (10 percent solution)	30 cc	2.4 fluid oz.
Water to make	1000 cc	80 fluid oz.

Figures 1–6 give further direct evidence for the assumption that the effect of x-rays on the photographic emulsion is due, at least to some

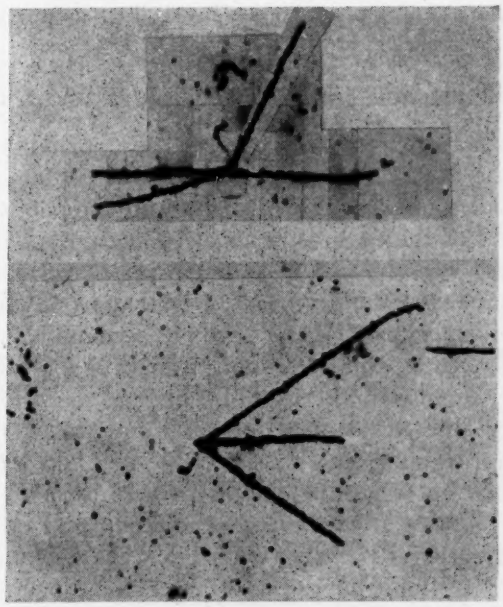

FIG. 7. Photomicrographic mosaics of plane projections of three-dimensional radiothorium stars, at the origin of which electron tracks are seen. Second electron track visible in (a) may be the end of a track of an electron of higher energy arising from the same origin. Magnification, 2400×.

** Kodinol Developer is not available in the United States. Similar results may be obtained using Kodak D-19 Developer and development for 20 minutes at 68°F.

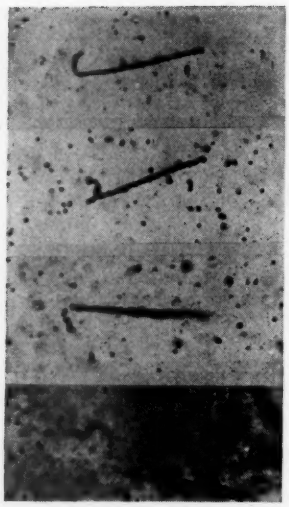

FIG. 8. Photomicrographs of alpha-particle tracks from uranium I; beta-tracks probably due to decay of uranium X_1. Beta-ray energy (d) should (according to Table II) correspond roughly to 35 kv. Magnification, 2000×.

extent, to the release of electrons that travel beyond the grain that initially absorbs the x-ray quantum, and produce developability in neighboring grains.

B. Electron Tracks in Radioactive Decay

It was expected that one of the applications of the NT2a Plates might be the recording of tracks of beta-particles emitted in radioactive decay of the natural radioactive elements. The plates were bathed in different concentrations of aqueous radioactive solutions of thorium and uranium nitrate. Since a small amount of a radioactive paint containing radium was available, tests were also made by soaking the plates in a diluted solution of this material. The concentrations used were 5, 3, 1, 0.1, and 0.01 percent by weight. Three plates were bathed for ten minutes in each of these solutions and then dried in light-tight cardboard boxes. One series was kept for 1 day, one for 1 week, and one for 4 weeks before processing. Examination of these plates under the microscope revealed no electron tracks from solutions with substantially greater concentrations than 0.1 percent, which appeared to be the optimum, although the number of alpha-particle tracks per unit area was considerable and roughly proportional to the concentrations. With 5 percent and 3 percent solutions, a desensitization effect was observed, since the grain density of alpha-particle tracks became strikingly smaller than in the plates of smaller concentrations. The number of electron tracks found was greater for longer exposure times; it was very considerably smaller than that of alpha-particle tracks, and hundreds of tracks and star formations had to be scanned in order to find electron tracks arising from the origin of the stars or single alpha-particle tracks. A few of these were photomicrographed (Figs. 7–9).

The scarcity of electron tracks in the emulsion is not surprising, when it is considered that only low energy electrons up to approximately 80 kv (Section III) can be recorded at present, and that tracks of high energy electrons will show only if the ends of their tracks happen to pass through the emulsion.

A greater number of electron tracks arising from radioactive decay were, however, obtained when blotting paper was impregnated with 10 percent radioactive solutions and placed about 1 mm distant from the emulsion. Some of the electrons lose their energy in the blotting paper and the ends of their tracks are then recorded in the emulsion.

C. Exposures in the Electron Microscope

Some preliminary exposures were made to 50-kv and 25-kv monoenergetic electrons in a Metropolitan-Vickers electron microscope. A

FIG. 9. Alpha-track due to thorium C and beta-track may be due to parent element, thorium B, which has been ejected before the alpha-emission. A second track of a beta-particle is believed to arise from the same origin. This may be attributed to the beta-emission of thorium C″. Identity of thorium C alpha-track was found by measuring the length of the track. Magnification, 2000×.

photomicrograph of such an exposure at 50 kv is shown in Fig. 10, and sections through heavily exposed emulsions (at 25 and 50 kv) are shown in Fig. 11. It is worth noting that the formation of electron tracks in photographic emulsions sets a limit to the resolving power in electron micrography in the same way that diffusion of light does in ordinary photomicrography.

D. Recording of Electron Tracks by Induced Radioactivity

Although electron tracks occurring in radioactive decay have been shown (Section IIB), tests have been carried out in order to check whether electrons from very feeble, induced radioactivity can be detected by photographic emulsions. An NT2a Plate covered by an aluminum foil 50 microns thick was exposed for five days to fast neutrons arising from a beryllium target, which was bombarded by alpha-particles from a 5-millicurie polonium source. According to the three possible nuclear reactions (n,p), (n,α), (n,γ) stated below, electrons are emitted by the decay of the three radioactive isotopes formed in this way:

$$_{13}Al^{27}+{}_0n^1\rightarrow{}_{12}Mg^{27}+H^1$$
$$_{12}Mg^{27}\rightarrow{}_{13}Al^{27}+\beta^-_{(1.8\ Mev)}\ T=10.2\ \text{min.};\qquad(1)$$
$$_{13}Al^{27}+{}_0n^1\rightarrow{}_{11}Na^{24}+{}_2He^4$$
$$_{11}Na^{24}\rightarrow{}_{12}Mg^{24}+\beta^-_{(1.4\ Mev)}\ T=14.8\ \text{hr.};\qquad(2)$$
$$_{13}Al^{27}+{}_0n^1\rightarrow{}_{13}Al^{28}+h\nu$$
$$_{13}Al^{28}\rightarrow{}_{14}Si^{28}+\beta^-_{(3.3\ Mev)}\ T=2.4\ \text{min.}\qquad(3)$$

A greater yield of these reactions can be obtained only by thermal neutrons. A slowing down of neutrons by a moderator was not attempted, because of the reduction of the neutron flux per unit area with increasing distance from the source. Thus, only a feeble, induced radioactivity can be expected. A photomicrograph of a few electron tracks obtained in this way is shown in Fig. 12.

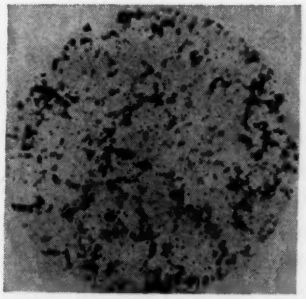

FIG. 10. Electron micrograph: 50-kv electrons. Magnification, 1200×

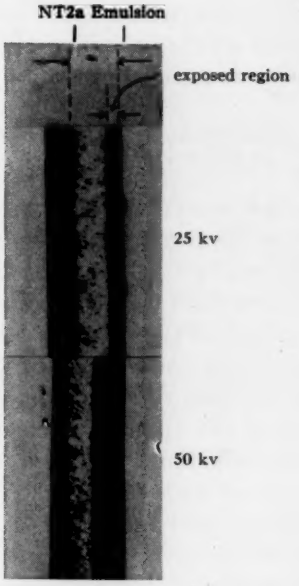

FIG. 11. Sections through NT2a Emulsion exposed to 25- and 50-kv monoenergetic electrons in electron microscope. Heavy density on the left of the sections is caused by another exposed emulsion on which the sections of NT2a Emulsion were placed. Magnification, 900×.

E. Auger Tracks

While scanning the electron tracks produced by x-rays, we observed that some tracks showed clumping of grains at the beginning and at the end of the tracks. (See arrows in Fig. 4.) This phenomenon can probably be attributed to the Auger effect.[2] Auger observed in Wilson cloud-chamber photographs a similar effect while using a heavy gas, such as argon, in the chamber. When he diluted this heavy gas by 95 percent of hydrogen, it could be seen that some of the tracks branched off at the beginning to form secondary tracks, which were due to the formation of secondary electrons. This led him to conclude that the K_α photon generated when an L electron jumps into a K-orbit frequently acts photoelectrically on another L or M electron in the same atom, which is thus ejected. Since silver and bromine are relatively heavy atoms,

[2] P. Auger, J. de phys. et rad. 6, 205 (1925).

it may be concluded that the cause of heavy ionization at the beginning of some tracks may be similar to that interpreted by Auger.

III. RELATIONSHIP BETWEEN ENERGY AND RANGE OF ELECTRON TRACKS

The release of photoelectrons by absorption of x-rays in the photographic emulsion is based on the photoelectric effect and can be represented by $h\nu=(mv^2/2)+w_K$, where $h\nu$ is the energy of the incident x-ray quantum, $mv^2/2$ is the kinetic energy of the electron released, and w_K is the energy required to remove an electron from the K level of the atom. The kinetic energy of the electron will then be $h\nu-w_K$. Similar effects will occur at each of the other absorbing levels, since the primary radiation, $h\nu$, may be absorbed in any of the energy levels in the atom. Hence, for an incident radiation of frequency, ν, groups of electrons will be released having energies, $h\nu-w_{K1}$, $h\nu-w_{L1}$, $h\nu-w_{L2}$, etc. With the increase of incident quantum energies, electron groups of higher energies will be released. If heterogeneous x-rays are used, a continuous electron spectrum comprising a wide range of electron energies can be expected. The greatest electron energy which will be produced by a heterogeneous x-ray beam will then be equal to the energy of the shortest x-ray wave-length present in the beam minus the work function equivalent to the highest electron level.

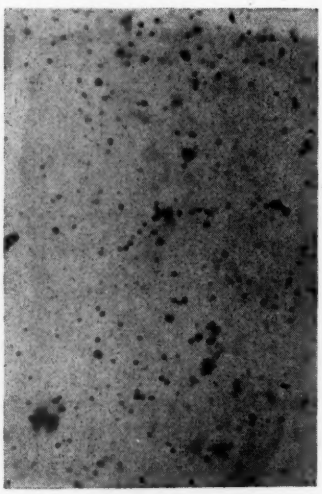

FIG. 12. Electron tracks produced by induced radioactivity. Magnification, 2500×.

In addition to the photoelectric absorption effect, the modified Compton effect will occur. This results in the emission of recoil electrons, the energies of which depend upon the angle of the scattered photon with respect to the direction of the primary beam. The energies of recoil electrons are considerably smaller than those of the photoelectrons for the same quantum energy incident and are independent of the material through which the photons pass.

Experimental

A series of strips of NT2a Plates, with an emulsion layer 30μ thick, were exposed to heavily filtered x-rays generated at increasing kilovoltages. The exposure times were so adjusted that the number of electron tracks revealed in the microscope field was roughly constant for all qualities of radiations. The kilovoltages, the corresponding filtrations, the milliamperage, and the exposure times are listed in Table I. The focus-plate distance for all exposures was 100 centimeters. At 69 kv the monochromatic K_α radiation of platinum was used. This radiation, corresponding to a wave-length of $\lambda=0.178$A, was obtained as a secondary characteristic radiation excited by the absorption of primary x-rays. The characteristic radiation was selectively filtered by a Kodak Ultra-Speed (calcium tungstate back) Intensifying Screen and was checked by means of an x-ray spectrograph.

The plates were given standard development, as mentioned in Section II, and then scanned by means of a projection microscope using an oil-immersion objective and an eyepiece. The number of developed grains of each track visible in the projected field was counted and plotted against the frequency of tracks. The counting was done independently by two observers, who, in order to avoid any bias during counting, were not told the generating kilovoltage at which the plates were exposed. For each kilovoltage, 50 tracks were counted and the grain number-frequency curve obtained is shown in Fig. 13. It can be seen from this graph that the maximum frequency shifts slightly towards a greater number of grains with increasing kilovoltage up to 65 kv and from 130–200 kv. No marked increase was found for the maximum number of grains with increasing kilovoltage, as might be expected.

The exposure with monochromatic radiation was made, as it was thought that this radiation might increase the maximum frequency towards a greater number of grains if compared with the 65-kv heterogeneous radiation. This is, however, not indicated by the distribution for monochromatic rays equivalent to 69 kv (Fig. 14). In this case, 200 tracks were counted.

Since the method of counting tracks in the field was very tedious, it was thought that a more satisfactory way of relating the range of tracks and the energy would result from scanning many hundreds of tracks of which only the longest tracks are selected and counted. This was done, and in a few cases where the tracks were at almost glancing angle with respects to the plane of the plate, length measurements of the curved path of tracks were made. The results of these measurements are tabulated in Table II.

TABLE II.

kv	Maximum number of grains	Range in microns (curved path)	Schönland and Varder (Calc. in microns)	Column 3×1.4 (curved path in microns)
35	13	8	6.1	8.5
50	18	14	10.6	14.8
65	16	—	16.7	23.4
69*	18	—	18.6	26.0
80	—	—	23.1	32.0
100	18	—	—	—
130	28	35	—	—
200	27	—	—	—

* Monochromatic K_α-radiation of platinum.

It will be seen from Table II that the maximum numbers of grains counted do not vary appreciably between 50–100 kv. No satisfactory explanation for this result can be given at present. It is possible, however, that the maximum number of grains obtainable is at 50 kv and that the greater counts obtained at 130- and 200-kv x-rays are due to erroneous counting. This uncertainty in counting may well be visualized by reference to Figs. 3, 5, and 6, which show photomicrographs of long electron tracks taken at 130- and 200-kv x-rays. It is difficult to decide whether these represent single or multiple tracks. Another possible explanation for the constancy of the number of grains counted between 50–100 kv might be the rising proportion of Compton recoil electrons which have, on the average, a considerably shorter range than the photoelectrons. However, the probability of the formation of recoil electrons, which is very high compared with that of the formation of photoelectrons from light atoms, such as are present in gelatin, decreases if heavy absorbing atoms, such as silver and bromine, are present. The effect mentioned is, therefore, difficult to understand if we consider the high silver bromide/gelatin ratio of the NT2a Plate. No marked influence can be expected from the ratio of the volumes of silver bromide to gelatin, which is approximately unity, since the ratio of the number of photo- and recoil electrons released depends basically upon the weight concerned. Some consideration

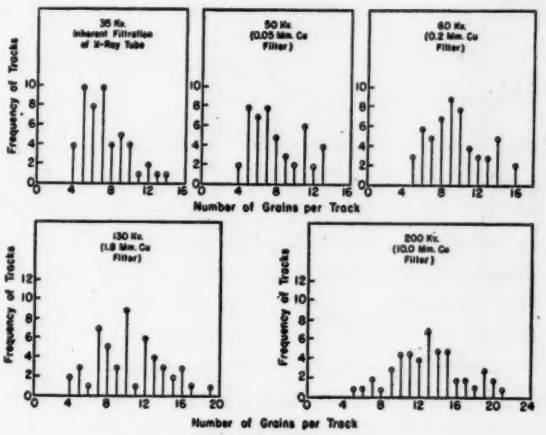

FIG. 13. Grain number-frequency curve.

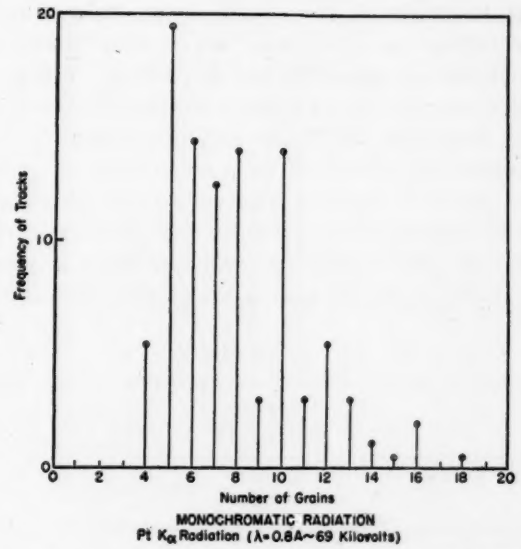

FIG. 14. Monochromatic radiation. Platinum K_α radiation ($\lambda = 0.178$A$\sim$69 kilovolts).

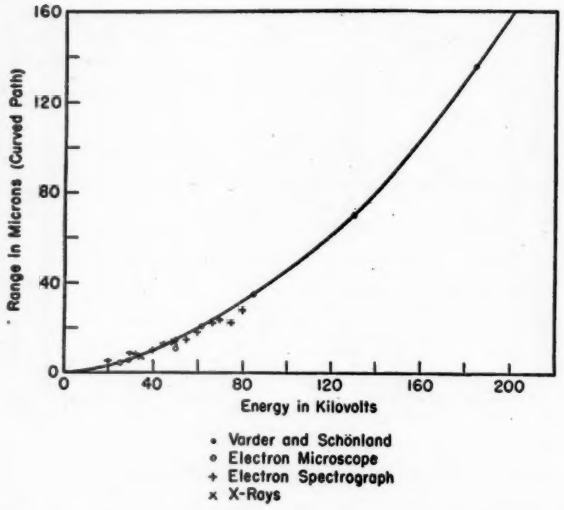

FIG. 15. Relationship between range in emulsion and energy (in E kv).

might be given to the release of electrons from the glass support, but no plausible explanation could be derived from such an effect either.

Length measurements were also carried out on sections of emulsions that had been subjected to heavy exposures to monoenergetic electrons in the electron microscope (Fig. 11). The plates were exposed with the electron beam perpendicular to the plane of the plate, and the widths of the exposed region of sections of the emulsions were measured. These widths can be regarded as the straight-line range of the electron path, since the majority of the tracks form zigzag lines. According to Williams,[3] the curved paths of electrons in metal should be, on the average, some 40 percent greater than the thickness of the metal foil. In Table III, the widths of the exposed region and of the curved path of tracks are given in microns. The values are the means of 15 measurements at 25 kv and at 50 kv in the electron microscope. The value at 50 kv is below that obtained with x-rays, which may be a result of the shrinkage effect of the emulsion in the plane perpendicular to the plate.

TABLE III.

kv	Width of exposed region (in microns)	Curved path of tracks (in microns)
25	3.2	4.5
50	8.2	11.5

After these length measurements were made, it appeared of interest to see how the results obtained agree with measurements taken by other workers. The thickness of various metals necessary to stop electrons of different velocities was determined by Schönland[4] and by Varder.[5] These workers found that the thickness is dependent only upon the mass per unit area. The range values of Schönland and Varder were converted into lengths in microns for the mass per unit area of NT2a Emulsion, and these values are quoted in column 3 of Table II. Column 4 shows the values of column 3 multiplied by 1.4 (curved path).

From the values in column 3 (Table II) and from the considerations regarding the constancy of grain numbers between 65 and 100 kv, it may be concluded that the maximum energy of electrons which can be recorded with the NT2a Emulsion will be at about 80 kv. This figure and the data just given might serve as a guide until more accurate measurements have been made by means of an electron spectrograph. Ross and Zajac[6] have carried out some preliminary measurements with the electron spectrograph, and their data are roughly in agreement with those tabulated.

Figure 15 shows the relationship between range

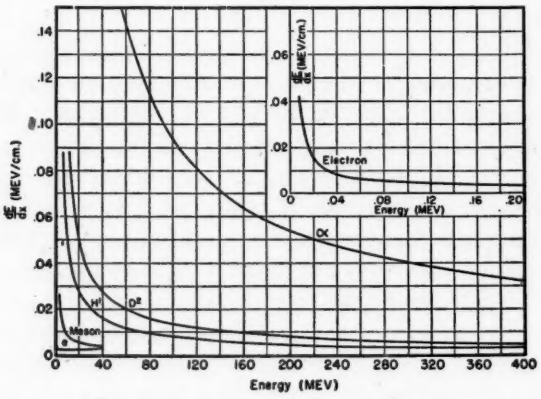

FIG. 16. Relationship between energy loss per centimeter of air and energy for alpha-particles, deuterons, protons, mesons, and electrons.

[3] E. J. Williams, Proc. Roy. Soc. (London) **130A**, 310 (1931).

[4] B. F. J. Schönland, Proc. Roy. Soc. (London) **104A**, 235 (1923); **108A**, 187 (1925).

[5] R. W. Varder, Phil. Mag. **29**, 726 (1915).

[6] M. A. S. Ross and B. Zajac, private communication.

in emulsion and energy (in E kv). The values obtained by x-rays, by the electron microscope, and by the electron spectrograph are indicated in the graph. The values taken with the electron spectrograph are preliminary data kindly sent by M. A. S. Ross and B. Zajac,[7] of the University of Edinburgh. The curve is plotted up to 200 kv from the values of Varder and Schönland converted into lengths in microns for the mass per unit area of the NT2a Emulsion and multiplied by 1.4.

IV. CONSIDERATIONS ON THE SENSITIVITY OF NT2a PLATES

In a recent paper, Webb[8] has shown the relationship between the energy loss per centimeter of air, (dE/dx) (Mev/cm), and energy for alpha-particles, deuterons, protons, mesons, and electrons (Fig. 16). Assuming that a safe limit for the recording of electron tracks with the NT2a Plate is 50 kv, this would correspond to an energy loss of 0.007 Mev per centimeter of air. The limiting energy values up to which the recording of other particles can be expected with this plate would be

200 Mev for deuterons,
100 Mev for protons,
>400 Mev for alpha-particles, and
10 Mev for mesons.

The number of ion pairs produced in a silver bromide grain for a given loss of a particle per centimeter in air can be computed, according to Webb, by

$$\text{Ion pairs/AgBr grain} = n \times s \times (\text{Ev.}_{\text{air}}/\text{Ev.}_{\text{AgBr}}) \times d,$$

where n = number of ion pairs per micron of air, s = stopping power of emulsion for electrons (at 50 kv = 3.7 cm air/1.4 10^{-3} cm AgBr = 2600), Ev._{air} = number of electron volts required per ion pair in air = 35 v, Ev._{AgBr} = number of electon volts required per ion pair in AgBr = 7.6 v, and d = diameter of grain in NT2a = 0.3 micron.

Since one ion pair in air corresponds to an energy dissipation of approximately 35 v, the energy loss of 0.007 Mev per centimeter of air (electrons at 50 kv) is equivalent to $0.7/35 = 0.02$ ion pair per micron in air. Using the figures above, the number of ion pairs required to render a grain of NT2a Plate developable would be 72. Since the number of ionizations decreases only slowly with increasing energy of electrons, and reaches a minimum at about 500–1000 kv (according to Heitler[9]), it can be assumed that an increase of sensitivity above that of NT2a Emulsion of about three times would be required for the recording of tracks of any electron energy. Similar conclusions were drawn by Berriman.[10]

ACKNOWLEDGMENT

The author wishes to thank Messrs. E. B. Kennedy and G. P. Cooke, who were responsible for much of the experimental work described in this paper.

[7] M. A. S. Ross and B. Zajac, Nature **162**, 923 (1948).
[8] J. H. Webb, Phys. Rev. **74**, 511 (1948).
[9] W. Heitler, *The Quantum Theory of Radiation* (Oxford University Press, London, 1944), p. 222.
[10] R. W. Berriman, Paper given at a Symposium on Photography in Nuclear Research, on March 18, 1948, at the Royal Photographic Society, London.

PHYSICAL REVIEW VOLUME 75, NUMBER 3 FEBRUARY 1, 1949

The Radiation Theories of Tomonaga, Schwinger, and Feynman

F. J. DYSON
Institute for Advanced Study, Princeton, New Jersey

(Received October 6, 1948)

A unified development of the subject of quantum electrodynamics is outlined, embodying the main features both of the Tomonaga-Schwinger and of the Feynman radiation theory. The theory is carried to a point further than that reached by these authors, in the discussion of higher order radiative reactions and vacuum polarization phenomena. However, the theory of these higher order processes is a program rather than a definitive theory, since no general proof of the convergence of these effects is attempted.

The chief results obtained are (a) a demonstration of the equivalence of the Feynman and Schwinger theories, and (b) a considerable simplification of the procedure involved in applying the Schwinger theory to particular problems, the simplification being the greater the more complicated the problem.

I. INTRODUCTION

As a result of the recent and independent discoveries of Tomonaga,[1] Schwinger,[2] and Feynman,[3] the subject of quantum electrodynamics has made two very notable advances. On the one hand, both the foundations and the applications of the theory have been simplified by being presented in a completely relativistic way; on the other, the divergence difficulties have been at least partially overcome. In the reports so far published, emphasis has naturally been placed on the second of these advances; the magnitude of the first has been somewhat obscured by the fact that the new methods have been applied to problems which were beyond the range of the older theories, so that the simplicity of the methods was hidden by the complexity of the problems. Furthermore, the theory of Feynman differs so profoundly in its formulation from that of Tomonaga and Schwinger, and so little of it has been published, that its particular advantages have not hitherto been available to users of the other formulations. The advantages of the Feynman theory are simplicity and ease of application, while those of Tomonaga-Schwinger are generality and theoretical completeness.

The present paper aims to show how the Schwinger theory can be applied to specific problems in such a way as to incorporate the ideas of Feynman. To make the paper reasonably self-contained it is necessary to outline the foundations of the theory, following the method of Tomonaga; but this paper is not intended as a substitute for the complete account of the theory shortly to be published by Schwinger. Here the emphasis will be on the application of the theory, and the major theoretical problems of gauge-invariance and of the divergencies will not be considered in detail. The main results of the paper will be general formulas from which the radiative reactions on the motions of electrons can be calculated, treating the radiation interaction as a small perturbation, to any desired order of approximation. These formulas will be expressed in Schwinger's notation, but are in substance identical with results given previously by Feynman. The contribution of the present paper is thus intended to be twofold: first, to simplify the Schwinger theory for the benefit of those using it for calculations, and second, to demonstrate the equivalence of the various theories within their common domain of applicability.*

[1] Sin-itiro Tomonaga, Prog. Theoret. Phys. **1**, 27 (1946); Koba, Tati, and Tomonaga, Prog. Theoret. Phys. **2**, 101 198 (1947); S. Kanesawa and S. Tomonaga, Prog. Theoret. Phys. **3**, 1, 101 (1948); S. Tomonaga, Phys. Rev. **74**, 224 (1948).

[2] Julian Schwinger, Phys. Rev. **73**, 416 (1948); Phys. Rev. **74**, 1439 (1948). Several papers, giving a complete exposition of the theory, are in course of publication.

[3] R. P. Feynman, Rev. Mod. Phys. **20**, 367 (1948); Phys. Rev. **74**, 939, 1430 (1948); J. A. Wheeler and R. P. Feynman, Rev. Mod. Phys. **17**, 157 (1945). These articles describe early stages in the development of Feynman's theory, little of which is yet published.

* After this paper was written, the author was shown a letter, published in Progress of Theoretical Physics **3**, 205 (1948) by Z. Koba and G. Takeda. The letter is dated May 22, 1948, and briefly describes a method of treatment of radiative problems, similar to the method of this paper.

II. OUTLINE OF THEORETICAL FOUNDATIONS

Relativistic quantum mechanics is a special case of non-relativistic quantum mechanics, and it is convenient to use the usual non-relativistic terminology in order to make clear the relation between the mathematical theory and the results of physical measurements. In quantum electrodynamics the dynamical variables are the electromagnetic potentials $A_\mu(\mathbf{r})$ and the spinor electron-positron field $\psi_\alpha(\mathbf{r})$; each component of each field at each point $\mathbf{r}$ of space is a separate variable. Each dynamical variable is, in the Schrödinger representation of quantum mechanics, a time-independent operator operating on the state vector Φ of the system. The nature of Φ (wave function or abstract vector) need not be specified; its essential property is that, given the Φ of a system at a particular time, the results of all measurements made on the system at that time are statistically determined. The variation of Φ with time is given by the Schrödinger equation

$$ih[\partial/\partial t]\Phi=\left\{\int H(\mathbf{r})d\tau\right\}\Phi, \qquad (1)$$

where $H(\mathbf{r})$ is the operator representing the total energy-density of the system at the point $\mathbf{r}$. The general solution of (1) is

$$\Phi(t)=\exp\left\{[-it/h]\int H(\mathbf{r})d\tau\right\}\Phi_0, \qquad (2)$$

with Φ_0 any constant state vector.

Now in a relativistic system, the most general kind of measurement is not the simultaneous measurement of field quantities at different points of space. It is also possible to measure independently field quantities at different points of space at different times, provided that the points of space-time at which the measurements are made lie outside each other's light cones, so that the measurements do not interfere with each other. Thus the most comprehensive general type of measurement is a measurement of field quantities at each point $\mathbf{r}$ of space at a time $t(\mathbf{r})$, the locus of the points $(\mathbf{r}, t(\mathbf{r}))$ in space-time forming a 3-dimensional surface σ which is space-like (i.e., every pair of points on it is separated by a space-like interval). Such a measurement will be called "an observation of the system on σ." It is easy to see what the result of the measurement will be. At each point $\mathbf{r}'$ the field quantities will be measured for a state of the system with state vector $\Phi(t(\mathbf{r}'))$ given by (2). But all observable quantities at $\mathbf{r}'$ are operators which commute with the energy-density operator $H(\mathbf{r})$ at every point $\mathbf{r}$ different from $\mathbf{r}'$, and it is a general principle of quantum mechanics that if B is a unitary operator commuting with A, then for any state Φ the results of measurements of A are the same in the state Φ as in the state $B\Phi$. Therefore, the results of measurement of the field quantities at $\mathbf{r}'$ in the state $\Phi(t(\mathbf{r}'))$ are the same as if the state of the system were

$$\Phi(\sigma)=\exp\left\{-[i/\hbar]\int t(\mathbf{r})H(\mathbf{r})d\tau\right\}\Phi_0, \qquad (3)$$

which differs from $\Phi(t(\mathbf{r}'))$ only by a unitary factor commuting with these field quantities. The important fact is that the state vector $\Phi(\sigma)$ depends only on σ and not on $\mathbf{r}'$. The conclusion reached is that observations of a system on σ give results which are completely determined by attributing to the system the state vector $\Phi(\sigma)$ given by (3).

The Tomonaga-Schwinger form of the Schrödinger equation is a differential form of (3). Suppose the surface σ to be deformed slightly near the point $\mathbf{r}$ into the surface σ', the volume of space-time separating the two surfaces being V. Then the quotient

$$[\Phi(\sigma')-\Phi(\sigma)]/V$$

tends to a limit as $V\to 0$, which we denote by $\partial\Phi/\partial\sigma(\mathbf{r})$ and call the functional derivative of Φ with respect to σ at the point $\mathbf{r}$. From (3) it follows that

$$ihc[\partial\Phi/\partial\sigma(\mathbf{r})]=H(\mathbf{r})\Phi, \qquad (4)$$

and (3) is, in fact, the general solution of (4).

The whole meaning of an equation such as (4) depends on the physical meaning which is attached to the statement "a system has a constant state vector Φ_0." In the present context, this statement means "results of measurements of

Results of the application of the method to a calculation of the second-order radiative correction to the Klein-Nishina formula are stated. All the papers of Professor Tomonaga and his associates which have yet been published were completed before the end of 1946. The isolation of these Japanese workers has undoubtedly constituted a serious loss to theoretical physics.

field quantities at any given point of space are independent of time." This statement is plainly non-relativistic, and so (4) is, in spite of appearances, a non-relativistic equation.

The simplest way to introduce a new state vector Ψ which shall be a relativistic invariant is to require that the statement "a system has a constant state vector Ψ" shall mean "a system consists of photons, electrons, and positrons, traveling freely through space without interaction or external disturbance." For this purpose, let

$$H(\mathbf{r})=H_0(\mathbf{r})+H_1(\mathbf{r}), \tag{5}$$

where H_0 is the energy-density of the free electromagnetic and electron fields, and H_1 is that of their interaction with each other and with any external disturbing forces that may be present. A system with constant Ψ is, then, one whose H_1 is identically zero; by (3) such a system corresponds to a Φ of the form

$$\Phi(\sigma)=T(\sigma)\Phi_0,$$

$$T(\sigma)=\exp\left\{-[i/\hbar]\int t(\mathbf{r})H_0(\mathbf{r})d\tau\right\}. \tag{6}$$

It is therefore consistent to write generally

$$\Phi(\sigma)=T(\sigma)\Psi(\sigma), \tag{7}$$

thus defining the new state vector Ψ of any system in terms of the old Φ. The differential equation satisfied by Ψ is obtained from (4), (5), (6), and (7) in the form

$$ihc[\partial\Psi/\partial\sigma(\mathbf{r})]=(T(\sigma))^{-1}H_1(\mathbf{r})T(\sigma)\Psi. \tag{8}$$

Now if $q(\mathbf{r})$ is any time-independent field operator, the operator

$$q(x_0)=(T(\sigma))^{-1}q(\mathbf{r})T(\sigma)$$

is just the corresponding time-dependent operator as usually defined in quantum electrodynamics.[4] It is a function of the point x_0 of space-time whose coordinates are $(\mathbf{r}, ct(\mathbf{r}))$, but is the same for all surfaces σ passing through this point, by virtue of the commutation of $H_1(\mathbf{r})$ with $H_0(\mathbf{r}')$ for $\mathbf{r}'\neq\mathbf{r}$. Thus (8) may be written

$$ihc[\partial\Psi/\partial\sigma(x_0)]=H_1(x_0)\Psi, \tag{9}$$

where $H_1(x_0)$ is the time-dependent form of the energy-density of interaction of the two fields with each other and with external forces. The left side of (9) represents the degree of departure of the system from a system of freely traveling particles and is a relativistic invariant; $H_1(x_0)$ is also an invariant, and thus is avoided one of the most unsatisfactory features of the old theories, in which the invariant H_1 was added to the non-invariant H_0. Equation (9) is the starting point of the Tomonaga-Schwinger theory.

III. INTRODUCTION OF PERTURBATION THEORY

Equation (9) can be solved explicitly. For this purpose it is convenient to introduce a one-parameter family of space-like surfaces filling the whole of space-time, so that one and only one member $\sigma(x)$ of the family passes through any given point x. Let $\sigma_0, \sigma_1, \sigma_2, \cdots$ be a sequence of surfaces of the family, starting with σ_0 and proceeding in small steps steadily into the past. By

$$\int_{\sigma_1}^{\sigma_0} H_1(x)dx$$

is denoted the integral of $H_1(x)$ over the 4-dimensional volume between the surfaces σ_1 and σ_0; similarly, by

$$\int_{-\infty}^{\sigma_0} H_1(x)dx, \quad \int_{\sigma_0}^{\infty} H_1(x)dx$$

are denoted integrals over the whole volume to the past of σ_0 and to the future of σ_0, respectively. Consider the operator

$$U=U(\sigma_0)=\left(1-[i/hc]\int_{\sigma_1}^{\sigma_0} H_1(x)dx\right)\times\left(1-[i/hc]\int_{\sigma_2}^{\sigma_1} H_1(x)dx\right)\cdots, \tag{10}$$

the product continuing to infinity and the surfaces $\sigma_0, \sigma_1, \cdots$ being taken in the limit infinitely close together. U satisfies the differential equation

$$ihc[\partial U/\partial\sigma(x_0)]=H_1(x_0)U, \tag{11}$$

and the general solution of (9) is

$$\Psi(\sigma)=U(\sigma)\Psi_0, \tag{12}$$

with Ψ_0 any constant vector.

[4] See, for example, Gregor Wentzel, *Einführung in die Quantentheorie der Wellenfelder* (Franz Deuticke, Wien, 1943), pp. 18–26.

Expanding the product (10) in ascending powers of H_1 gives a series

$$U=1+(-i/\hbar c)\int_{-\infty}^{\sigma_0} H_1(x_1)dx_1+(-i/\hbar c)^2 \times\int_{-\infty}^{\sigma_0} dx_1\int_{-\infty}^{\sigma(x_1)} H_1(x_1)H_1(x_2)dx_2+\cdots. \quad (13)$$

Further, U is by (10) obviously unitary, and

$$U^{-1}=\bar{U}=1+(i/\hbar c)\int_{-\infty}^{\sigma_0} H_1(x_1)dx_1+(i/\hbar c)^2 \times\int_{-\infty}^{\sigma_0} dx_1\int_{-\infty}^{\sigma(x_1)} H_1(x_2)H_1(x_1)dx_2+\cdots. \quad (14)$$

It is not difficult to verify that U is a function of σ_0 alone and is independent of the family of surfaces of which σ_0 is one member. The use of a finite number of terms of the series (13) and (14), neglecting the higher terms, is the equivalent in the new theory of the use of perturbation theory in the older electrodynamics.

The operator $U(\infty)$, obtained from (10) by taking σ_0 in the infinite future, is a transformation operator transforming a state of the system in the infinite past (representing, say, converging streams of particles) into the same state in the infinite future (after the particles have interacted or been scattered into their final outgoing distribution). This operator has matrix elements corresponding only to real transitions of the system, i.e., transitions which conserve energy and momentum. It is identical with the Heisenberg S matrix.[5]

IV. ELIMINATION OF THE RADIATION INTERACTION

In most of the problem of electrodynamics, the energy-density $H_1(x_0)$ divides into two parts—

$$H_1(x_0)=H^i(x_0)+H^e(x_0), \quad (15)$$

$$H^i(x_0)=-[1/c]j_\mu(x_0)A_\mu(x_0), \quad (16)$$

the first part being the energy of interaction of the two fields with each other, and the second part the energy produced by external forces. It is usually not permissible to treat H^e as a small perturbation as was done in the last section. Instead, H^i alone is treated as a perturbation, the aim being to eliminate H^i but to leave H^e in its original place in the equation of motion of the system.

Operators $S(\sigma)$ and $S(\infty)$ are defined by replacing H_1 by H^i in the definitions of $U(\sigma)$ and $U(\infty)$. Thus $S(\sigma)$ satisfies the equation

$$i\hbar c[\partial S/\partial\sigma(x_0)]=H^i(x_0)S. \quad (17)$$

Suppose now a new type of state vector $\Omega(\sigma)$ to be introduced by the substitution

$$\Psi(\sigma)=S(\sigma)\Omega(\sigma). \quad (18)$$

By (9), (15), (17), and (18) the equation of motion for $\Omega(\sigma)$ is

$$i\hbar c[\partial\Omega/\partial\sigma(x_0)]=(S(\sigma))^{-1}H^e(x_0)S(\sigma)\Omega. \quad (19)$$

The elimination of the radiation interaction is hereby achieved; only the question, "How is the new state vector $\Omega(\sigma)$ to be interpreted?," remains.

It is clear from (19) that a system with a constant Ω is a system of electrons, positrons, and photons, moving under the influence of their mutual interactions, but in the absence of external fields. In a system where two or more particles are actually present, their interactions alone will, in general, cause real transitions and scattering processes to occur. For such a system, it is rather "unphysical" to represent a state of motion including the effects of the interactions by a constant state vector; hence, for such a system the new representation has no simple interpretation. However, the most important systems are those in which only one particle is actually present, and its interaction with the vacuum fields gives rise only to virtual processes. In this case the particle, including the effects of all its interactions with the vacuum, appears to move as a free particle in the absence of external fields, and it is eminently reasonable to represent such a state of motion by a constant state vector. Therefore, it may be said that the operator,

$$H_T(x_0)=(S(\sigma))^{-1}H^e(x_0)S(\sigma), \quad (20)$$

on the right of (19) represents the interaction of a physical particle with an external field, including radiative corrections. Equation (19) describes the extent to which the motion of a

[5] Werner Heisenberg, Zeits. f. Physik 120, 513 (1943), 120, 673 (1943), and Zeits. f. Naturforschung 1, 608 (1946).

single physical particle deviates, in the external field, from the motion represented by a constant state-vector, i.e., from the motion of an observed "free" particle.

If the system whose state vector is constantly Ω undergoes no real transitions with the passage of time, then the state vector Ω is called "steady." More precisely, Ω is steady if, and only if, it satisfies the equation

$$S(\infty)\Omega=\Omega. \tag{21}$$

As a general rule, one-particle states are steady and many-particle states unsteady. There are, however, two important qualifications to this rule.

First, the interaction (20) itself will almost always cause transitions from steady to unsteady states. For example, if the initial state consists of one electron in the field of a proton, H_I will have matrix elements for transitions of the electron to a new state with emission of a photon, and such transitions are important in practice. Therefore, although the interpretation of the theory is simpler for steady states, it is not possible to exclude unsteady states from consideration.

Second, if a one-particle state as hitherto defined is to be steady, the definition of $S(\sigma)$ must be modified. This is because $S(\infty)$ includes the effects of the electromagnetic self-energy of the electron, and this self-energy gives an expectation value to $S(\infty)$ which is different from unity (and indeed infinite) in a one-electron state, so that Eq. (21) cannot be satisfied. The mistake that has been made occurred in trying to represent the observed electron with its electromagnetic self-energy by a wave field with the same characteristic rest-mass as that of the "bare" electron. To correct the mistake, let δm denote the electromagnetic mass of the electron, i.e., the difference in rest-mass between an observed and a "bare" electron. Instead of (5), the division of the energy-density $H(\mathbf{r})$ should have taken the form

$$H(\mathbf{r})=(H_0(\mathbf{r})+\delta mc^2\psi^*(\mathbf{r})\beta\psi(\mathbf{r})) +(H_1(\mathbf{r})-\delta mc^2\psi^*(\mathbf{r})\beta\psi(\mathbf{r})).$$

The first bracket on the right here represents the energy-density of the free electromagnetic and electron fields with the observed electron rest-mass, and should have been used instead of $H_0(\mathbf{r})$ in the definition (6) of $T(\sigma)$. Consequently, the second bracket should have been used instead of $H_1(\mathbf{r})$ in Eq. (8).

The definition of $S(\sigma)$ has therefore to be altered by replacing $H^i(x_0)$ by[6]

$$H^I(x_0)=H^i(x_0)+H^S(x_0)=H^i(x_0) -\delta mc^2\bar{\psi}(x_0)\psi(x_0). \tag{22}$$

The value of δm can be adjusted so as to cancel out the self-energy effects in $S(\infty)$ (this is only a formal adjustment since the value is actually infinite), and then Eq. (21) will be valid for one-electron states. For the photon self-energy no such adjustment is needed since, as proved by Schwinger, the photon self-energy turns out to be identically zero.

The foregoing discussion of the self-energy problem is intentionally only a sketch, but it will be found to be sufficient for practical applications of the theory. A fuller discussion of the theoretical assumptions underlying this treatment of the problem will be given by Schwinger in his forthcoming papers. Moreover, it must be realized that the theory as a whole cannot be put into a finally satisfactory form so long as divergencies occur in it, however skilfully these divergencies are* circumvented; therefore, the present treatment should be regarded as justified by its success in applications rather than by its theoretical derivation.

The important results of the present paper up to this point are Eq. (19) and the interpretation of the state vector Ω. The state vector Ψ of a system can be interpreted as a wave function giving the probability amplitude of finding any particular set of occupation numbers for the various possible states of free electrons, positrons, and photons. The state vector Ω of a system with a given Ψ on a given surface σ is, crudely speaking, the Ψ which the system would have had in the infinite past if it had arrived at the given Ψ on σ under the influence of the interaction $H^I(x_0)$ alone.

The definition of Ω being unsymmetrical between past and future, a new type of state vector Ω' can be defined by reversing the direction of time in the definition of Ω. Thus the Ω' of a system with a given Ψ on a given σ is the Ψ

* Here Schwinger's notation $\bar{\psi}=\psi^*\beta$ is used.

which the system would reach in the infinite future if it continued to move under the influence of $H^I(x_0)$ alone. More simply, Ω' can be defined by the equation

$$\Omega'(\sigma)=S(\infty)\Omega(\sigma). \tag{23}$$

Since $S(\infty)$ is a unitary operator independent of σ, the state vectors Ω and Ω' are really only the same vector in two different representations or coordinate systems. Moreover, for any steady state the two are identical by (21).

V. FUNDAMENTAL FORMULAS OF THE SCHWINGER AND FEYNMAN THEORIES

The Schwinger theory works directly from Eqs. (19) and (20), the aim being to calculate the matrix elements of the "effective external potential energy" H_T between states specified by their state vectors Ω. The states considered in practice always have Ω of some very simple kind, for example, Ω representing systems in which one or two free-particle states have occupation number one and the remaining free-particle states have occupation number zero. By analogy with (13), $S(\sigma_0)$ is given by

$$S(\sigma_0)=1+(-i/\hbar c)\int_{-\infty}^{\sigma_0}H^I(x_1)dx_1+(-i/\hbar c)^2 \times\int_{-\infty}^{\sigma_0}dx_1\int_{-\infty}^{\sigma(x_1)}H^I(x_1)H^I(x_2)dx_2+\cdots, \tag{24}$$

and $(S(\sigma_0))^{-1}$ by a corresponding expression analogous to (14). Substitution of these series into (20) gives at once

$$H_T(x_0)=\sum_{n=0}^{\infty}(i/\hbar c)^n\int_{-\infty}^{\sigma(x_0)}dx_1\int_{-\infty}^{\sigma(x_1)}dx_2\cdots \times\int_{-\infty}^{\sigma(x_{n-1})}dx_n\times[H^I(x_n),\,[\cdots,\,[H^I(x_2),\,[H^I(x_1),\,H^e(x_0)]]\cdots]]. \tag{25}$$

The repeated commutators in this formula are characteristic of the Schwinger theory, and their evaluation gives rise to long and rather difficult analysis. Using the first three terms of the series, Schwinger was able to calculate the second-order radiative corrections to the equations of motion of an electron in an external field, and obtained satisfactory agreement with experimental results. In this paper the development of the Schwinger theory will be carried no further; in principle the radiative corrections to the equations of motion of electrons could be calculated to any desired order of approximation from formula (25).

In the Feynman theory the basic principle is to preserve symmetry between past and future. Therefore, the matrix elements of the operator H_T are evaluated in a "mixed representation;" the matrix elements are calculated between an initial state specified by its state vector Ω_1 and a final state specified by its state vector Ω_2'. The matrix element of H_T between two such states in the Schwinger representation is

$$\Omega_2{}^*H_T\Omega_1=\Omega_2'{}^*S(\infty)H_T\Omega_1, \tag{26}$$

and therefore the operator which replaces H_T in the mixed representation is

$$H_F(x_0)=S(\infty)H_T(x_0) =S(\infty)(S(\sigma))^{-1}H^e(x_0)S(\sigma). \tag{27}$$

Going back to the original product definition of $S(\sigma)$ analogous to (10), it is clear that $S(\infty)\times(S(\sigma))^{-1}$ is simply the operator obtained from $S(\sigma)$ by interchanging past and future. Thus,

$$R(\sigma)=S(\infty)(S(\sigma))^{-1}=1+(-i/\hbar c) \times\int^{\infty}H^I(x_1)dx_1+(-i/\hbar c)^2\int_{\sigma}^{\infty}dx_1 \times\int_{\sigma(x_1)}^{\infty}H^I(x_2)H^I(x_1)dx_2+\cdots. \tag{28}$$

The physical meaning of a mixed representation of this type is not at all recondite. In fact, a mixed representation is normally used to describe such a process as bremsstrahlung of an electron in the field of a nucleus when the Born approximation is not valid; the process of bremsstrahlung is a radiative transition of the electron from a state described by a Coulomb wave function, with a plane ingoing and a spherical outgoing wave, to a state described by a Coulomb wave function with a spherical ingoing and a plane outgoing wave. The initial and final states here belong to different orthogonal systems of wave functions, and so the transition matrix elements are calculated in a mixed representation. In the Feynman theory the situation is

analogous; only the roles of the radiation interaction and the external (or Coulomb) field are interchanged; the radiation interaction is used instead of the Coulomb field to modify the state vectors (wave functions) of the initial and final states, and the external field instead of the radiation interaction causes transitions between these state vectors.

In the Feynman theory there is an additional simplification. For if matrix elements are being calculated between two states, either of which is steady (and this includes all cases so far considered), the mixed representation reduces to an ordinary representation. This occurs, for example, in treating a one-particle problem such as the radiative correction to the equations of motion of an electron in an external field; the operator $H_F(x_0)$, although in general it is not even Hermitian, can in this case be considered as an effective external potential energy acting on the particle, in the ordinary sense of the words.

This section will be concluded with the derivation of the fundamental formula (31) of the Feynman theory, which is the analog of formula (25) of the Schwinger theory. If

$$F_1(x_1), \quad \cdots, \quad F_n(x_n)$$

are any operators defined, respectively, at the points $x_1, \cdots, x_n$ of space-time, then

$$P(F_1(x_1), \quad \cdots, \quad F_n(x_n)) \tag{29}$$

will denote the product of these operators, taken in the order, reading from right to left, in which the surfaces $\sigma(x_1), \cdots, \sigma(x_n)$ occur in time. In most applications of this notation $F_i(x_i)$ will commute with $F_j(x_j)$ so long as x_i and x_j are outside each other's light cones; when this is the case, it is easy to see that (29) is a function of the points $x_1, \cdots, x_n$ only and is independent of the surfaces $\sigma(x_i)$. Consider now the integral

$$I_n = \int_{-\infty}^{\infty} dx_1 \cdots \int_{-\infty}^{\infty} dx_n P(H^e(x_0), H^I(x_1), \cdots, H^I(x_n)).$$

Since the integrand is a symmetrical function of the points $x_1, \cdots, x_n$, the value of the integral is just $n!$ times the integral obtained by restricting the integration to sets of points $x_1, \cdots, x_n$ for which $\sigma(x_i)$ occurs after $\sigma(x_{i+1})$ for each i. The unrestricted integral can then be further divided into $(n+1)$ parts, the j'th part being the integral over those sets of points with the property that $\sigma(x_0)$ lies between $\sigma(x_{j-1})$ and $\sigma(x_j)$ (with obvious modifications for $j=1$ and $j=n+1$). Therefore,

$$I_n = n! \sum_{j=1}^{n+1} \int_{-\infty}^{\sigma(x_0)} dx_j \cdots \int_{-\infty}^{\sigma(x_{n-1})} dx_n \times \int_{\sigma(x_0)}^{\infty} dx_{j-1} \cdots \int_{\sigma(x_1)}^{\infty} dx_1 \times H^I(x_1) \cdots H^I(x_{j-1}) H^e(x_0) H^I(x_j) \cdots H^I(x_n). \tag{30}$$

Now if the series (24) and (28) are substituted into (27), sums of integrals appear which are precisely of the form (30). Hence finally

$$H_F(x_0) = \sum_{n=0}^{\infty} (-i/\hbar c)^n [1/n!] I_n = \sum_{n=0}^{\infty} (-i/\hbar c)^n [1/n!] \int_{-\infty}^{\infty} dx_1 \cdots \int_{-\infty}^{\infty} dx_n \times P(H^e(x_0), H^I(x_1), \cdots, H^I(x_n)). \tag{31}$$

By this formula the notation $H_F(x_0)$ is justified, for this operator now appears as a function of the point x_0 alone and not of the surface σ. The further development of the Feynman theory is mainly concerned with the calculation of matrix elements of (31) between various initial and final states.

As a special case of (31) obtained by replacing H^e by the unit matrix in (27),

$$S(\infty) = \sum_{n=0}^{\infty} (-i/\hbar c)^n [1/n!] \int_{-\infty}^{\infty} dx_1 \cdots \int_{-\infty}^{\infty} dx_n \times P(H^I(x_1), \cdots, H^I(x_n)). \tag{32}$$

VI. CALCULATION OF MATRIX ELEMENTS

In this section the application of the foregoing theory to a general class of problems will be explained. The ultimate aim is to obtain a set of rules by which the matrix element of the operator (31) between two given states may be written down in a form suitable for numerical evaluation, immediately and automatically. The fact that such a set of rules exists is the basis of the Feynman radiation theory; the derivation in this section of the same rules from what is

fundamentally the Tomonaga-Schwinger theory constitutes the proof of equivalence of the two theories.

To avoid excessive complication, the type of matrix element considered will be restricted in two ways. First, it will be assumed that the external potential energy is

$$H^e(x_0) = -[1/c]j_\mu(x_0)A_\mu{}^e(x_0), \qquad (33)$$

that is to say, the interaction energy of the electron-positron field with electromagnetic potentials $A_\mu{}^e(x_0)$ which are given numerical functions of space and time. Second, matrix elements will be considered only for transitions from a state A, in which just one electron and no positron or photon is present, to another state B of the same character. These restrictions are not essential to the theory, and are introduced only for convenience, in order to illustrate clearly the principles involved.

The electron-positron field operator may be written

$$\psi_\alpha(x) = \sum_u \phi_{u\alpha}(x)a_u, \qquad (34)$$

where the $\phi_{u\alpha}(x)$ are spinor wave functions of free electrons and positrons, and the a_u are annihilation operators of electrons and creation operators of positrons. Similarly, the adjoint operator

$$\bar{\psi}_\alpha(x) = \sum_u \bar{\phi}_{u\alpha}(x)\bar{a}_u, \qquad (35)$$

where $\bar{a}_u$ are annihilation operators of positrons and creation operators of electrons. The electromagnetic field operator is

$$A_\mu(x) = \sum_v (A_{v\mu}(x)b_v + A_{v\mu}{}^*(x)\bar{b}_v), \qquad (36)$$

where b_v and $\bar{b}_v$ are photon annihilation and creation operators, respectively. The charge-current 4-vector of the electron field is

$$j_\mu(x) = iec\bar{\psi}(x)\gamma_\mu\psi(x); \qquad (37)$$

strictly speaking, this expression ought to be antisymmetrized to the form[7]

$$j_\mu(x) = \tfrac{1}{2}iec\{\bar{\psi}_\alpha(x)\psi_\beta(x) - \psi_\beta(x)\bar{\psi}_\alpha(x)\}(\gamma_\mu)_{\alpha\beta}, \qquad (38)$$

but it will be seen later that this is not necessary in the present theory.

Consider the product P occurring in the n'th integral of (31); let it be denoted by P_n. From (16), (22), (33), and (37) it is seen that P_n is a sum of products of $(n+1)$ operators ψ_α, $(n+1)$ operators $\bar{\psi}_\alpha$, and not more than n operators A_μ, multiplied by various numerical factors. By Q_n may be denoted a typical product of factors ψ_α, $\bar{\psi}_\alpha$, and A_μ, not summed over the indices such as α and μ, so that P_n is a sum of terms such as Q_n. Then Q_n will be of the form (indices omitted)

$$Q_n = \bar{\psi}(x_{i_0})\psi(x_{i_0})\bar{\psi}(x_{i_1})\psi(x_{i_1})\cdots\bar{\psi}(x_{i_n})\psi(x_{i_n}) \times A(x_{j_1})\cdots A(x_{j_m}), \qquad (39)$$

where $i_0, i_1, \cdots, i_n$ is some permutation of the integers $0, 1, \cdots, n$, and $j_1, \cdots, j_m$ are some, but not necessarily all, of the integers $1, \cdots, n$ in some order. Since none of the operators $\bar{\psi}$ and ψ commute with each other, it is especially important to preserve the order of these factors. Each factor of Q_n is a sum of creation and annihilation operators by virtue of (34), (35), and (36), and so Q_n itself is a sum of products of creation and annihilation operators.

Now consider under what conditions a product of creation and annihilation operators can give a non-zero matrix element for the transition $A \rightarrow B$. Clearly, one of the annihilation operators must annihilate the electron in state A, one of the creation operators must create the electron in state B, and the remaining operators must be divisible into pairs, the members of each pair respectively creating and annihilating the same particle. Creation and annihilation operators referring to different particles always commute or anticommute (the former if at least one is a photon operator, the latter if both are electron-positron operators). Therefore, if the two single operators and the various pairs of operators in the product all refer to different particles, the order of factors in the product can be altered so as to bring together the two single operators and the two members of each pair, without changing the value of the product except for a change of sign if the permutation made in the order of the electron and positron operators is odd. In the case when some of the single operators and pairs of operators refer to the same particle, it is not hard to verify that the same change in order of factors can be made, provided it is remembered that the division of the operators into pairs is no longer unique, and the change of order is to

[7] See Wolfgang Pauli, Rev. Mod. Phys. **13**, 203 (1941), Eq. (96), p. 224.

be made for each possible division into pairs and the results added together.

It follows from the above considerations that the matrix element of Q_n for the transition $A \rightarrow B$ is a sum of contributions, each contribution arising from a specific way of dividing the factors of Q_n into two single factors and pairs. A typical contribution of this kind will be denoted by M. The two factors of a pair must involve a creation and an annihilation operator for the same particle, and so must be either one $\bar{\psi}$ and one ψ or two A; the two single factors must be one $\bar{\psi}$ and one ψ. The term M is thus specified by fixing an integer k, and a permutation $r_0, r_1, \cdots, r_n$ of the integers $0, 1, \cdots, n$, and a division (s_1,t_1), (s_2,t_2), $\cdots$, (s_h,t_h) of the integers $j_1, \cdots, j_m$ into pairs; clearly $m=2h$ has to be an even number; the term M is obtained by choosing for single factors $\bar{\psi}(x_k)$ and $\psi(x_{r_k})$, and for associated pairs of factors $(\bar{\psi}(x_i),\psi(x_{r_i}))$ for $i=0, 1, \cdots, k-1, k+1, \cdots, n$ and $(A(x_{s_i}),A(x_{t_i}))$ for $i=1, \cdots, h$. In evaluating the term M, the order of factors in Q_n is first to be permuted so as to bring together the two single factors and the two members of each pair, but without altering the order of factors within each pair; the result of this process is easily seen to be

$$Q_n' = \epsilon P(\bar{\psi}(x_0),\psi(x_{r_0})) \cdots P(\bar{\psi}(x_n),\psi(x_{r_n})) \times P(A(x_{s_1}),A(x_{t_1})) \cdots P(A(x_{s_h}),A(x_{t_h})), \quad (40)$$

a factor ϵ being inserted which takes the value ± 1 according to whether the permutation of $\bar{\psi}$ and ψ factors between (39) and (40) is even or odd. Then in (40) each product of two associated factors (but not the two single factors) is to be independently replaced by the sum of its matrix elements for processes involving the successive creation and annihilation of the same particle.

Given a bilinear operator such as $A_\mu(x)A_\nu(y)$, the sum of its matrix elements for processes involving the successive creation and annihilation of the same particle is just what is usually called the "vacuum expectation value" of the operator, and has been calculated by Schwinger. This quantity is, in fact (note that Heaviside units are being used)

$$\langle A_\mu(x)A_\nu(y)\rangle_0 = \tfrac{1}{2}\hbar c\delta_{\mu\nu}\{D^{(1)}+iD\}(x-y),$$

where $D^{(1)}$ and D are Schwinger's invariant D functions. The definitions of these functions will not be given here, because it turns out that the vacuum expectation value of $P(A_\mu(x),A_\nu(y))$ takes an even simpler form. Namely,

$$\langle P(A_\mu(x),A_\nu(y))\rangle_0 = \tfrac{1}{2}\hbar c\delta_{\mu\nu}D_F(x-y), \quad (41)$$

where D_F is the type of D function introduced by Feynman. $D_F(x)$ is an even function of x, with the integral expansion

$$D_F(x) = -[i/2\pi^2]\int_0^\infty \exp[i\alpha x^2]d\alpha, \quad (42)$$

where x^2 denotes the square of the invariant length of the 4-vector x. In a similar way it follows from Schwinger's results that

$$\langle P(\bar{\psi}_\alpha(x),\psi_\beta(y))\rangle_0 = \tfrac{1}{2}\eta(x,y)S_{F\beta\alpha}(x-y), \quad (43)$$

where

$$S_{F\beta\alpha}(x) = -(\gamma_\mu(\partial/\partial x_\mu)+\kappa_0)_{\beta\alpha}\Delta_F(x), \quad (44)$$

κ_0 is the reciprocal Compton wave-length of the electron, $\eta(x,y)$ is -1 or $+1$ according as $\sigma(x)$ is earlier or later than $\sigma(y)$ in time, and Δ_F is a function with the integral expansion

$$\Delta_F(x) = -[i/2\pi^2]\int_0^\infty \exp[i\alpha x^2 - i\kappa_0^2/4\alpha]d\alpha. \quad (45)$$

Substituting from (41) and (44) into (40), the matrix element M takes the form (still omitting the indices of the factors $\bar{\psi}$, ψ, and A of Q_n)

$$M = \epsilon \prod_{i\neq k}(\tfrac{1}{2}\eta(x_i,x_{r_i})S_F(x_i-x_{r_i})) \times \prod_j(\tfrac{1}{2}\hbar c D_F(x_{s_j}-x_{t_j}))P(\bar{\psi}(x_k),\psi(x_{r_k})). \quad (46)$$

The single factors $\bar{\psi}(x_k)$ and $\psi(x_{r_k})$ are conveniently left in the form of operators, since the matrix elements of these operators for effecting the transition $A \rightarrow B$ depend on the wave functions of the electron in the states A and B. Moreover, the order of the factors $\bar{\psi}(x_k)$ and $\psi(x_{r_k})$ is immaterial since they anticommute with each other; hence it is permissible to write

$$P(\bar{\psi}(x_k),\psi(x_{r_k})) = \eta(x_k,x_{r_k})\bar{\psi}(x_k)\psi(x_{r_k}).$$

Therefore (46) may be rewritten

$$M = \epsilon' \prod_{i\neq k}(\tfrac{1}{2}S_F(x_i-x_{r_i}))\prod_j(\tfrac{1}{2}\hbar c D_F(x_{s_j}-x_{t_j})) \times \bar{\psi}(x_k)\psi(x_{r_k}), \quad (47)$$

with

$$\epsilon' = \epsilon\prod_i \eta(x_i,x_{r_i}). \quad (48)$$

Now the product in (48) is $(-1)^p$, where p is the number of occasions in the expression (40) on which the ψ of a P bracket occurs to the left of the $\bar{\psi}$. Referring back to the definition of ϵ after Eq. (40), it follows that ϵ' takes the value $+1$ or -1 according to whether the permutation of $\bar{\psi}$ and ψ factors between (39) and the expression

$$\bar{\psi}(x_0)\psi(x_{r0})\cdots\bar{\psi}(x_n)\psi(x_{r_n}) \tag{49}$$

is even or odd. But (39) can be derived by an even permutation from the expression

$$\bar{\psi}(x_0)\psi(x_0)\cdots\bar{\psi}(x_n)\psi(x_n), \tag{50}$$

and the permutation of factors between (49) and (50) is even or odd according to whether the permutation $r_0, \cdots, r_n$ of the integers $0, \cdots, n$ is even or odd. Hence, finally, ϵ' in (47) is $+1$ or -1 according to whether the permutation $r_0, \cdots, r_n$ is even or odd. It is important that ϵ' depends only on the type of matrix element M considered, and not on the points $x_0, \cdots, x_n$; therefore, it can be taken outside the integrals in (31).

One result of the foregoing analysis is to justify the use of (37), instead of the more correct (38), for the charge-current operator occurring in H^e and H^i. For it has been shown that in each matrix element such as M the factors $\bar{\psi}$ and ψ in (38) can be freely permuted, so that (38) can be replaced by (37), except in the case when the two factors form an associated pair. In the exceptional case, M contains as a factor the vacuum expectation value of the operator $j_\mu(x_i)$ at some point x_i; this expectation value is zero according to the correct formula (38), though it would be infinite according to (37); thus the matrix elements in the exceptional case are always zero. The conclusion is that only those matrix elements are to be calculated for which the integer r_i differs from i for every $i \neq k$, and in these elements the use of formula (37) is correct.

To write down the matrix elements of (31) for the transition $A \rightarrow B$, it is only necessary to take all the products Q_n, replace each by the sum of the corresponding matrix elements M given by (47), reassemble the terms into the form of the P_n from which they were derived, and finally substitute back into the series (31). The problem of calculating the matrix elements of (31) is thus in principle solved. However, in the following section it will be shown how this solution-in-principle can be reduced to a much simpler and more practical procedure.

VII. GRAPHICAL REPRESENTATION OF MATRIX ELEMENTS

Let an integer n and a product P_n occurring in (31) be temporarily fixed. The points $x_0, x_1, \cdots, x_n$ may be represented by $(n+1)$ points drawn on a piece of paper. A type of matrix element M as described in the last section will then be represented graphically as follows. For each associated pair of factors $(\bar{\psi}(x_i), \psi(x_{r_i}))$ with $i \neq k$, draw a line with a direction marked in it from the point x_i to the point x_{r_i}. For the single factors $\bar{\psi}(x_k)$, $\psi(x_{r_k})$, draw directed lines leading out from x_k to the edge of the diagram, and in from the edge of the diagram to x_{r_k}. For each pair of factors $(A(x_{s_i}), A(x_{t_i}))$, draw an undirected line joining the points x_{s_i} and x_{t_i}. The complete set of points and lines will be called the "graph" of M; clearly there is a one-to-one correspondence between types of matrix element and graphs, and the exclusion of matrix elements with $r_i = i$ for $i \neq k$ corresponds to the exclusion of graphs with lines joining a point to itself. The directed lines in a graph will be called "electron lines," the undirected lines "photon lines."

Through each point of a graph pass two electron lines, and therefore the electron lines together form one open polygon containing the vertices x_k and x_{r_k}, and possibly a number of closed polygons as well. The closed polygons will be called "closed loops," and their number denoted by l. Now the permutation $r_0, \cdots, r_n$ of the integers $0, \cdots, n$ is clearly composed of $(l+1)$ separate cyclic permutations. A cyclic permutation is even or odd according to whether the number of elements in it is odd or even. Hence the parity of the permutation $r_0, \cdots, r_n$ is the parity of the number of even-number cycles contained in it. But the parity of the number of odd-number cycles in it is obviously the same as the parity of the total number $(n+1)$ of elements. The total number of cycles being $(l+1)$, the parity of the number of even-number cycles is $(l-n)$. Since it was seen earlier that the ϵ' of Eq. (47) is determined just by the parity of the permutation $r_0, \cdots, r_n$, the above argu-

ment yields the simple formula

$$\epsilon' = (-1)^{l-n}. \tag{51}$$

This formula is one result of the present theory which can be much more easily obtained by intuitive considerations of the sort used by Feynman.

In Feynman's theory the graph corresponding to a particular matrix element is regarded, not merely as an aid to calculation, but as a picture of the physical process which gives rise to that matrix element. For example, an electron line joining x_1 to x_2 represents the possible creation of an electron at x_1 and its annihilation at x_2, together with the possible creation of a positron at x_2 and its annihilation at x_1. This interpretation of a graph is obviously consistent with the methods, and in Feynman's hands has been used as the basis for the derivation of most of the results, of the present paper. For reasons of space, these ideas of Feynman will not be discussed in further detail here.

To the product P_n correspond a finite number of graphs, one of which may be denoted by G; all possible G can be enumerated without difficulty for moderate values of n. To each G corresponds a contribution $C(G)$ to the matrix element of (31) which is being evaluated.

It may happen that the graph G is disconnected, so that it can be divided into subgraphs, each of which is connected, with no line joining a point of one subgraph to a point of another. In such a case it is clear from (47) that $C(G)$ is the product of factors derived from each subgraph separately. The subgraph G_1 containing the point x_0 is called the "essential part" of G, the remainder G_2 the "inessential part." There are now two cases to be considered, according to whether the points x_k and x_{r_k} lie in G_2 or in G_1 (they must clearly both lie in the same subgraph). In the first case, the factor $C(G_2)$ of $C(G)$ can be seen by a comparison of (31) and (32) to be a contribution to the matrix element of the operator $S(\infty)$ for the transition $A \to B$. Now letting G vary over all possible graphs with the same G_1 and different G_2, the sum of the contributions of all such G is a constant $C(G_1)$ multiplied by the total matrix element of $S(\infty)$ for the transition $A \to B$. But for one-particle states the operator $S(\infty)$ is by (21) equivalent to the identity operator and gives, accordingly, a zero matrix element for the transition $A \to B$. Consequently, the disconnected G for which x_k and x_{r_k} lie in G_2 give zero contribution to the matrix element of (31), and can be omitted from further consideration. When x_k and x_{r_k} lie in G_1, again the $C(G)$ may be summed over all G consisting of the given G_1 and all possible G_2; but this time the connected graph G_1 itself is to be included in the sum. The sum of all the $C(G)$ in this case turns out to be just $C(G_1)$ multiplied by the expectation value in the vacuum of the operator $S(\infty)$. But the vacuum state, being a steady state, satisfies (21), and so the expectation value in question is equal to unity. Therefore the sum of the $C(G)$ reduces to the single term $C(G_1)$, and again the disconnected graphs may be omitted from consideration.

The elimination of disconnected graphs is, from a physical point of view, somewhat trivial, since these graphs arise merely from the fact that meaningful physical processes proceed simultaneously with totally irrelevant fluctuations of fields in the vacuum. However, similar arguments will now be used to eliminate a much more important class of graphs, namely, those involving self-energy effects. A "self-energy part" of a graph G is defined as follows; it is a set of one or more vertices not including x_0, together with the lines joining them, which is connected with the remainder of G (or with the edge of the diagram) only by two electron lines or by one or two photon lines. For definiteness it may be supposed that G has a self-energy part F, which is connected with its surroundings only by one electron line entering F at x_1, and another leaving F at x_2; the case of photon lines can be treated in an entirely analogous way. The points x_1 and x_2 may or may not be identical. From G a "reduced graph" G_0 can be obtained by omitting F completely and joining the incoming line at x_1 with the outgoing line at x_2 to form a single electron line in G_0, the newly formed line being denoted by λ. Given G_0 and λ, there is conversely a well determined set Γ of graphs G which are associated with G_0 and λ in this way; G_0 itself is considered also to belong to Γ. It will now be shown that the sum $C(\Gamma)$ of the contributions $C(G)$ to the matrix element of (31) from all the graphs G of Γ reduces to a single term $C'(G_0)$.

Suppose, for example, that the line λ in G_0 leads from a point x_3 to the edge of the diagram. Then $C(G_0)$ is an integral containing in the integrand the matrix element of

$$\bar{\psi}_\alpha(x_3) \tag{52}$$

for creation of an electron into the state B. Let the momentum-energy 4-vector of the created electron be p; the matrix element of (52) is of the form

$$Y_\alpha(x_3)=a_\alpha \exp[-i(p\cdot x_3)/\hbar] \tag{53}$$

with a_α independent of x_3. Now consider the sum $C(\Gamma)$. It follows from an analysis of (31) that $C(\Gamma)$ is obtained from $C(G_0)$ by replacing the operator (52) by

$$\sum_{n=0}^{\infty}(-i/\hbar c)^n[1/n!]\int_{-\infty}^{\infty}dy_1\cdots\int_{-\infty}^{\infty}dy_n \times P(\bar{\psi}_\alpha(x_3), H^I(y_1), \cdots, H^I(y_n)). \tag{54}$$

(This is, of course, a consequence of the special character of the graphs of Γ.) It is required to calculate the matrix element of (54) for a transition from the vacuum state O to the state B, i.e., for the emission of an electron into state B. This matrix element will be denoted by Z_α; $C(\Gamma)$ involves Z_α in the same way that $C(G_0)$ involves (53). Now Z_α can be evaluated as a sum of terms of the same general character as (47); it will be of the form

$$Z_\alpha=\sum_i\int_{-\infty}^{\infty}K_i^{\alpha\beta}(y_i-x_3)\,Y_\beta(y_i)dy_i,$$

where the important fact is that K_i is a function only of the coordinate differences between y_i and x_3. By (53), this implies that

$$Z_\alpha=R_{\alpha\beta}(p)\,Y_\beta(x_3), \tag{55}$$

with R independent of x_3. From considerations of relativistic invariance, R must be of the form

$$\delta_{\beta\alpha}R_1(p^2)+(p_\mu\gamma_\mu)_{\beta\alpha}R_2(p^2),$$

where p^2 is the square of the invariant length of the 4-vector p. But since the matrix element (53) is a solution of the Dirac equation,

$$p^2=-\hbar^2\kappa_0^2, \quad (p_\mu\gamma_\mu)_{\beta\alpha}Y_\beta=i\hbar\kappa_0 Y_\alpha,$$

and so (55) reduces to

$$Z_\alpha=R_1Y_\alpha(x_3),$$

with R_1 an absolute constant. Therefore the sum $C(\Gamma)$ is in this case just $C'(G_0)$, where $C'(G_0)$ is obtained from $C(G_0)$ by the replacement

$$\bar{\psi}(x_3)\rightarrow R_1\bar{\psi}(x_3). \tag{56}$$

In the case when the line λ leads into the graph G_0 from the edge of the diagram to the point x_3, it is clear that $C(\Gamma)$ will be similarly obtained from $C(G_0)$ by the replacement

$$\psi(x_3)\rightarrow R_1^*\psi(x_3). \tag{57}$$

There remains the case in which λ leads from one vertex x_3 to another x_4 of G_0. In this case $C(G_0)$ contains in its integrand the function

$$\tfrac{1}{2}\eta(x_3,x_4)S_{F\beta\alpha}(x_3-x_4), \tag{58}$$

which is the vacuum expectation value of the operator

$$P(\bar{\psi}_\alpha(x_3),\psi_\beta(x_4)) \tag{59}$$

according to (43). Now in analogy with (54), $C(\Gamma)$ is obtained from $C(G_0)$ by replacing (59) by

$$\sum_{n=0}^{\infty}(-i/hc)^n[1/n!]\int_{-\infty}^{\infty}dy_1\cdots\int_{-\infty}^{\infty}dy_n \times P(\bar{\psi}_\alpha(x_3), \psi_\beta(x_4), H^I(y_1), \cdots, H^I(y_n)), \tag{60}$$

and the vacuum expectation value of this operator will be denoted by

$$\tfrac{1}{2}\eta(x_3,x_4)S'_{F\beta\alpha}(x_3-x_4). \tag{61}$$

By the methods of Section VI, (61) can be expanded as a series of terms of the same character as (47); this expansion will not be discussed in detail here, but it is easy to see that it leads to an expression of the form (61), with $S_F'(x)$ a certain universal function of the 4-vector x. It will not be possible to reduce (61) to a numerical multiple of (58), as Z_α was in the previous case reduced to a multiple of Y_α. Instead, there may be expected to be a series expansion of the form

$$S_{F\beta\alpha}(x)=(R_2+a_1(\Box^2-\kappa_0^2)+a_2(\Box^2-\kappa_0^2)^2 +\cdots)S_{F\beta\alpha}(x)+(b_1+b_2(\Box^2-\kappa_0^2)+\cdots) \times(\gamma_\mu[\partial/\partial x_\mu]-\kappa_0)_{\beta\gamma}S_{F\gamma\alpha}(x), \tag{62}$$

where $\Box^2$ is the Dalembertian operator and the a, b are numerical coefficients. In this case $C(\Gamma)$ will be equal to the $C'(G_0)$ obtained from $C(G_0)$ by the replacement

$$S_F(x_3-x_4)\rightarrow S_F'(x_3-x_4). \tag{63}$$

Applying the same methods to a graph G with a self-energy part connected to its surroundings by two photon lines, the sum $C(\Gamma)$ will be obtained as a single contribution $C'(G_0)$ from the reduced graph G_0, $C'(G_0)$ being formed from $C(G_0)$ by the replacement

$$D_F(x_3-x_4)\rightarrow D_F'(x_3-x_4). \tag{64}$$

The function D_F' is defined by the condition that

$$\tfrac{1}{2}\hbar c\delta_{\mu\nu}D_F'(x_3-x_4) \tag{65}$$

is the vacuum expectation value of the operator

$$\sum_{n=0}^{\infty}(-i/\hbar c)^n[1/n!]\int_{-\infty}^{\infty}dy_1\cdots\int_{-\infty}^{\infty}dy_n$$

$$\times P(A_\mu(x_3), A_\nu(x_4), H^I(y_1), \cdots, H^I(y_n)), \tag{66}$$

and may be expanded in a series

$$D_F'(x)=(R_2+c_1\Box^2+c_2(\Box^2)^2+\cdots)D_F(x). \tag{67}$$

Finally, it is not difficult to see that for graphs G with self-energy parts connected to their surroundings by a single photon line, the sum $C(\Gamma)$ will be identically zero, and so such graphs may be omitted from consideration entirely.

As a result of the foregoing arguments, the contributions $C(G)$ of graphs with self-energy parts can always be replaced by modified contributions $C'(G_0)$ from a reduced graph G_0. A given G may be reducible in more than one way to give various G_0, but if the process of reduction is repeated a finite number of times a G_0 will be obtained which is "totally reduced," contains no self-energy part, and is uniquely determined by G. The contribution $C'(G_0)$ of a totally reduced graph to the matrix element of (31) is now to be calculated as a sum of integrals of expressions like (47), but with a replacement (56), (57), (63), or (64) made corresponding to every line in G_0. This having been done, the matrix element of (31) is correctly calculated by taking into consideration each totally reduced graph once and once only.

The elimination of graphs with self-energy parts is a most important simplification of the theory. For according to (22), H^I contains the subtracted part H^S, which will give rise to many additional terms in the expansion of (31). But if any such term is taken, say, containing the factor $H^S(x_i)$ in the integrand, every graph corresponding to that term will contain the point x_i joined to the rest of the graph only by two electron lines, and this point by itself constitutes a self-energy part of the graph. Therefore, all terms involving H^S are to be omitted from (31) in the calculation of matrix elements. The intuitive argument for omitting these terms is that they were only introduced in order to cancel out higher order self-energy terms arising from H^i, which are also to be omitted; the analysis of the foregoing paragraphs is a more precise form of this argument. In physical language, the argument can be stated still more simply; since δm is an unobservable quantity, it cannot appear in the final description of observable phenomena.

VIII. VACUUM POLARIZATION AND CHARGE RENORMALIZATION

The question now arises: What is the physical meaning of the new functions D_F' and S_F', and of the constant R_1? In general terms, the answer is clear. The physical processes represented by the self-energy parts of graphs have been pushed out of the calculations, but these processes do not consist entirely of unobservable interactions of single particles with their self-fields, and so cannot entirely be written off as "self-energy processes." In addition, these processes include the phenomenon of vacuum polarization, i.e., the modification of the field surrounding a charged particle by the charges which the particle induces in the vacuum. Therefore, the appearance of D_F', S_F', and R_1 in the calculations may be regarded as an explicit representation of the vacuum polarization phenomena which were implicitly contained in the processes now ignored.

In the present theory there are two kinds of vacuum polarization, one induced by the external field and the other by the quantized electron and photon fields themselves; these will be called "external" and "internal," respectively. It is only the internal polarization which is represented yet in explicit fashion by the substitutions (56), (57), (63), (64); the external will be included later.

To form a concrete picture of the function D_F', it may be observed that the function $D_F(y-z)$ represents in classical electrodynamics the retarded potential of a point charge at y acting upon a point charge at z, together with the re-

tarded potential of the charge at z acting on the charge at y. Therefore, D_F may be spoken of loosely as "the electromagnetic interaction between two point charges." In this semiclassical picture, D_F' is then the electromagnetic interaction between two point charges, including the effects of the charge-distribution which each charge induces in the vacuum.

The complete phenomenon of vacuum polarization, as hitherto understood, is included in the above picture of the function D_F'. There is nothing left for S_F' to represent. Thus, one of the important conclusions of the present theory is that there is a second phenomenon occurring in nature, included in the term vacuum polarization as used in this paper, but additional to vacuum polarization in the usual sense of the word. The nature of the second phenomenon can best be explained by an example.

The scattering of one electron by another may be represented as caused by a potential energy (the Møller interaction) acting between them. If one electron is at y and the other at z, then, as explained above, the effect of vacuum polarization of the usual kind is to replace a factor D_F in this potential energy by D_F'. Now consider an analogous, but unorthodox, representation of the Compton effect, or the scattering of an electron by a photon. If the electron is at y and the photon at z, the scattering may be again represented by a potential energy, containing now the operator $S_F(y-z)$ as a factor; the potential is an exchange potential, because after the interaction the electron must be considered to be at z and the photon at y, but this does not detract from its usefulness. By analogy with the 4-vector charge-current density j_μ which interacts with the potential D_F, a spinor Compton-effect density u_α may be defined by the equation

$$u_\alpha(x)=A_\mu(x)(\gamma_\mu)_{\alpha\beta}\psi_\beta(x),$$

and an adjoint spinor by

$$\bar{u}_\alpha(x)=\bar{\psi}_\beta(x)(\gamma_\mu)_{\beta\alpha}A_\mu(x).$$

These spinors are not directly observable quantities, but the Compton effect can be adequately described as an exchange potential, of magnitude proportional to $S_F(y-z)$, acting between the Compton-effect density at any point y and the adjoint density at z. The second vacuum polarization phenomenon is described by a change in the form of this potential from S_F to S_F'. Therefore, the phenomenon may be pictured in physical terms as the inducing, by a given element of Compton-effect density at a given point, of additional Compton-effect density in the vacuum around it.

In both sorts of internal vacuum polarization, the functions D_F and S_F, in addition to being altered in shape, become multiplied by numerical (and actually divergent) factors R_3 and R_2; also the matrix elements of (31) become multiplied by numerical factors such as $R_1R_1^*$. However, it is believed (this has been verified only for second-order terms) that all n'th-order matrix elements of (31) will involve these factors only in the form of a multiplier

$$(eR_2R_3^{\frac{1}{2}})^n;$$

this statement includes the contributions from the higher terms of the series (62) and (67). Here e is defined as the constant occurring in the fundamental interaction (16) by virtue of (37). Now the only possible experimental determination of e is by means of measurements of the effects described by various matrix elements of (31), and so the directly measured quantity is not e but $eR_2R_3^{\frac{1}{2}}$. Therefore, in practice the letter e is used to denote this measured quantity, and the multipliers R no longer appear explicitly in the matrix elements of (31); the change in the meaning of the letter e is called "charge renormalization," and is essential if e is to be identified with the observed electronic charge. As a result of the renormalization, the divergent coefficients R_1, R_2, and R_3 in (56), (57), (62), and (67) are to be replaced by unity, and the higher coefficients a, b, and c by expressions involving only the renormalized charge e.

The external vacuum polarization induced by the potential A_μ^e is, physically speaking, only a special case of the first sort of internal polarization; it can be treated in a precisely similar manner. Graphs describing external polarization effects are those with an "external polarization part," namely, a part including the point x_0 and connected with the rest of the graph by only a single photon line. Such a graph is to be "reduced" by omitting the polarization part entirely and renaming with the label x_0 the

point at the further end of the single photon line. A discussion similar to those of Section VII leads to the conclusion that only reduced graphs need be considered in the calculation of the matrix element of (31), and that the effect of external polarization is explicitly represented if in the contributions from these graphs a replacement

$$A_\mu^e(x) \rightarrow A_\mu^{e\prime}(x) \tag{68}$$

is made. After a renormalization of the unit of potential, similar to the renormalization of charge, the modified potential $A_\mu^{e\prime}$ takes the form

$$A_\mu^{e\prime}(x) = (1+c_1\Box^2+c_2(\Box^2)^2+\cdots)A_\mu^e(x), \tag{69}$$

where the coefficients are the same as in (67).

It is necessary, in order to determine the functions D_F', S_F', and $A_\mu^{e\prime}$, to go back to formulas (60) and (66). The determination of the vacuum expectation values of the operators (60) and (66) is a problem of the same kind as the original problem of the calculation of matrix elements of (31), and the various terms in the operators (60) and (66) must again be split up, represented by graphs, and analyzed in detail. However, since D_F' and S_F' are universal functions, this further analysis has only to be carried out once to be applicable to all problems.

It is one of the major triumphs of the Schwinger theory that it enables an unambiguous interpretation to be given to the phenomenon of vacuum polarization (at least of the first kind), and to the vacuum expectation value of an operator such as (66). In making this interpretation, profound theoretical problems arise, particularly concerned with the gauge invariance of the theory, about which nothing will be said here. For Schwinger's solution of these problems, the reader must refer to his forthcoming papers. Schwinger's argument can be transferred without essential change into the framework of the present paper.

Having overcome the difficulties of principle, Schwinger proceeded to evaluate the function D_F' explicitly as far as terms of order $\alpha=(e^2/4\pi\hbar c)$ (heaviside units). In particular, he found for the coefficient c_1 in (67) and (69) the value $(-\alpha/15\pi\kappa_0^2)$ to this order.[8] It is hoped to publish in a sequel to the present paper a similar evaluation of the function S_F'; the analysis involved is too complicated to be summarized here.

[8] Schwinger's results agree with those of the earlier, theoretically unsatisfactory treatment of vacuum polarization. The best account of the earlier work is V. F. Weisskopf, Kgl. Danske Sels. Math.-Fys. Medd. **14**, No. 6 (1936).

IX. SUMMARY OF RESULTS

In this section the results of the preceding pages will be summarized, so far as they relate to the performance of practical calculations. In effect, this summary will consist of a set of rules for the application of the Feynman radiation theory to a certain class of problems.

Suppose an electron to be moving in an external field with interaction energy given by (33). Then the interaction energy to be used in calculating the motion of the electron, including radiative corrections of all orders, is

$$\begin{aligned} H_E(x_0) &= \sum_{n=0}^{\infty} (-i/\hbar c)^n[1/n!]J_n \\ &= \sum_{n=0}^{\infty} (-i/\hbar c)^n[1/n!]\int_{-\infty}^{\infty} dx_1 \cdots \int_{-\infty}^{\infty} dx_n \\ &\quad \times P(H^e(x_0), H^i(x_1), \cdots, H^i(x_n)), \end{aligned} \tag{70}$$

with H^i given by (16), and the P notation as defined in (29).

To find the effective n'th-order radiative correction to the potential acting on the electron, it is necessary to calculate the matrix elements of J_n for transitions from one one-electron state to another. These matrix elements can be written down most conveniently in the form of an operator K_n bilinear in $\bar{\psi}$ and ψ, whose matrix elements for one-electron transitions are the same as those to be determined. In fact, the operator K_n itself is already the matrix element to be determined if the $\bar{\psi}$ and ψ contained in it are regarded as one-electron wave functions.

To write down K_n, the integrand P_n in J_n is first expressed in terms of its factors $\bar{\psi}$, ψ, and A, all suffixes being indicated explicitly, and the expression (37) used for j_μ. All possible graphs G with $(n+1)$ vertices are now drawn as described in Section VII, omitting disconnected graphs, graphs with self-energy parts, and graphs with external vacuum polarization parts as defined in Section VIII. It will be found that in each graph there are at each vertex two electron lines and one photon line, with the exception of x_0 at which there are two electron lines only; further,

such graphs can exist only for even n. K_n is the sum of a contribution $K(G)$ from each G.

Given G, $K(G)$ is obtained from J_n by the following transformations. First, for each photon line joining x and y in G, replace two factors $A_\mu(x)A_\nu(y)$ in P_n (regardless of their positions) by

$$\tfrac{1}{2}\hbar c\delta_{\mu\nu}D_F'(x-y), \tag{71}$$

with D_F' given by (67) with $R_3=1$, the function D_F being defined by (42). Second, for each electron line joining x to y in G, replace two factors $\bar{\psi}_\alpha(x)\psi_\beta(y)$ in P_n (regardless of positions) by

$$\tfrac{1}{2}S'_{F\beta\alpha}(x-y) \tag{72}$$

with S_F' given by (62) with $R_2=1$, the function S_F being defined by (44) and (45). Third, replace the remaining two factors $P(\bar{\psi}_\gamma(z),\psi_\delta(w))$ in P_n by $\bar{\psi}_\gamma(z)\psi_\delta(w)$ in this order. Fourth, replace $A_\mu^e(x_0)$ by $A_\mu^{e\prime}(x_0)$ given by

$$A_\mu^{e\prime}(x)=A_\mu^e(x)-[\alpha/15\pi\kappa_0^2]\Box^2A_\mu^e(x) \tag{73}$$

or, more generally, by (69). Fifth, multiply the whole by $(-1)^l$, where l is the number of closed loops in G as defined in Section VII.

The above rules enable K_n to be written down very rapidly for small values of n. It should be observed that if K_n is being calculated, and if it is not desired to include effects of higher order than the n'th, then D_F', S_F', and $A_\mu^{e\prime}$ in (71), (72), and (73) reduce to the simple functions D_F, S_F, and A_μ^e. Also, the integrand in J_n is a symmetrical function of $x_1, \cdots, x_n$; therefore, graphs which differ only by a relabeling of the vertices $x_1, \cdots, x_n$ give identical contributions to K_n and need not be considered separately.

The extension of these rules to cover the calculation of matrix elements of (70) of a more general character than the one-electron transitions hitherto considered presents no essential difficulty. All that is necessary is to consider graphs with more than two "loose ends," representing processes in which more than one particle is involved. This extension is not treated in the present paper, chiefly because it would lead to unpleasantly cumbersome formulas.

X. EXAMPLE—SECOND-ORDER RADIATIVE CORRECTIONS

As an illustration of the rules of procedure of the previous section, these rules will be used for writing down the terms giving second-order radiative corrections to the motion of an electron in an external field. Let the energy of the external field be

FIG. 1.

$$-[1/c]j_\mu(x_0)A_\mu^e(x_0). \tag{74}$$

Then there will be one second-order correction term

$$U=[\alpha/15\pi\kappa_0^2][1/c]j_\mu(x_0)\Box^2A_\mu^e(x_0)$$

arising from the substitution (73) in the zero-order term (74). This is the well-known vacuum polarization or Uehling term.[9]

The remaining second-order term arises from the second-order part J_2 of (70). Written in expanded form, J_2 is

$$J_2=ie^3\int_{-\infty}^{\infty}dx_1\int_{-\infty}^{\infty}dx_2P(\bar{\psi}_\alpha(x_0)(\gamma_\lambda)_{\alpha\beta}\psi_\beta(x_0)A_\lambda^e(x_0),$$
$$\bar{\psi}_\gamma(x_1)(\gamma_\mu)_{\gamma\delta}\psi_\delta(x_1)A_\mu(x_1),$$
$$\bar{\psi}_\epsilon(x_2)(\gamma_\nu)_{\epsilon\zeta}\psi_\zeta(x_2)A_\nu(x_2)).$$

Next, all admissable graphs with the three vertices x_0, x_1, x_2 are to be drawn. It is easy to see that there are only two such graphs, that G shown in Fig. 1, and the identical graph with x_1 and x_2 interchanged. The full lines are electron lines, the dotted line a photon line. The contribution $K(G)$ is obtained from J_2 by substituting according to the rules of Section IX; in this case $l=0$, and the primes can be omitted from (71), (72), (73) since only second-order terms are required. The integrand in $K(G)$ can be reassembled into the form of a matrix product, suppressing the suffixes $\alpha, \cdots, \zeta$. Then, multiplying by a factor 2 to allow for the second graph, the complete second-order correction to (74) arising from J_2 becomes

$$L=-i[e^3/8\hbar c]\int_{-\infty}^{\infty}dx_1\int_{-\infty}^{\infty}dx_2D_F(x_1-x_2)A_\mu^e(x_0)\cdot$$
$$\times\bar{\psi}(x_1)\gamma_\nu S_F(x_0-x_1)\gamma_\mu S_F(x_2-x_0)\gamma_\nu\psi(x_2).$$

[9] Robert Serber, Phys. Rev. 48, 49 (1935); E. A. Uehling, Phys. Rev. 48, 55 (1935).

This is the term which gives rise to the main part of the Lamb-Retherford line shift,[10] the anomalous magnetic moment of the electron,[11] and the anomalous hyperfine splitting of the ground state of hydrogen.[12]

The above expression L is formally simpler than the corresponding expression obtained by Schwinger, but the two are easily seen to be equivalent. In particular, the above expression does not lead to any great reduction in the labor involved in a numerical calculation of the Lamb shift. Its advantage lies rather in the ease with which it can be written down.

In conclusion, the author would like to express his thanks to the Commonwealth Fund of New York for financial support, and to Professors Schwinger and Feynman for the stimulating lectures in which they presented their respective theories.

Notes added in proof (To Section II). The argument of Section II is an over-simplification of the method of Tomonaga,[1] and is unsound. There is an error in the derivation of (3); derivatives occurring in $H(r)$ give rise to non-commutativity between $H(r)$ and field quantities at r' when r is a point on σ infinitesimally distant from r'. The argument should be amended as follows. Φ is defined only for flat surfaces $t(r)=t$, and for such surfaces (3) and (6) are correct. Ψ is defined for general surfaces by (12) and (10), and is verified to satisfy (9). For a flat surface, Φ and Ψ are then shown to be related by (7). Finally, since H_1 does not involve the derivatives in H, the argument leading to (3) can be correctly applied to prove that for general σ the state-vector $\Psi(\sigma)$ will completely describe results of observations of the system on σ.

(To Section III). A covariant perturbation theory similar to that of Section III has previously been developed by E. C G. Stueckelberg, Ann. d. Phys. **21**, 367 (1934); Nature, **153**, 143 (1944).

(To Section V). Schwinger's "effective potential" is not H_T given by (25), but is $H_T'=QH_TQ^{-1}$. Here Q is a "square-root" of $S(\infty)$ obtained by expanding $(S(\infty))^{\frac{1}{2}}$ by the binomial theorem. The physical meaning of this is that Schwinger specifies states neither by Ω nor by Ω', but by an intermediate state-vector $\Omega''=Q\Omega=Q^{-1}\Omega'$, whose definition is symmetrical between past and future. H_T' is also symmetrical between past and future. For one-particle states, H_T and H_T' are identical.

Equation (32) can most simply be obtained directly from the product expansion of $S(\infty)$.

(To Section VII). Equation (62) is incorrect. The function S_F' is well-behaved, but its fourier transform has a logarithmic dependence on frequency, which makes an expansion precisely of the form (62) impossible.

(To Section X). The term L still contains two divergent parts. One is an "infra-red catastrophe" removable by standard methods. The other is an "ultraviolet" divergence, and has to be interpreted as an additional charge-renormalization, or, better, cancelled by part of the charge-renormalization calculated in Section VIII.

[10] W. E. Lamb and R. C. Retherford, Phys. Rev. **72**, 241 (1947).
[11] P. Kusch and H. M. Foley, Phys. Rev. **74**, 250 (1948).
[12] J. E. Nafe and E. B. Nelson, Phys. Rev. **73**, 718 (1948); Aage Bohr, Phys. Rev. **73**, 1109 (1948).

PHYSICAL REVIEW VOLUME 75, NUMBER 3 FEBRUARY 1, 1949

Note on a Theorem of Bloch Concerning Possible Causes of Superconductivity

D. BOHM
Physics Department, Princeton University, Princeton, New Jersey
(Received September 13, 1948)

Attention is called to a theorem of Bloch, from which it is shown that even when inter-electronic interactions are taken into account, the state of lowest electronic free energy corresponds to a zero net current. This result contradicts the hypothesis that superconductivity is caused by spontaneous currents.

MANY attempts[1,2] have been made to explain superconductivity in terms of spontaneous currents, which arise because there is a special group of states of the electron gas as a whole, for which the free energy, $F=E-TS$, is lower when a finite current flows than when no current flows at all. In some of the theories, it is suggested that the current-carrying states in question may have energies which are below that of the state of zero current, while in others, it is suggested that the current-carrying states may have so high a statistical weight that their free energy is

[1] W. Heisenberg, Zeits. f. Naturforschg **32**, 65 (1948).
[2] M. Born and K. C. Cheng, Nature **161**, 1017 (1948).

a minimum, even though the energy itself may not be a minimum. It is generally realized that the Bloch one-particle wave functions always make the state of lowest free energy one of zero current, but it is hoped that the inter-electronic interactions, not taken into account completely by these wave-functions, may change this result. Bloch has, however, proved[3,4] a theorem from which one can deduce that even when these interactions are taken into account, the state of lowest free energy still corresponds to zero net current. Since this result does not appear to be widely known, and since it is not treated in much detail in the existing literature, a brief note on the subject is perhaps desirable here.

Let the Hamiltonian be denoted by

$$\mathcal{H}=\sum_n [V(\mathbf{X}_n)-\hbar^2\nabla_n^2/2m]+\tfrac{1}{2}\sum_{m\neq n} V(\mathbf{X}_{mn}).$$

$V(\mathbf{X}_n)$ represents the potential of the nth electron in the field of the ion lattice, while $V(\mathbf{X}_{mn})$ represents the potential energy of inter-electronic interaction (coulomb).

Let us observe that the total current, $\mathbf{j}$, is related to the total electronic momentum, $\mathbf{P}$, by $\mathbf{j}=e\mathbf{P}/m$.

In the first part of the proof, we assume temporarily that the lowest state carries a current, in order to show that one is thereby led to a contradiction. Suppose that the exact wave-function is $\psi(\mathbf{X}_1, \mathbf{X}_2, \cdots \mathbf{X}_n \cdots)$. Let us consider a slightly different wave function,

$$\phi=\exp[(i\delta\mathbf{P}/\hbar\sum_n \mathbf{X}_n)]\psi$$

where $\delta\mathbf{P}$ is very small. This corresponds to a state in which each electron has been given an additional momentum, $\delta\mathbf{P}$. If $\mathbf{P}_0$ is the total electronic momentum in the state, ψ, then their total momentum in the state, ϕ, is

$$\mathbf{P}=\mathbf{P}_0+N\delta\mathbf{P},$$

where N is the total number of electrons. (Note that if ψ is totally anti-symmetric in space and spin coordinates of all the particles, then ϕ must possess the same antisymmetry, because the exponential factor is a totally symmetric function of the particle coordinates.)

[3] Appendix to L. Brillouin, J. de phys. et rad. 4, 334 (1933).

[4] H. G. Smith and J. O. Wilhelm, Rev. Mod. Phys. 7, 266 (1935).

Let us now compute the mean electronic energy for the wave function, ϕ. It is clear that the potential energy is exactly the same as when the wave function is ψ. If T_0 represents the mean kinetic energy in the state, ψ, one obtains, however,

$$T=-\hbar^2/2m\sum_n\left(\int \phi^*\nabla_n^2\phi dX_1 dX_2\cdots dX_n\cdots\right)$$

$$=T_0+\frac{N(\mathbf{P}_0\cdot\delta\mathbf{P})}{m}+\frac{N(\delta P)^2}{2m}$$

$$=T_0+m\mathbf{j}_0\cdot\delta\mathbf{j}/e^2+m(\delta j)^2/2Ne^2.$$

One can choose $\delta\mathbf{P}$ opposite in sign to $\mathbf{P}_0$, so that $\mathbf{P}_0\cdot\delta\mathbf{P}$ is negative. If $\delta\mathbf{P}$ is small enough, the term involving $(\delta P)^2$ can be neglected. One concludes that for the state ϕ, the kinetic energy and therefore the total energy, is less than for the state ψ. Although the function, ϕ, is not necessarily a solution of Schrödinger's equation, it is a well-known theorem that the energy of the lowest state must be lower than the mean energy calculated with any other wave function. We have thus proved that unless $\mathbf{j}_0=0$, the state, ψ, cannot be the lowest.

One can conclude immediately from the above that if superconductivity is due to spontaneous currents, then it must disappear at absolute zero, where the system occupies the lowest state. It is possible to go farther, however, and to show that states of finite current cannot be thermodynamically the most stable even at non-zero temperatures. To do this, we show that for each solution of Schrodinger's equation with a non-vanishing current, there exists another solution with a lower current and with a lower energy.

Let us denote by $\psi_i(\mathbf{X}_1, \mathbf{X}_2, \cdots \mathbf{X}_n \cdots)$, the complete set of orthonormal exact solutions of Schrödinger's equations, possessing energies, E_i. We then define an alternative set of functions,

$$\phi_i=\exp[(i\delta\mathbf{P}/\hbar)\cdot\sum_n \mathbf{X}_n]\psi_i,$$

which are also clearly orthonormal, but which are not, in general, exact solutions of Schrödinger's equation. The Hamiltonian matrix can be expressed in terms of the functions, ϕ_i, as

follows

$$H_{ij}=\int((\phi_i^* H\phi_j)dX_1 dX_2\cdots dX_n\cdots)$$

$$=\left(E_i+\frac{N(\delta P)^2}{2m}\right)\delta_{ij}$$

$$+(\hbar/im)\delta\mathbf{P}\cdot\int(\psi_i^*\textstyle\sum_n\nabla_n\psi_j)dX_1\cdots dX_n.$$

If $\mathbf{j}_i$ represents the mean current in the state ψ_i, the diagonal elements are

$$H_{ii}=E_i+N(\delta P)^2/2m+\mathbf{j}_i\cdot\delta\mathbf{P}/e$$

while the off-diagonal elements are

$$H_{ij}=(\hbar\delta\mathbf{P}/i)\cdot\int(\psi_i^*\textstyle\sum_n\nabla_n\psi_j)dX_1 dX_2\cdots dX_n\cdots.$$

If $\delta\mathbf{P}$ is small, H_{ij} is a small perturbation, and one can by standard perturbation procedures, obtain a solution for the wave-functions and energy levels. The off-diagonal elements of $\mathcal{H}$ contribute to the energy only in second order. Thus, one obtains for the energy of the state for which ϕ_i is the zeroth approximation

$$W_i=E_i+\mathbf{j}_i\cdot\delta\mathbf{P}/e+\text{terms of order }(\delta P)^2.$$

By choosing $\delta\mathbf{P}$ opposite in sign to $\mathbf{j}_i$ and very small, one obtains, for each ψ_i, another state having an energy lower than that of ψ_i. Thus, if we assume that there is a group of states carrying some current, $\mathbf{j}_i$, they cannot have a minimum free energy, because there is always another group of states with the same statistical weight, but with a lower energy, hence with a lower free energy.

It has sometimes been suggested that superconductivity is always associated with circulating currents, such as those in a superconducting ring. Since the total current, $\mathbf{j}_i$, vanishes here, it is clear that the above results do not apply. By noting that the current for this case is proportional to the total electronic angular momentum, however, one can give a similar treatment, and one obtains again the result that the state of lowest free energy corresponds to zero net current.* Even when the magnetic field caused by the electronic motion is taken into account, the same result is obtained. The proof of the theorem requires, however, that the coupling between electron spin and orbital magnetic fields be neglected. It would seem safe to conclude that the spontaneous current hypothesis cannot explain superconductivity, unless one wishes to show that the energy stabilizing the state of finite current is due to coupling between electron spin and orbital magnetic fields.

It would seem preferable to state that if superconductivity is caused by interactions between electrons, it is probably due to a somewhat localized tendency for electrons of the same velocity to move together as a unit, which is held together in some way by the inter-electronic forces. In order to stop such a group of electrons, it would be necessary to scatter all of them at once. Such a process would be enormously less probable than one in which electrons are scattered individually by lattice vibrations, or other irregularities in the lattice. The formation of such localized groups of co-moving particles would liberate energy, thus making the superconducting state the most stable one. Yet, it would still remain true that a superconducting state which was carrying a large current would have a higher energy than one which carried no current; the current carrying state would then be very long-lived because of the small probability of scattering. It is possible to regard the theories of Heisenberg and Born from this viewpoint, provided that one interprets the interaction energy as associated with a local ordering of velocities, rather than with the stabilization of spontaneous currents. The author is also planning to publish a theory shortly in which another example of this type of explanation is studied in detail, through the means of treating inter-electronic interactions in terms of plasma oscillations.

* In carrying out this treatment, one multiplies the wave function by $\exp[(im/\hbar)\Sigma_i\phi_i]$, where m is an integer. Since m must be at least unity, the smallest change of angular momentum obtainable in this way is $N\hbar$. In order to obtain an arbitrarily small change of current, however, one can consider a superconducting ring of radius, r, made of a very thin wire. The total change of current density is then $\rho\hbar/mr$, where ρ is the electron density. By going to very large r, one can obtain arbitrarily small changes in current. Hence, for a large enough ring, one can certainly apply the same argument as with non-circulating currents. Since the limiting current for a superconductor is known to be independent of the ring diameter, it is clear that one can, in this way, show that spontaneous currents are not the cause of superconductivity in such a ring.

A Precision Study of the Tungsten K Spectrum Using the 2-Meter Focusing Curved Crystal Spectrometer*

BERNARD B. WATSON,** WILLIAM J. WEST, DAVID A. LIND, AND JESSE W. M. DUMOND
California Institute of Technology, Pasadena, California

(Received August 16, 1948)

Using the 2-meter focusing curved crystal gamma-ray spectrometer, careful measurements were made of the wave-lengths of the K series lines and K absorption edge of tungsten for the dual purpose of establishing a precision linkage between wave-length measurements in the gamma- and x-ray regions and of improving our knowledge of the tungsten wave-lengths. The high precision, resolution, and luminosity of the instrument made possible the complete resolution of the β-doublet, the partial resolution of the γ-doublet, and the detection and measurement of a δ-line close to the absorption edge. Absolute determinations of the Bragg angles for Mo $K\alpha_1$ and W $K\alpha_1$ reflected from the (310) planes of quartz by W. J. West in this laboratory, using a precision 2-crystal spectrometer, are described. These were undertaken (a) to standardize the tungsten K spectrum with higher accuracy in terms of the Siegbahn scale of x-ray wave-lengths and (b) to yield on this scale a precision determination of the grating constant of the quartz (310) planes. Adopting W. J. West's value of 208.575±0.008 x.u. (Siegbahn scale) for the wave-length of the α_1 line, the wave-lengths of the K series lines and K edge were found to be:

Siegbahn notation	α_2	α_1	β_3	β_1	β_2^{II}	β_2^{I}		Abs. edge.
Sommerfeld notation	α_2	α_1	β_2	β_1	γ_2	γ_1	δ	Abs. edge.
Transition	$K-L_{II}$	$K-L_{III}$	$K-M_{II}$	$K-M_{III}$	$K-N_{II}$	$K-N_{III}$	$K-O_{II,III}$	$K-\infty$
Wave-length x.u. (Siegbahn scale)	213.387 ±0.010	208.575 ±0.008	184.772 ±0.020	183.967 ±0.020	179.212 ±0.020	179.038 ±0.020	178.052 ±0.020	177.947 ±0.020
Wave-length A	0.213818 ±0.000010	0.208996 ±0.000008	0.185145 ±0.000020	0.184339 ±0.000020	0.179574 ±0.000020	0.179400 ±0.000020	0.178412 ±0.000020	0.178306 ±0.000020

West's 2-crystal spectrometer study gives for the (310) planes of quartz at 18°C the grating constant

$d=1177.637\pm0.020$ x.u. (Siegbahn scale).

INTRODUCTION

THE 2-meter curved crystal focusing spectrometer[1] used in the precision determination[2] of the wave-length of the 0.41-Mev line of Au^{198} was designed so that it could be used for measurements in the x-ray as well as in the gamma-ray regions of the spectrum in order to make possible the direct comparison of gamma-ray wave-lengths with the better known x-ray wave-lengths. The calibration of the instrument has now been carried out using the K series lines of tungsten reflected from the (310) planes of the curved quartz lanina.

The tungsten lines were chosen for this calibration work, in spite of the fact that the 2-meter curved crystal instrument admits of studying wave-lengths as long as the silver K spectrum, (a) because it was deemed wise to utilize portions of the precision wave-length screw not too far removed from the γ-ray region for whose study the instrument was primarily designed, and (b) because of the ready availability of a tungsten target tube suitable for this purpose.

Since the K series lines of tungsten have themselves not been studied as carefully or as extensively as some of the softer x-ray lines, a separate study with the 2-crystal spectrometer by W. J. West was also simultaneously undertaken in this laboratory to relate the $K\alpha_1$ line of tungsten to the $K\alpha_1$ line of molybdenum with all possible precision. Since the (310) planes of quartz were also used in this 2-crystal spectrometer study, a precision value of the grating constant, d, for (310) planes of quartz was thus also obtained.

The high resolving power of the 2-meter

* Work supported by contract with the Office of Naval Research.

** Now at Temple University, Philadelphia, Pennsylvania.

[1] J. W. M. DuMond, Rev. Sci. Inst. 18, 626 (1947).

[2] J. W. M. DuMond, D. A. Lind, and B. B. Watson, Phys. Rev. 73, 1392 (1948).

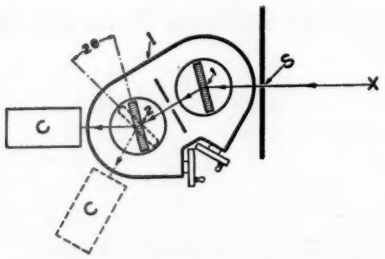

FIG. 1. Schematic illustration of the geometry used in two-crystal spectrometer precision Bragg angle determinations of W$K\alpha_1$ and Mo $K\alpha_1$ reflected from the (310) planes of quartz by transmission of the x-ray beam through 1-mm thick quartz plates. X represents the focal spot of the x-ray tube, S the first slit or stop. The full lines show the general position for the parallel rocking curve. The dotted lines show the position for the antiparallel rocking curve. The xenon-filled counter is at C and is supported on an arm pivoted about the axis of crystal 2. The instrument I can as a whole be rotated on a pivot coincident with the pivot of crystal 1.

curved crystal spectrometer has made possible the complete resolution of the $K\beta$-doublet (Siegbahn notation: $K\beta_1$, $K\beta_3$) and the partial resolution—reported previously by Hudson and Vogt and by E. Ingelstam[3] of the $K\gamma$-doublet (Siegbahn notation: $K\beta_2$). The high precision afforded by the instrument has made possible a more precise determination than has heretofore been reported of the wave-lengths of the K series lines relative to that of the α_1 line, and of the various doublet separations. The high luminosity of the instrument has endowed the $K\delta$-line, resulting from a $K-O_{II}O_{III}$ transition, with sufficient intensity to make possible an accurate measurement of its wave-length. In addition, a precise measurement of the position of the tungsten K edge was made with a result that is appreciably different from that of previous measurements by Mack and Cork and by I. Manescu.[4]

APPARATUS

The spectrometer and the multicellular counter used for the detection of the diffracted beam have been described by DuMond.[1] In the present case the gamma-ray source holder which occupies a position on the focal circle was replaced by a narrow slit behind which, supported on the upper beam of the spectrometer, was situated a tungsten "shock proof" type x-ray tube operated at 140 kv and 5.0 ma. The measurements on the lines were made with 0.016 inch of lead in the beam in order to keep the peak counting rates from being excessively high.[5] For the deter-

TABLE I. 2-crystal spectrometer Bragg angle determinations of Mo $K\alpha_1$ and W$K\alpha_1$ on quartz (310) planes.

Mo $K\alpha_1$ line Deviation of beam by crystal No. 1 to	Run No.	Parallel position reading	Worm wheel correction	Parallel corrected	Antiparallel position reading	Worm wheel correction	Antiparallel position corrected	2θ	θ Bragg angle
Left	1	73°13′54″	+4½″	73°13′58½″	108°12′31½″	+3½″	108°12′34¾″	34°58′36¼″	17°29′18¼″
Left	2	73°13′55½″	+4½″	73°13′59¾″	108°12′32¾″	+3½″	108°12′36″	34°58′36½″	17°29′18⅜″
Left	3	73°13′55½″	+4½″	73°13′59¾″	108°12′32½″	+3½″	108°12′35½″	34°58′35¾″	17°29′17⅞″
Left	4	893°14′1″	−2″	893°13′59″	928°12′35¾″	+1″	928°12′36¾″	34°58′37¾″	17°29′18⅞″
Right	5	928°12′39¾″	+1″	928°12′40¾″	893°14′8″	−2″	893°14′6″	34°58′34¾″	17°29′17⅜″
Right	6	927°58′43¼″	+1″	927°58′44¼″	893°0′8½″	−2″	893°0′6½″	34°58′37¼″	17°29′18⅛″
Average value of θ for Mo $K\alpha_1$ on (310) planes of quartz 17°29′18.2″±0.3″.									
W$K\alpha_1$ line									
Right	1	95°48′5.6″	+5″	95°48′10.6″	85°38′35.3″	−3.5″	85°38′31.8″	10°9′38 8″	5°4′49.4″
Right	2	95°45′35.0″	+5″	95°45′40″	85°36′5.5″	−3.5″	85°36′2″	10°9′38.0″	5°4′49.0″
Right	3	95°25′4.6″	+5″	95°25′9.6″	85°15′36.6″	−4.1″	85°15′32.5″	10°9′37.1″	5°4′48.6″
Right	4	915°13′4.0″	+2″	915°13′6.0″	905°3′37.8″	−9.4″	905°3′28.4″	10°9′37.6″	5°4′48.8″
Right	5	915°13′4.8″	+2″	915°13′6.8″	905°3′38.4″	−9.4″	905°3′29.0″	10°9′37.8″	5°4′48.9″
Left	6	905°3′36.6″	−9.4″	905°3′27.2″	915°13′1.3″	+2″	915°13′3.3″	10°9′36.1″	5°4′48.1″
Left	7	905°3′34.6″	−9.4″	905°3′25.2″	915°13′2.6″	+2″	915°13′4.6″	10°9′39.4″	5°4′49.7″
Left	8	85°3′29.6″	−4.6″	85°3′25.0″	95°12′58.6″	+5.4″	95°13′4″	10°9′39.0″	5°4′49.5″
Left	9	85°3′30.3″	−4.6″	85°3′25.7″	95°12′59.0″	+5.4″	95°13′4.4″	10°9′38.7″	5°4′49.3″
Average value of θ for W$K\alpha_1$ on (310) planes of quartz 5°4′49.0″±0.2″.									

[3] H. C. Hudson and H. G. Vogt, Proc. Nat. Acad. Sci. 19, 444 (1933); E. Ingelstam, (4) No. 5 Nova Acta Reg. Soc. Sci., Upsal. (1936).

[4] J. E. Mack and J. M. Cork, Phys. Rev. 30, 741 (1927); I. Manescu, Comptes Rendus 216, 732 (1943).

[5] This lead filter can be shown to produce a change in absorption with wave-length in going across the profile of a line (say 0.2 x.u.) which results in a difference of less than 1 percent in the observed intensity on the two extreme sides, and the shift in line position will hence be negligible from this cause.

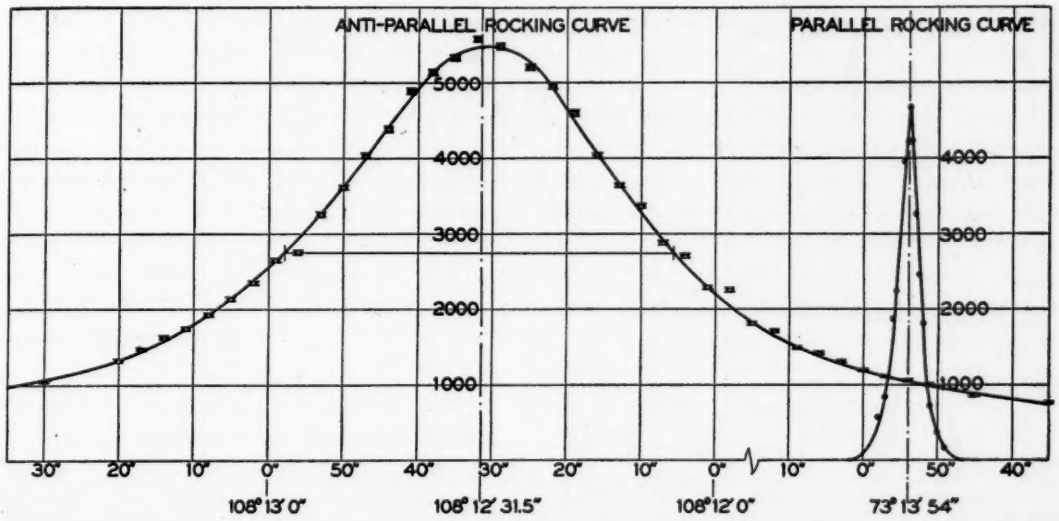

FIG. 2. Typical 2-crystal spectrometer rocking curve of molybdenum $K\alpha_1$ line (run No. 1) reflected from (310) planes of quartz in first-order, parallel, and antiparallel positions. The ordinate numbers on the parallel and antiparallel rocking curves give the number of counts in two minutes. The vertical heights of the rectangular dots on the antiparallel curve are indicative of the statistical uncertainty of counting (square root of total counts). On the parallel rocking curve the statistical uncertainty is not thus known.

mination of the K edge the lead absorber was replaced by tungsten foil 0.0034 inch thick. The multicellular counter consisted of four sections with partitions (cathodes) of 100-mesh monel metal gauze plated with a layer of silver about 0.001 inch thick.

In addition to the 2-meter curved crystal spectrometer, a precision 2-crystal spectrometer[6] with specially lapped and calibrated worm wheels was used by W. J. West to determine with high absolute precision the Bragg angles of reflection for both the tungsten and molybdenum $K\alpha_1$ lines. Two optically flat 1-mm thick plates of quartz (in all respects identical to, and cut from, the same crystal specimen as the lamina used in the 2-meter curved crystal spectrometer) were mounted on the 2-crystal spectrometer, one over each pivot, so that the (310) reflecting planes of the quartz (normal to the surfaces of the lamina) were accurately parallel to the axis of each pivot (as shown by photographic tests of reflections from both sides of these planes with films placed some 2 meters distant from the crystals). Great care was taken to mount the quartz plates without subjecting them to mechanical strain which might bend them. The reflections were studied with the beam *transmitted through* the plates. A Geiger-Müller counter filled with 10 cm of xenon and a small amount (about 0.3 cm) of petroleum ether was used and found very satisfactory for the intensity measurements. Crystal No. 1 was left stationary in the appropriate position to reflect the $K\alpha_1$, α_2 lines, the geometry of lead stops and x-ray tube being such as to select these lines alone. Crystal No. 2 was rotated so that rocking curves both in the (1,1) and (1,−1) or "antiparallel" and "parallel" positions were observed, the antiparallel curves being the profiles of the $K\alpha_1$ line, and the angular displacement between the (1,1) and (1,−1) settings then gave the precision data from which the Bragg angle could be computed. The primary purpose of this 2-crystal spectrometer work was to establish with high precision the ratio of the wave-lengths of the tungsten $K\alpha_1$ line to that of the Mo $K\alpha_1$ line. This last has been determined with such care that it may well be regarded as the standard for the entire Siegbahn scale of wave-lengths.

PRECISION STANDARDIZATION OF TUNGSTEN $K\alpha_1$ WITH THE 2-CRYSTAL SPECTROMETER

Six complete and independent sets of measurements of the Bragg angle for Mo $K\alpha_1$, and nine

[6] For a complete description of this instrument, together with the methods of correcting the worm wheels and calibrating their residual errors, see Jesse W. M. DuMond, Rev. Sci. Inst. 8, 112 (1937).

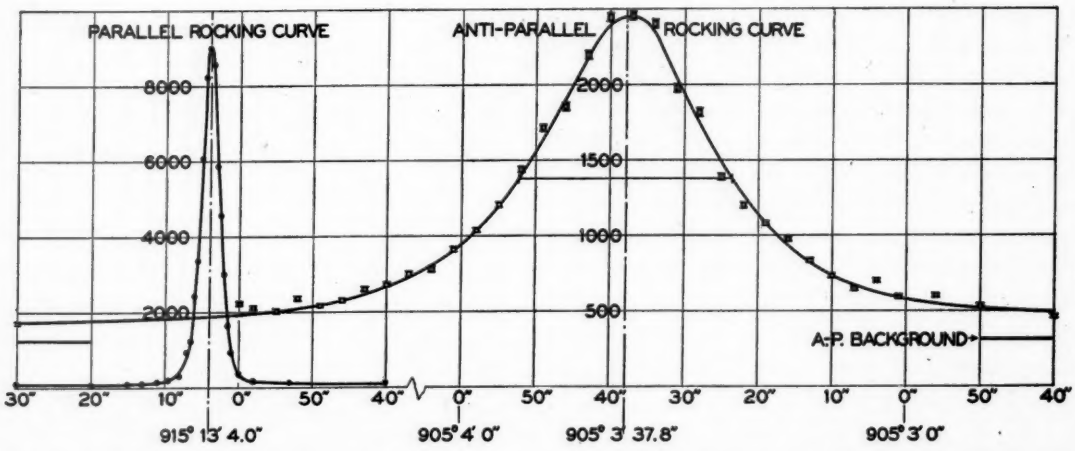

FIG. 3. Typical 2-crystal spectrometer rocking curve of tungsten $K\alpha_1$ line (run No. 4) reflected from (310) planes of quartz in first-order, parallel, and antiparallel positions. The ordinate numbers on the parallel rocking curve give the number of counts in 2 minutes, those on the antiparallel curve the number in 5 minutes. The vertical heights of the rectangular dots on the antiparallel curve are indicative of the statistical uncertainty of counting (square root of total counts). On the parallel rocking curve the statistical uncertainty is not thus shown.

similar measurements for $WK\alpha_1$, were made in such a way as to utilize different parts of the calibrated precision worm wheels for the angle measurements. Each Bragg angle measurement consisted in the complete delineation of a parallel and an antiparallel position rocking curve. Figure 1 shows schematically the geometry of the parallel and antiparallel settings. In some of the measurements the beam was deviated to the left by crystal No. 1, and in others to the right. The number and variety of the worm wheel settings was also increased by turning crystal No. 2

TABLE II. Tungsten K spectrum measured with 2-meter curved crystal spectrometer.

	Siegbahn notation	α_2	α_1	β_3	β_1	β_2^{II}	β_2^{I}	
	Sommerfeld notation	α_2	α_1	β_2	β_1	γ_2	γ_1	δ
	Transition	K–L_{II}	K–L_{III}	K–M_{II}	K–M_{III}	K–N_{II}	K–N_{III}	K–$O_{II,III}$
1	Run 1	213.451	208.639	184.824	184.020			
2	Run 2	213.425	208.611	184.811	184.002	179.242	179.068	178.081
3	Run 3		208.619		184.006			
4	Average x.u. nominal screw scale	213.438	208.623	184.818	184.009	179.242	179.068	178.081
5	Average x.u. assuming West's value α_1	213.387 ±0.010	208.575 ±0.008*	184.772 ±0.020	183.967 ±0.020	179.212 ±0.020	179.038 ±0.020	178.052 ±0.020
	Other determinations for comparison:							
6	E. Ingelstam[a]	213.382	208.571	184.795	183.991	179.232	179.049	178.073
7	Hudson and Vogt[a]	213.38	208.57	184.73	183.93	179.13	178.95	177.99
8	J. H. Williams[b]	213.37	208.56	184.75	183.97	179.06		
9	Duane and Stenström[c]	213.48	208.67	184.26		179.07		
10	Siegbahn[d]	213.52	208.85	184.36		179.40		
11	Stephenson and Cork[e]	213.45	208.62	184.22		178.98		
12	Rechou[f]	213.41	208.50	184.16		179.00		

* This value with its probable error is from the 2-crystal spectrometer work of W. J. West.
[a] See reference 3.
[b] See reference 7.
[c] See reference 13.
[d] M. Siegbahn, Physik. Zeits. 20, 533 (1919).
[e] B. R. Stephenson and J. M. Cork, Phys. Rev. 27, 138 (1926).
[f] G. Rechou, Comptes Rendus 180, 1107 (1925).

Note.—Line 4 in the above table gives wave-lengths in instrumental screw divisions *averaged by columns*. These values were not used, however, in computing line 5. The values in line 5 (which we regard as our final best results) were computed in the following way. The wave-length value of α_1 in line 4 in nominal screw divisions was compared with W. J. West's absolute determination of this wave-length so as to yield the instrumental scale factor, 1.00023 screw divisions per x.u. Wave-length *differences for each run* between all lines and the $WK\alpha_1$ line *of that run* were then determined in nominal scale units. The mean values of these differences for the different runs in which they occurred were then converted to x.u. using the above scale factor. These differences were then combined by adding or subtracting them from West's value of α_1 to give the other values in line 5.

We believe that small mechanical hysteresis effects in the screw, carriage, and upper arm of the spectrometer, which probably account for the residual irreproducibility in the readings, exert, by-this procedure, a minimum effect on the results.

through 180° for some of the Bragg angle determinations so that in such cases the entry and exit sides of the quartz plate were interchanged. This 2-crystal instrument[6] is provided with four independent motions of rotation actuated by worm wheel drives which permit (a and b) precision settings of the 2-crystal tables to about $\frac{1}{4}$ second of arc, (c) angular setting of the instrument as a whole about an axis coincident with that of crystal No. 1 relative to the primary x-ray beam, and (d) angular setting of the arm supporting the ion chamber or counter about an axis coincident with crystal No. 2. This extreme flexibility greatly facilitates the determinations here described since, for any desired configuration, the correct angular position for all the elements of the instrument can be approximately calculated and set up on the four worm wheels as soon as the settings for one particular configuration have been accurately established.

The very small grating content of the quartz (310) planes (only slightly more than one-third as great as that for the cleavage planes of calcite, for example) is of considerable value in increasing the precision of the work since the angles measured are for this reason much larger relative to the precision of the worm wheels. Table I lists the results of the separate measurements of the Bragg angles. The corrections made for the residual errors of the worm wheels are shown. The final result of these measurements gives for the wave-length of the tungsten $K\alpha_1$ line in x-units (on the Siegbahn scale for which the $K\alpha_1$ line of molybdenum has the wave-length value 707.831 x.u.)

$$\lambda W K\alpha_1 = 208.575 \pm 0.008 \text{ x.u.}$$

This result agrees satisfactorily with a determination by Ingelstam,[3] who found $\lambda W K\alpha_1 = 208.571$ x.u., and it compares favorably also with measurements by J. H. Williams[7]—208.56 x.u.

THE GRATING CONSTANT FOR THE QUARTZ (310) PLANES

It can be shown that no correction for refractive index is needed for the case of a beam

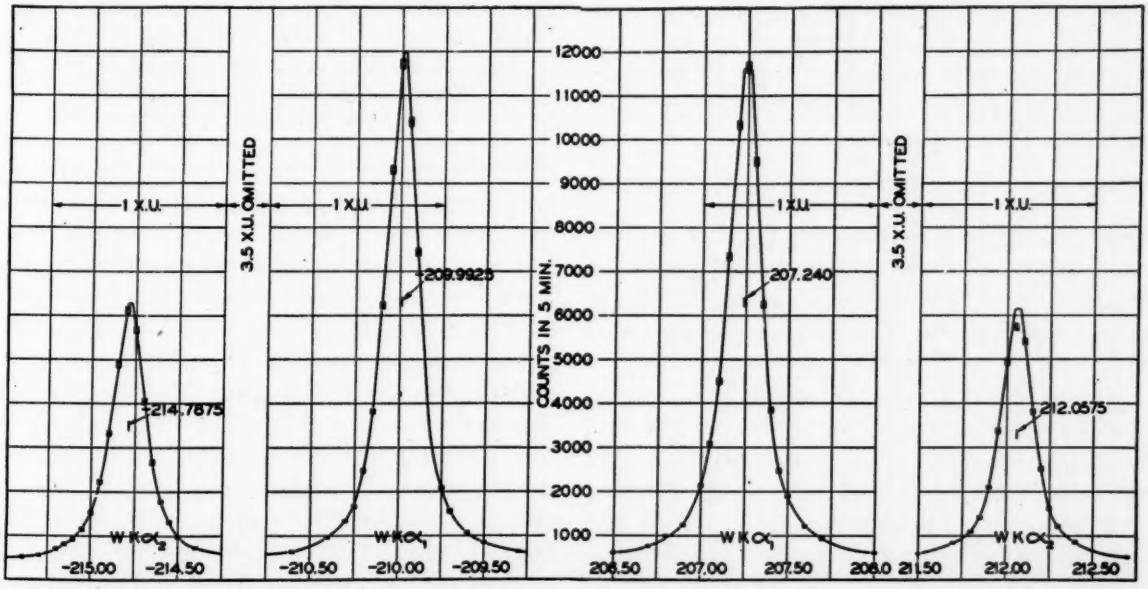

FIG. 4. Tungsten $K\alpha$ lines obtained by reflection from opposite sides of the (310) planes of quartz with the 2-meter focusing curved crystal spectrometer. The effective "window curve" of the spectrometer is narrow—of the order of 0.1 x.u.—resulting in line widths only slightly greater than the natural line widths. The vertical heights of the small rectangles are indicative of the statistical uncertainty of counting—square root of the number of counts. The abscissa scale readings are in nominal x-units as read on the wave-length drum of the spectrometer. The "zero" of these readings is not exactly centered on the zero wave-length position, and the true wave-lengths are to be obtained by taking half the difference between the right and left-hand positions. A multiplying factor differing slightly from unity must also be applied to these figures to convert nominal drum x.u. to true x.u. The wave-length scale is broken between the α_1 and α_2 lines which would otherwise be separated more than three times as far as here shown.

[7] J. H. Williams, Phys. Rev. 40, 791 (1932).

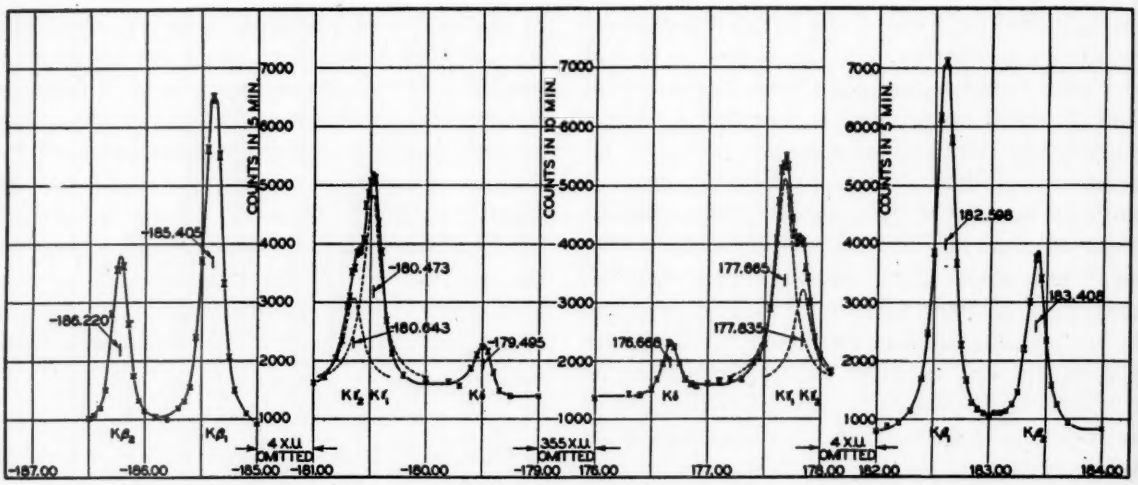

FIG. 5. Tungsten $K\beta_1$, γ- and δ-lines obtained by reflection from opposite sides of the (310) planes of quartz with the 2-meter focusing curved crystal spectrometer. The general remarks in the caption of Fig. 4 apply here also.

of x-rays transmitted through a plate with reflection from internal planes if these latter lie normal to the entry and exit faces.[8] The observations were made at a temperature of 22°C. They indicate for this temperature a grating constant for the (310) planes of quartz, $d_{22°}=1177.705$ x.u. Reducing this to the usually accepted standard value of 18°C by applying the thermal expansion coefficient[9] of 14.5×10^{-6} per degree C for expansion normal to the optic axis, we obtain for the (310) planes

$$d_{18°}=1177.637\pm0.02 \text{ x.u. (Siegbahn scale).}$$

This result agrees well with a value of 1177.64 x.u. calculated from measurements made by Bergquist[10] on the (100) or prism planes of quartz, and it is also in agreement with the value 1177.6 given by E. Ingelstam.[11]

Figures 2 and 3 show two sets of the 2-crystal spectrometer rocking curves in (1,1) and (1,−1) positions typical, of those from which the data of Table I were obtained, Fig. 2 being taken from the runs with molybdenum radiation and Fig. 3 from the runs with tungsten radiation. The extreme narrowness of the parallel position rocking curves for these quartz planes (about 2.8 seconds of arc full width at half-maximum height in the case of tungsten) is remarkable.[12] The breadths of the lines in the antiparallel case are so much greater than the parallel position rocking curves that they may be regarded as virtually perfect delinations of the spectral line profiles for W$K\alpha_1$ and Mo $K\alpha_1$.

CALIBRATION OF THE 2-METER CURVED CRYSTAL SPECTROMETER AND RESULTING WAVE-LENGTH MEASUREMENTS OF THE TUNGSTEN *K* SPECTRUM

Measurements on the diffracted x-ray beams were made on both sides of the (310) planes of the curved quartz crystal.

The curved crystal gamma-ray spectrometer is so designed[1] that the wave-length of the diffracted radiation entering the detector may be determined directly from the reading of a drum and vernier attached to a precision screw which drives the source holder along the focal circle. The geometry of the mechanism is such that the displacement of this screw is directly proportional to the *sine of the Bragg angle* of the diffracted radiation entering the detector and hence to its wave-length. Thus, the difference between the reading on the scale when the spectrometer is set to detect a given wave-length after reflection from one side of the crystal planes and that for reflection from the opposite side of these planes gives twice the wave-length of the radia-

[8] See, for example, Jesse DuMond, Rev. Sci. Inst. **18**, 629 (1947), Fig. 4 and accompanying text.
[9] Determined by A. H. Jay, Proc. Roy. Soc. **142**, 237 (1933).
[10] O. Bergquist, Zeits. f. Physik **66**, 496 (1930).
[11] E. Ingelstam, Arkiv. f. Mat., Astr. o. Fys. **27B**, No. 4 (1939).
[12] Work is now in progress to determine reflection coefficients of these 310 planes, using the set-up here described.

tion. The dimensions of the spectrometer were so chosen that one turn of the screw is almost exactly equal to one x.u. By means of the vernier, readings of wave-length to 0.001 x.u. may easily be made. The screw of the spectrometer has been calibrated for deviations from linearity over the entire range from +300 x.u. to −300 x.u. by comparison with a National Bureau of Standards calibrated glass scale using a 100-power microscope and working to 0.001 x.u. The chief departures from linearity are (a) a quasi-periodic error (with one rotation of the screw as the fundamental period) whose profile changes slowly as one progresses along the screw and (b) an aperiodic error. It may be said, in general, that the deviation from linearity from both these errors nowhere exceeds 0.020 x.u. over the range +300 x.u. to −300 x.u. By using the calibration curve to make corrections, it is estimated that readings are probably correct to within 0.020 x.u.

The precise calibration of the scale of the instrument was made by observing the displacement of the screw between the two settings for the W$K\alpha_1$ line. An average of three such determinations yielded a wave-length in scale divisions of 208.623±0.008. If the wave-length of the W$K\alpha_1$ line is taken as 208.575 x.u. (W. J. West's 2-crystal spectrometer value), the scale factor for the spectrometer becomes 1.00023 divisions per x.u. Using this value, the wave-lengths of the other K series lines and that of the K edge may be determined. The results obtained in this way are shown in Table II. For comparison, the values obtained by other observers are indicated. The measurements of Hudson and Vogt were relative measurements based on the assumption of the α_1 and α_2 wave-length values obtained by Duane and Stenström.[13] For the purpose of this comparison they have been restated, assuming the validity of the results obtained by W. J. West for the W-$K\alpha_1$ wave-length. All values shown in the table are in x.u. (Siegbahn scale) based on the convention that the effective grating space in the first order for calcite at 18°C is 3029.04 x.u. Figures 4 and 5 show graphically the results of one complete run over the tungsten K spectrum on the two sides of the atomic reflecting planes. The vertical strokes at each observed point are indicative of the statistical uncertainty (the square root of the total number of counts observed). Large gaps are necessarily left in the wave-length scale between lines to permit reproducing the plot in reasonable compass.

[13] W. Duane and W. Stenström, Proc. Nat. Acad. Sci. 6, 477 (1920).

DOUBLET SEPARATIONS

The 4.812±0.007-x.u. separation between the components of the α-doublet is in good agreement with that obtained by Ingelstam by Williams and by Duane and Stenström, and it is to be expected from the energy difference between the L_{II} and L_{III} levels.

The separation of 0.805±0.001 x.u. between the components of the β-doublet agrees well with that obtained by Seemann,[14] and it is also in good agreement with the measurements of Hudson and Vogt, and of Ingelstam. It differs from the 0.78 x.u. separation reported by Williams, whose measurements may be in error because of a failure completely to resolve the doublet. The wave-length separation of this doublet computed from the more accuately

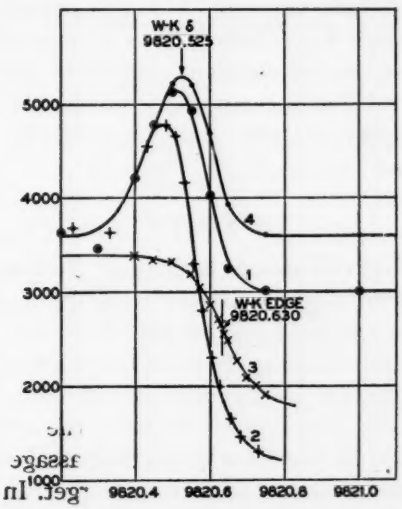

FIG. 6. Separation of W−K edge and W−K δ-line, using metallic tungsten foil absorber 0.0034 inch thick. Curve 1 is the spectrum without any external absorber. The effect of the K absorption edge of the tungsten *in the target itself* can be clearly seen superposed on the δ-line. Curve 2 is the spectrum with the absorbing foil in the beam *normalized to coincide with curve 1 on the left-hand or soft side.* Curve 3 plots the ratio of 2 to 1. The wave-length position assigned as the "edge" has been chosen as nearly as possible at the point of inflection of 3. Curve 4 is corrected to remove target absorption, using curve 3 for this purpose.

[14] H. Seemann, Zeits. f. Physik 73, 87 (1931).

TABLE III.

Siegbahn notation	α_2	α_1	β_2	β_1	β_3^{II}	β_3^{I}		Abs. edge.
Sommerfeld notation	α_2	α_1	β_2	β_1	γ_2	γ_1	δ	Abs. edge.
Transition	$K-L_{II}$	$K-L_{III}$	$K-M_{II}$	$K-M_{III}$	$K-N_{II}$	$K-N_{III}$	$K-O_{II,III}$	$K-\infty$
Wave-length x.u. (Siegbahn scale)	213.387 ±0.010	208.575 ±0.008	184.772 ±0.020	183.967 ±0.020	179.212 ±0.020	179.038 ±0.020	178.052 ±0.020	177.947 ±0.020
Wave-length A	0.213818 ±0.000010	0.208996 ±0.000008	0.185145 ±0.000020	0.184339 ±0.000020	0.179574 ±0.000020	0.179400 ±0.000020	0.178412 ±0.000020	0.178306 ±0.000020

measured L_I-M_{II} and L_I-M_{III} transitions is 0.807 x.u.

The partial resolution of the $K\gamma$-doublet is apparent in Fig. 5. E. Richard Cohen has obtained the two components shown in the figure which give a composite curve closely fitting the experimental curve except for a slight deviation at the wings. The best fit was obtained for components which differ in wave-length by 0.17 x.u. and which have an intensity ratio of 2 to 0.94. The small departure from the expected 2 to 1 ratio may be due to slightly greater absorption of the longer wave-length component in the target, lead filter, and counter window. Our value for the doublet separation is in good agreement with the value of 0.18 x.u. reported by Hudson and Vogt and 0.183 x.u. reported by Ingelstam, and in excellent agreement with the value of 0.171 x.u. computed from the measured wave-lengths of the L_I-N_{II} and L_I-N_{III} transitions.

K EDGE

The effect of passage through the K absorption edge of tungsten is apparent from the distorted profile of the $K\delta$-line and the obviously lower background value on the short wave-length side. Since there was no tungsten in the x-ray beam after its emergence from the tube, the observed effect must be associated with the passage of the beam through a thin layer of the target. In order to correct the line profile for the purpose of determining the wave-length value at its center and to determine the position of the absorption edge, a 0.0034-inch thick tungsten foil was placed in the beam, and readings of the intensity were made both with and without this additional tungsten. The ratio of the intensity measured with the tungsten foil in the beam to that without the foil was plotted against wave-length, and the point of steepest slope of the curve was taken as the position of the edge. Figure 6 illustrates how this was done. In this way the edge was found to be 0.105 x.u. from the center of the δ-line, giving the wave-length associated with the tungsten K absorption discontinuity as 177.947 x.u. This value differs by 0.27 x.u. from the value of 178.22 obtained by Mack and Cork,[4] and by 0.063 x.u. from the value 178.01 of Manescu.[4]

CONCLUSIONS

The curved crystal spectrometer employed in this work is easily capable of giving wave-length separations to within 0.01 x.u. Since the wave-length of the $WK\alpha_1$ line as measured by W. J. West is of comparable precision, we may tabulate (Table III) values of the tungsten K series lines good to 0.02 x.u. or better. The values are also given in angström units, following the recent recommendation of the X-Ray Analysis Group of the Institute of Physics (England) that $\lambda(A)=1.00202\lambda(kx.u.)$. This factor differs only slightly from that given by DuMond and Cohen[15] based chiefly on the work of J. A. Bearden for converting wave-lengths in x.u. to grating wave-lengths.

[15] J. W. M. DuMond and E. R. Cohen, Rev. Mod. Phys. 20, 82 (1948).

Beta-Decay of Be^{10} and Theory of Beta-Decay

R. E. MARSHAK
University of Rochester, Rochester, New York

(Received November 24, 1948)

If a spin change of three units is involved in the $Be^{10}\rightarrow B^{10}$ transition—as seems to be indicated at present—theoretical predictions of the minimum half-life lead to an essentially unique beta-ray spectrum very different from the allowed shape. Measurement of this spectrum will provide a crucial test of existing theories of beta-decay.

THE nucleus Be^{10} decays to B^{10} with the emission of electrons having a maximum energy of 570 ± 10 kev and with a half-life of $2.7\pm0.4\cdot10^6$ years; no γ-ray is observed.[1] On the other hand, C^{10} decays to B^{10} with the emission of positrons having a maximum energy of 2.2 Mev and with a half-life of 19.1 sec.; in this case a γ-ray is observed.[2] Recently, the spin of B^{10} was measured[3] and found to be 3. Finally, it is almost certain[4] that both Be^{10} and C^{10} possess spin 0. It would thus appear that the great difference in half-life between Be^{10} and C^{10} can now be understood: the long half-life of Be^{10} is due to a spin change of three units associated with a transition to the ground state[5] of B^{10}, whereas the short half-life of C^{10} is made possible by the transition of C^{10} to an excited level of B^{10} (which may be assigned spin 0 or 1, depending on whether the Fermi or Gamow-Teller selection rules are presumed to hold). However, a correct theory of beta-decay must explain not only the half-life but also the energy spectrum of the beta-rays. A closer examination of the Be^{10} situation reveals that a reasonably accurate measurement of the beta-ray spectrum from Be^{10} will provide a crucial test of all existing theories of beta-decay—provided that the spin of Be^{10} is really 0.

We have calculated the energy spectra corresponding to a spin change of 3 for the $Be^{10}\rightarrow B^{10}$ transition on the basis of the five possible interactions. Since current nuclear theory does not account for the measured spin of B^{10}, we shall also disregard its parity predictions. Calculations have therefore been performed on both suppositions, assuming that the parities of the ground states of Be^{10} and B^{10} are the same and that they are different. A beta-transition with a spin change of 3 and no parity change requires at least a second forbidden tensor or axial vector transition or a third forbidden pseudoscalar transition. Parity change requires at least a third forbidden scalar, axial vector, tensor, or vector transition. Using a notation similar to that of a previous paper,[6] we write:

no parity change,

$$C_{3T}=D_2|Q_3(\beta\sigma,r)|^2;\quad C_{3A}=D_2|Q_3(\sigma,r)|^2;$$
$$C_{3P}=D_1'|Q_3(\beta\gamma_5 r,r)|^2.$$

Parity change,

$$C_{3S}=D_1'|Q_3(\beta r,r)|^2;\quad C_{3A}=D_4|Q_3(\sigma\times r,r)|^2;$$
$$C_{3T}=D_1|Q_3(\beta\sigma\times r,r)|^2+D_2|Q_3(\beta\alpha,r)|^2$$
$$-D_3[Q_3(\beta\sigma\times r,r)Q_3^*(\beta\alpha,r)+\text{cc}];$$
$$C_{3V}=D_1''|Q_3(r,r)|^2+D_2|Q_3(\alpha,r)|^2$$
$$+iD_3[Q_3(\alpha,r)Q_3^*(r,r)-\text{cc}].$$

Figure 1 gives the results, taking $W_0=2.118$ (in units of mc^2) as the upper limit of the spectrum. We have not plotted D_1' and D_1'' since they do not differ from D_4 and D_1, respectively, by more than 17 percent over the entire range. The first five transitions yield unique energy spectra, whereas the last two yield arbitrary linear combinations of three different types of spectra, since the values of the matrix elements are unknown.

[1] D. J. Hughes and C. Eggler, Phys. Rev. **74**, 1239 (1948); also private communication from Dr. Hughes.
[2] R. Sherr, H. R. Muether, and M. G. White, Phys. Rev. **74**, 1239 (1948); also private communication from Dr. White.
[3] W. Gordy, H. Ring, and A. B. Burg, Phys. Rev. **74**, 1191 (1948).
[4] All measured spins of even-even nuclei have been found to be 0, including the homologous radioactive nucleus C^{14}; we assume spin 0 for Be^{10} and C^{10} for the purposes of our discussion.
[5] M. Goldhaber, Phys. Rev. **74**, 1194 (1948).
[6] R. E. Marshak, Phys. Rev. **70**, 980 (1946); see also E. Greuling, Phys. Rev. **61**, 568 (1942).

TABLE I. Values of L_i.

L_1	L_1'	L_1''	L_2	L_3	L_4
0.070	0.046	0.074	0.052	0.058	0.042

Thus far, we have not eliminated any of the interactions by comparing the minimum theoretical half-life with the observed half-life. If we write $\tau_i=\tau_0/|Q_3|^2L_i$, where

$$L_i=\int_1^{W_0} D_iW(W^2-1)^{\frac{1}{2}}(W_0-W)^2dW,$$

we shall obtain the minimum value of τ_i by choosing the maximum value of $|Q_3|^2$. The values of the six L_i's are listed in Table I. It is seen that the variation in L is less than a factor 2, so that the differences in half-lives will arise chiefly from the variation of $|Q_3|^2$ (see Table II below). The maximum value of $|Q_3|^2$ is arrived at by setting the square of the matrix element equal to the isotopic number of Be^{10} (i.e., 2) and by inserting the proper statistical weight of the ground state of B^{10} (i.e., 7). Table II lists the maximum value[7] of the distinct $|Q_3|^2$. In Table II, ρ is the radius of Be^{10} (in units of $\hbar/mc$), namely, $8.6\cdot10^{-3}$, while α^2 is the square of the matrix element of the Dirac α-operator taken between the ground states of Be^{10} and B^{10}. We

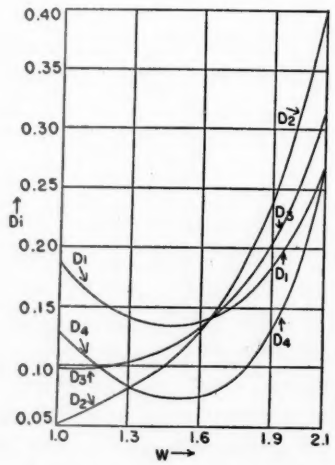

FIG. 1. Values of D_i as a function of energy. The upper limit of the spectrum W_0 is taken as 2.118 in units of mc^2.

[7] E. Greuling, see reference 6; see also R. E. Marshak, Phys. Rev. 61, 431 (1942).

TABLE II. Maximum values of the distinct $|Q_3|^2$.

$\lvert Q_3(\sigma,r)\rvert^2$	$\lvert Q_3(\beta\gamma\sigma,r)\rvert^2$	$\lvert Q_3(r,r)\rvert^2$	$\lvert Q_3(\sigma\times r,r)\rvert^2$	$\lvert Q_3(\alpha,r)\rvert^2$
$\frac{28}{15}\rho^4$	$\frac{4}{5}\alpha^2\rho^6$	$\frac{4}{5}\rho^6$	$\frac{16}{15}\rho^6$	$\frac{28}{15}\alpha^2\rho^4$

have not distinguished between matrix elements involving the Dirac β-operator since we may set $\beta=1$ in the non-relativistic approximation for the nucleons. Moreover, we have not included values for the cross-terms in C_{3T} and C_{3A} since we may use the geometric means of the other two terms in each interaction.

The value of τ_0 depends on the radioactive nucleus chosen as the norm. In principle, τ_0 should be taken from the decay of the neutron. However, since the measured half-life of the neutron[8] is quite unreliable at the present time, the comparison nucleus most suitable for our purposes is He^6. The maximum energy of the electron associated with the $He^6\rightarrow Li^6$ transition is 3.7 ± 0.2 Mev, and the half-life is 0.82 ± 0.06 sec.; there is no evidence for a γ-ray.[9] If the decay of He^6 is to the ground state of Li^6, the Gamow-Teller selection rules apply, and τ_0 becomes $5.8\cdot10^3$ sec.[10] If the decay of He^6 is to a very low excited level (less than 100 kev[9]) of Li^6 possessing spin 0, so that the Fermi selection rules apply, τ_0 is three times smaller, namely, $1.9\cdot10^3$ sec., for the scalar and vector interactions, and $1.9\cdot10^4$ for the pseudoscalar interaction (setting $\alpha^2=1/10$). Table III lists the minimum half-lives for the five transitions which

[8] A very preliminary value for the half-life of the neutron is about 30 minutes (A. H. Snell and L. C. Miller, Phys. Rev. 74, 1217 (1948)). If this value is adopted, τ_0 becomes $2.4\cdot10^3$ sec. for the scalar, axial vector, tensor, and vector interactions, and $1.5\cdot10^4$ times smaller for the pseudoscalar interaction (see J. Tiomno and J. A. Wheeler, forthcoming publication). The value of τ_0 obtained for the S, A, T, and V interactions is essentially identical with that obtained from the He^6 decay. The value obtained for the P interaction is very different and is a consequence of the extremely small (and known) value of the Dirac α-operator found in the neutron decay as contrasted with the large value (for lack of specific information) used for the He^6 decay (see footnote 11 below).

[9] W. J. Knox, Phys. Rev. 74, 1192 (1948).

[10] This value is obtained by choosing the maximum value for the square of the matrix element, i.e., 2. It is conceivable that the ground state wave functions of He^6 and Li^6 are much more orthogonal to each other than those for Be^{10} and B^{10}, making τ_0 several orders of magnitude smaller, but very unlikely. Other beta-ray evidence, especially the mirror nuclei, leads to approximately the same value for τ_0. Of course, an accurate determination of the half-life of the neutron will fix τ_0.

TABLE III. Minimum half-lives for the five transitions associated with the single matrix elements.

2T	2A	3A	3P	3S
$3.5\cdot10^5$ yr.	$3.5\cdot10^5$ yr.	$1.0\cdot10^{10}$ yr.	$4.1\cdot10^9$ yr.	$4.1\cdot10^9$ yr.

are associated with single matrix elements, the appropriate τ_0 being used in each case. It is seen from Table III that the minimum half-lives for $3A$, $3P$, and $3S$ are much too long to be reconciled with the observed half-life; these three transitions must therefore be discarded.[11] The minimum half-lives associated with $2T$ and $2A$ *are* consistent with the observed half-life. If we now examine the two remaining transitions, $3T$ and $3V$, which involve two distinct matrix elements apiece, we find that the first matrix element of $3T$ yields a minimum half-life identical with that listed for $3A$, whereas the first matrix element of $3V$ yields a minimum half-life identical with that listed for $3S$. The second matrix element of $3T$ yields a minimum half-life of $3.5\cdot10^6$ yr. (choosing the rather large value of 1/10 for α^2). The second matrix element of $3V$ leads to a minimum half-life three times shorter. Both of these latter half-lives are consistent with the observed half-life if we are willing to stretch the numbers somewhat (for W_0, ρ, etc.). It is clear that the cross-terms in both $3T$ and $3V$ yield minimum half-lives which are much too long.

We may therefore conclude that the observed half-life of Be^{10} requires the rejection of *all* matrix elements[11] except the four ($Q_3(\beta\sigma, r)$, $Q_3(\sigma, r)$, $Q_3(\beta\alpha, r)$, $Q_3(\alpha, r)$) which are associated with the energy spectrum given by D_2. Of these four, three ($2T$, $2A$, $3T$) are Gamow-Teller-type interactions, and one ($3V$) is a Fermi-type interaction. The D_2 spectrum is so different from the allowed spectrum that a careful measurement of the beta-spectrum from Be^{10} should be decisive for present-day theories of beta-decay. If the spectrum turns out to be allowed, as seems to be indicated by a preliminary measurement,[1] it will follow that present theories of beta-decay will have to undergo serious modification.

The author is indebted to Messrs. Albert Simon and Clayton Black for assistance with the numerical calculations.

[11] There is one loophole in this argument: *if* the half-life of the neutron is 30 minutes and *if* α^2 for the $Be^{10}\rightarrow B^{10}$ transition is as much as 1/10, the minimum half-life for the $3P$ transition would turn out to be $2.8\cdot10^6$ yr., consistent with the observed half-life. Other beta-ray evidence does not lend support to the pseudoscalar interaction (E. P. Wigner, private communication). However, even accepting this possibility, the predicted spectrum would be very different from the allowed spectrum (see curve D_4 in Fig. 1), and the measurement of the beta-spectrum from Be^{10} would still provide a crucial test of beta-theory. It is interesting to note that above $W=1.6$, D_4 and D_2 have roughly the same shape.

PHYSICAL REVIEW VOLUME 75, NUMBER 3 FEBRUARY 1, 1949

The Beta-Spectrum of Be^{10}

D. J. HUGHES, C. EGGLER, AND C. M. HUDDLESTON
Argonne National Laboratory, Chicago, Illinois

(Received December 14, 1948)

RECENT investigations have thrown much light on the disintegration of Be^{10}, long an outstanding problem of nuclear structure and beta-theory. The accompanying paper of Marshak reviews the recent evidence and points out that, while the large spin change involved in the disintegration explains the long half-life, it also predicts a surprisingly unique spectrum shape. Because of the resulting importance of the experimental Be^{10} spectrum to beta-theory, it is desirable to report some results already obtained on the spectrum using an absorption method.

Measurements[1] made since the activity was first isolated by McMillan and Ruben[2] in 1940

[1] J. Levinger and E. Meiners, Phys. Rev. 71, 586 (1947); D. J. Hughes, C. Eggler, and C. M. Huddleston, Phys. Rev. 71, 269 (1947); A. K. Pierce and F. W. Brown, III, Phys. Rev. 70, 779 (1946); E. M. McMillan, Phys. Rev. 72, 591 (1947).

[2] E. M. McMillan and S. Ruben, Phys. Rev. 70, 123 (1946).

have fixed the disintegration constants of Be^{10} quite well, even though it has been impossible to prepare sources of high specific activity. A consideration of all the experimental data leads to the following results:

$T_{\frac{1}{2}} = (2.7 \pm 0.4) \times 10^6$ years,
beta-energy $= 570 \pm 10$ kev,
no gamma.

The half-life is based on the values of McMillan and of Hughes, Eggler, and Huddleston which were obtained by independent methods and which agreed closely. The beta-end-point energy is the result of recent work of our own designed to eliminate errors in the absorption method as usually applied. If the maximum range is estimated by locating the intersection of the beta-portion of the absorption curve with the "tail" of the curve (caused by counter background, bremsstrahlung, or hard radiation), it is clear that, because the beta-curve approaches the tail asymptotically, the apparent end point will be less than the true maximum beta-range by an amount depending on the strength of the sample used. In fact, it is quite certain that this method will always result in a serious underestimate, for a simple analysis (similar to that given later—see Eq. (1)) shows that the beta-curve will approach zero as the fourth power of the residual range and hence will be impossible to measure near the maximum range. The Feather method, designed to circumvent the difficulty just described, is unsafe to apply to weak samples because the end point obtained will depend on the shape of the absorption curve which in turn will depend on the spectrum shape. In addition, the method gives end points relative to RaE, which was estimated visually and hence certainly underestimated. In order to obtain the Be^{10} end point with the weak samples available, the absorption curve was extrapolated to the end point by comparison with an accurately determined W^{185} absorption curve near the end point. The end-point energy of W^{185} has been carefully measured by Saxon, and it was possible to obtain samples of extremely high specific activity for its absorption curve. The shape of the W^{185} curve near its end point corresponds closely to the fourth power of the residual range, and a plot of the fourth root of the counting rate against absorber thickness proved to be a simple linear extrapolation to the end point. In order to elimi-

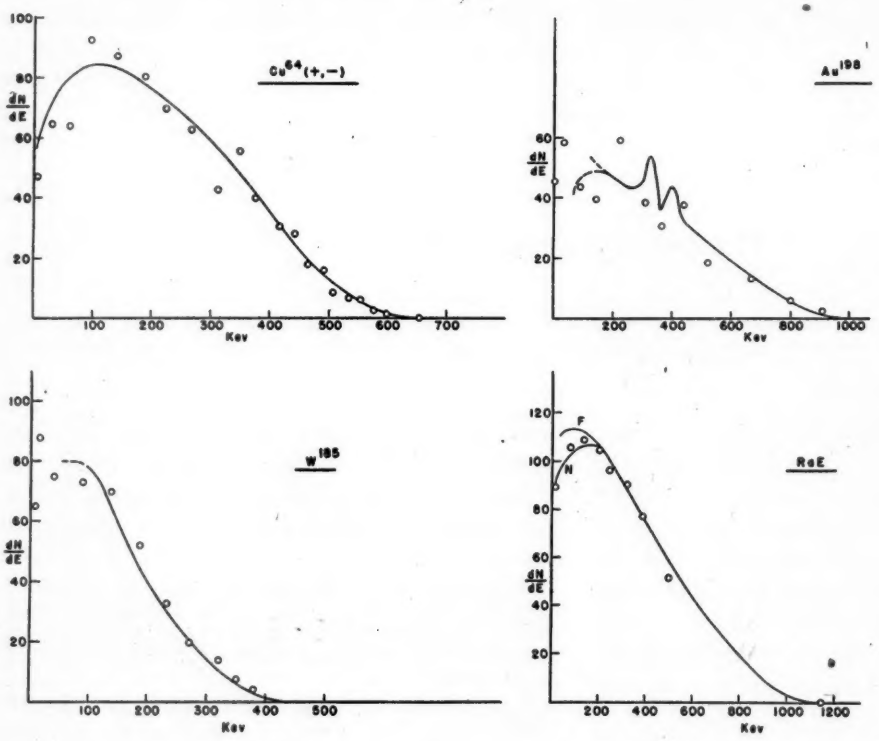

FIG. 1. Comparison of spectrum shapes given by the absorption method with spectrometer results.

nate any error in the usual beta-range-energy curves (which correspond to Feather ranges generally) a small part of the curve was established carefully using the range-energy results for W^{185} and similar data obtained for RaE. Although some of the early measurements had indicated the presence of a gamma in the disintegration of Be^{10}, more detailed work showed that the gamma was caused by impurities. In order to investigate the matter as carefully as possible, we have recently made measurements with various counter fillings, lead radiators, etc., to show the presence of gammas of different energies. The results show that there is much less than one gamma per disintegration for any gamma-energy above about 5 kev.

As it was clear that Be^{10} of high specific activity would not be available for some time, investigations were begun[3] to ascertain whether significant information on the spectrum shape could be obtained with weak samples. The method chosen was a comparison of the shape of the Be^{10} spectrum with the spectra of various "standards" possessing well-known spectrum shapes. The comparison was made both by means of the shape of the beta-absorption curve and of the beta-momentum distribution in a cloud chamber. In effect, the use of well-known comparison spectra serves to eliminate the many corrections that would be necessary if one were to attempt the absolute determination of the spectrum from the absorption curve or from the cloud-chamber momentum distribution. At the present time it is desired to consider only the possibility of the spectrum shapes calculated by Marshak, and for this purpose only the absorption method will be used.

If the law of absorption of initially monoenergetic electrons in a given counter geometry were known, then it would be a simple matter to calculate the beta-spectrum from an accurate absorption curve. As an example of monoenergetic electron absorption, the curve for In^{115} conversion electrons (300 kev) was first measured in the standard counter geometry (foil about $\frac{1}{2}''$ from a mica end-window counter) and was found to be approximately linear. If it is assumed that

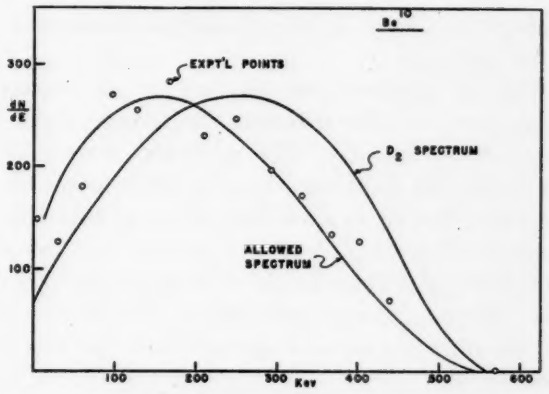

FIG. 2. The experimental Be^{10} spectrum and the calculated allowed and forbidden spectra.

monoenergetic electrons are absorbed in a strictly linear manner, then the beta-spectrum (dN/dE) follows from the absorption curve directly:

$$(dN/dE)=R(d^2I/dR^2)(dR/dE). \qquad (1)$$

Here I is the counting rate at absorber thickness R, and E is the electron energy corresponding to the range R. For values of R near the end point, it follows from Eq. (1) and from the beta-distribution that I will vary as the fourth power of the residual range. A spectrum obtained from an absorption curve by use of Eq. (1) would be expected to show some distortion because of the

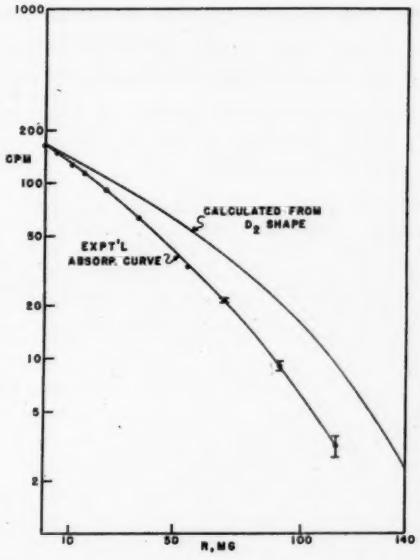

FIG. 3. Initial portions of the experimental absorption curve and the curve to be expected from the D_2 spectrum of Marshak.

[3] Some of the early results were reported at the 1948 Washington meeting of the Physical Society, Phys. Rev. 74, 1239 (1948).

known departure of actual electron absorption from linearity.

Careful absorption curves were run for a series of spectra, and the spectrum shapes were calculated from Eq. (1). The resulting shapes all differed from the known true shapes in the same manner, that is, in each case the most probable energy ("maximum" of the curve) was about 100 kev higher than for the true shape, although the end-point energy was correct. This shift was in the direction to be expected from the linear assumption, for the In^{115} curves had shown a slower than linear initial absorption which results in a depletion of the low energies when Eq. (1) is used. It was decided from these results that a simple method, and one of sufficient accuracy for obtaining an approximate beta-spectrum, would be to obtain a spectrum by use of Eq. (1) then shift the points by 100 kev (the value appropriate for an end point of 600 kev; the "shift" increases slowly with end-point energy). This method was tried for the standard spectra, using Eq. (1) and making the correction for nonlinearity by the simple shift, with the results shown in Fig. 1. The solid curves of Fig. 1 are the known[4] spectrum shapes, and the points are the results of the present analysis. The rather large scatter of the points is caused by the statistical error of the original data, but, within this error, the results of the method seem to compare quite well with the actual spectra.

As the absorption method in the simple form described gave consistent results, it was then applied to Be^{10}. Because of the weakness of the samples available it was difficult to obtain statistical accuracy, but an accurate absorption curve was finally obtained for which many of the points required several days counting apiece. Application of the standard method to the absorption curve then gave the spectrum shown in Fig. 2. On Fig. 2 there also appears the allowed spectrum for Be^{10} and the D_2 spectrum calculated by Marshak (see his paper for details). It seems quite definite that the experimental spectrum given by this method is in disagreement with the D_2 shape, and, in fact, in agreement with the allowed spectrum within experimental error. It is very difficult, of course, to fix the error of the present method quantitatively, and it is only because the D_2 shape is so unusual that a definite conclusion can be reached. As discussed by Marshak, there is a possibility that the D_4 shape could be consistent with the Be^{10} half-life. However, the D_4 does not differ from the allowed shape by a large enough amount so that it can be conclusively ruled out by the present measurements.

At the suggestion of Marshak the absorption curve to be expected from the D_2 shape was calculated by reversing the method. The calculated absorption curve for D_2 is given in Fig. 3 as well as the initial portion of the experimental Be^{10} absorption curve. The curves show again that the difference between D_2 and the allowed shape is much greater than the experimental errors of the absorption curve. We are continuing the cloud-chamber measurement of the spectrum which is in substantial agreement with the absorption work and at the same time are preparing material which will be of sufficient activity to be used in a spectrograph. We wish to express our thanks to D. Sherman and E. Hupke who have helped in some of the exceedingly tedious phases of this work.

[4] The curves are from the following sources: W^{185}, D. Saxon, private communication; Cu^{64}, C. S. Cook and L. M. Langer, Phys. Rev. 73, 601 (1948); Au^{198}, D. Saxon, Phys. Rev. 73, 811 (1948); RaE, Flammersfeld (F) and Neary (N) from data quoted by Konopinski, Rev. Mod. Phys. 15, 229 (1943).

Letters to the Editor

PUBLICATION of brief reports of important discoveries in physics may be secured by addressing them to this department. The closing date for this department is five weeks prior to the date of issue. No proof will be sent to the authors. The Board of Editors does not hold itself responsible for the opinions expressed by the correspondents. Communications should not exceed 600 words in length.

Absorption of Penetrating Shower Primaries*

JOHN TINLOT AND B. GREGORY
Department of Physics and Laboratory for Nuclear Science and Engineering, Massachusetts Institute of Technology, Cambridge, Massachusetts
December 21, 1948

AN experiment was conducted on the top of Mt. Evans, Colorado (altitude 14,200 feet) to determine the absorption in lead and iron of the ionizing radiation producing penetrating showers. Six trays of Geiger-Mueller counters one inch in diameter and ten inches in active length were arranged as shown in Fig. 1. A fast addition circuit (resolving time 1.4 μsec.) was used to detect multiple coincidences of the counters in tray B; the counters in each of the trays A, C, and D were connected in parallel, as were the eight counters in trays E. The horizontally shaded portion of the figure represents the position of absorbing material placed above tray A, whose thickness was varied from zero to about 14 inches in each case. No absorber was placed between trays A and B, which were separated by an air space of four inches; four inches of lead separated trays B and E from trays C and D, and there were at least four inches of lead shielding on all sides of the counter array. Trays C and D were separated from each other by two inches of lead.

The event recorded was a coincidence $ABCD$ with the condition that not more than one counter be discharged in tray B, and no counter discharged in trays E. This event will be referred to by the symbol γ. The graph of Fig. 2 shows the rate (in counts per hour) of this event as a function of iron and lead absorber thickness in g cm^{-2}. It is seen

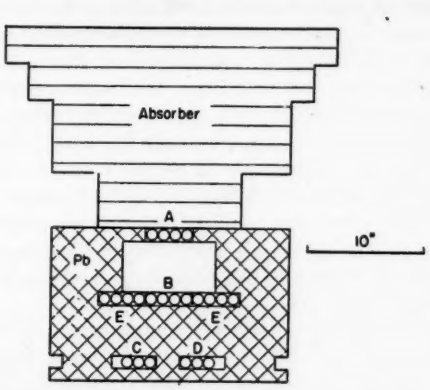

FIG. 1. Penetrating shower detector showing position of absorber.

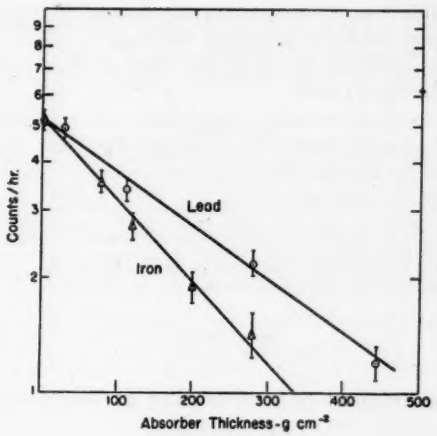

FIG. 2. Rate of occurrence of event γ vs. absorber thickness (see text).

that in both cases the rates vary exponentially with absorber thickness within the experimental errors. The mean free paths corresponding to the straight lines drawn in Fig. 2 are 310 g cm^{-2} for lead, and 200 g cm^{-2} for iron.

The event γ is interpreted as representing a penetrating shower produced by an ionizing particle interacting in the layer of lead between tray B and trays C and D. It will be noted that, as a result of the geometrical arrangement described, the event γ does not include penetrating showers produced above tray A, since it is impossible for such a shower to discharge both trays C and D without discharging two counters in tray B or one in tray B and one in trays E. The same holds true for any air showers sufficiently penetrating to affect trays C and D. It is unlikely that any purely electronic showers generated below tray B can be detected, since trays C and D are separated by two inches of lead; for the same reason, detection of a meson and knock-on electron is very improbable. Accidental coincidences are of negligible importance, since the resolving time for detection of a coincidence $ABCD$ is very small (about 2 μsec.).

In interpreting the experimental results one must consider (1) that the cross section for nuclear interactions may be a function of the energy of the interacting particle (experimental evidence to this effect has been obtained recently[1]) and (2) that the incident particle may interact more than once before losing all of its energy and that its secondaries may produce more nuclear interactions.

If the latter effect occurs frequently, the *absorption mean free path* will be different from the *collision mean free path*.[2] In the present experiment a particle which interacts in the absorber above tray A is likely to discharge a counter in trays E or more than one counter in tray B. When this happens, the event is rejected even if the particle interacts again in the absorber below tray B. Thus one may expect that the quantity measured in the present experiment approaches the collision mean free path. Evidently, however, the above argument breaks down in the case of very large absorber thicknesses.

It should be mentioned that a correction was applied for the effect of atmospheric pressure variation, resulting in

a variable flux of the penetrating shower primaries. The maximum correction necessary was found to be about five percent, assuming the mean free path of the primaries in air to be 120 g cm^{-2}.[3]

We received valuable suggestions and encouragement from Doctor B. Rossi. Operation on Mt. Evans was made possible by the cooperation of the Inter-University High Altitude Laboratory.

* Assisted by the joint program of the ONR and the AEC.

[1] W. Walker, private communication.
[2] B. Rossi, Rev. Mod. Phys. 20, 537 (1948), Section 20.
[3] J. Tinlot, Phys. Rev. 73, 1476 (1948).

Correlation of Penetrating Showers with Air Showers*

JOHN TINLOT AND B. GREGORY
Department of Physics and Laboratory for Nuclear Science and Engineering, Massachusetts Institute of Technology, Cambridge, Massachusetts
December 21, 1948

IN order to investigate the relationship between locally produced penetrating showers and air showers, an experiment was performed on Mt. Evans, Colorado, in conjunction with the one described in the previous letter. Two trays of counters, labeled F and G ("extension trays") were placed at distances of 1.0 m and 2.5 m, respectively, from the axis of the penetrating shower detector. Tray F contained eight counters connected to form four pairs and had a total effective area of 520 cm^2. An addition circuit permitted the detection of multiple coincidences between pairs of counters. Such coincidences will be referred to by the symbol F_α, where $\alpha=1$, 2, 3, or 4, signifying the simultaneous discharge of one or more, two or more, three or more, or all four pairs. Tray G contained four counters connected in parallel and having a total effective area of 260 cm^2.

The following events were recorded: γF_1, γF_2, γF_3, γF_4, and γG, where the symbol γ refers to the event described in the previous letter. The total number of counts for each of these events, and for the event γ, were recorded with different thicknesses of iron and lead absorber placed above the penetrating shower detector; these are reproduced in Table I.

The most striking fact evident from the data of Table I is the great rarity of events γ accompanied by discharges of the extension trays. Of a total of 2084 counts obtained with the two absorbers, there were only 17 cases of γF_1, and 3 cases of γF_2. The rate of γF_1 was three times and the rate of γF_2 twenty times the expected accidental rate, so that these can be considered as real events. The event γG, on the other hand, can be explained as entirely the result of accidental coincidences.

TABLE I. Rate of occurrence of air showers coincident with penetrating showers as defined by the event γ (see text).

Absorbing material	Thickness g cm^{-2}	Total counts γ	γF_1	γF_2	γF_3	γF_4	γG
Lead	0	314	2	1	0	0	0
	115	444	5	0	0	0	1
	445	264	2	1	0	0	0
	1100	85	0	0	0	0	0
	1760	103	1	0	0	0	0
Iron	0	314	2	1	0	0	0
	315	262	3	0	0	0	1
	475	179	1	0	0	0	0
	790	116	0	0	0	0	0
	1105	103	1	0	0	0	0

As described previously, the event γ can be attributed to a penetrating shower produced by a single ionizing particle interacting in the layer of lead between tray B and trays C and D in the detector system. Any group of penetrating particles from the air capable of discharging C and D is rejected.

The few events of the type γF_α that were detected may be explained by assuming that very rarely a particle capable of producing penetrating showers is accompanied by an air shower of small density (since in no case were more than two counters discharged in tray E). These showers could be produced, for instance, by a knock-on process in the air. It is also possible, however, that events γF_α are caused by secondary particles originating in the nuclear interactions and projected through the tray F.

In any case, the important result is that dense air showers do not contain single particles capable of producing penetrating showers. They may, however, contain groups of penetrating particles, some of which may interact to produce nuclear events. This type of air shower would be rejected by the penetrating shower detector, and therefore nothing can be said about this possibility on the basis of this experiment.

The facilities for operation on Mt. Evans were made available by the Inter-University High Altitude Laboratory.

* Assisted by the joint program of the ONR and the AEC.

Excited-State Bands of Atmospheric CO_2

ORREN C. MOHLER, ROBERT R. MCMATH, AND LEO GOLDBERG
McMath-Hulbert Observatory of the University of Michigan, Ann Arbor, Michigan
December 15, 1948

IN a recent note, McMath and Mohler[1] have reported the presence of two new band structures in the telluric spectrum at approximately 2.04μ and 2.08μ. The bands were found on high resolution tracings obtained with the McGregor spectrometer and Cashman PbS cell of the McMath-Hulbert Observatory. The band at 2.04μ has already been identified[2] as the positive branch of the 00_00-12_01 band[3] of the isotope molecule $C^{13}O_2^{16}$. Following suggestions by Professor D. M. Dennison of the University of Michigan and Dr. W. S. Benedict of the National Bureau of Standards, we have made a further study of the 2.08μ band, which indicates with considerable certainty that it is the negative branch of the CO_2 band resulting from the transition 01_10-05_11.

The first few lines at the high frequency end of the 2.08μ band are nearly uniformly spaced, the separations being about one-half those of the band lines originating from the ground state 00_00 of CO_2. In the direction of lower frequen-

cies, the band lines draw together in pairs, forming a series of doublets, in which the splitting decreases rapidly until the components of the doublets merge to form single lines. The 2.08μ band occurs in a relatively clear region of the spectrum on the long wave-length side of the strong 00_00-04_01 band of CO_2. Close inspection reveals the presence of a second doublet band at the high frequency side of the 2.08μ band. The second band, whose components are partially blended with those of the 00_00-04_01 band, is a mirror image of the 2.08μ band; that is to say, the doublet splitting decreases with increasing frequency. The two new bands are quite evidently positive and negative branches of a single band.

The appearance of the 2.08μ band is precisely that which would be expected from a $\Pi-\Pi$-transition in the CO_2 molecule.[4] If the statistical weight factors of symmetric and antisymmetric levels in CO_2 were equal, the rotational structure of a $\Pi-\Pi$-band would appear as a series of doublets in which the splitting increased with increasing J. The splitting is a consequence of the so-called "l-type doubling."[5] Because of the zero nuclear spins of the oxygen atoms, however, transitions are permitted only between symmetric levels. The resulting band is made up of two series of lines, one series involving transitions from lower levels of even J and the other from those of odd J. Because of the l-type doubling, the two series converge at different rates and, consequently, the lines coalesce at large values of J.

In addition to the foregoing qualitative argument, additional experimental and theoretical evidence has been secured to strengthen the identification of the 2.08μ band as a $\Pi-\Pi$-transition in CO_2. First, a laboratory tracing of the CO_2 spectrum in the 2μ region clearly shows the presence of the new band. Second, band centers have been calculated for the triad of transitions from lower state 01_10 to the three upper states 05_11, 13_11, and 21_11, following the theory developed by Adel and Dennison.[6] The center calculated for the 01_10-05_11 band is 4805.6 cm^{-1}, which is in excellent agreement with the observed center, 4807.60 cm^{-1}, of the 2.08μ band. The calculated centers of the 01_10-13_11 and 01_10-21_11 bands, 4970.5 cm^{-1} and 5131.6 cm^{-1}, respectively, fall within and are overlapped by the corresponding ground-state bands 00_00-12_01 and 00_00-20_01. Numerous individual lines of both bands appear to be present on the tracings, however, and they exhibit the expected doublet pattern.

Wave-lengths have been measured for 18 lines in the positive branch and for 29 lines in the negative branch of the 01_10-05_11 band. A weak, unresolved Q branch appears also to be present, although blended with a line of water vapor. Analyses have been carried out for the two separate series of odd and even J. It is interesting that the l-type doubling is large enough to cause the two series to coalesce at about $J=25$ in the positive branch and at $J=31$ in the negative branch. The following rotational constants have been calculated: $B_{010}(\text{odd})=0.38969$, $B_{010}(\text{even})=0.39029$, $B_{051}(\text{odd})=0.38705$, $B_{051}(\text{even})=0.38847$. The constants q of the l-type doubling are therefore $q_{010}=0.00060$ and $q_{051}=0.00142$.

The identification of the $\Pi-\Pi$-bands is of significance in that it represents the first evidence for absorptive transitions from an excited molecular state in the earth's atmosphere.

[1] McMath and Mohler, P.A.S.P. 60, 119 (1948).
[2] Goldberg, Mohler, and McMath, Phys. Rev. 74, 1881 (1948).
[3] This band is one of the triad of bands resulting from transitions between the ground level and the resonating levels 20_01, 12_01, and 04_01. Professor D. M. Dennison has kindly pointed out to us that the existence of the resonance interaction makes it actually improper to designate a level by any one of these symbols. It will be convenient for the present discussion, however, to so designate the levels in question, making the level of highest energy 20_01 and that of the lowest energy 04_01. The same convention will be used in describing the upper stage bands of this type.
[4] G. Herzberg, *Infrared and Raman Spectra* (D. van Nostrand and Company, Inc., New York, 1945), p. 389.
[5] G. Herzberg, Rev. Mod. Phys. 14, 219 (1942).
[6] See David M. Dennison, Rev. Mod. Phys. 12, 175 (1940).

Passage of Finite Amplitude Pressure Waves through Temperature Discontinuities

BRUNO W. AUGENSTEIN
Department of Aeronautics, Purdue University, Lafayette, Indiana
December 15, 1948

THE purposes of the present note are twofold:

(a) To derive the transmission properties of isentropic pressure waves of large amplitude through temperature discontinuities.
(b) To linearize the results for very small amplitude waves, and thereby show that the usual equations of acoustic theory result.

Let us assume two masses of perfect gas, separated by an infinite plane temperature discontinuity normal to the x axis. If we assume the gas to be the same on both sides of the interface, and the ratio of the specific heats, $\gamma=C_P/C_V$, to be the same, then we can characterize the temperature difference by the difference in the speed of sound on the two sides of the interface. Initially, a common pressure P_0 is present on both sides of the interface; a pressure wave moving to the right then impinges normally on the interface. We wish to determine the amplification of this pressure wave after the transmission and reflection of the incident wave have taken place.

We consider that the state changes though the wave fronts are isentropic, though, of course, the two gas masses have initially different entropies; these different entropies do not change with the transmission and reflection of the pressure waves. (See paragraph 7.) The problem then resolves into the solution of two partial differential equations on each side of the interface:

$$[(\gamma-1)/2]a[du/dx]+[da/dt]+u[da/dx]=0, \quad (1)$$

$$[du/dt]+u[du/dx]+[2/(\gamma-1)]a[da/dx]=0. \quad (2)$$

a is the speed of sound; u is the particle velocity. Velocities are positive to the right. These are the equations of continuity and momentum for one-dimensional constant area wave motion. Because of the assumption of isentropic state changes, the energy equation need not be used explicitly. The appropriate boundary conditions at the interface are

TABLE I.

Incident wave (P_1/P_0)	Transmitted wave ($P_1^*/P_0=P_2/P_0$)	Reflected wave (P_2/P_1)
Compression: $P_1/P_0>1$	$a_0^*>a_0$: Weaker compression $a_0^*<a_0$: Stronger compression	Rarefaction Compression
Rarefaction: $P_1/P_0<1$	$a_0^*>a_0$: Weaker rarefaction $a_0^*<a_0$: Stronger rarefaction	Compression Rarefaction

continuity of pressure, and equal particle velocities on both sides of the interface for all time.

We consider the gas masses originally at rest, with pressure P_0, and speeds of sound a_0 in the gas to the left of the interface, a_0^* to the right of the interface. Call the pressure ratio of the incident wave moving to the right P_1/P_0, the particle velocity after it u_1, and the speed of sound after it a_1; the relationships are

$$P_1/P_0=(a_1/a_0)^{2\gamma/(\gamma-1)}=[1+((\gamma-1)/2)(u_1/a_0)]^{2\gamma/(\gamma-1)}. \quad (3)$$

Call the pressure ratio after the reflected wave P_2/P_0, the speed of sound after it a_2, and finally the pressure ratio of the transmitted wave $P_1^*/P_0=P_2/P_0$, and the speed of sound after the transmitted wave a_1^*.

The solution of Eqs. (1) and (2) subject to the boundary conditions mentioned then leads to the following relation between P_1/P_0, the incident pressure ratio, and $P_1^*/P_0=P_2/P_0$, the pressure ratio of the waves resulting from the impingement of the original pressure wave on the interface:

$$\frac{P_2}{P_0}=\left\{\frac{2(P_1/P_0)^{(\gamma-1)/2\gamma}+(a_0^*/a_0)-1}{(a_0^*/a_0)+1}\right\}^{2\gamma/(\gamma-1)}. \quad (4)$$

The use of Eq. (4) gives us Table I. The velocity with which the interface moves after the wave has impinged is given by

$$u_I=\frac{2a_0}{\gamma-1}\cdot\left\{\frac{2(a_0^*/a_0)}{(a_0^*/a_0)+1}\right\}\cdot\left\{\left(\frac{P_1}{P_0}\right)^{(\gamma-1)/2\gamma}-1\right\}. \quad (5)$$

This is at the same time the net particle velocity behind the transmitted and reflected wave fronts after impingement of the incident wave has taken place.

For the case of acoustic waves, we set

$$P_1/P_0=1+(\Delta P_1/P_0),\quad P_2/P_0=1+(\Delta P_2/P_0),$$

where $(\Delta P_1/P_0)$, $(\Delta P_2/P_0)$ are both small compared to 1.0; then (4) becomes

$$1+\frac{\Delta P_2}{P_0}=\left\{\frac{2[1+(\gamma-1/2\gamma)(\Delta P_1/P_0)]+(a_0^*/a_0)-1}{(a_0^*/a_0)+1}\right\}^{2\gamma/(\gamma-1)}=1+\frac{2}{(a_0^*/a_0)+1}\frac{\Delta P_1}{P_0};$$

or

$$\frac{P_2}{P_0}=1+\frac{2}{(a_0^*/a_0)+1}\left(\frac{P_1}{P_0}-1\right), \quad (6)$$

while (5) becomes, for $\Delta P_1/P_0\ll 1$, using (3):

$$\frac{u_I}{a_0}=\frac{2(a_0^*/a_0)}{(a_0^*/a_0)+1}\frac{u_1}{a_0}. \quad (7)$$

Equations (6) and (7) are the usual equations of acoustic theory.[1]

These results have been extended, using graphical methods, to the following cases:

(a) γ different on the two sides of the interface.
(b) Shock waves (non-isentropic state changes through the pressure waves) incident on the interface, both with constant γ and varying γ.

It is of interest to note that the use of (4) gives results differing by only a few percent from the values obtained by use of exact shock wave theory, for values of P_1/P_0 up to 4; the range of validity of (5) is somewhat less.

[1] Rayleigh, *Theory of Sound*, Article 270, Chapter XIII. Note that (6) gives reasonably correct results when compared with (4), even when we are far outside the range of P_1/P_0 upon which the derivation of (6) from (4) hinges.

The Magnetic Moment of Tl^{203} *

W. G. PROCTOR
Department of Physics, Stanford University, Stanford, California
December 20, 1948

THE ratios of the frequencies of the nuclear magnetic resonances of the two thallium isotopes to that of the proton and to each other have been measured with a nuclear induction apparatus made into a recording spectrometer which is similar in principle to one developed by Pound.[1] However, perpendicular transmitter and receiver coils are used instead of a radiofrequency bridge. This has the advantage of allowing determination of relative signs of nuclear moments since the phase of the radiofrequency voltage induced in the receiver coil by the nuclei depends upon the sign of their magnetic moment.[2] The steady magnetic field is modulated with a small sweep, so that the component of the signal from the receiver at the sweep frequency is approximately proportional to the derivative of the resonance mode being observed; when the receiver output is detected by a lock-in amplifier, this derivative is plotted by a recording d.c. milliammeter. The transmitter and receiver tuning condensers are ganged, and their common frequency is changed at a slow rate by a clock drive. The record from the milliammeter is divided into 25-kc intervals by the markers which occur as the transmitter is tuned through the harmonics of a 25-kc multivibrator. A single sample consisting of 3 cc of an aqueous solution of 2.6-molar thallium acetate with 0.03-molar manganese sulfate in a $\frac{1}{2}$" test tube was used in the experiment.

All together, eight determinations of the resonant frequency ratios were made. Each determination was computed from the record which was made by observing the resonances of Tl^{203}, Tl^{205}, and H^1 in turn until each had been observed four times, a process which required about three hours and permitted the magnetic field drifts to be calculated. The first four determinations were made with

a current regulated magnet with 8-in. pole faces operating near 1500 gauss and the others with a battery operated magnet with 10-in. pole faces operating near 1900 gauss. The ratios of the resonance frequencies in the same field were found to be

$$\nu(Tl^{203})/\nu(H^1)=0.5714\pm0.0001,$$
$$\nu(Tl^{205})/\nu(H^1)=0.5770\pm0.0001,$$
$$\nu(Tl^{203})/\nu(Tl^{205})=0.9903\pm0.0002.$$

This result for Tl^{205} agrees within experimental errors with that given by Poss in a previous letter.[3] He did not make precise measurements on the Tl^{203} resonance because of a low signal-to-noise ratio but stated that for the same frequency its resonance could be found at a field one percent lower than that required for Tl^{205}. In the present experiment the signal-to-noise ratio for the Tl^{203} resonance was about ten, and thus allowed a considerably more accurate location of the resonance frequency.

The magnetic moments of the nuclei of both thallium isotopes were found to be positive, and their integrated resonance amplitudes were each consistent with a spin of $\frac{1}{2}$, as given by spectroscopic data.[4] If the magnetic moment of the proton is taken to be $(2.7928\pm0.0008)\mu_N$[5] and a correction for electronic diamagnetism is made,[6] which for this computation has been assigned an error of 15 percent, then

$$\mu(Tl^{203})=(1.614\pm0.003)\mu_N,$$
$$\mu(Tl^{205})=(1.629\pm0.003)\mu_N.$$

The ratio $\mu(Tl^{203})/\mu(Tl^{205})=0.9903\pm0.0002$ is, of course, much more accurately known.[7]

* Assisted by the Joint Program of the ONR and the AEC.
[1] R. V. Pound, Phys. Rev. 72, 527 (1947).
[2] Note Eq. (40b) in the paper by F. Bloch, Phys. Rev. 70, 460 (1946).
[3] H. L. Poss, Phys. Rev. 72, 637 (1947).
[4] H. Schüler and J. E. Keyston, Zeits. f. Physik 70, 1 (1931); H. Schüler and T. Schmidt, Zeits. f. Physik 104, 468 (1937).
[5] This value differs from the value (2.7896 ± 0.0008) given by S. Millman and P. Kusch, Phys. Rev. 60, 91 (1941), by the correction for the magnetic moment of the electron $[1+(\alpha/2\pi)]$ suggested by J. Schwinger, Phys. Rev. 73, 416 (1941).
[6] W. E. Lamb, Jr., Phys. Rev. 60, 817 (1941).
[7] Upon completion of this work, our attention was drawn to more recent results by Poss, reported in the Quarterly Progress Report of the Research Laboratory of Electronics, Massachusetts Institute of Technology, July 15, 1948, p. 32. The results given above are in substantial agreement with those of Poss.

H^3 and the Mass of the Neutrino

W. A. Bowers and Nathan Rosen
University of North Carolina, Chapel Hill, North Carolina
December 20, 1948

LAST year Konopinski[1] pointed out that, on the basis of data available at that time concerning the half-life[2] and maximum beta-ray energy[3] of tritium, the value of $|M|^2ft$ for H^3 was roughly 1/10 as large as for He^6, if zero neutrino rest mass was assumed. To remove this discrepancy with beta-decay theory, which predicts the same order of magnitude of $|M|^2ft$ for allowed transitions in all nuclei, Konopinski found it necessary to take the neutrino rest mass to be a few percent of that of the electron.

We should like to point out that more recent work on the half-life of tritium[4] and on its beta-spectrum[5] gives results which appear to remove the above-mentioned discrepancy with a zero neutrino mass. If one takes the upper limit of the tritium spectrum[5] to be 17 kev, one finds[6] for a zero neutrino mass, taking into account the Coulomb field, $f=2.2\times10^{-6}$. With a half-life[4] $t=12$ years and with $|M|^2=3$, this gives $|M|^2ft=2500$ sec., which is of the same order of magnitude as the value 5760 sec. given by Konopinski[1] for He^6.

This result is in agreement with the conclusions of several workers[5,7] concerning the neutrino mass based on the shapes of beta-energy distribution curves near their upper limits.

[1] E. J. Konopinski, Phys. Rev. 72, 518 (1947).
[2] R. J. Watts and D. Williams, Phys. Rev. 70, 640 (1946).
[3] R. D. O'Neal and M. Goldhaber, Phys. Rev. 58, 574 (1940).
[4] Aaron Novick, Phys. Rev. 72, 972 (1947).
[5] S. C. Curran, J. Angus, and A. L. Cockcroft, Nature 162, 302 (1948).
[6] E. J. Konopinski, Rev. Mod. Phys. 15, 209 (1943).
[7] C. S. Cook, L. M. Langer, and H. C. Price, Jr., Phys. Rev. 73, 1395 (1948).

γ-Radiation from Au^{198}

Kai Siegbahn and Arne Hedgran
Nobel Institute for Physics, Stockholm, Sweden
December 14, 1948

SEVERAL papers[1] have lately been published in this journal regarding the γ-radiation following the β-disintegration of Au^{198}. We have made a careful study of the γ-radiation in order to be able to find any γ-radiation besides the well-known γ-ray at 411 kev. The investigation was performed with our new double focusing spectrometer ($\rho=50$ cm) (in course of publication). The resolving power of the spectrometer was set to 0.8 percent and the lead converter used was only 3.7μ thick in order to make full use of the resolving power of the instrument itself. The results are shown in Fig. 1. The Compton distribution, the K, L, and M photo-lines of the 411-kev γ-ray, is clearly seen. Levy and Greuling[2] have reported γ-rays of 157 and 207 kev with an intensity of ≤15 percent of the 411-kev ray. We have paid special attention to the region 800–1250 $H\rho$, where the K photo-lines of these rays should be

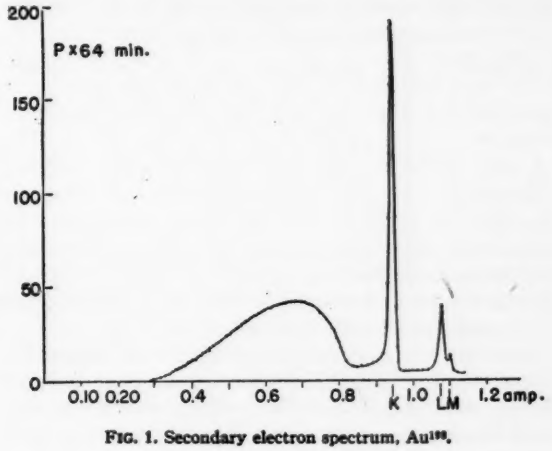

FIG. 1. Secondary electron spectrum, Au^{198}.

found but, as is seen in Fig. 1, we are unable to detect them. We believe that we can put an upper limit for the intensity of these rays to be 2 percent of the 411-kev ray.

Furthermore, a γ-ray of only 1 or 2 percent abundance could not explain the coincidence effect found in some earlier cases. On the other hand, it might be questioned if this effect is real (see E. T. Jurney[1]). The rather extensive $\gamma-\gamma$-coincidence measurements we have performed in this laboratory also give a small $\gamma-\gamma$-coincidence effect but, if one compares this effect with the spurious $\gamma-\gamma$-effect obtained from Fe^{59} with two uncorrelated γ-rays, the whole effect just disappears. The magnitude of this extra coincidence effect, clearly demonstrated in Fe^{59}, may very well depend on the actual experimental arrangement but has to be taken into account. In our arrangement which otherwise is designed to prevent coincidences due to scattering, the spurious effect with Fe^{59} decreases when lead foil is wrapped around our γ-tubes and disappears almost completely when the lead thickness is 1 mm.

We have also measured the primary β-spectrum in order to determine the internal conversion coefficients of the K, L, and M lines of the 411-kev radiation. The sample obtained from Harwell was evaporated in a thin layer to eliminate absorption effects. We obtained $\alpha_K = 3.0$ percent; $\alpha_L = 1.0$ percent; $\alpha_M \sim 0.3$ percent.

To get a precise determination of the γ-line energy we put Cu^{64} and Au^{198} in the same converter and measured the L photo-line from Au^{198} against the K photo-line of the 510.8-kev radiation from Cu^{64}. These two lines then formed a rather close "doublet" which makes a comparison of the two energies reliable. In this way we obtained a value for the Au^{198} line to be 411.0 ± 1 kev, in close agreement with Dumond's[3] crystal value. We believe that this kind of measurement in the β-spectrometer can be made still more accurate in the near future.

[1] For references see E. T. Jurney, Phys. Rev. 74, 1049 (1948).
[2] P. Levy and E. Greuling, Phys. Rev. 73, 83 (1948).
[3] J. Dumond, D. Lind, and B. Watson, Phys. Rev. 73, 1392 (1948).

V-2 Cloud-Chamber Observation of a Multiply Charged Primary Cosmic Ray*

S. E. Golian,** C. Y. Johnson, E. H. Krause, M. L. Kuder,*** G. J. Perlow, and C. A. Schroeder
U. S. Naval Research Laboratory, Washington, D. C.
December 13, 1948

A SIX-INCH cloud chamber was flown in a V-2 to a height of 159 km (99 miles) on January 22, 1948. The chamber was six inches in diameter and contained argon and alcohol-water vapor at two atmospheres pressure. Two lead plates, each 1 cm thick, crossed the chamber which was illuminated for a depth of one inch. Stereo photographs were taken at 25-second intervals.

Since the V-2 was in free fall after its fuel burned out, droplets formed in the chamber remained stationary until the gas was recompressed. This reduced several sources of track distortion, but eliminated the cleaning out by falling droplets of uncharged condensation nuclei. As a result, a progressive fogging took place rendering the later photographs unusable.

Figure 1 is half a stereo photograph taken 175 seconds after launching. The height was 145 km and the outside atmospheric pressure $\sim 10^{-5}$ mm Hg. Besides the background fog, one may observe a large number of fast particles, for example, at b and c, many of which have a common origin. However, the most prominent particle (marked a) is not associated with any observable shower. It traverses both lead plates and ionizes heavily. Its scattering is less than the perceptible limit which we take conservatively as 1°. We may test the possibility that it is a proton by noting whether the momentum required for penetration of the lead is consistent with the heavy ionization and small scattering. Its path in plate II is 1.6 cm. Considering only this plate, it must have a ratio of incident momentum to characteristic momentum of $p/\mu c \geq 0.48$[1] corresponding to an energy $E \geq 102$ Mev. The incident ionization relative to the minimum which a proton can have[2] is then $I/I_{\min} \leq 3.3$. Inspection of the photograph does not permit an assumption of $I/I_{\min.} < \sim 3$. Then we must have $p/\mu c < 0.53$. For the latter value, the expected scattering may be computed. The differential mean square scattering for a particle of mass μ and charge number z in traversing a thickness dx of material may be put in the form $d(\theta^2)_{Av} = (z^2/\mu^2) f(p/\mu c) dx$.[2,3] By graphical integration one obtains $\Delta\theta = 5.0°$ as the expected r.m.s. projected angle of scattering in 1.6 cm Pb. Since the distribution in angle is Gaussian,[3] the probability P of observing scattering of less than 1° may be calculated from a table of the error integral. One gets $P(<1°) = 0.16$. It is therefore possible, but not likely, that the particle is a proton.

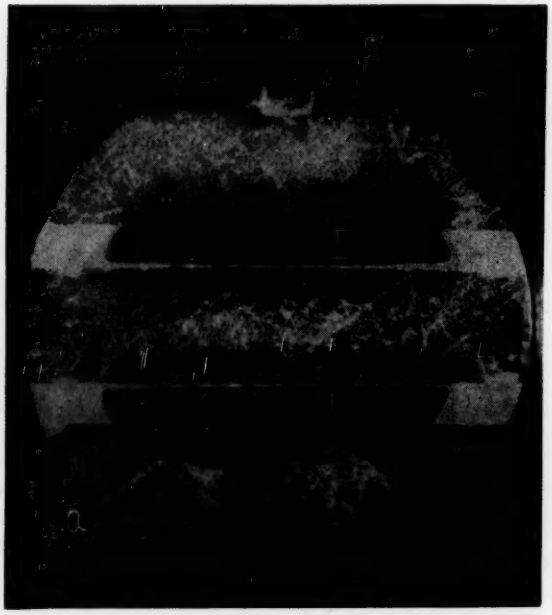

FIG. 1. Cloud-chamber photograph at height of 145 km.

A more reasonable conjecture is that the track is due to an alpha-particle or one of still higher z. For the alpha $(p/\mu c) \geq 0.48$, and $(I/I_{\min.}) \leq 3.3$ again, but $I_{\min.}$ for the alpha is 4 times that for the proton. Thus, any value of incident $(p/\mu c)$ sufficient to penetrate is acceptable on our criterion. The loss in relative momentum $-\Delta(p/\mu c)$ in traversing the plate depends on z^2/μ and is therefore the same for protons and alphas of the same initial speed. However, the scattering $d(\theta^2)_{Av}$ is proportional to z^2/μ^2 and is therefore reduced by a factor of 4 for an alpha. The r.m.s. expected scattering is thus reduced by a factor of 2 and $P(<1°)$ is roughly doubled. It then becomes difficult to assign a definite energy range to the alpha on the basis of scattering. For particles of larger z, the scattering will be still smaller for the same speed on emerging from the plate. One may not, therefore, discriminate between $z=2$ and $z>2$ on this basis.

We conclude that the track is due either to an alpha-particle of energy greater than 400 Mev, or to a more highly charged nucleus of energy greater than a correspondingly higher minimum. It does not appear likely that energetic *complex* particles should be produced in a nuclear process within the rocket material. It, therefore, seems probable that we are observing primary cosmic rays of greater charge and mass than the proton.

* Presented at the American Physical Society Meeting April 1948.
** Now at Brookhaven National Laboratory.
*** Now at National Bureau of Standards.
[1] J. A. Wheeler and R. Ladenburg, Phys. Rev. 60, 754 (1941).
[2] B. Rossi and K. Greisen, Rev. Mod. Phys. 13, 240 (1941).
[3] E. J. Williams, Phys. Rev. 58, 292 (1940).

Ferromagnetic Resonance in Iron Oxides

G. E. Crouch, Jr.
Plastics Laboratory, Princeton University, Princeton, New Jersey
December 20, 1948

CURVES of the magnetic permeability $(\mu' - j\mu'')$ of ferrous oxide powder *versus* frequency are shown in Fig. 1. These curves are drawn from composite data, extrapolated to 100 percent concentration with Lichtenecker's relation, which Birks[1] has given and which we have obtained at 1.2 cm. It is interesting to note that the permeability μ' becomes appreciably less than unity at certain frequencies and that there is a broad region of natural ferromagnetic resonance. This resonance has been interpreted as being caused by the interaction of a magnetic field at microwave frequencies with the Larmor spin precession about the internal anisotropic magnetic field. The resonance frequency is given by

$$\nu_n = (g\mu_e/h)H_n.$$

μ_e is the magnetic moment of the electron and H_n is the internal magnetic field intensity. Further examination of the curves with regard to the Kronig-Kramers susceptibility relations[2]

$$\psi'(\nu) - \psi'(\infty) = 2/\pi \int_0^\infty [\nu'\psi''(\nu')d\nu'/(\nu'^2 - \nu^2)],$$

$$\psi''(\nu) = (-2\nu/\pi) \int_0^\infty [(\psi'(\nu) - \psi'(\infty))/(\nu'^2 - \nu^2)]d\nu',$$

indicates that, by comparing various calculated curves with the observed curves, one can more nearly approximate conditions with a Lorentz absorption curve than with a Gaussian absorption curve. Neither interpretation agrees with the observations at frequencies above 10,000 mc/sec., however. The frequency dependence of $\psi''(\nu)$ is given by the shape function[3] $g(\nu)$

$$\psi''(\nu) = \pi\psi_0\nu_n g(\nu),$$

$$\int_0^\infty g(\nu)d\nu = 1, \quad T_2 = \tfrac{1}{2}[g(\nu)]_{\max},$$

where ψ_0 is the static ferromagnetic susceptibility. There remains, however, a considerable discrepancy between the expected μ' curve and the measured μ' curve, the latter being more reliable than the measured μ'' curve. Reasonable observed values of ν_n and H_n are:

$$\nu_n \leqq 1700 \text{ mc/sec.},$$
$$H_n \leqq 600 \text{ gauss.}$$

(This value of H_n is not in all cases consistent with a g value of 2.)

A possible explanation of this broad resonance seems to lie in the interaction of magnetic dipoles to affect the value of the internal magnetic field about which there is spin precession. Each atomic dipole, representing an iron atom and situated at definite points in the cubic Fe_3O_4 lattice, is considered to be in an effective magnetic field $H_{(eff)}$. If the dipoles align either in the same or opposite direction to the internal field,

$$H_{(eff)} = H_n \pm (a\mu_i/r^3),$$

where μ_i is the magnetic moment of the iron atom and (a) is a parameter of the order of 1 or 2. In considering nearest neighbors only, one would thus be led to expect the width $(\Delta\nu)$ of the absorption band to be of the order of μ_i/r^3. Consideration of dipoles farther removed would tend to give a continuous absorption band. This simplification seems somewhat justified in view of the success of a similar interpretation of nuclear resonance absorption and because

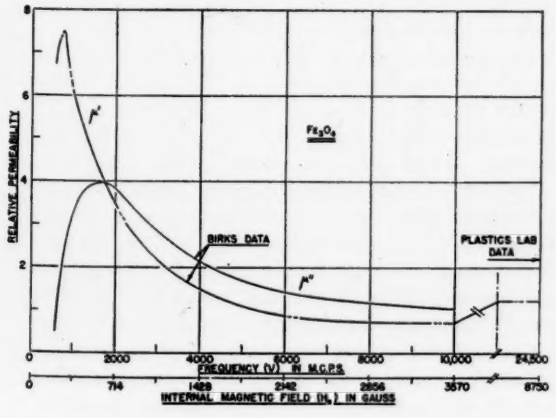

FIG. 1. Relative permeability *versus* frequency for Fe_3O_4.

a more rigorous analysis[4] for nuclear absorption yields results substantiating the simpler assumptions, even though not in agreement with a Lorentz absorption mechanism. On this basis calculated values are

$$(\Delta\nu) \leqq 5000 \text{ mc/sec.},$$
$$(\Delta H) \leqq 1400 \text{ gauss.}$$

μ_i has been taken as 2 Bohr magnetrons, r has been taken as 3A, and a has been taken as 1. These values are rather consistent with the observations in Fig. 1 so that apparently the broad resonance is accounted for. Factors entering a more rigorous analysis would be difficult to examine because of experimental accuracy in measuring μ' and μ''.

Magnetic permeability measurements of gamma-ferric oxide indicates a similar resonance. The magnetic field resulting from anisotropy is found to be smaller, a fact which is consistent with the crystalline structure of this material and the larger separation of iron atoms.

The research reported here was sponsored by the Army Signal Corps and Naval Bureau of Ships, Bureau of Ordnance, Bureau of Aeronautics, and ONR under Signal Corps Contract No. W-36-039-sc-32011.

[1] J. B. Birks, Nature 160, 535 (1947).
[2] G. E. Pake and E. M. Purcell, Phys. Rev. 74, 1184 (1948).
[3] N. Bloomberger, E. M. Purcell, and R. V. Pound, Phys. Rev. 73, 679 (1948).
[4] G. E. Pake, J. Chem. Phys. 16, 327 (1948).

Cadmium Sulfide as a Crystal Counter*

G. J. GOLDSMITH AND K. LARK-HOROVITZ
Purdue University, Lafayette, Indiana
December 20, 1948

AHEARN,[1] Hofstadter,[2] and others[3–5] have recently reported obtaining counts for α- and β-particles and γ-rays with diamonds at room temperature. More recently,[6,7] there have been reported similar results for α- and β-counts with zinc sulfide and with cadmium sulfide. Cadmium sulfide has been investigated in this laboratory, with the following results.

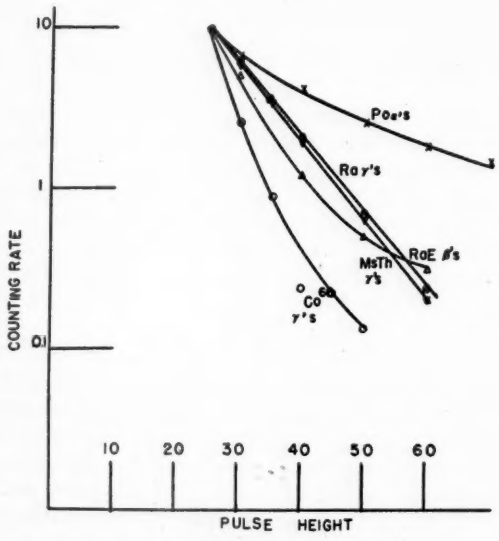

FIG. 1. Pulse heights and counting rates for α-, β-, and γ-rays from various sources.

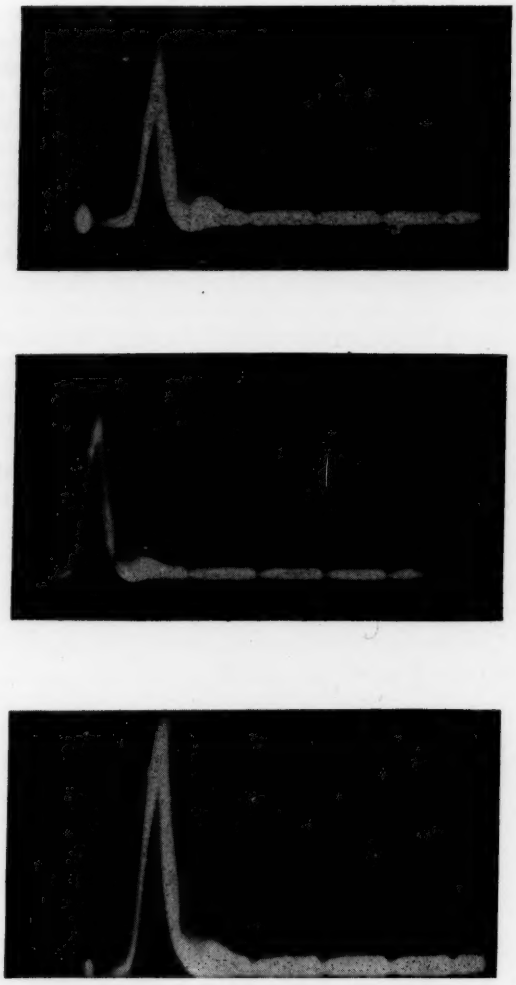

FIG. 2. Top to bottom: Ra γ's, RaE β's, Po α's. Timing markers 1 microsecond. Amplifier gain raised by factor of 2 for γ-ray photo.

The crystals used in the investigations were made by the vapor phase condensation method of Frerichs[8] and supplied by him through the courtesy of the Bureau of Ships.** Of the crystals obtained, only one type was suitable for our purposes. These were irregularly shaped single crystals, as confirmed by Laue x-ray diffraction pattern, about two-millimeters thick and about a half-centimeter on a side. The crystals were cleaved and small portions about 1×2 mm investigated for photo-conductive properties. Crystals which displayed a dark resistance of at least in excess of 10^9 ohms and a light resistance of the order of 10^6 ohms or less were useful as counters.

The electrodes were prepared by evaporating thin gold foils on two opposite faces. They were then mounted on a silver block 2-mm square and clamped with a thin phosphor

bronze spring. The entire assembly was placed in a light-tight copper box, which was in turn mounted directly on the preamplifier. The amplifier is a commercially available linear amplifier having a rise time of 0.2 microsecond and a gain of about 3500 at that rise time.

Plots of pulse height *versus* counting rate have been taken for Po alpha-particles; RaE β's; Ra, MsTh, and Co^{60} γ's (Fig. 1). It was found that the pulse heights observed were a function of the applied voltage from 30 volts to about 200 volts—beyond that value the maximum pulse height remained constant but the crystal background increased considerably. In some crystals surface leakage or other conductive effects limited the voltage to around 300.

At a potential of 70 volts the rise time of the pulse appears to be slightly greater than that of the amplifier, but beyond that value, the recorded pulse rise is equal to or less than the limiting 0.2-microsecond rise time (Fig. 2).

Measurements of maximum pulse heights gave 12 mv for alpha-particles, 6 mv for RaE β's, and about 2.5 mv for Ra γ's.

These experiments are being continued.

* This work was supported in part by the ONR and the Signal Corps.
[1] A. J. Ahearn, Phys. Rev. 73, 1113 (1948).
[2] Robert Hofstadter, Phys. Rev. 73, 631 (1948); Phys. Rev. 72, 1120 (1947).
[3] Wooldridge, Ahearn, and Burton, Phys. Rev. 71, 913 (1947).
[4] W. Jentschke, Phys. Rev. 73, 77 (1948).
[5] L. F. Curtiss and B. W. Brown, Phys. Rev. 72, 643 (1947).
[6] *Report of Conference on Scintillation Counters and Crystal Counters*, Rochester, New York (1948).
[7] European Scientific Notes 2, 299 (1948).
[8] Rudolf Frerichs, Phys. Rev. 72, 594 (1947).
** We want to thank Professor R. J. Cashman (Northwestern University), director, Navy Contract NO65 45068, for making the material available to us.

Yields of the Platinum Group Radio-Isotopes in the High Energy Helium-Ion Bombardment of Uranium

R. D. WOLFE* AND N. E. BALLOU*
Radiation Laboratory, University of California, Berkeley, California
December 6, 1948

INVESTIGATIONS by O'Connor[1] in 1947 on the radioactive products of the bombardment of uranium with high energy deuterons and helium ions in the Berkeley 184-inch cyclotron indicated the possibility of a continuous yield of products, the isotopes in the heavy region of mass numbers arising from spallation, and those in the middle region of mass numbers arising from fission.

In order to supplement these results, additional experiments were performed at the suggestion of G. T. Seaborg. Determinations were made of the relative yields of the six platinum metals (ruthenium, rhodium, palladium, osmium, iridium, and platinum) when natural uranium is bombarded with 380-Mev helium ions. The reason for interest in the yields of these elements is that the last three lie near the region of mass 180, where the plot of yield *vs.* mass number may change from a fission-yield curve to a spallation-yield curve. In addition, the first three lie in a region from mass 103 to 112, which should indicate whether the center of the curve has a large dip (as does the slow-neutron fission-yield curve), or a single maximum indicating symmetrical fission (as in the case of bismuth[2]), or something intermediate (as in the case of thorium[3,4]).

A new procedure for the radio-chemical analysis of the platinum metals was developed, to which the existing procedures for ruthenium and palladium were adapted as required. Several short bombardments of thin-gauge uranium strips (2 cm×0.5×0.1 cm) were made with 380-Mev helium ions, the target dissolved, the platinum metals isolated, and their chemical yields determined. Yields of activities produced were determined by counting with thin end-window Geiger-Müller counters of the bell jar type, having a known counting efficiency. Direct comparison of samples was made possible by use of identical mountings and shelf geometry throughout. All samples were corrected to 100 percent chemical yield, total sample, and zero absorber. Yield for each isotope was determined relative to the yield of 12.8-day Ba^{140} as a standard of comparison. The cross section for production of the Ba^{140} is estimated as 3×10^{-3} barn.

As was expected, yields of osmium, iridium, and platinum were much lower than those of ruthenium, rhodium, and palladium. The yield of the mass 105 chain was obtained by isolation of both 4.5-hr. Ru^{105} and 36-hr. Rh^{105}. The other isotopes of ruthenium, one of palladium, two of osmium, one of iridium, and one of platinum were identified by decay characteristics and by absorption characteristics were possible. In every case observed values agreed with published data.[5]

The results, plotted as relative yield *vs.* mass number, are shown in Fig. 1. The solid portion of the curve passes through the experimentally determined points; the dashed portion is drawn by analogy to other known fission-yield curves to connect the two experimentally determined sec-

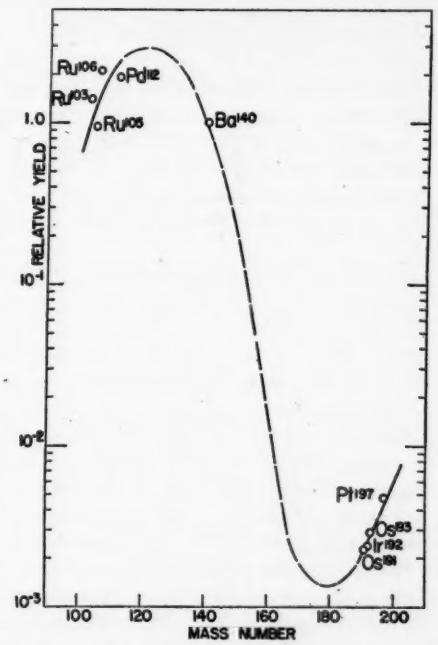

FIG. 1. Relative yield of platinum elements *vs.* mass number for 380-Mev helium ions on uranium.

tions. The ruthenium and palladium points give no evidence for a dip in the middle of the fission-yield curve; on the contrary, it appears more likely that the curve has a single smooth maximum in the vicinity of mass 120, i.e., a maximum yield for the symmetrical splitting of the fissioning nucleus. This hypothesis has since been supported by the subsequent work of O'Connor and Seaborg[6] during the summer of 1948. Furthermore, the osmium, iridium, and platinum points indicate that the fission-yield curve apparently becomes continuous with a spallation-yield curve at a minimum of about 0.1 percent the yield of Ba^{140} at around mass 180. These results likewise are confirmed by the work of O'Connor and Seaborg.[6]

We should like to thank Dr. A. S. Newton for his advice during the experiments, and Mr. J. T. Vale and Dr. D. C. Sewell and the cyclotron crew for their cheerful cooperation in conducting the bombardments. This work was performed under the auspices of the Atomic Energy Commission.

* Present address: Naval Radiological Defense Laboratory, San Francisco Naval Shipyard, San Francisco 24, California.

[1] P. R. O'Connor, *The Chemical Identification of Isotopes Formed in the Bombardment of Uranium with High-Energy Particles* (Doctor of Philosophy Thesis, University of California, Berkeley, August 18, 1947).
[2] R. H. Goeckermann and I. Perlman, Phys. Rev. **73**, 1127 (1948).
[3] A. S. Newton, Phys. Rev. **75**, 17 (1949).
[4] A. Turkevich, presented at meeting of A.A.A.S. in Chicago (December, 1947).
[5] G. T. Seaborg and I. Perlman, "Table of the isotopes," Rev. Mod. Phys. **20**, 585 (1948).
[6] P. R. O'Connor and G. T. Seaborg, Phys. Rev. **74**, 1189 (1948).

Maximum Positron to Negatron Ratio in the Decay of Cl^{36}

FRANCIS JOHNSTON AND JOHN E. WILLARD
Department of Chemistry, University of Wisconsin, Madison, Wisconsin
December 15, 1948

BY positron emission Cl^{36} (*ca.* 10^6 yr. half-life[1]) may conceivably decay either to stable S^{36} or, by negatron emission, to stable A^{36}. With a Cl^{36} sample of very low activity, Grahame and Walke[2] observed, in a series of 18 pairs of cloud-chamber photographs, 16 tracks which they ascribed to negatrons and three which they ascribed to positrons.

With very much more active samples of Cl^{36} [3] we have found a maximum value of *ca.* 3×10^{-4} for the fraction of the Cl^{36} beta-disintegrations which produce positrons. This value is determined on the basis of the lead absorption curve (Fig. 1) of the penetrating radiations from a 2.25-g sample of NaCl with an activity of 2×10^8 Cl^{36} beta-disintegrations per minute. The curve was made with the sample in a glass cup 3.5 cm from the mica window of a Geiger-Mueller counter tube in an aluminum-lined lead housing and with the absorbers placed directly on top of the sample. Nearly all of the Cl^{36} beta-particles were absorbed by the sample. The curve, which starts with 175 mg of added absorber, can be resolved into two components, one with a half-thickness of 300 mg/cm² corresponding to a 0.10-Mev gamma-ray and the other with a half-thickness of 5.1 g/cm² corresponding to a 0.57-Mev gamma-ray.[4]

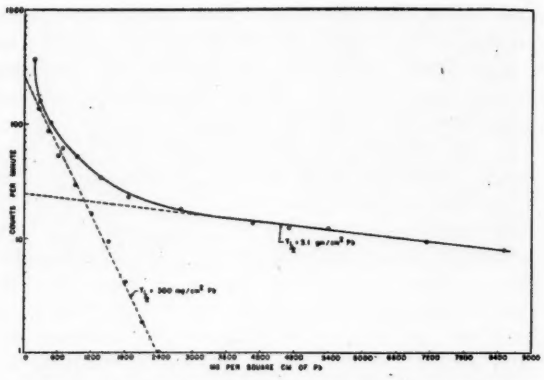

FIG. 1. Absorption curve of Cl^{36}.

These may both be due to bremsstrahlung radiation produced by the absorption of the Cl^{36} beta-particles in the sample, or they may be due to gamma-rays emitted in a small fraction of the beta-disintegrations or in decay by *K*-capture. It is possible, however, that the apparent 0.57-Mev component is the result of absorption of 0.501-Mev positron annihilation radiation, under experimental conditions where scattering effects give a different slope than was obtained under the conditions used in making the standard[4] curves. We have assumed that this component may be due to annihilation radiation and have estimated its absolute emission rate from the sample with the aid of a reference sample of Co^{60} mounted in the same way as the NaCl sample and counted with the same set of absorbers. The disintegration rate of the stock solution of Co^{60} from which an aliquot was taken for the reference sample was determined by comparison with a Bureau of Standards standard Co^{60} solution. The assumptions were made that the Co^{60} emits two gamma-rays per disintegration (*1.1* and *1.3* Mev[5]) and that these have twice as high a counting efficiency[6] as two 0.5-Mev gamma-rays from positron annihilation. It was further assumed that any annihilation radiation produced originated within the NaCl sample, since essentially all positrons would be absorbed within the sample unless their energy greatly exceeded the maximum negatron energy.

On the basis of the above measurements and assumptions, the extrapolated counting rate of 25 c/m of the apparent 0.57-Mev component of Fig. 1 was estimated to indicate a total of 11.6×10^4 gamma-rays per minute emitted from the sample, or a total of 5.8×10^4 positrons per minute if this is annihilation radiation. The beta-disintegration rate of the sample was estimated to be 1.9×10^8 dis/min. by comparing the beta-counting rate of an aliquot of the sample with that of an aliquot of the Co^{60} reference sample counted under identical conditions, both values being extrapolated to zero absorber. A similar comparison with a Bureau of Standards RaE standard gave a value of 2.1×10^8 beta-dis/min. From these results it seems certain that the fraction of the total Cl^{36} decay which occurs by positron emission is very low, probably no greater than 3×10^{-4}, and it is possible that there is no decay by positron emission.

This work was supported in part by the University Research Committee with funds made available by the Wisconsin Alumni Research Foundation.

[1] R. T. Overman, Abstracts Am. Chem. Soc. Meeting 111, p. 44P, paper 70 (1947).
[2] D. Grahame and H. Walke, Phys. Rev. 60, 909 (1941).
[3] U. S. Atomic Energy Commission Isotopes Catalog No. 2, Item 16. The sample used in this work was of much higher specific activity than the standard sample listed in the catalog and had been chemically purified from S^{35} formed by the $Cl^{35}(n, p)S^{35}$ reaction. With unpurified samples a high background of bremsstrahlung from the intense S^{35} beta-radiation is observed.
[4] L. E. Glendenin, Nucleonics 2, 29, Fig. 15 (1948).
[5] L. C. Miller and L. F. Curtiss, Bur. Stand. J. Research 38, 359 (1947).
[6] C. D. Coryell, *The Use of Isotopes in Biology and Medicine* (University of Wisconsin Press, Madison, 1948), p. 127.

Magnetic Multipole Internal Conversion

I. S. Lowen and N. Tralli
Physics Department, Washington Square College, New York University, New York, New York
December 9, 1948

THE use of the ratio of the K to L shell internal conversion coefficients has been suggested for determining the multipole nature of radiation emitted from the atomic nucleus.[1] Curves showing the values of this ratio as a function of energy for $Z=35$ have been given for electric multipoles[1] valid for the region of low energies.

To facilitate the comparison with the experimental data, it is desirable to have curves for the magnetic multipole case valid in the same region of energy. This has been accomplished by using for the K shell a rigorously correct expression specialized to the case of non-relativistic energies for the magnetic multipole internal conversion, due to Bessey,[2] based on the Dirac equation, and an analogously derived formula for the L shell internal conversion. Figure 1 shows curves for the K to L ratio evaluated for $Z=35$ in the magnetic multipole case taking into account screening as in Hebb and Nelson. For the sake of comparison, the curves of Hebb and Nelson for the electric case are included. The Hebb and Nelson curve for $l=4$ has been omitted, whereas for the experimental application, this must of course be used with the $l=3$ magnetic case.

The K to L ratios for the magnetic multipole radiation have been previously calculated by the Born approximation[1,3] for use with the K to L electric multipole low energy curves. For comparison of the relative values of the magnetic multipole ratios in the two approximations, we have shown in Fig. 2 curves for the Born approximation as well

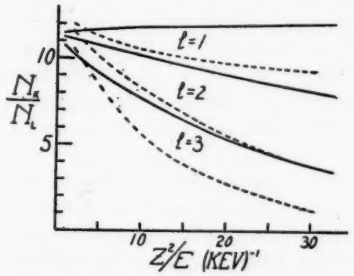

FIG. 1. Curves for N_K/N_L as a function of Z^2/E. Solid line—magnetic multipole, broken line—electric multipole.

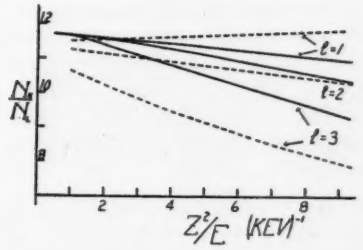

FIG. 2. Curves for N_K/N_L for magnetic multipoles as a function of Z^2/E. Solid line—Born approximation, broken line—Pauli approximation.

as those mentioned above for the rigorous low energy case. From these curves it appears that the Born approximation ratios for $l=1$, 2 differ from our low energy approximation by less than 10 percent in the neighborhood of 10^5 ev, and greater, gamma-ray energy. However, it should not be concluded that the K and L magnetic internal conversion coefficients, β_K and β_L, calculated in the two ways agree that well. For example, for $l=1$ and 2×10^5-ev gamma-ray energy the difference in the β_K's so determined is approximately 15 percent and in the β_L's approximately 12 percent. For $l=3$ it is clear that the difference in the ratios for the two approximations is appreciably larger than for $l=1$, 2. Consequently, caution is required in assuming equivalence of the two approximations for the ratio in this energy range in the general case, at least for $Z=35$ and higher.

Finally the L shell electric multipole conversion has been calculated in the region of low energies, starting from the Dirac equation, to ascertain whether additional contributions from the spin might alter the value for this quantity as determined by Hebb and Nelson using Schroedinger theory. The answer is in the negative.

In conclusion, we wish to express our gratitude to Dr. J. R. Bessey for sending us the correct expression for the low energy K conversion in the magnetic case[4] before publication and to Professor G. E. Uhlenbeck for his kind interest in this work.

[1] M. H. Hebb and E. Nelson, Phys. Rev. 58, 486 (1940).
[2] Bessey, Thesis, University of Michigan, 1942. Cf. also Drell, Bull. Am. Phys. Soc. 23, 18 (1948).
[3] M. H. Hebb and G. E. Uhlenbeck, Physica 7, 605 (1938); S. M. Dancoff and P. Morrison, Phys. Rev. 55, 122 (1939).
[4] The results of G. Goertzel and J. S. Lowen, Phys. Rev. 67, 203 (1945) and of V. Berestetzky, J. de Phys. U.S.S.R. 10, 137 (1946), using the elementary Pauli theory for the K shell, while in agreement with each other, are incorrect owing to failure of the simple Pauli theory which does not take into account correctly contributions from the origin in the case of the highly singular magnetic multipole potentials. See reference 2.

O^{17} and S^{36} in the Rotational Spectrum of OCS*

W. Low and C. H. Townes
Columbia University, New York, New York
December 10, 1948

THE transitions $J=1\rightarrow2$ of $O^{16}C^{12}S^{36}$ and $O^{17}C^{12}S^{32}$ have been detected. Abundance and mass of S^{36} were determined. The spin of S^{36} appears to be zero, and there is some indication that the spin of O^{17} is $\frac{1}{2}$.

S^{36} was discovered by Nier[1] who stated its abundance as 1:6000, so that a very sensitive spectrograph was needed

TABLE I. Measured OCS lines.

Transition	Molecule	Standard	Frequency interval between standard and measured line (Megacycles)	Frequency (Megacycles)
J 1→2	$O^{17}C^{12}S^{32}$	$O^{16}C^{12}S^{34}$	196.62±0.04	23534.67
J 1→2	$O^{16}C^{12}S^{36}$	$O^{16}C^{12}S^{34}$	532.63±0.04	23198.66
J 1→2 $V_1=1$	$O^{16}C^{12}S^{34}$	$O^{16}C^{12}S^{34}$	14±1	23661

TABLE II. Relative intensity measurements.

Molecules	Measured intensity ratio	Relative abundance	Relative abundance from Segrè chart
$\frac{O^{16}C^{12}S^{34}}{O^{17}C^{12}S^{32}}$	1.26±0.05	1.25±0.05	1.26
$\frac{O^{17}C^{12}S^{32}}{O^{16}C^{12}S^{36}}$	2.84±0.14	2.71±0.14	2.34

to detect its line in OCS near 1.3-cm wave-length. A Stark modulation system[2] was used with a modulation frequency of 50 kc and a 10-ft. wave-guide absorption cell cooled to −78°C to enhance intensities. The detected signal was fed through a phase detecting or "lock in" amplifier to an Esterline-Angus recording ammeter, giving a narrow band width for elimination of noise. A clock motor varied the signal oscillator uniformly in time so that the ammeter pen of the recorder produced a spectral plot. The marking pen was connected to a frequency measuring system similar to that used with oscilloscope presentation[3] so that frequency markers could be set on a line to a reproducibility of about 0.02 mc. Relative abundances of isotopes were determined by comparison of heights of recorded lines with crystal current, gas pressure, and Stark voltage kept constant. Relative abundances were obtained from these relative heights after a small correction was made to allow for variation of absorption intensity with frequency.

An OCS^{36} line is shown in Fig. 1. Its absorption coefficient is 7×10^{-9} cm^{-1} at room temperature, and it may be seen that a line of intensity 5×10^{-10} cm^{-1} would be approximately equal to noise deflection, so that the spectrograph can detect even rarer isotopes. A modulation frequency of 200 kc decreases noise considerably, but did not appreciably increase sensitivity because of other types of variations.[4]

The $O^{17}CS$ and OCS^{36} lines were examined closely with half-widths of about 1 mc and no hyperfine components found, indicating that the quadrupole coupling constants in both cases are less than 5 mc. Since eqQ for OCS^{36} is known to be 28.5 mc, this is a good indication that the spin of S^{36} is zero. However, since eqQ for O^{17} might be expected to be small, even with a spin of $\frac{1}{2}$, the small value of eqQ does not justify a definite conclusion that the spin of O^{17} is $\frac{1}{2}$.

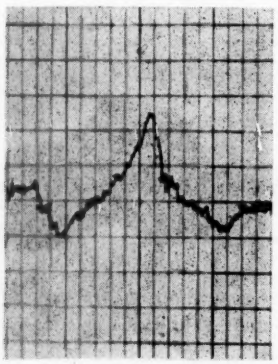

FIG. 1. OCS^{36} $J=1\rightarrow2$ transition. Undisplaced line is represented by a peak in center and Stark components $M=0$ and $M=1$ by valleys on the right and left, respectively.

Measured frequency intervals and line frequencies calculated from them are given in Table I. From these figures and published frequencies for other isotopes the ratio of mass differences $(O^{17}-O^{16}/O^{18}-O^{17})=1.00420$ and $(S^{36}-S^{34}/S^{34}-S^{32})=1.001826$ are obtained.[5] The first figure agrees well with the value $(O^{18}-O^{17}/O^{17}-O^{16})=1.004098$ from Segrè.[6] If the microwave data were used to evaluate the mass of O^{17}, the value obtained would differ only 0.00005 mass unit from the accepted mass. The ratios obtained for the sulfurs, combined with other measurements of S^{32} and S^{34} masses,[7] allow a determination of the mass difference $S^{36}-S^{34}=2.00055\pm0.0003$ and hence the hitherto unmeasured S^{36} mass as 35.97834±0.0004 m.u.

Relative abundances and intensities are given in Table II. The $(O^{16}C^{12}S^{34}/O^{17}C^{12}S^{32})$ ratio agrees very well with previous measurements, but the ratio $(O^{17}C^{12}S^{32}/O^{16}C^{12}S^{36})$ disagrees slightly more than the error ±10 percent given by Nier[1] for his ratio of 1:6000 for the abundance of S^{36} to S^{32}. The present measurement gives an abundance for S^{36} of 0.0136±0.0010 percent or 1:7000 relative to S^{32}.

* Work supported by the Signal Corps.

[1] A. O. Nier, Phys. Rev. 53, 282 (1938).
[2] R. H. Hughes and E. B. Wilson, Phys. Rev. 71, 562 (1947).
[3] C. H. Townes, A. N. Holden, and F. R. Merritt, Phys. Rev. 74, 1113 (1938).
[4] Cf. Columbia Radiation Lab., *Progress Report*, Sept. 30, 1948.
[5] For discussion of this type calculation see reference 3.
[6] E. Segrè Chart, *The Science and Engineering of Nuclear Power* (Addison-Wesley Press, Inc., 1947).
[7] P. Davison, Phys. Rev. 74, 1233 (1948).

On the Geiger-Nuttall Relationship

SUKUMAR BISWAS
Institute of Nuclear Physics, University of Calcutta, Calcutta, India
December 13, 1948

THE Geiger-Nuttall relation, $\log\lambda=a+bE$, which has played a fundamental part in the understanding of nuclear phenomena, is modified and refined in the present work. It is shown that instead of plotting the isotopes of each radioactive series as is usually done,[1] the relationship will be valid and the curve will be a smooth one only when isotopes of same atomic number are plotted, as suggested by Berthellot.[2]

The theoretical background of this assumption is as follows. Assuming the potential barrier near a nucleus to be the result of an inverse square field up to a distance r_0 and a rectangular hole for distance less than r_0, the transparency of the potential barrier for α-particles, as calculated by A. K. Saha,[3] is $T=2e^{-2K}$. With semiclassical argu-

TABLE I. Polonium.

Isotopes	Observed half-life	α/β ratio	λ_α (sec.$^{-1}$)	α-energy (Mev)	Decay energy E, (Mev)
Po^{206}	9 d	$\frac{\alpha}{K}=\frac{10}{90}$	8.92×10^{-8}	5.2	5.3
Po^{207}	5.7 hr.	$\frac{\alpha}{K}\simeq\frac{0.01}{99.99}$	3.38×10^{-5}	5.1	5.2
Po^{208}	~3 yr.		7.33×10^{-9}	5.14	5.24
Po^{209}	?				
Po^{210}	140 d		5.89×10^{-8}	5.303	5.405
Po^{211}	5×10^{-3} sec.		1.39×10^{2}	7.434	7.543
Po^{212}	3.0×10^{-7} sec.		2.31×10^{6}	8.776	8.944
Po^{213}	3.2×10^{-6} sec.		1.58×10^{5}	8.336	8.496
Po^{214}	1.5×10^{-4} sec.		4.62×10^{3}	7.680	7.827
Po^{215}	1.83×10^{-3} sec.		3.79×10^{2}	7.365	7.504
Po^{216}	0.158 sec.	$\frac{99.086}{0.014}$	4.39	6.774	6.902
Po^{217}	?				
Po^{218}	3.05 min.	$\frac{99.96}{0.04}$	3.77×10^{-3}	5.998	6.110

ments of Laue[4] the disintegration constant comes out as

$$\lambda=(v/r_0)e^{-2K}, \tag{1}$$

where v=velocity of the α-particle, r_0=radius of the nucleus, $Z-2$, $2K=[16\pi e^2(Z-2)/hv][u_0-\sin u_0\cos u_0]$, $u_0=\cos^{-1}[mv^2r_0/4e^2(Z-2)]^{\frac{1}{2}}$.
From Eq. (1)

$$\log\lambda=\log v-\log r_0-0.4343[16\pi e^2(Z-2)/hv]\times[u_0-\sin u_0\cos u_0]. \tag{2}$$

In these calculations, the effect of relative motion of $(Z-2)$ nucleus is to be taken into account. So we are to use total decay energy $E=E_\alpha[1+(m_\alpha/m_r)]$, relative velocity of the α-particle $v=v_\alpha[1+(m_\alpha/m_r)]$, and reduced mass $m=m_\alpha m_r/(m_\alpha+m_r)$ in place of E_α, v_α, and m_α, respectively.

Transforming the above relation (2) in terms of energy in Mev, we have

$$\log\lambda=21.8428+\tfrac{1}{2}\log E_V+0.217(m_\alpha/m_r)-\log r_0-1.104\frac{(Z-2)}{E_V^{\frac{1}{2}}[1+(m_\alpha/m_r)]^{\frac{1}{2}}}\times\cos^{-1}[0.5896(E_V^{\frac{1}{2}}r_0^{\frac{1}{2}}/(Z-2)^{\frac{1}{2}})]+0.6504\frac{(Z-2)^{\frac{1}{2}}r_0^{\frac{1}{2}}}{[1+(m_\alpha/m_r)]^{\frac{1}{2}}}-0.1131\frac{r_0^{\frac{1}{2}}}{(Z-2)^{\frac{1}{2}}[1+(m_\alpha/m_r)]^{\frac{1}{2}}}\cdot E_V, \tag{3}$$

where E_V=decay energy in Mev, r_0=radius in 10^{-13}-cm unit. From this explicit relation between λ, E, r_0, and Z, it is seen that $\log\lambda$ depends not only on E but also on $(Z-2)$ and r_0. So in general cases it cannot be represented in a two-dimensional curve. However, the curve $\log\lambda$ against E is approximately valid if $(Z-2)$ is kept constant, since the variation of r_0 is small from one isotope to the other ones ($r_0\backsimeq R\cdot A^{\frac{1}{3}}$). The reason why Geiger-Nuttall could get a more or less smooth curve by plotting $\log\lambda$ against E, as pointed out by Gamow,[1] is due to the fact that variation of Z, E, and r_0 in a radioactive series is practically monotonic as we go down the series. Anomalies occur in original Geiger-Nuttall curves where this regularity breaks down. Thus the Geiger-Nuttall curves with constant Z will be more refined and less suceptible to anomalies.

These results can be compared with the available data of α-active nuclei. Since P_0 contains the largest number of α-active isotopes, the validity of the refined Geiger-Nuttall relation can be tested with it. In case of isotopes which decay both ways by α-disintegration and β-decay or K-capture, experiments give us only the composite life T, given by

$$1/T=(1/T_\alpha)+(1/T_\beta).$$

With another relation T_β/T_α=ratio particles disintegrating by α-decay to β-decay, the value of T_α is calculated, from which λ_α is to be plotted. The useful data for P_0 is given in Table I, taken from published data.[5-7]

With these data the plotted curve for Po is seen to be a smooth one (Fig. 1c). Only three points fall slightly outside the curve. Data for these require rechecking.

In order to compare this curve with the theoretical relation (3) we take the value of r_0 for the middle member Po^{216} ($r_0=8.63\times10^{-13}$ cm). With this constant value of r_0 in relation (3) we have

$$\log\lambda=38.0664-\frac{89.71}{E_V^{\frac{1}{2}}}\cos^{-1}(0.1923E_V^{\frac{1}{2}})+\tfrac{1}{2}\log E_V-0.3225E_V. \tag{4}$$

Plotting this we get the theoretical curve given in Fig. 1a. It is seen that the agreement with the experimental curve is satisfactory in the middle part but on both sides the theoretical curve diverges. However, instead of taking r_0 constant for all isotopes we can take the variation of r_0 from one isotope to another according to relation $r_0=R\cdot A^{\frac{1}{3}}$. Thus another theoretical curve is drawn from relation (3) (Fig. 1b). This curve (b) approaches the experimental curve (c) at the ends, but discrepancy still remains at the two ends, which shows that the theory of α-particle emission fails to account for very short-lived products as well as very long-lived ones.

Similarly, smooth, modified Geiger-Nuttall curves have been obtained for all elements from Bi to Pu. From a critical study of isotopes in this region, probable α- and β-activities as yet unknown have been predicted. The complete text will be published elsewhere.

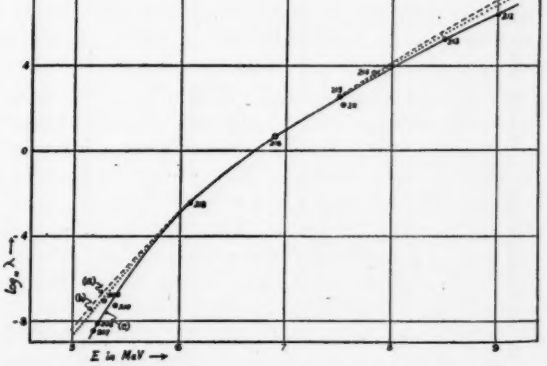

FIG. 1. The modified Geiger-Nuttall curve for polonium. (a) Theoretical curve with constant r_0. (b) Theoretical curve with $r_0=R\cdot A^{\frac{1}{3}}$. (c) Experimental curve.

The author is grateful to Professor M. N. Saha, F.R.S., for his continued interest and guidance of this work.

[1] G. A. Gamow, *Structure of Atomic Nuclei and Nuclear Transformations* (Clarendon Press, Oxford, 1937).
[2] Berthellot, J. de phys. et rad. 3, 52 (1942).
[3] A. K. Saha, Proc. Nat. Inst. Sci. Ind. 10, 373 (1944).
[4] Max von Laue, Zeits. f. Physik 52, 726 (1929).
[5] Glenn T. Seaborg, Rev. Mod. Phys. 16, 1 (1944).
[6] Templeton, Howland, and Perlman, Phys. Rev. 72, 758 (1947).
[7] English, Cranshaw, Demers, Harvey, Hincks, Jelley, and May, Phys. Rev. 72, 253 (1947).

A Model for Nuclear Capture of μ-Mesons

MARSHALL N. ROSENBLUTH*
University of Chicago, Chicago, Illinois
December 20, 1948

IT has been observed that negative μ-mesons, when stopped in materials of high atomic number, do not emit the energetic light charged particle usually associated with μ-meson decay.[1] This has been interpreted as meaning that the μ-meson in these cases is captured from its K-orbit by the nucleus.

It has further been established from photographic and cloud-chamber evidence that capture is not accompanied by formation of a "star,"[2] which excludes the possibility that a large fraction of the rest energy of the meson is converted into excitation of the nucleus. Christy has suggested that this be explained by assuming that most of the energy is carried off by a light neutral particle which is emitted in the capture.

It is the purpose of this letter to make an approximate quantitative study of the consequences of this model. We assume the nucleus to be a degenerate Fermi gas of free nucleons, with one of which the meson interacts, converting it from a proton to a neutron. The recoil energy of this nucleon is then quickly distributed throughout the nucleus by nucleon-nucleon collisions and should be regarded as an excitation energy of the nucleus.

Conservation of energy and momentum plus the condition that the neutron must go into a previously unoccupied state then determine a distribution of excitation energies which is to a first approximation independent of the details of the meso-nuclear interaction.

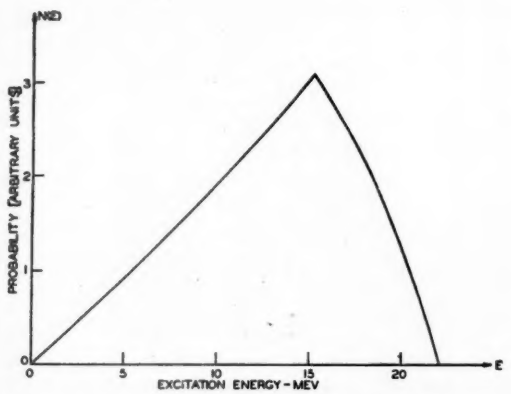

FIG. 1. Distribution of excitation energies.

We plot this distribution in Fig. 1 under the assumptions that (a) the number of neutrons and protons in the original nucleus is equal, (b) the μ-meson has a mass 210 times that of the electron, (c) the outgoing light particle has zero mass, (d) the momentum of the incident μ-meson is neglected, and (e) the nuclear radius is given by $r_0 = 1.5 \times 10^{-13} A^{\frac{1}{3}}$ cm.

The excited nucleus is the original nucleus with one proton converted to a neutron. From consideration of the binding energies of different types of particles in such a nucleus, and of the effect of the potential barrier, one is able to conclude that emission of anything but a neutron is highly improbable.

Moreover, since the binding energy of a neutron in a medium weight nucleus is about 8 Mev, one sees that the most probable number of neutrons emitted in a capture process is one—and that the average number of neutrons given off is also roughly one. It turns out that this conclusion is valid even in the case of heavy nuclei since the lowering of the neutron binding energy is compensated by the change which the large neutron excess in such nuclei causes in the distribution of excitation energies.

This model agrees with experimental evidence[3, 4] insofar as it predicts neutron emission, although the observed number of neutrons per capture seems to be larger than predicted here.

A more detailed investigation of this model is being made.

* National Research Council Fellow.
[1] M. Conversi, E. Pancini, and O. Piccioni, Phys. Rev. 71, 209 (1947).
[2] C. M. G. Lattes, G. P. S. Occhialini, and C. F. Powell, Nature 160, 453 (1947).
[3] G. W. McClure and G. Groetzinger, Bull. Am. Phys. Soc. 23, 7, 20 (1948).
[4] R. D. Sard, Bull. Am. Phys. Soc. 23, 7, 13 (1948).

Mass Spectrometer Determination of the Half-Life of Xe^{133}

J. MACNAMARA, C. B. COLLINS, AND H. G. THODE
Department of Chemistry, McMaster University, Hamilton, Ontario, Canada
December 13, 1948

THE half-life of Xe^{133} was determined from mass spectrometer abundance data in the course of our investigations of the rare gas fission products produced in uranium metal irradiated with thermal neutrons. Its value was found to be 5.271 ± 0.002 days. The mass spectrometer method of determining half-lives, first used by Thode and Graham,[1] completely eliminates difficulties from contamination with other radioactive isotopes and provides a most accurate means for determining half-life values in the range from several days to several years.

A. Langsdorf, Jr.,[2] bombarded thorium with neutrons and obtained a noble gas emitting soft radiations with an apparent period of 5.5 days. Since then various experimenters[3-11] have published values ranging from 4.3 ± 0.4 days[3] to 7 days[6] for the half-life of Xe^{133}. The most likely value given in the Plutonium Project Report (D. W. Engelkemeir and N. Sugarman) is 5.3 days. These values, obtained by radio-chemical methods, are accurate to only 1 or 2 percent, whereas the mass spectrometer method

TABLE I. Xe^{133} half-life from mass spectrometer abundance data.

Ratio of Xe mass ion currents×100	Time after first analysis (hr) 0	45.83	92.91	Xe^{133} half-life calculated (days)
133/(131+132)	34.60±0.005	26.91±0.006	20.79±0.015	5.263 5.276 5.270
133/(131+132+134+136)		7.022±0.01	5.430±0.02	5.276
			Average	5.271± 0.002

which involves comparative abundance data is good to 0.1 percent.

A small disk of uranium metal was irradiated and the rare gases extracted, purified, and analyzed within 10 days after the irradiation period. By comparing the abundance of the Xe^{133} isotopes with that of a stable xenon isotope (Table I) over time intervals of approximately two days, it was possible to follow the decay rate of Xe^{133}. Employing the decay equation $n = n_0 e^{-\lambda t}$, where n is the concentration at time t, n_0 is the concentration at zero time, and λ equals $(0.6932/T_{\frac{1}{2}})$, where $T_{\frac{1}{2}}$ is the half-life of the isotope in question, and substituting, for example, the 133/(131+132) ratio obtained with the mass spectrometer at different time intervals for n/n_0, the half-life of Xe^{133} can be found by solving for $T_{\frac{1}{2}}$.

Previous authors[4-8,10] have identified the mass chain of the 5-day β-emitter as 133 by the following reactions:

(1) $Cs^{133}(n, p)Xe^{133}$
(2) $Ba^{136}(n, \alpha)Xe^{133}$
(3) $Te^{130}(\alpha, n)Xe^{133}$
(4) $Xe^{132}(d, p)Xe^{133}$.

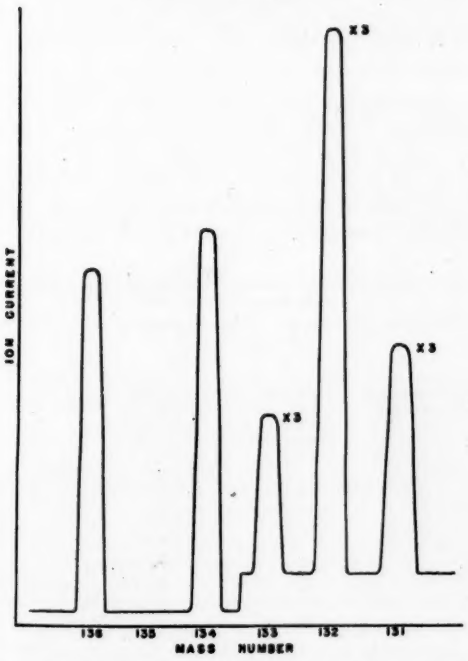

FIG. 1. Stable isotopes of fission product xenon, also xenon[133].

The mass spectrometer identification of Xe^{133}, see Fig. 1, together with abundance data for calculating its half-life is, of course, further direct evidence for the mass assignment of the fission chain leading to five-day xenon. Previous spectrograms by H. G. Thode and R. L. Graham[1] show no Xe^{133} because the uranium rods were allowed to stand for a number of months after irradiation to permit the various fission product chains to decay to the stable Xe^{131}, Xe^{132}, Xe^{134}, Xe^{136} isotopes.

The accurate half-life determinations possible from mass spectrometer abundance data for such isotopes as Xe^{133} and Kr^{85}, suggest that gases containing these isotopes be used in checking the efficiency of counters for absolute β-counting. Actually, the half-life values obtained for C^{14} by different workers vary from 4700 to 6400 years[12,13] largely because of difficulties in determining the efficiency of the counting equipment. There is a need, therefore, for gases convenient to handle for which the specific activity is accurately known.

We wish to thank the National Research Council of Canada for financial assistance and to acknowledge the use of facilities of the Chalk River Laboratories, particularly those of the Chemistry Division.

[1] H. G. Thode and R. L. Graham, Can. J. Research **A25**, 1–14 (1947).
[2] A. Langsdorf, Jr., Phys. Rev. **56**, 205 (1939).
[3] R. W. Dodson and R. D. Fowler, Phys. Rev. **57**, 967 (1940).
[4] Edward P. Clancy, Phys. Rev. **60**, 87 (1941).
[5] Chien-Shiung Wu and E. Segrè, Phys. Rev. **67**, 142 (1945).
[6] W. Riezler, Naturwiss. **31**, 326 (1943).
[7] W. Seelmann-Eggebert, Naturwiss. **31**, 491 (1943).
[8] Chien-Shiung Wu, Phys. Rev. **58**, 926 (1940).
[9] H. J. Born and W. Seelmann-Eggebert, Naturwiss. **31**, 201 (1943).
[10] Hilding Slätis, Arkiv f. Mat., Astr. o. Fys. **A32**, No. 16, 12 (1946).
[11] D. W. Engelkemeir and N. Sugarman, Plutonium Project Report 1946.
[12] L. D. Norris and M. G. Inghram, Phys. Rev. **73**, 350 (1948).
[13] Hawkins, Hunter, Mann, and Stevens, Phys. Rev. **74**, 696 (1948).

Natural Abundance Measurements on Germanium*

R. F. HIBBS, J. W. REDMOND, H. R. GWINN, AND W. D. HARMAN
Assay Laboratory Department, Carbide and Carbon Chemicals Corporation, Oak Ridge, Tennessee
December 10, 1948

IN conjunction with the electromagnetic separation of stable isotopes at the Y-12 Plant of Carbide and Carbon Chemicals Corporation, Oak Ridge, Tennessee, it became necessary for the Assay Laboratory Department to develop methods for the routine isotopic analyses of enriched germanium samples. Review of the literature failed to reveal recent measurements of the natural isotopic composition of this element, and the results of Aston's[1] work are shown in Table I. To check the reproducibility of the method and to provide more accurate data on the natural composition, these values were redetermined.

For the routine method, the compounds used had to be reliably prepared from small quantities of material, yielding a reproducibly pure product. Germanium tetraiodide and germanium tetrafluoride met these requirements. The tetraiodide was distilled through a heated delivery tube, and germanium tetrafluoride was admitted into the instru-

TABLE I. Relative abundances of germanium isotopes from measurements on GeF_4 and GeI.

Mass	70	72	73	74	76
GeF_3^+	20.60	27.38	7.83	36.40	7.78
Mean Dev.	±0.06	±0.08	±0.06	±0.10	±0.05
GeI^+	20.65	27.43	7.86	36.34	7.72
Mean Dev.	±0.04	±0.02	±0.04	±0.05	±0.01
Aston[a]	21.2	27.3	7.9	37.1	6.5

[a] See reference 1.

ment through a capillary leak. Ionization in the Nier-type mass spectrometer was accomplished by slow electron bombardment of the vapors. The ions thus formed were accelerated by a potential of 2000 volts and separated with the conventional sector magnet. The resulting ion currents were measured with an FP54 electrometer tube, balancing the potential developed across the grid resistor with a potential from a precision potentiometer. The ion currents were also recorded by use of a Victoreen VX-41 electrometer tube, driving a standard Brown Electronik Recorder. The vacuum was approximately 5×10^{-7} mm of Hg, and the resolution in all cases was perfect.

In the case of the tetrafluoride, the measurements were made upon the GeF_3^+ ion, and the GeI^+ ion was used for measurements when the tetraiodide was distilled into the instrument. The results obtained with these compounds are shown in Table I.

The abundances, using GeF_4, are the result of three samples in two instruments and the GeI_4 measurements of two samples in one instrument. It was found that variations between instruments and between ion sources in the same instrument were larger than variations between samples. Investigation of the mass region, adjacent to the measured ions, revealed it exceptionally free from interfering ions of other materials.

* This document is based on work performed for the AEC by Carbide and Carbon Chemicals Corporation, at Oak Ridge, Tennessee.

[1] Aston, *Mass Spectra and Isotopes* (Edward Arnold and Company, London, 1944), p. 154.

Erratum: Significance of the Radioactivity of Potassium in Geophysics. II

[Phys. Rev. 74, 831 (1948)]

T. GRÅF
L. Meitner Laboratory of Nuclear Physics, IVA:s Försöksstation, Stockholm, Sweden

December 15, 1948

THE sentence at the end of the second paragraph on page 832 should read:

"In addition, to account for the large amounts of atmospheric argon, it should then be assumed that all argon produced in a 40-kilometer deep crustal layer, since the origin of the earth, has escaped into the atmosphere."

Not ". . . that all argon was produced in a 40-kilometer deep crustal layer, since the origin of the earth has escaped into the atmosphere."

Erratum: Line Shapes in Nuclear Paramagnetism

[Phys. Rev. 74, 1184 (1948)]

G. E. PAKE AND E. M. PURCELL
Lyman Laboratory of Physics, Harvard University, Cambridge, Massachusetts

A FACTOR ½ should be supplied to the right member of each of Eqs. (8), Eq. (10), Eq. (11), and the first of Eqs. (1) to make these formulae accurate for frequency ν in the vicinity of the resonant frequency ν_0. The graphs in Figs. 2 and 3 will then read properly if ordinates are measured in units of $\frac{1}{2}\chi_0\omega_0T_2$.

It should be emphasized that the approximations $\nu/(\nu'+\nu)\cong\frac{1}{2}$ and $\nu'/(\nu'+\nu)\cong\frac{1}{2}$, which hold near resonance and lead to the special forms (3), (4), and (5) of the Kronig-Kramers relations, are evidently not valid at $\nu=0$. Thus the forms of $\chi'(\nu)$ derived from these approximations do not reduce to χ_0 at $\nu=0$ as stated in the paper, but should reduce to $\frac{1}{2}\chi_0$ instead. Supplying the above-mentioned factors ½ takes care of this point, which the authors regrettably overlooked.

On the Numerical Calculation of the Internal Conversion in the *K*-Shell; the Electric Dipole Case

B. A. GRIFFITH AND J. P. STANLEY
University of Toronto, Toronto, Canada

October 25, 1948

THE accurate calculation of internal conversion coefficients is a problem in which recent experimental advances have stimulated considerable interest. Some months ago at the instigation of members of the staff of the National Research Council of Canada at Chalk River, the writers undertook an extensive tabulation of such coefficients in connection with a computational program at the University of Toronto. Recently, it has been learned that similar calculations are being done with the aid of the Harvard Mk II computer. Accordingly, further work here has been suspended pending publication of the Harvard calculations. However, the results which the writers have

TABLE I. Values of the coefficient $2I_k$ for the two electrons of the *K*-shell.

θ \ Z	89	84	79	74	69
0.05	0.00007429	0.00006297	0.00005390		
0.10	0.0002008	0.0001667	0.0001393		
0.15	0.0003772	0.0003056	0.0002530		
0.20	0.0005938	0.0004769	0.0003941		
0.25	0.0008497	0.0006773	0.0005611		
0.50	0.002706	0.002228	0.001825	0.001485	0.001198
0.70	0.004922	0.004112	0.003405	0.002797	0.002280
1.00	0.009736	0.008304	0.006956	0.005810	0.004805
1.50	0.02248	0.01956	0.01687	0.01440	0.01214
1.70	0.02949	0.02593	0.02253	0.01936	0.01642

Note. In the above Table, $2I_k$ denotes the fraction of photons with energy $h\nu$, emitted by the nucleus, which are absorbed by either of the two electrons in the *K*-shell with ejection of the absorbing electron from the atom. No allowance for screening effects has been made.

The parameters Z and θ denote, respectively, the atomic number and the ratio $mc^2/h\nu$, where mc^2 is the smallest relative energy of a free electron. The value 1/137 has been taken for the fine structure constant.

already obtained for the conversion coefficient ($2I_k$) corresponding to the K-shell in the electric dipole case may be of some interest and are tabulated below (Table I).

These values for I_k were calculated with the aid of a Fridén Calculating Machine (Model ST-10) and five significant digits were carried throughout the calculations. Results, however, are quoted to four significant digits only. The formula on which these calculations are based is essentially that given by Hulme.[1] Actually it has been found that Hulme's formula for I_k may be written in the following simplified form:

$$I_k=\frac{\gamma^{3+2\beta}\{[1+\beta+(1/\theta)]^2-1\}^{(\frac{1}{2}+\beta)}e^{b\pi}|\Gamma(1+\beta-ib)|^2}{24(137)(2+\beta)\Gamma(3+2\beta)|(-z)-(1+\beta-ib)|^2}\times[2|P|^2+|Q|^2],$$

where

$$|Q|^2=8(2+\beta)(1-\theta)^2|(1-z^{-1})^{-(1+\beta+ib)}|^2,$$

$$P=P_1+\frac{\Gamma(s+2+\beta)\Gamma(-\beta-1+ib)\Gamma(s+2-ib)}{\Gamma(s+1-\beta)\Gamma(s+1+ib)\Gamma(1+\beta-ib)}\times(-z)^{-(1+\beta-ib)}P_2,$$

and

$$P_1=vF(s+1+ib,\ ib-s-1,\ ib-\beta,\ z^{-1})+wz^{-1}\left[\frac{1-s+i(b+c)}{1-s-i(b+c)}\right]\left[\frac{s+1+ib}{-\beta+ib}\right]\times F(s+2+\beta,\ \beta-s,\ 2+\beta-ib,\ z^{-1}),$$

$$P_2=vF(s+2+ib,\ ib-s,\ ib-\beta+1,\ z^{-1})+w\left[\frac{1-s+i(b+c)}{1-s-i(b+c)}\right]\left[\frac{-\beta-1+ib}{s+1-ib}\right]\times F(s+2+\beta,\ \beta-s,\ 1+\beta-ib,\ z^{-1}),$$

$$v=\gamma(\theta(2+\beta)+1)^{\frac{1}{2}}(\theta-1)+i[-3(\theta(2+\beta)+1)^{\frac{1}{2}}+(\theta\beta+1)^{\frac{1}{2}}(1-\beta+\theta\{2+\beta\})],$$

$$w=-\gamma(\theta(2+\beta)+1)^{\frac{1}{2}}(\theta-1)+i[+3(\theta(2+\beta)+1)^{\frac{1}{2}}+(\theta\beta+1)^{\frac{1}{2}}(1-\beta+\theta\{2+\beta\})].$$

The notation is that of Hulme.

With this simplified formula for I_k, it was possible for one of the writers to complete the calculations for the forty values tabulated in approximately eight (8) weeks. A more detailed account of this work has been submitted to the National Research Council of Canada for publication at an early date.

[1] H. R. Hulme, "The internal conversion of radium C," Proc. Roy. Soc. **A138**, 642 (1932).

Relativistic Formulation of the Quantum Theory of Radiation

S. T. Ma
Dublin Institute for Advanced Studies, Dublin, Eire
December 10, 1948

IN the usual formulation of the quantum theory of radiation it is customary to eliminate from the theory the time and longitudinal components of the electromagnetic potential, and only the transverse components of the field are quantized.[1] It has recently been attempted by several authors to put the time and longitudinal components on the same footing with the transverse components by dealing with four different kinds of photons. The advantage of the new idea is obvious, but it may be worth while to point out a special situation which arises in a generalized theory of this kind.

Consider an arbitrary Fourier component of the electromagnetic field in vacuum. Let a_0 and $a_i (i=1, 2, 3)$ be the Fourier transforms of the time, longitudinal and transverse components of the electromagnetic potential multiplied by suitable numerical factors. Let $\bar{a}_0$ and $\bar{a}_i$ be their Hermitian conjugate operators (not to be confused with the adjoint operators in a theory involving indefinite metric). These operators satisfy the commutation rules

$$[a_0, \bar{a}_0]=-1, \quad [a_i, \bar{a}_i]=+1. \tag{1}$$

A straightforward generalization of the customary theory consists in introducing a representation in which the operators $a_0\bar{a}_0$ and $\bar{a}_i a_i$ are diagonal with non-negative integral eigenvalues n_0, n_i. The physical interpretation is that n_0, n_1, n_2, n_3 are, respectively, the numbers of temporal, longitudinal and transverse photons, a_0 and $\bar{a}_0$ are the emission and absorption operators for the temporal photons, $\bar{a}_i$ and a_i are the corresponding operators for the longitudinal and transverse photons. We denote by $\psi(n_0, n_1, n_2, n_3)$ the normalized eigenvectors.

A Hilbert vector Ψ representing a state of the electromagnetic field is subject to the supplementary conditions

$$(a_0-a_1)\Psi=0, \quad (\bar{a}_0-\bar{a}_1)\Psi=0. \tag{2}$$

In accordance with the superposition principle we express Ψ in the form

$$\Psi=\sum_{n_0, n_1, n_2, n_3}^{\infty} c(n_0, n_1, n_2, n_3)\psi(n_0, n_1, n_2, n_3). \tag{3}$$

From (1), (2), (3) it follows that

$$c(n_0, n_1, n_2, n_3)=0, \quad (n_0\neq n_1), \tag{4}$$

$$|c(0, 0, n_2, n_3)|=|c(1, 1, n_2, n_3)|=|c(2, 2, n_2, n_3)|=\cdots. \tag{5}$$

Equations (4) and (5) can also be derived from Dirac's theory of expansors. From these results we can draw the following conclusions: For any given number of transverse photons, Ψ does not represent a pure state but the superposition of an infinite number of states with equal numbers of temporal and longitudinal photons. These two kinds of photons have energies of opposite signs, so they do not contribute to the total energy of the electromagnetic field. They are present even when the total energy vanishes. They have, therefore, quite different properties from those of the transverse photons. A further new feature is that the vector Ψ has an infinite length unless all the c's are zero, and therefore cannot be normalized.

The situation pointed out here should be cleared up in connection with the recent discussions of Schwinger's formulation of quantum electrodynamics.[2]

[1] P. A. M. Dirac, *Principles of Quantum Mechanics* (Oxford University Press, London, 1947), Chap. XII; W. Heitler, *Quantum Theory of Radiation* (Oxford University Press, London, 1944), Chap. II. A relativistic formulation of the elimination has recently been developed by S. Hayakawa, Y. Miyamoto, and S. Tomonaga, by J. Schwinger, and by S. Ashauer.

[2] G. Wentzel, Phys. Rev. 74, 1070 (1948); F. J. Belinfante, Bull. Am. Phys. Soc. 23, No. 7, 17 (1948).

THE AMERICAN INSTITUTE OF PHYSICS

INCORPORATED

57 East 55 Street New York 22, N.Y.

MEMBER SOCIETIES:

American Physical Society
KARL K. DARROW, *Secretary*, Columbia University, New York 27, New York.

Optical Society of America
ARTHUR C. HARDY, *Secretary*, Massachusetts Institute of Technology, Cambridge 39, Massachusetts.

Acoustical Society of America
WALLACE WATERFALL, *Secretary*, 57 East 55th Street, New York 22, New York.

Society of Rheology
EARL K. FISCHER, *Secretary*, Institute of Textile Technology, Charlottesville, Virginia.

American Association of Physics Teachers
C. J. OVERBECK, *Secretary*, Northwestern University, Evanston, Illinois.

AFFILIATED SOCIETIES:

American Society for X-Ray and Electron Diffraction

Electron Microscope Society of America

Physical Society of Pittsburgh

Physics Club of Chicago

Physics Club of Philadelphia

Cleveland Physics Society

Physics Club of the Lehigh Valley

ASSOCIATES:

Over seventy-five leading industrial enterprises and other institutions which contribute to the support of the Institute.

JOURNALS:

The Physical Review
JOHN T. TATE, *Editor*, University of Minnesota, Minneapolis, Minnesota.

Reviews of Modern Physics
J. W. BUCHTA, *Editor*, University of Minnesota, Minneapolis, Minnesota.

Journal of the Optical Society of America
GEORGE R. HARRISON, *Editor*, Massachusetts Institute of Technology, Cambridge, Massachusetts.

The Journal of the Acoustical Society of America
FLOYD A. FIRESTONE, *Editor*, 3318 Fessenden Street, N.W., Washington, D. C.

American Journal of Physics
THOMAS H. OSGOOD, *Editor*, Michigan State College, East Lansing, Michigan.

The Review of Scientific Instruments
GAYLORD P. HARNWELL, *Editor*, Randal Morgan Laboratory of Physics, University of Pennsylvania, Philadelphia, Pennsylvania.

The Journal of Chemical Physics
JOSEPH E. MAYER, *Editor*, Kent Chemical Laboratory, University of Chicago, Chicago 37, Illinois.

Journal of Applied Physics
ELMER HUTCHISSON, *Editor*, Case Institute of Technology, Cleveland 6, Ohio.

Physics Today
DAVID A. KATCHMAN, *Editor*, American Institute of Physics, 57 East 55 Street, New York 22, New York.

OFFICERS

GEORGE R. HARRISON, *Chairman*
Massachusetts Institute of Technology

WALLACE WATERFALL, *Secretary*
The Celotex Corporation

LAURENCE B. PEGRAM, *Treasurer*
Columbia University

JOHN T. TATE,
Adviser on Publications
University of Minnesota

GOVERNING BOARD

LUIS W. ALVAREZ
ROBERT B. BROOM
E. U. CONDON
A. J. DEMPSTER
W. F. FAIR, JR.
HARVEY FLETCHER
R. C. GIBBS
GEORGE R. HARRISON
W. V. HOUSTON
PAUL E. KLOPSTEG
F. W. LOOMIS
PHILIP M. MORSE
GEORGE B. PEGRAM
A. H. PFUND
JOHN T. TATE
WALLACE WATERFALL
M. W. WHITE
A. G. WORTHING

Consultant on Printing
MELVIN LOOS

ADMINISTRATIVE STAFF

HENRY A. BARTON, *Director*
CLEVELAND NORCROSS,
General Manager
THEODORE VORBURGER,
Business Manager
RUTH F. BRYANS,
Publication Manager
BETTY HOFSTADTER, *Office Manager*
EILEEN B. NEUBERGER,
Circulation Manager

THE American Institute of Physics was founded in 1931 as a federation of leading societies in the field of Physics. It combines into one operating agency those functions on behalf of physics which can best be done by the Societies jointly. Its purpose is the advancement and diffusion of physics and its application to human welfare. To this end it publishes for itself or the Societies the nine journals listed on this page; promotes unity and effectiveness of effort among all who are interested in physics; renders numerous direct services to physicists and to the public; and cooperates with government agencies, national associations, educational institutions, technical industries, and others in such manner as to realize the opportunities and fulfill the responsibilities of physics as an important and constructive human activity.

CONTENTS

THE PHYSICAL REVIEW — SECOND SERIES, VOL. 75, NO. 9 — PAGE

Experiments on [illegible] . . . J. HADLEY, E. KELLY, C. LEITH, E. SEGRÈ, C. WIEGAND, AND [illegible]

Stars in Photographic [illegible] Produced by Deuterons: Part I. Experimental . . . EUGENE GARDNER AND [illegible]

Stars in Photographic [illegible] Produced by Deuterons: Part II. Theoretical . . . W. HEITLER AND [illegible]

Stars in Photographic [illegible] Produced by Deuterons: Part III. Statistical . . . EUGENE GARDNER

Positive Mesons [illegible] Nuclear Disintegrations . . . JAMES HADLEY, EUGENE GARDNER, AND [illegible]

On the Self-[illegible] . . . NORMAN M. KROLL AND WILLIS E. [illegible]

Study of Phase [illegible] of Nuclear Magnetic Resonance Phenomena . . . [illegible]

High Frequency [illegible] . . . A. D. MACDONALD AND [illegible]

On the Scattering of [illegible] . . . C. L. CRITCHFIELD AND [illegible]

Investigation of [illegible] of the Nuclear Interaction of Indium . . . WALTER C. MILLER AND [illegible]

82-Mev Gamma-Ray [illegible] . . . JAMES [illegible]

Angular and Lateral [illegible] . . . JAMES ROBSON AND L. W. [illegible]

Application of a [illegible] to the Measurement of Gamma-Radiation from Rn and Ra . . . HILDRED N. JENSEN, L. JACKSON LABLETT, AND WILLIAM [illegible]

Magnetic Susceptibility [illegible] . . . CLYDE A. HUTCHISON, JR.

Multiple Compton [illegible] . . . W. R. KANNE AND M. [illegible]

Conductivity Induced [illegible] Luminescence in Thin Insulating Films . . . [illegible]

Recording of Electron [illegible] . . . [illegible]

Radiation Theories of [illegible] . . . [illegible]

Note on a Theorem of [illegible] Quantum Theory of Superconductivity . . . [illegible]

Precision Study of the [illegible] Spectrometer Using the 2-Meter Bending Curved Crystal Spectrometer . . . HERBERT A. WATSON, WILLARD J. WEST, DAVID A. LIND, AND JESSE W. M. [illegible]

Beta-Decay of Ba[illegible] and [illegible] Beta-Decay . . . [illegible]

Beta-Spectrum of Ba[illegible] . . . D. J. HUGHES, C. ROSNER, AND C. H. [illegible]

Letters to the Editor:

Absorption of [illegible] Protons . . . JOHN TUPPY AND [illegible]

Correlation of [illegible] and Gamma-Rays . . . JOHN TAYLOR AND [illegible]

Excited States of [illegible] . . . GEORGE C. MORRIS, ROBERT R. MCMATH, AND [illegible]

Passage of [illegible] Protons through Thin Films at High Temperatures . . . ERWIN W. [illegible]

Magnetic [illegible] . . . W. [illegible]

H^3 and the [illegible] Reaction . . . W. A. BOWERS AND [illegible]

τ-Radiation [illegible] . . . KAI SIEGBAHN AND [illegible]

V-2 Cloud [illegible] of a Highly Charged Primary Cosmic Ray . . . [illegible]

[illegible] . . . E. [illegible], M. L. KIDDER, G. J. PERLOW, AND C. A. [illegible]

Fermentation [illegible] Iron Cooling . . . G. E. [illegible]

Cadmium [illegible] Counter . . . G. J. GOLDSMITH AND E. [illegible]

Yields of [illegible] Beta-Emitters in the High Energy Helium-Ion Bombardment of [illegible] . . . E. D. WOLFE AND M. S. [illegible]

Maximum [illegible] Radiation from the Decay of Cl^{38} . . . FRANCIS JOHNSTON AND JOHN S. [illegible]

Magnetic [illegible] . . . I. S. LOWEN AND M. [illegible]

O^{17} and F^{19} [illegible] . . . W. J. LOW AND C. H. [illegible]

On the [illegible] . . . [illegible]

Model for [illegible] of β-Decay . . . MAHESHA N. [illegible]

Mass Spectroscopic [illegible] of the Half-Life of Kr^{85} . . . J. MACNAMARA, C. E. COLLINS, AND E. G. [illegible]

Natural [illegible] in Germanium . . . [illegible]

Erratum: [illegible] . . . E. P. HARRIS, J. W. KENNEDY, H. R. GRIEGO, AND W. [illegible]

Erratum: [illegible] . . . G. E. PAKE AND [illegible]

On the [illegible] of the Removal Correction in the K-Shell; the Electron [illegible] . . . E. A. GRIFFITH AND [illegible]

Relativistic [illegible] of the Quantum Theory of Radiation . . . [illegible]

LANCASTER PRESS, INC., [illegible]